Proceedings

of the Third Seminar on

THE MECHANICS OF MULTIFUNCTIONAL MATERIALS

J. Schröder, D.C. Lupascu, H. Wende, D. Brands (Eds.)

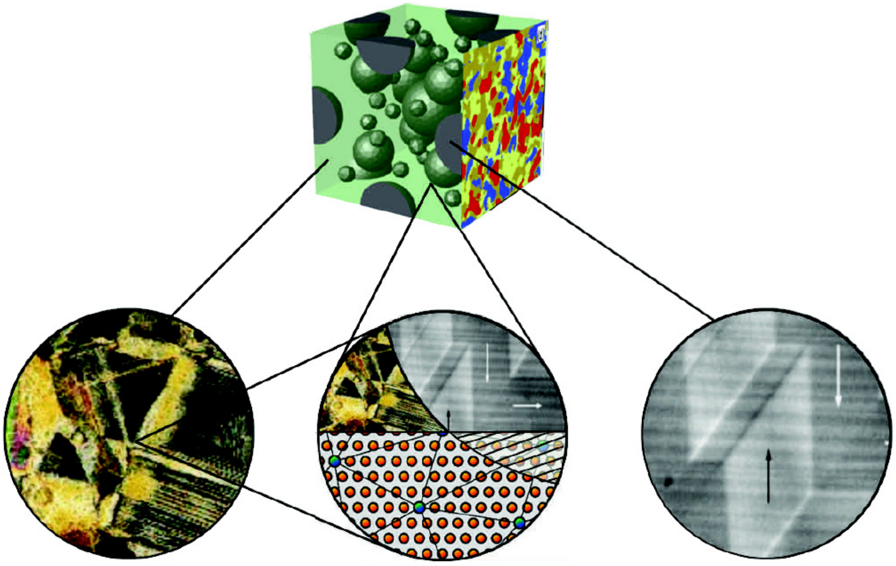

Physikzentrum Bad Honnef

June 11 - 15, 2018

Report No. 18
Institute of Mechanics
Department of Civil Engineering
Faculty of Engineering
University of Duisburg-Essen

Editors:

Prof. Dr.-Ing. habil. Jörg Schröder
University of Duisburg-Essen
Faculty of Engineering
Department of Civil Engineering
Institute of Mechanics
Universitätsstr. 15
45141 Essen

Prof. Dr. rer. nat. Doru C. Lupascu
University of Duisburg-Essen
Faculty of Engineering
Institute for Materials Science and Center for Nanoengineering Duisburg-Essen (CENIDE)
Universitätsstr. 15
45141 Essen

Prof. Dr. rer. nat. Heiko Wende
University of Duisburg-Essen
Faculty of Physics and
Center for Nanoengineering
Duisburg-Essen (CENIDE)
Lotharstr. 1
47048 Duisburg

Dr.-Ing. Dominik Brands
University of Duisburg-Essen
Faculty of Engineering
Department of Civil Engineering
Institute of Mechanics
Universitätsstr. 15
45141 Essen

ISBN-10 3-9818074-4-8
ISBN-13 978-3-9818074-4-8
EAN 9783981807448

Preface

Multifunctional materials are key ingredients in many modern technical devices ranging from consumer market items to applications in high-end equipment for automobile, aircraft, spacecraft, and information technology. The understanding and development of multifunctional materials is based on a comprehensive understanding of both the experimental and the theoretical details of these materials. Thus, we are delighted to welcome in this seminar national and international experts in continuum mechanics, applied mathematics, and materials science. The topics addressed in the lectures will span modeling, simulation, and experiments in fields ranging from ferroelectrics and -magnets, multiferroics and multiferroic composites, magnetorheological and electroactive elastomers, lithium ion batteries, to polymer blends, alloys, and porous media. This great range of inherently allied fields allows for a broad and deep insight into the scientific activities and advancements of all the reasearch disciplines involved.

Thus, we are happy to welcome more than 50 attendees to this seminar which takes place at the *Physikzentrum* Bad Honnef. The *Physikzentrum* has been serving as the main meeting point of the German Physical Society since 1976. Located close to Germany's oldest nature preserve with beautiful views on the Rhine river the place offers a perfect platform for intensive discussions. Therefore, we hope that the seminar will be successful in fostering greater interactions among all the scientific disciplines involved as well as between young and established researchers.

The proceedings at hand provide the extended abstracts of 36 lectures presented at the seminar. We would like to heartily thank all authors and participants for their kind cooperation and contribution to this workshop. We wish all participants a fruitful seminar and a nice stay at the *Physikzentrum*.

Sincerely,
The organizers

Jörg Schröder,
Doru C. Lupascu,
Heiko Wende,
Dominik Brands

Acknowledgement

The financial support through the *Deutsche Forschungsgemeinschaft* in the framework of the Research Unit 1509 “Ferroic Functional Materials – Multiscale Modeling and Experimental Characterization” is gratefully acknowledged.

Sincerely,
The organizers

Extended Abstracts

RELAXOR FERROELECTRIC NA$_{1/2}$BI$_{1/2}$TIO$_3$ STUDIED BY FIRST-PRINCIPLES CALCULATIONS: PHASE TRANSFORMATION KINETICS AND IONIC CONDUCTIVITY

Kai Meyer, Leonie Koch and Karsten Albe[*]

Fachgebiet Materialmodellierung, Institut für Materialwissenschaft, Technische Universität Darmstadt
Otto-Berndt-Str. 3, D-64287 Darmstadt, Germany

Abstract. *$Na_{1/2}Bi_{1/2}TiO_3$ (NBT) and its solid solutions with other lead-free perovskite materials are of interest for applications in actuators, sensors, and transducers due to their excellent piezoelectric properties. Bi-deficient NBT is an excellent ion conductor and the materials has also been discussed for applications in solid state refigeration, because of a significant negative electrocaloric effect. The physical origins of these properties are, however, still unclear. In this contribution, results of first-principles calculations will be presented which address coupling of cation order and tilt kinetics as well as impact of phase transitions on the ionic conductivity of this material.*

Chemically disordered ferroelectric perovskites very often exhibit relaxor properties characterized by a strong frequency- dependent dielectric susceptibility. Relaxors possess giant piezoelectric constants, which make them technologically interesting for actuator and ultrasonic transducer applications. It is assumed that chemical disorder induces local random fields, which are responsible for the existence of the so-called polar nanoregions. One class of materials interesting to study in this context is A-site mixed bismuth titanates $M_{1/2}Bi_{1/2}TiO_3$, with the relaxor ferroelectric $Na_{1/2}Bi_{1/2}TiO_3$ (NBT) being the most prominent representative.

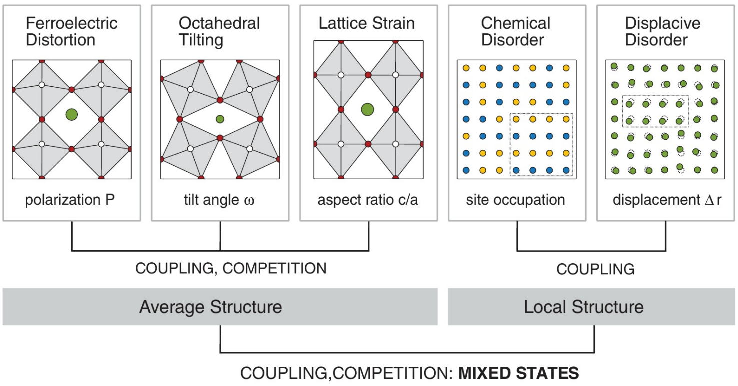

Figure 1: Order parameters relevant in $Na_{1/2}Bi_{1/2}TiO_3$. Ferroelectric distortion, octahedral tilting, and anisotropic lattice strain characterize the average crystal structure, while chemical and displacive disorder/short-range order lead to deviations from the average structure on the local scale. The given order parameters can interact by coupling or competition. If different local structures, for example, chemically ordered and disordered areas, favor different average structures, mixed phase states can result.

---

[*] Corresponding author: K. Albe (✉ albe@mm.tu-darmstadt.de)

⇒ TABLE OF CONTENTS

Bi^{3+} possesses the same kind of stereochemically active $6s^2$ lone-pair as Pb^{2+} , which leads to pronounced cation off- centring and which is considered to be decisive for the development of strong ferroelectricity. The delicate interplay of various order parameters (see Fig. 1) characterizing this material makes the physical understanding of its properties challenging. In this contribution, results from total energy calculations within electronic density functional theory will be presented. We specifically address the interplay of cation order and octahedral tilting [3, 4, 5] and the coupling of phase transitions to the defect chemistry [1, 2] A defect chemical model is proposed to explaing the extraordinary ionic conductivity of Bi-deficient $Na_{1/2}\,Bi_{1/2}\,TiO_3$.

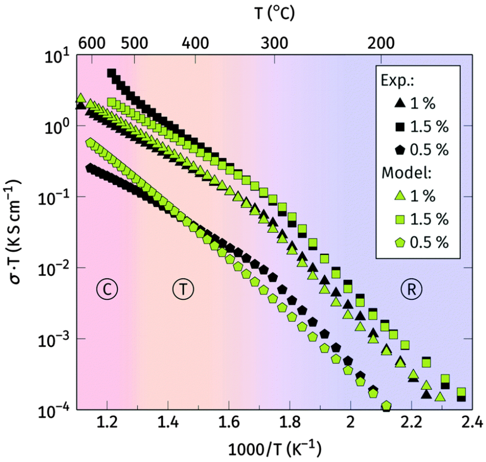

Figure 2: Phase dependent conductivity model. Background colors again specify the phases present at certain temperatures

REFERENCES

[1] Leonie Koch, Sebastian Steiner, Kai-Christian Meyer, In-Tae Seo, Karsten Albe, and Till Froemling. Ionic conductivity of acceptor doped sodium bismuth titanate: Influence of dopants, phase transitions and defect associates. *J. Mater. Chem. C*, 5(35):8958–8965, September 2017. ISSN 2050-7526. doi: 10.1039/c7tc03031b.

[2] Kai-Christian Meyer and Karsten Albe. Influence of phase transitions and defect associates on the oxygen migration in the ion conductor Na1/2Bi1/2TiO3. *J. Mater. Chem. A*, 5(9): 4368–4375, 2017. ISSN 2050-7488. doi: 10.1039/c6ta10566a.

[3] Kai-Christian Meyer, Melanie Gröting, and Karsten Albe. Octahedral tilt transitions in the relaxor ferroelectric $Na_{1/2}Bi_{1/2}TiO_3$. *J Solid State Chem*, 227:117 – 122, 2015. doi: 10.1016/j.jssc.2015.03.023.

[4] Kai-Christian Meyer, Leonie Koch, and Karsten Albe. Phase transformations in the relaxor Na $_{1/2}$ Bi $_{1/2}$ TiO $_3$ studied by means of density functional theory calculations. *J. Am. Ceram. Soc.*, 101(1):472–482, January 2018. ISSN 00027820. doi: 10.1111/jace.15207.

[5] Florian Pforr, Kai-Christian Meyer, Márton Major, Karsten Albe, Wolfgang Donner, Uwe Stuhr, and Alexandre Ivanov. Relaxation of dynamically disordered tetragonal platelets in the relaxor ferroelectric 0.964 Na 1 / 2 Bi 1 / 2 TiO 3 - 0.036 BaTiO 3. *Phys. Rev. B*, 96 (18), November 2017. ISSN 2469-9950, 2469-9969. doi: 10.1103/PhysRevB.96.184107.

⇒ TABLE OF CONTENTS

BULK PHOTOVOLTAIC EFFECTS AND STRAIN-RELATED PHOTO-EFFECTS IN NON-CENTROSYMMETRIC MATERIALS

Marin Alexe

Department of Physics, University of Warwick
Gibbet Hill Road, Coventry, UK

Abstract. Two years after the invention of modern prototype solar cells, it was found that a ferroelectric material, $BaTiO_3$, exhibits a photovoltaic effect distinct from that of *p-n* junctions, later called the bulk photovoltaic (BPV) effect. Under uniform illumination, a homogeneous ferroelectric material gives rise to a current under zero bias, i.e. short-circuit current (I_{SC}), that depends on the polarization state of the incident light, and produces an anomalously large photo-voltage well exceeding the bandgap energy. The microscopic origins of this effect are still under debate. It supposed to originate from the asymmetric distribution of photoexcited non-equilibrium carriers in *k*-space, caused by absence of centrosymmetry in the material. In the recent past, the entire field of photo-ferroelectrics has been revitalized by the reports of photovoltaic effect in $BiFeO_3$ (BFO), which is a ferroelectric/multiferroic material with one of the lowest band gap and significant semiconducting properties.

The present lecture will firstly present a short history and the basics of the bulk photovoltaic effect, tip enhancement, as well as the electronic origin of the anomalous BPV in some materials such as $BiFeO_3$. Later, potential applications such as energy harvesting or light-induced reversible switching of ferroelectric polarization at room temperature. I will show how the tip-enhanced effect, i.e. enhancement of the short-circuit photocurrent density at an AFM tip contact area, may be at the basis of harvesting devices with efficiency exceeding the Schokely-Quesser limit or, alternatively, generate a local electric field well exceeding ferroelectric coercive fields. Finally, I may discuss a new photovoltaic effect which turns the BPV effect into a universal effect allowed in all semiconductors by mediation of the flexoelectric effect. [1]

REFERENCES

[1] Yang, M.-M., Kim, D. J., & Alexe, M., Flexo-photovoltaic effect, Science, DOI: 10.1126/science.aan3256, 2018.

---

[*] Corresponding author: M.Alexe@warwick.ac.uk

⇒ TABLE OF CONTENTS

DERIVATION OF ENERGY BOUNDS VIA PERTURBATIONS OF CURL-FREE AND DIVERGENCE-FREE FIELDS—APPLICATION TO MAGNETIZABLE SOLIDS

T. Bartel[1], **B. Kiefer**[2,*], **and A. Menzel**[1,3]

[1] Institute of Mechanics, TU Dortmund
Leonhard-Euler-Str. 5, 44227 Dortmund, Germany

[2] Institute of Mechanics and Fluid Dynamics, TU Bergakademie Freiberg
Lampadiusstr. 4, 09596 Freiberg, Germany

[3] Division of Solid Mechanics, Lund University
PO Box 118, 22100 Lund, Sweden

Abstract. *The accurate prediction of the effective macroscopic behaviour of materials, whose microstructure and in particular its evolution plays a significant role, is a challenging task. In this context, energy relaxation methods were shown to provide sophisticated frameworks for the modelling of the behavior of phase-transforming materials such as shape memory alloys. Based on non-convex multi-well energy landscapes, the derivation of, e.g., rank-one-convex, polyconvex, or convex hulls aim at the approximation of the quasiconvex envelope. The quasiconvexification exhibits three major benefits: (i) It provides mathematically sound models due to its relation to existence proofs, (ii) it provides physically sound models due to the fact that the related minimizing sequences show strong similarities to real microstructures, and (iii) it provides the optimal homogenization method. In this regard, the rank-one convexification w.r.t. first order laminates is the most commonly used scheme to approximate the quasiconvex hull. In this contribution, first-order-laminate-based perturbations of scalar and vector-valued magnetic potentials are discussed. With this, energy relaxation schemes are applied to magnetizable solids, where in particular the perturbation of the vector-valued magnetic potential yields a lower bound to the quasiconvex envelope.*

1 Introduction

In this section, the basic concept of energy relaxation methods shall be outlined for the purely mechanical case, where the framework is restricted to two phases of the underlying material. As a basis, an energy density of the phase mixture is defined according to

$$\psi(\boldsymbol{F}, [\![\boldsymbol{F}]\!], \xi) := [1-\xi]\,\psi_{(1)}(\boldsymbol{F}_{(1)} \cdot [\boldsymbol{F}^{\mathrm{in}}_{(1)}]^{-1}) + \xi\,\psi_{(2)}(\boldsymbol{F}_{(2)} \cdot [\boldsymbol{F}^{\mathrm{in}}_{(2)}]^{-1})\ . \tag{1}$$

The indices (1) and (2) refer to different phases, $\boldsymbol{F}_{(i)}$ is the total deformation gradient in phase i, accordingly, $\boldsymbol{F}^{\mathrm{in}}_{(i)}$ is the related inelastic part of the deformation gradient, and ξ denotes the volume fraction of phase 2. The total deformation gradients may differ from each other with $[\![\boldsymbol{F}]\!] := \boldsymbol{F}_{(2)} - \boldsymbol{F}_{(1)}$. In general, the (partial) relaxation of the underlying averaged energy density can be formulated as

$$\psi^{\mathrm{rel}}(\boldsymbol{F}, \xi) := \inf_{[\![\boldsymbol{F}]\!]} \{\psi(\boldsymbol{F}, [\![\boldsymbol{F}]\!], \xi)\}\ . \tag{2}$$

---

[*] Corresponding author: T. Bartel (✉ thorsten.bartel@udo.edu)

Depending on the specific ansatz for the jump of the deformation gradient, different relaxation or, in other words, homogenization schemes are obtained. For example, the rank-one-convexification w.r.t. first order laminates is obtained via

$$[\![\boldsymbol{F}]\!] \in \left\{ \boldsymbol{a} \otimes \boldsymbol{n} | \boldsymbol{a} \in \mathbb{R}^3 \right\} \ , \tag{3}$$

where $\boldsymbol{n}$ is the unit outward normal of the interface. This ansatz, which is is also known as Hadamard compatibility, fulfills both equilibrium of forces normal to the interface and kinematical compatibility perpendicular to the interface normal. However, a major drawback of this approach is that it yields an upper bound to the quasiconvex envelope and thus, the underlying "global" problem may still be ill-posed. This motivates the aims of the present contribution: (i) in general, the application of energy relaxation schemes to magnetizable solids, (ii) in particular, the derivation of a lower bound to the quasiconvex hull based on first order laminates.

The essential aspects and some enhancements of the standard approach to model phase transformations using laminate-based energy relaxation schemes can, for example, be found in [1] in the context of shape memory alloys. This concept has been adapted to magnetomechanically coupled materials such as magnetic shape memory alloys in [2], where energy relaxation was only applied to the mechanical part, though. The essential ideas behind the modelling framework elaborated in this contribution can also be found in [3].

2 Relaxation methods for magnetizable solids

The point of departure is the definition of energy densities for each single phase, viz.

$$\psi_{(i)}(\boldsymbol{b}_{(i)}) := \frac{1}{2} \, [\boldsymbol{b}_{(i)} - \boldsymbol{b}^{\text{rem}}_{(i)}] \cdot \boldsymbol{\beta}_{(i)} \cdot [\boldsymbol{b}_{(i)} - \boldsymbol{b}^{\text{rem}}_{(i)}] + \psi^{\text{cal}}_{(i)} \tag{4}$$

as a function of the reversible magnetic induction, which is additively decomposed into the total magnetic induction $\boldsymbol{b}_{(i)}$ and a remanent contribution $\boldsymbol{b}^{\text{rem}}_{(i)}$. The quantities $\boldsymbol{\beta}_{(i)}$ reflect positive definite coefficient tensors and $\psi_{(i)}$ denote temperature-dependent caloric energy contributions. In order to derive analogous schemes, where the magnetic field $\boldsymbol{h}$ is the primary variable, the phase energy densities itself may be reformulated according to the Fenchel transformation

$$\psi'_{(i)}(\boldsymbol{h}_{(i)}) = \inf_{\boldsymbol{b}_{(i)}} \left\{ \psi_{(i)}(\boldsymbol{b}_{(i)}) - \boldsymbol{h}_{(i)} \cdot \boldsymbol{b}_{(i)} \right\} \tag{5}$$

which yields the free enthalpy densities

$$\psi'_{(i)}(\boldsymbol{h}_{(i)}) = -\frac{1}{2} \, \boldsymbol{h}_{(i)} \cdot \boldsymbol{\beta}^{-1}_{(i)} \cdot \boldsymbol{h}_{(i)} - \boldsymbol{h}_{(i)} \cdot \boldsymbol{b}^{\text{rem}}_{(i)} + \psi^{\text{cal}}_{(i)} \ . \tag{6}$$

2.1 Perturbation of the scalar magnetic potential

For the derivation of the relaxed enthalpy density, the scalar magnetic perturbation field ϕ^{pert} is introduced. According to the underlying first order laminates, ϕ^{pert} is piecewise linear and exhibits a kink at the interface such that the total magnetic field in each phase is given by

$$\boldsymbol{h}_{(i)} = \boldsymbol{h} - \operatorname{grad} \phi^{\text{pert}}_{(i)} \ . \tag{7}$$

The related (partially) relaxed enthalpy density $\overline{\psi}'^{\,\text{rel}}$ is generally obtained via

$$\overline{\psi}'^{\,\text{rel}}(\boldsymbol{h}, \xi) := \sup_{\phi^{\text{pert}}} \left\{ \frac{1}{V_\Omega} \int_\Omega \left[[1 - \xi] \, \psi'_{(1)} + \xi \, \psi'_{(2)} \right] \, \mathrm{d}V \right\} \ . \tag{8}$$

⇒ TABLE OF CONTENTS

This scheme can be shown to fulfill both tangential continuity of the magnetic field $[\![\boldsymbol{h}]\!] \times \boldsymbol{n} = \boldsymbol{0}$ as well as interface compatibility of the magnetic induction $[\![\boldsymbol{b}]\!] \cdot \boldsymbol{n} = 0$. The volume fraction of phase 2 is assumed to minimize the (partially relaxed) enthalpy, thus

$$\xi = \arg\min\{\overline{\psi}'^{\,\mathrm{rel}}\} \tag{9}$$

has to hold. The effective material response in terms of the magnetic induction is given by

$$\boldsymbol{b} = -\partial_{\boldsymbol{h}}\psi' = [1-\xi]\,[\boldsymbol{\beta}_{(1)}^{-1} \cdot \boldsymbol{h}_{(1)} + \boldsymbol{b}_{(1)}^{\mathrm{rem}}] + \xi\,[\boldsymbol{\beta}_{(2)}^{-1} \cdot \boldsymbol{h}_{(2)} + \boldsymbol{b}_{(2)}^{\mathrm{rem}}]\,. \tag{10}$$

2.2 Perturbation of the magnetic vector potential

In analogy to the energy hull discussed above, a perturbed magnetic vector potential $\boldsymbol{\phi}^{\mathrm{pert}}$—which is identical to the scalar perturbation w.r.t. every coordinate—is introduced. The resulting total magnetic induction in each phase then reads

$$\boldsymbol{b}_{(i)} = \boldsymbol{b} + \mathrm{curl}\,\boldsymbol{\phi}_{(i)}^{\mathrm{pert}}\,. \tag{11}$$

The related (partially) relaxed energy density $\overline{\psi}^{\,\mathrm{rel}}$ is generally obtained via

$$\overline{\psi}^{\,\mathrm{rel}}(\boldsymbol{b},\xi) := \inf_{\boldsymbol{\phi}^{\mathrm{pert}}} \left\{ \frac{1}{V_{\mathrm{RVE}}} \int_{\mathrm{RVE}} \big[[1-\xi]\,\psi_{(1)} + \xi\,\psi_{(2)}\big]\;\mathrm{d}V \right\}\,. \tag{12}$$

This scheme can also be shown to fulfill both tangential continuity of the magnetic field $[\![\boldsymbol{h}]\!] \times \boldsymbol{n} = \boldsymbol{0}$ as well as interface compatibility of the magnetic induction $[\![\boldsymbol{b}]\!] \cdot \boldsymbol{n} = 0$. The volume fraction of phase 2 is assumed to minimize the (partially relaxed) energy, thus

$$\xi = \arg\min\{\overline{\psi}^{\,\mathrm{rel}}\} \tag{13}$$

has to hold. The effective material response in terms of the magnetic field is given by

$$\boldsymbol{h} = \partial_{\boldsymbol{b}}\psi = [1-\xi]\,\boldsymbol{\beta}_{(1)} \cdot [\boldsymbol{b} - \boldsymbol{b}_{(1)}^{\mathrm{rem}}] + \xi\,\boldsymbol{\beta}_{(2)} \cdot [\boldsymbol{b} - \boldsymbol{b}_{(2)}^{\mathrm{rem}}]\,. \tag{14}$$

3 Numerical exmaples

Figure 1 shows the effective material response obtained by the framework based on the perturbation of the scalar magnetic potential for a prescribed homogeneous magnetic field $\overline{\boldsymbol{h}} = \overline{h}_1\,\boldsymbol{e}_1$. The relaxed enthalpy density (red line in Figure 1a)) obviously reflects a lower bound of the "quasiconcave" hull which is conceptually equivalent to an upper bound of a quasiconvex envelope. Thus, problems relying on this enthalpy density would still be ill-posed. Figure 2 shows the effective material response obtained by the framework based on the perturbation of the vector-valued magnetic potential for a prescribed homogeneous magnetic induction $\overline{\boldsymbol{b}} = \overline{b}_1\,\boldsymbol{e}_1$. The relaxed energy density (red line in Figure 2a)) obviously reflects a lower bound of the quasiconvex hull. Thus, problems relying on this energy density would be well-posed.

4 Conclusion

In this contribution, the application of energy relaxation schemes to phase transformations in magnetizable solids is elaborated. Two different laminate-based schemes are presented which make use of perturbations of the scalar and the vector-valued magnetic potential. In particular, the approach based on the vector-valued magnetic potential yields a lower bound to the quasiconvex hull and thus, this method would result in well-posed problems. As an outlook, the

⇒ TABLE OF CONTENTS

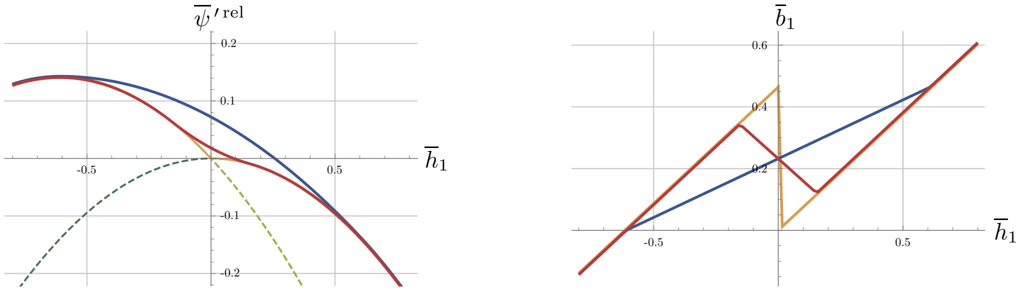

a) b)

Figure 1: a) Relaxed enthalpy potentials and b) effective material response in terms of the magnetic induction $\boldsymbol{b}$. The colored solid lines indicate results obtained by different approaches: yellow—Voigt assumption of homogeneous magnetic field, blue—Reuss assumption of homogeneous magnetic induction, red—relaxed energy density based on the perturbation of the scalar magnetic potential. The dashed lines in a) symbolize the single phase enthalpy densities.

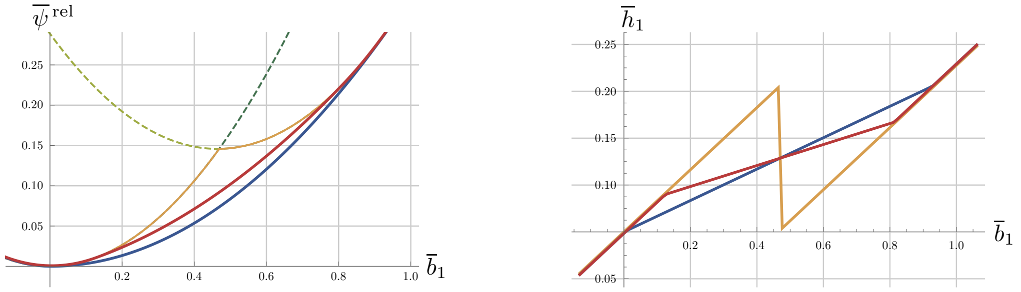

a) b)

Figure 2: a) Relaxed energy potentials and b) effective material response in terms of the magnetic field $\boldsymbol{h}$. The colored solid lines indicate results obtained by different approaches: yellow—Voigt assumption of homogeneous magnetic induction, blue—Reuss assumption of homogeneous magnetic field, red—relaxed energy density based on the perturbation of the vector-valued magnetic potential. The dashed lines in a) symbolize the single phase energy densities.

specific energy relaxation scheme using perturbations of divergence-free fields will be transferred to the mechanical case, where such perturbations were so far—at least to the author's knowledge—only applied to curl-free fields. In addition, combined relaxation approaches for the magnetomechanically coupled case will be established, for example in the context of the constitutive modeling of magnetic shape memory alloys.

REFERENCES

[1] T. Bartel, B. Kiefer, K. Buckmann, A. Menzel. A Kinematically-Enhanced Relaxation Scheme for the Modeling of Displacive Phase Transformations, *Journal of Intelligent Material Systems and Structures* 26: 701–717, 2015.

[2] B. Kiefer, K. Buckmann, T. Bartel. Numerical Energy Relaxation to Model Microstructure Evolution in Functional Magnetic Materials, *GAMM-Mitteilungen* 38: 171–196, 2015.

[3] B. Kiefer, T. Bartel. On Variationally-Consistent Homogenization Approaches in Multi-Phase Magnetic Solids, *Proceedings in Applied Mathematics and Mechanics* 17: 517–518, 2017.

THIN SHEETS OF LIQUID CRYSTAL ELASTOMERS

Kaushik Bhattacharya

Division of Engineering and Applied Science, California Institute of Technology, Pasadena CA 91125, USA

Abstract. *Liquid crystal elastomers are rubbery solids with liquid crystal mesogens incorporated into their main or side chains. They display an isotropic to nematic phase transformation accompanied by a large spontaneous deformation. This gives rise to a range of interesting thermomechanical properties. When made as thin sheets, the combination of properties and geometric nonlinearity can lead to a range of fascinating and unexpected phenomena including sheets that can smoothly drape complex surfaces, sheets that do not wrinkle when stretched, sheets that spontaneously deform into complex shapes etc. We introduce a simple model of liquid crystal elastomers and show how complex phenomena arise from this simple model.*

1 Introduction

Slender structures – where one or more dimensions is much smaller than the others as in strings, rods, membranes, plates and shells – are common in nature, and have been widely exploited in engineering. The slenderness and the resulting flexibility coupled with possible geometric constraints endows such structures with a rich range of mechanical response. Thus, the study of the mechanics of slender structures has been the subject of much research. Much of this literature relates to materials whose constitutive response is relatively simple. The recent decades have seen the introduction and study of multifunctional materials that deform spontaneously in the presence of a stimulus. These materials including shape-memory alloys, ferroelectrics, electroactive polymers and liquid crystal elastomers also have rich mechanics, but much of this mechanics has been explored in the context of simple uniaxial or bulk structures. This work seeks to combine these two lines work and study new phenomena that arise in thin sheets of liquid crystal elastomers.

Liquid crystal elastomers are rubbery solids with liquid crystal mesogens incorporated into their main or side chains [6]. They display an isotropic to nematic phase transformation accompanied by a large spontaneous deformation, giving rise to a range of interesting thermomechanical properties. Depending on how these materials are made, the nematic director is either free to rotate with respect to the material frame (free director) or frozen with the material frame (frozen director). We consider both classes of materials and show that each has its own range of fascinating behavior.

2 Ultra-soft wrinkle-free LCE sheets

Thin membranes of cloth, rubber and other elastic materials often wrinkle when stretched, or are draped over complex surfaces (those with nonzero Gaussian curvature). This creates challenges in various applications including those in fashion, medicine, packaging and deployable space structures. In this work, we show that thin sheet of LCEs where the director can freely

---

[*] Corresponding author: Kaushik Bhattacharya (🖂 bhatta@caltech.edu)

⇒ TABLE OF CONTENTS

rotate are able to undergo shear deformation without any shear stress, and thus are able to resist wrinkling on stretch and drape complex shapes. These LCE sheets can display fine-scale features both due to wrinkling that one expects in thin elastic membranes and due to oscillations in the nematic director. Starting from a well-established Warner-Terentjev theory of LCEs [6] and using $\Gamma-$ convergence, we obtain an explicit characterization of the effective energy density of membranes and the effective state of stress as a function of the planar deformation gradient [1]. We show the existence of a region where one has shear strain but no shear stress. We build on this and develop a Koiter type theory that implicitly but rigorously accounts for the microstructure but explicitly computes the details of out-of-plane deformations. Using both analytical and numerical studies, we show that nematic elastomer sheets can suppress wrinkling by modifying the expected state of stress through the formation of microstructure [2]. We provide experimental evidence for our predictions and discuss the implications in application.

3 Nonisometric origami with LCE sheets

LCEs where the director is frozen can be exploited to create sheets that spontaneously deform into complex shapes when subjected to stimuli like light and heat. The key idea is that some director patterns can lead to an incompatible pattern of spontaneous deformation when subjected to light or temperature change. In a thin sheets, this incompatibility can be relieved by deforming out of plane. We present a systematic framework for the design of complex three dimensional shapes through the actuation of heterogeneously patterned nematic elastomer sheets. These sheets are composed of piecewise uniform director patterns which, when appropriately linked together, can actuate into a diverse array of three dimensional faceted shapes. We demonstrate both theoretically [3, 4] and experimentally [5] that the nonisometric origami building blocks actuate in the predicted manner, and that the integration of multiple building blocks leads to complex, yet predictable and robust, shapes.

Acknowledgement This summary draws on collaborations with Paul Plucinsky, Mark Warner, Pierluigi Cesana, Marium Lemm, Ben Kowalski, Carl Modes and Tim White, and the support of NASA and the US AFOSR.

REFERENCES

[1] P Cesana, P Plucinsky, and K Bhattacharya. Effective behavior of nematic elastomer membranes. *Arch. Rat. Mech. Anal.*, 218(2):863–905, May 2015.

[2] P Plucinsky and K Bhattacharya. Microstructure-enabled control of wrinkling in nematic elastomer sheets. *J Mech Phys Solids*, 102:125–150, May 2017.

[3] P Plucinsky, M Lemm, and K Bhattacharya. Programming complex shapes in thin nematic elastomer and glass sheets . *Phys Rev E*, 94:010701, 2016.

[4] P Plucinsky, M Lemm, and K Bhattacharya. Actuation of Thin Nematic Elastomer Sheets with Controlled Heterogeneity. *Arch. Rat. Mech. Anal.*, 227(1):149–214, September 2017.

[5] P Plucinsky, B A Kowalski, T J White, and K Bhattacharya. Patterning nonisometric origami in nematic elastomer sheets. *Soft Matter*, 14:3127–3134, April 2018.

[6] M Warner and E M Terentjev. *Liquid crystal elastomers*. International Series of Monographs of Physics. Oxford University Press, 2nd paperback edition, 2007.

ON ATOMISTIC-TO-CONTINUUM MULTISCALE MODELING WITH COULOMB INTERACTIONS IN IONIC CRYSTALS

Vishal Boddu[1,*], **Denis Davydov**[1], **Bernhard Eidel**[2], **and Paul Steinmann**[1]

[1] Chair of Applied Mechanics, University of Erlangen-Nuremberg
Paul-Gordan-Strae 3, 91052 Erlangen, Germany

[2] Institute for Mechanics, University of Siegen
Paul-Bonatz-Strae 9-11, 57076 Siegen, Germany

Abstract. *In this work we examine whether or not cutoff-based methods to account for Coulomb interactions are suitable within the context of atomistic-to-continuum multiscale methods. To this end we choose the quasicontinuum method along with the Wolf summation method to account for Coulomb interactions in ionic crystals for demonstration.*

1 Introduction

The state of the art in material modeling offers highly accurate methods for each individual scale, from density functional theory (DFT) and molecular mechanics at the lower scales to continuum theories for the macroscale. A wide gap exists, however, due to a lack of models applicable at intermediate scales. Here, the continuum hypothesis fails because the atomic discreteness of materials becomes apparent and molecular methods tend to incur prohibitively high computational costs [1, 2].

The quasicontinuum (QC) method was introduced to bridge from the atomistic to the continuum level by applying finite element interpolation schemes to lattice sites in a crystalline material [3]. The quasicontinuum method is composed of three components: kinematic constraints (to interpolate the lattice site positions from a reduced set of representative atoms), summation rules (to avoid the computation of thermodynamic quantities from the full atomistic ensemble), and model adaptation schemes (to localize regions of interests for atomistic resolution).

Existing atomistic-to-continuum multiscale methods, such as the quasicontinuum method, are applicable exclusively in cases where the atomic interactions are short-ranged. This restriction on the nature of atomic-level interactions for the multiscale methods exclude an extremely large class of materials, essentiallyall dielectrics, polarizable solids and ionic solids, that are central to numerous scientific and industrial applications.

So far there has been only one approach, to the best of our knowledge, that enables the applicability of atomistic-to-continuum methods for ionic crystals. The method involves coarse-graining of the long-range Coulomb interactions in ionic crystals [4]. In doing so, the ionic charges are expressed in terms of a charge density field defined on two different length scales, namely the length scale of atomic unit cell and the characteristic continuum length scale. However, this approach assumes complete separation of scales and for a finite atomistic system this is naturally not true. Furthermore, realizing adaptive refinement and seamless coarse-graining using this approach is not trivial.

---

[*] Corresponding author: Vishal Boddu (✉ vishal.boddu@fau.de)

2 Quasicontinuum Method

The quasicontinuum method has three integral components [3, 5]:

- kinematic constraints,
$$\mathbf{x}_l = \mathbf{X}_l + \boldsymbol{u}(\mathbf{X}_l), \ \forall\, l \in \mathscr{L}, \tag{1}$$
where $\mathscr{L}$ denotes the index set of all the atoms in the system,
$$\boldsymbol{u}(\boldsymbol{X}) = \sum_{i \in \mathcal{D}} u_i \boldsymbol{N}_i(\boldsymbol{X}) \tag{2}$$
is the unknown displacement field in the vector-valued finite element space with
$\boldsymbol{N}_i(\boldsymbol{X})$ being the vector-valued shape function and
u_i being the value associated to the degree of freedom i,
$\mathbf{X}_l$ and $\mathbf{x}_l$ denote the initial and current positions of an atom $l \in \mathscr{L}$.
- summation rules to reduce computational costs by approximating the total energy using sampling atoms as
$$E^{tot} = \sum_{k \in \mathcal{C}} w_k \, E_k, \tag{3}$$
where w_k and E_k are the sampling weight and energy of sampling atom k and $\mathcal{C}$ is the set of carefully chosen sampling atoms, and
- model adaptation to identify problem dependent regions of interest and localize atomistic resolution to reduce the computational costs.

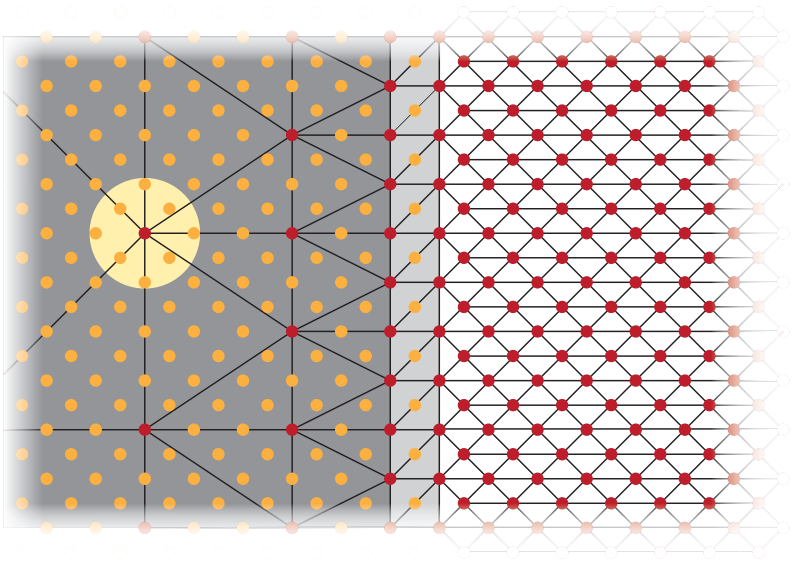

Figure 1: Spatial quasicontinuum set-up of a crystal lattice with representative atoms (rep-atoms) in red–consisting of non-local region, interface region (shown in light gray elements) and local region (shown in dark gray elements). Atoms on which kinematic constraints are imposed are shown in orange. A sampling cluster (in yellow) of a single representative atom is shown for illustration.

⇒ TABLE OF CONTENTS

In the case when the atomistic model potential is a pair potential of the form $\phi(r_{ij})$, with $\mathbf{r}_{ij} = \mathbf{x}_j - \mathbf{x}_i$ the total energy and its gradient with respect to the degree of freedom i read as

$$E^{tot} = \sum_{k \in \mathcal{C}} w_k \sum_{l \in \mathscr{L}} \phi(|\mathbf{r}_{kl}|), \tag{4}$$

$$g_i = \sum_{k \in \mathcal{C}} w_k \sum_{l \in \mathscr{L}} \frac{\partial \phi(r_{kl})}{\partial u_i} \tag{5}$$

$$= \sum_{k \in \mathcal{C}} w_k \sum_{l \in \mathscr{L}} \frac{\partial \phi(r_{kl})}{\partial r_{kl}} \frac{\mathbf{r}_{kl}}{r_{kl}} \cdot \left[\boldsymbol{N}_i(\mathbf{X}_l) - \boldsymbol{N}_i(\mathbf{X}_k) \right], \tag{6}$$

respectively.

3 Modeling Coulomb Interactions in Ionic Crystals

Unphysical artifacts of the direct cutoff-based truncated sum to evaluate Coulomb interactions in ionic solids have been pointed out in a number of studies. However, recently it is understood that the artifacts of the direct cutoff-based truncated sum can be significantly minimized if a suitable correction term is added [6]. In this work we examine whether or not such cutoff-based methods are suitable to carry out the accumulation of the Coulomb interactions within the context of atomistic-to-continuum multiscale methods. In this regard, we choose the quasicontinuum method from the existing collection of the multiscale methods for demonstration.

REFERENCES

[1] D.M. Kochmann, J.S. Amelang. The quasicontinuum method: theory and applications, In: C.R. Weinberger and G.J. Tucker (eds.), *Multiscale Materials Modeling for Nanomechanics*, 159–195, Springer, New York, 2016.

[2] E.B. Tadmor, M. Ortiz and R. Phillips. Quasicontinuum analysis of defects in solids, *Philosophical magazine A*, 73 (6): 1529-1563, 1996

[3] R.E. Miller and E.B. Tadmor. The quasicontinuum method: Overview, applications and current directions, *Journal of Computer-Aided Materials Design*, 9(3): 203–239, 2002

[4] J. Marshall and K. Dayal. Atomistic-to-continuum multiscale modeling with long-range electrostatic interactions in ionic solids, *Journal of the Mechanics and Physics of Solids*, 62: 137–162, 2014

[5] B. Eidel and A. Stukowski. A variational formulation of the quasicontinuum method based on energy sampling in clusters, *Journal of the Mechanics and Physics of Solids*, 57(1): 87–108, 2009

[6] I. Fukuda and H. Nakamura. Non-Ewald methods: theory and applications to molecular systems, *Biophysical reviews*, 4(3): 161–170, 2012

OPTICAL AND ELECTRONIC PROPERTIES IN FERROELECTRIC BARIUM TITANATE-BASED COMPOUNDS

Halyna Volkova[1, *], Pascale Gemeiner[1], Grégory Geneste[2], Jêrome Guillot[3], Carlos Frontera[4], Nidal Banja[1], Fabienne Karolak[1], Christine Bogicevic[1], Brahim Dkhil[1], Nicolas Chauvin[5], Damien Lenoble[3], and Ingrid C. Infante[5]

[1] Laboratoire Structures, Propriétés et Modélisation des Solides, CentraleSupélec, CNRS-UMR8580, Université Paris-Saclay
8-10 rue Joliot-Curie, Gif-sur-Yvette, France

[2] CEA, DAM
DIF, Arpajon, France

[3] Luxembourg Institute of Science and Technology, Materials Research and Technology Department
41 rue du Brill, Belvaux, Luxembourg

[4] Institut de Ciència de Materials de Barcelona, Consejo Superior de Investigaciones Científicas
Campus de la UAB, Bellaterra, Spain

[5] Institut de Nanotechnologies de Lyon, CNRS-UMR5270 ECL INSA UCBL CPE, Université de Lyon
7 avenue Jean Capelle, Villeurbanne, France

Abstract. *The bandgap energy values for the ferroelectric* $BaTiO_3$*-based solid solutions with isovalent substitution* $Ba_{1-x}Sr_xTiO_3$, $BaZr_xTi_{1-x}O_3$ *and* $BaSn_xTi_{1-x}O_3$ *were determined using diffuse reflectance spectra. While the corresponding unit cell volume follows Vegard's law in accordance with the different ionic radii of the ionic substitutions, the bandgap values depict non-linear compositional dependences for all the solid solutions. The effect is considerably large for* $BaZr_xTi_{1-x}O_3$ *and* $BaSn_xTi_{1-x}O_3$ *solutions, depicting a bandgap linear compositional dependence up to* $x=0.6$*, for* $x>0.6$ $BaZr_xTi_{1-x}O_3$ *compounds present much larger bandgap values than* $BaSn_xTi_{1-x}O_3$ *counterparts. Electronic properties have been investigated through X-ray photoelectron spectroscopy in* $BaSn_xTi_{1-x}O_3$ *compounds, indicating that the Sn 3d and Ti 2p core levels shift against the Ba 3d ones within the whole compositional range with the same energy trend as that observed for the optical bandgap. Since for* $Ba_{1-x}Sr_xTiO_3$ *compounds no major bandgap variation is observed, we conclude that the bandgap compositional dependences observed for* $BaSn_xTi_{1-x}O_3$ *compounds and* $BaZr_xTi_{1-x}O_3$ *ones are originated from the structural sensitivity of the O, Ti and Sn or Zr electronic bands involved in the bandgap transition of these compounds. With this work, we underline the reliability of the bandgap determined from diffuse reflectance spectrometry experiments, as a means to non-invasively evaluate the electronic properties of powder materials.*

1 Introduction

Since the theoretical efficiency limit of single p-n junction solar cell was calculated by Shockley and Queisser [1], there is a challenge of finding new ways to bypass it. A way to intrinsically increase the efficiency could be to use alternative materials such as ferroelectrics (FEs). Unlike p-n junctions, the potential difference in ferroelectrics arises from their non-centrosymmetric unit cell providing the so-called bulk photovoltaic effect [2]. Among them, $BaTiO_3$ is a well-referenced, relatively cheap to produce, and environmentally friendly FE. In view of finding new ways to obtain FE-control of the optical properties, $BaTiO_3$-solid solutions have been studied, as potentially depicting FE-order with simultaneously enhanced photoconductive properties. Here we present the work on three solid solutions with isovalent substitutions, in view of understanding the pure structural and electronic

---

[*] Corresponding author: H. Volkova (halyna.volkova@centralesupelec.fr)

⇒ TABLE OF CONTENTS

effects and minimizing the point defect contributions. With Sr^{2+} substituting Ba^{2+}, the $Ba_{1-x}Sr_xTiO_3$ is a family of solid solutions with ferroelectricity remaining at low temperature up to x_Sr~0.9 [3]. $BaZr_xTi_{1-x}O_3$ and $BaSn_xTi_{1-x}O_3$ are solid solutions with Ti^{4+} being substituted by Zr^{4+} and Sn^{4+}, respectively, thus presenting conduction band where Zr 4d and Sn 5s 5p states will be added to Ti 3d ones, which in principle will depict much different effective mass and mobility, for the potential photoconduction properties that we are seeking. The phase diagrams of $BaZr_xTi_{1-x}O_3$ [4] and $BaSn_xTi_{1-x}O_3$ [5] display rich polar features, evolving at room temperature from a pure tetragonal FE in the Ti-rich region towards a paraelectric cubic structure in the Ti-poor region. In-between, the compositions are FE-relaxors characterized by polar disorder and average cubic structure.

2 Experimental procedures

$Ba_{1-x}Sr_xTiO_3$ (x_Sr = 0, 0.25, 0.5, 1), $BaZr_xTi_{1-x}O_3$ (x_Zr = 0, 0.1, 0.2, 0.3, 0.4, 0.5, 0.6, 0.7, 0.8, 0.9, 1) and $BaSn_xTi_{1-x}O_3$ (x_Sn = 0, 0.1, 0.2, 0.4, 0.5, 0.6, 0.8, 0.9, 1) samples were synthesized by solid state reaction from starting materials, $BaCO_3$ (99.9%), $SrCO_3$ (99.9%), TiO_2 (99%), ZrO_2 (99.9%), and SnO_2 (99.9%). After homogenization in a mortar, by ultrasonic bath and by magnetic mixing, the powders were calcined at temperatures between 800°C and 1200°C, and subsequently ground with polyvinyl alcohol and pressed into pellets. Two annealing steps at 600°C and 800°C insured the evaporation of binding agent. The sintering was held at temperatures of 1280-1450°C adjusting the dwell times, resulting in pellet density of ~92-95%. Structural evaluation by X-ray diffraction (XRD) was performed using a Bruker D2 Phaser diffractometer on finely ground and annealed powders, with 0.02° step and acquisition times adjusted for different angular ranges (10 sec/step for 2θ=20-35°, 30 sec/step for 35-60°, 55 sec/step for 60-120°). Unit cell volume was determined using Le Bail analysis through devoted crystallographic software (Jana2006). The ultraviolet-visible-near-infrared spectrometry experiments were performed on a Perkin Elmer Lambda 850 spectrometer in diffuse reflectance geometry using a Harrick's Praying Mantis™ accessory, from finely grinded and annealed powders to minimize mechanical stresses. From the raw reflectance, *R*, the absorption coefficient *k* is determined according to Kubelka-Munk reemission function F_{KM} transformation [6], within the assumption the scattering coefficient *s* is independent of the photon energy:

$$F_{KM} = \frac{k}{s} = \frac{(1-R)^2}{2R}. \tag{1}$$

The optical bandgap is determined from a linear fit to the onset of the absorption edge obtained after converting the F_{KM} following Tauc formalism, which for the present study we consider as direct bandgap. X-ray photoelectron spectroscopy (XPS) studies were carried out on powder and ceramic samples. Axis Ultra DLD spectrometer with Al Kα X-ray source operated at 50W was used, together with charge neutralizer. For the analysis of the XPS data (CasaXPS), we have used the internal reference of the Ba $3d_{7/2}$ core level energy, fixed at 778.5eV, as considered to be the ion with very limited changes in its electronic state due to chemical, electronic and structural effects.

3 Results and Discussion

From the XRD collected (Figure 1a-c), we deduce the stabilization of a pure perovskite phase for each solid solution compound, with unit cell volume following Vegard's law (Figure 1d). The larger compositional slope for Zr-compounds than for Sn-ones is in agreement with the expected effect induced by the difference in ionic radius of Zr^{4+} against Sn^{4+}, depicting the Sr^{2+}-compounds a volume reduction, as expected [8].

Optical properties of the different compositions are shown in Figure 2a-d. Diffuse reflectance raw data in Figure 2a point out the large absorption differences of parent compounds. Optical absorption features are seen in the Kubelka-Munk functions F_{KM} depending of the solid solution. A large increase of F_{KM} is characteristic of the optical absorption edge at a given photon energy, being the

Zr-compounds (Figure 2c) those presenting the larger variation of the photon energy onset. No remarkable onset change is seen for Sr-compounds (Figure 2b), and weak and non-monotonic ones for Sn-compounds (Figure 2d). The chemical substitution effect on the occupied electronic states is directly investigated on Sn-based compounds through XPS core level acquisition. Using Ba3d$_{7/2}$ state as the perovskite energy reference, we plot in Figure 2e-k the different characteristic O1s, Sn3d and Ti2p occupied states. Fine analysis of these levels indicate a shift of the energy positions of Sn and Ti as a function of the Sn-content (Figure 2i and k).

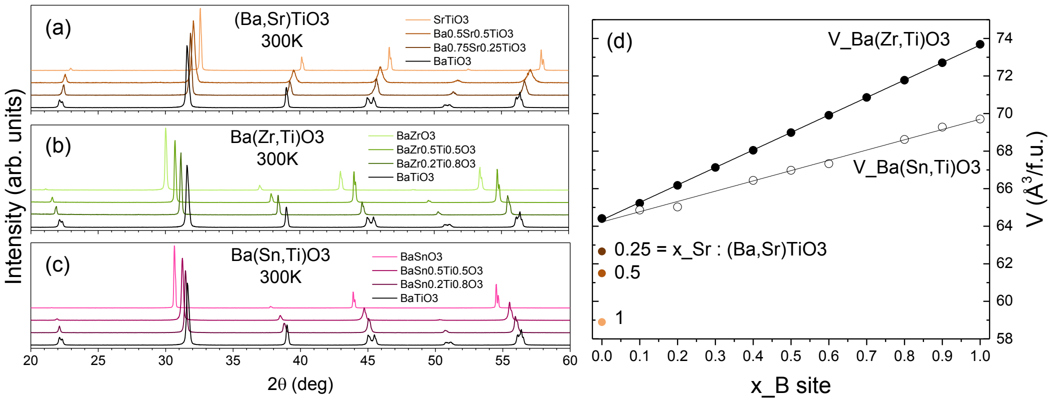

Figure 1: Room temperature X-ray diffraction [(a)-(c)] powder patterns and (d) unit cell volume determined from the XRD patterns, for different $BaTiO_3$-based compounds. [(a)-(c)]: (a) $Ba_{1-x}Sr_xTiO_3$ with x_Sr=0, 0.25, 0.5, 1 (bottom to top), (b) $BaZr_xTi_{1-x}O_3$ with x_Zr=0, 0.2, 0.5, 1 (bottom to top), and (c) $BaSn_xTi_{1-x}O_3$ with x_Sn=0, 0.2, 0.5, 1 (bottom to top); (d) Pseudocubic cell volume per formula unit as a function of x_B site (Zr or Sn) (symbols), corresponding linear fits are shown.

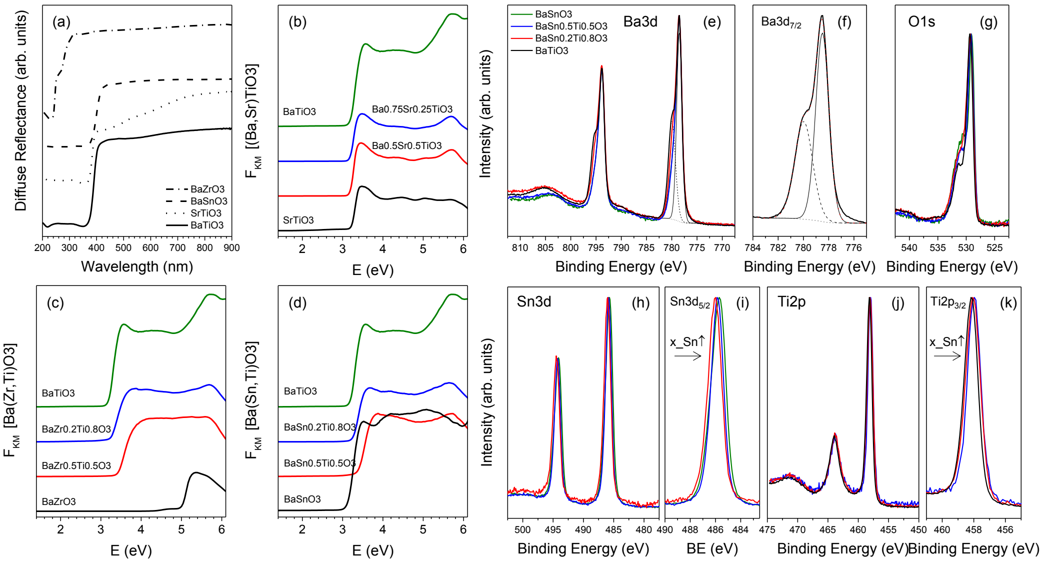

Figure 2: [(a)-(d)] Optical properties from $BaTiO_3$-solid solutions, and [(e)-(k)] X-ray photoelectron spectroscopy (XPS) core level data from $Ba(Sn,Ti)O_3$. [(a)-(d)]: (a) Diffuse reflectance spectra from parent compounds ($BaTiO_3$, $SrTiO_3$, $BaSnO_3$ and $BaZrO_3$, bottom to top), and [(b)-(d)] Kubelka-Munk F_{KM} functions *vs* photon energy E determined for (b) $Ba_{1-x}Sr_xTiO_3$ with x_Sr=0, 0.25, 0.5, 1 (top to bottom), (c) $BaZr_xTi_{1-x}O_3$ with x_Zr=0, 0.2, 0.5, 1 (top to bottom), and (d) $BaSn_xTi_{1-x}O_3$ with x_Sn=0, 0.2, 0.5, 1 (top to bottom). [(e)-(k)]: Core levels from $BaSn_xTi_{1-x}O_3$ compounds (x_Sn=0, 0.2, 0.5, 1) (a) Ba3d, (g) O1s, (h) Sn3d, (i) Sn3d$_{7/2}$, (j) Ti2p, (j) Ti2p$_{3/2}$, together with the example on $BaTiO_3$ sample of the different components used for Ba3d$_{5/2}$ fitting (Ba within $BaCO_3$, dash line, Ba within the perovskite -here, $BaTiO_3$- fill line, and background, dotted line).

⇒ TABLE OF CONTENTS

Bandgap values as a function of Sn- or Zr- substitution (Figure 3a) account for the large differences previously noticed from direct analysis of the optical properties through F_{KM}. Remarkably, for x_B > 0.2, both solution compounds depict polar disorder, being relaxors at room temperature, follow the same initial trend up to x_B ~ 0.6. For x > 0.6, Zr-compounds present larger bandgap values while lower ones are determined for Sn-compounds. Comparing the obtained optical bandgap values for Sn-compounds with the energy differences of the XPS Ti2p and Sn3d electronic bands (Figure 3b-c), we notice a similar substitution dependence. Moreover, these XPS energy differences are fully in agreement with the observed bandgap variation, being for optical and XPS results this energy difference of ~ 0.35eV between $BaTiO_3$ and x_Sn = 0.8. Investigations are ongoing to determine the precise origin of this behavior and its coupling to the relaxor properties.

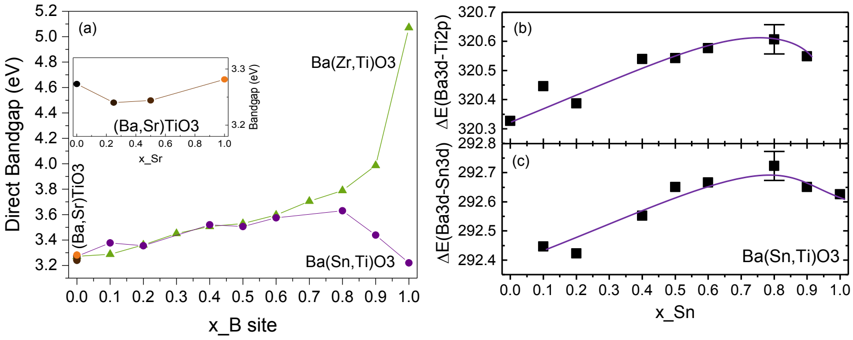

Figure 3: (a) Bandgap values as a function of the x_B site substitution for different $BaTiO_3$-solid solutions, determined using F_{KM} and Tauc plot linear fits, assuming direct bandgap. Inset: Bandgap for the $Ba_{1-x}Sr_xTiO_3$ compounds *vs* x_Sr substitution. [(b),(c)]: B-site core level energy difference (ΔE) relative to the perovskite $Ba3d_{7/2}$ core level position for different $BaSn_xTi_{1-x}O_3$ compounds and as a function of the x_Sn substitution, being (b) $Ti2p_{5/2}$ and (c) $Sn3d_{7/2}$ (lines are a guide for the eye).

4 Conclusions

Combining structural, optical and electronic characterization tools on pure perovskite $Ba_{1-x}Sr_xTiO_3$, $BaZr_xTi_{1-x}O_3$ and $BaSn_xTi_{1-x}O_3$ solid solutions, we proved that we can precisely determine their bandgap values. We have successfully presented the potential of diffuse reflectance spectrometry for the determination of the optical and electronic properties of single phase perovskite oxides, and similar approaches can be exploited for investigating the optical transitions of other materials.

REFERENCES

[1] W. Shockley and H. J. Queisser. Detailed Balance Limit of Efficiency of p-n Junction Solar Cells, *Journal of Applied Physics*, 32, 510. 1961.

[2] A. M. Glass et al. High-voltage bulk photovoltaic effect and the photorefractive process in $LiNbO_3$, *Applied Physics Letters*, 25, 233. 1974.

[3] C. Ménoret et al. Structural evolution and polar order in $Sr_{1-x}Ba_xTiO_3$, *Physical Review B*, 65, 224104. 2002.

[4] T. Maiti, R.Guo and A. S. Bhalla. Structure-Property Phase Diagram of $BaZr_xTi_{1-x}O_3$ System, *Journal of the American Ceramics Society*, 91, 1769. 2008.

[5] X. Wei and X. Yao. Preparation, structure and dielectric property of barium stannate titanate ceramics, *Materials Science and Engineering: B*, 137, 184. 2007.

[6] B. Philips-Invernizzi, D. Dupont and C. Cazé. Bibliographical review for reflectance of diffusing media, *Optical engineering*, 40, 1082. 2001.

[7] J. Tauc, R. Grigorovici, and A. Vancu. Optical Properties and Electronic Structure of Ge, *Physica Status Solidi*, 15, 627. 1966.

[8] R. D. Shannon. Revised Effective Ionic Radii and Systematic Studies of Interatomic Distances in Halides and Chaleogenides, *Acta Crystallographica*, A32, 751. 1976.

⇒ TABLE OF CONTENTS

FLEXOELECTRICITY: FROM NANOMECHANICS TO BONE HEALING

Gustau Catalan[1,2,*], **Fabian Vasquez-Sancho**[2,*], **Kumara Cordero-Edwards**[2], **Amir Abdollahi**[2,3], **Neus Domingo**[2]

[1] ICREA-Institucio Catalana de Recerca Estudis Avançats, Barcelona, Catalonia

[2] ICN2-Institut Catala de Nanociencia i Nanotecnologia
Barcelona, Catalonia

[3]Laboratori de Calcul Numeric (LaCaN), Universitat Politecnica de Catalunya, Barcelona, Catalonia

Abstract. *At small length-scales, strain gradients can be much bigger than at the macroscale. Therefore, any property dependent on strain gradients can also be bigger. One such property is flexoelectricity, which is a dielectric polarization caused by a strain gradient. In this talk I will give a quick overview of flexoelectricity at the micro and nano-scale, focusing on the two most recent results from our lab.*

The first is the discovery that, for ferroelectrics subject to indentation, the interaction between flexoelectricity and piezoelectricity results in an asymmetric mechanical response. This means that the mechanical response, including toughness and and crack propagation, can be switched when the ferroelectric polarization is switched. This provides a mechanism for reading polarization by pure mechanical means, as well as the exciting possibility of having "smart mechanical coatings" whose mechanical response can be modified with a voltage.

The second result is the discovery that hydroxyapatite, the mineral that makes up our bones, is flexoelectric, and that hydroxyapatite flexoelectricity may play a very important role in healing bone micro-fractures.

1 Introduction

Strain gradients are essentially difference in strain divided by relaxation length. Because the relaxation length is in the denominator, small relaxation lengths lead to large strain gradients. Accordingly, properties depending on strain gradients, such as flexoelectricity (polarization induced by strain gradients) can be larger at the nanoscale than at the macroscale. This is important because the nanoscale is obviously the scale of nanotechnology, but the microscale is also the scale of cells, which are the constituent blocks of life. Flexoelectricity, as I will show, has profound implications that range for the nanomechanics of ferroelectrics to the physiology of our own bones.

2 Summary

It has already been noticed that the flexoelectric field generated by the strain gradient induced by the tip of an atomic force microscope is locally large enough to even be able to switch the polarization of a ferroelectric [1]. It was thus proposed (and demonstrated) that tip-pressure could be used as a mechanism to "write" ferroelectric polarization bits in a ferroelectric memory.

More recently, we have discovered that the interaction between the flexoelectric polarization and the ferroelectric polarization also has mechanical consequences. In particular, depending on whether these two polarizations are parallel or antiparallel, the mechanical response of the material will be

---

[*] Corresponding author: Gustau Catalan (gustau.catalan@icn2.cat)

different (see figure 1). This means that it is possible to use flexoelectricity not just to write, but also to read the polarity of a ferroelectric domain, thus opening the door for the purely mechanical (voltage-free) operation of a ferroelectric memory [2]. Extending beyond this result, I will also show that switching the polarity of a ferroelectric can also be used to control crack propagation in it, a result that has important implications for our understanding of electromechanical fatigue.

On a different note, we have also measured the bending-induced polarization of bone and pure hydroxyapatite [3], finding both of them to be of the same order of magnitude (around 1nC/m). This implies that the piezoelectricity of collagen (another ingredient of bone) does not appear to contribute to the electromechanical response of bone to local deformations.

One such type of deformation is fracture. The tip of any crack concentrates the largest amount of strain that a material can withstand, in the smallest possible region (a crack junction is atomically sharp). Using our measured flexoelectric coefficients of hydroxyapatite, we have calculated the flexoelectric fields generated by micro-fractures in bone (figure 2), and discovered that they are large enough to even cause apoptosis (programmed cell death) of osteocites, which is the known first step of bone healing. Flexoelectricity thus appears to be a principal actor in the process by which our bones heal themselves.

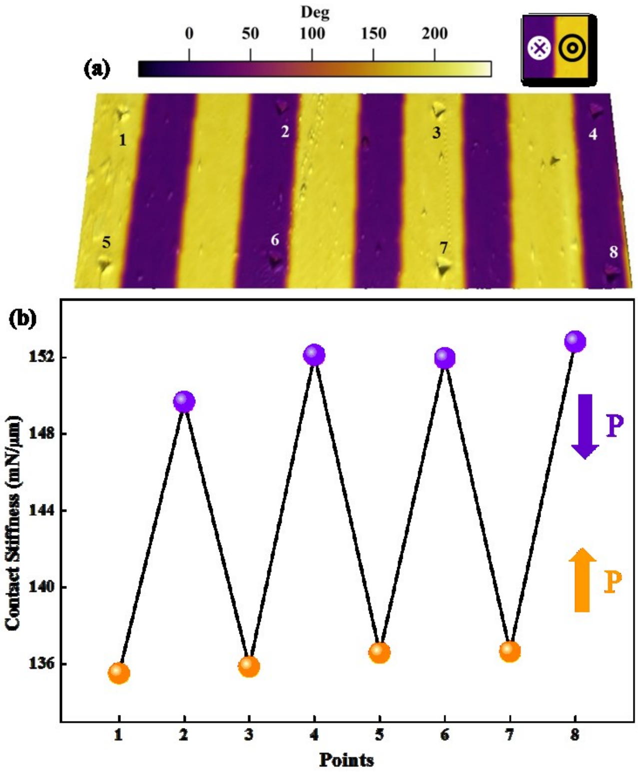

Figure 1: (a) piezoresponse force microscopy of a periodically polarized crystal of ferroelectric LiNbO3, with antiparallel ferroelectric domains (b) indentation measurement showing a clear contrast between the indentation stiffness of the up-polarized and down-polarized domains.

⇒ TABLE OF CONTENTS

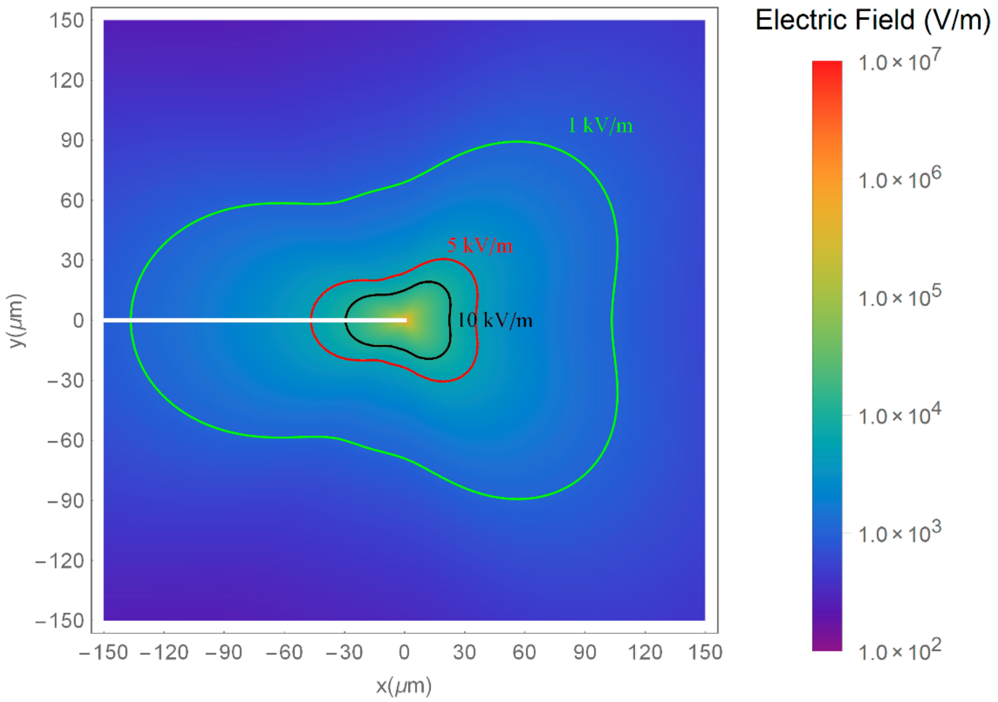

Figure 2: Calculated flexoelectric fields around a fracture in hydroxyapatite (bone mineral). The isoelectric contours mark the critical electric fields for the induction of necrosis (black) apoptosis (red) and stimulated mineralization (green). The lengthscales at which these flexoelectric fields are active are the same (few microns to tens of microns) at which cells operate.

REFERENCES

[1] H. Lu, C.-W. Bark, D. Esque de los Ojos, J. Alcala, C. B. Eom, **G. Catalan**, A. Gruverman, Mechanical Writing of Ferroelectric Polarization, *Science* **336**, 59-61 (2012).

[2] K. Cordero, N. Domingo, A. Abdollahi, J. Sort, **G. Catalan**, Ferroelectrics as Smart Mechanical Materials, *Advanced Materials* 29, 1702210 (2017).

[3] F. Vasquez-Sancho, A. Abdollahi, D. Damjanovic, G. Catalan. Flexoelectricity in bones. Advanced Materials. 1705316 (2018).

⇒ TABLE OF CONTENTS

TEMPERATURE INFLUENCE ON FERROELECTRIC MATERIALS

Omar El-Khatib[1,*], **and Meinhard Kuna**[1]

[1] Institute of Mechanics and Fluid Dynamics, TU Bergakademie Freiberg
Lampadiusstrasse 4, Freiberg 09596, Germany

Abstract. *In this paper the influence of temperature on the behavior of ferroelectric materials is presented. To predict the temperature effect, the 3D micromechanical model for tetragonal domain types is extended. Besides of external heat sources, a change of temperature is considered by internal heat generated due to domain switching. The material properties are assumed to be linearly dependent on the temperature. The temperature influence on the behavior of ferroelectrics is shown by means of the strain and polarization hysteresis loops.*

1 Introduction

Ferroelectric materials are nowadays used widely in various applications such as actuators, sensors, fuel injectors and etc. Many of these devices are subjected to high electric fields in an elevated temperature environment. Thermal effects due to ambient temperature change or self-heating could affect the ferroelectric behavior and may have a large influence on the fracture mechanics and failure behavior of such materials. Sakai and Kawamoto [1] observed a temperature increase of 75 °C during the operation of a piezoelectric stack actuator at an ambient temperature of 120 °C. This increase was caused by the self heating of the specimen and deteriorated the functionality of the actuators. During operation of actuators and sensors, the thermal drift will change the characteristic curves. Therefore, investigating the temperature influence is important to understand the real behavior of ferroelectric materials.

2 Micromechanical model for Thermo-ferroelectrics

In the present work an extension to the micromechanical model for the tetragonal domain switching in ferroelectric ceramics [2] is implemented where the influence of temperature is taken into consideration. The material model employed is mainly based on works of Huber et al and Pathak, McMeeking [3, 4]. The non-linear ferroelectric constitutive equations are extended to capture the thermal effects in the following form:

$$\sigma_{ij} = \underbrace{C_{ijkl}\left(\varepsilon_{kl} - \varepsilon^R_{kl}\right)}_{\text{elasticity}} - \underbrace{e_{ijk}E_k}_{\text{conv.piezoelectricity}} - \underbrace{\lambda_{ij}\theta}_{\text{thermal stresses}} , \tag{1}$$

$$D_i = \underbrace{e_{ijk}\left(\varepsilon_{jk} - \varepsilon^R_{jk}\right)}_{\text{direct piezoelectricity}} + \underbrace{\kappa_{ij}E_j}_{\text{permitivity}} + \underbrace{P^R_i}_{\text{rem.pol}} + \underbrace{p_i\theta}_{\text{pyroelectricity}} . \tag{2}$$

Hereby, $\sigma_{ij}, D_i, \varepsilon_{kl}, E_k, C_{ijkl}, e_{ijk}, \kappa_{ij}$ are the mechanical stresses, electric displacements, mechanical strains, electric field, elastic constants, piezoelectric-stress constants and dielectric coefficients, respectively. The nonlinear effect is described by means of the remanent parts of

---

[*] Corresponding author: Omar El-Khatib (✉ omar.el-khatib@imfd.tu-freiberg.de)

⇒ TABLE OF CONTENTS

the strain ε_{kl}^R and polarization P_i^R. Thermal stresses and pyroelectric effect correspond to the temperature (θ) effect, where λ_{ij} are the thermal stress coefficients and p_i are the pyroelectric constants.

The switching criterion used for each domain is based on requirement of energy supply to overcome an energy barrier:

$$\sigma_{ij}\varepsilon_{ij} + \sigma_{ij}\Delta\varepsilon_{ij}^R + E_i D_i + E_i \Delta P_i^R \geq \omega_c, \tag{3}$$

the critical energy barrier for domain switching is

$$\omega_c^{\pm 90^\circ} = \sqrt{2} P^{sp} E_c, \qquad \omega_c^{180^\circ} = 2 P^{sp} E_c, \tag{4}$$

where P^{sp} is the spontaneous polarization and E_c in the coercive electric field strength of the ferroelectric material.

The material model has been implemented in the commercial finite element software ABAQUS by means of a three-dimensional user element and a user material routine.

3 Heat generation due to domain switching

Under external electrical or mechanical loading the domains start to switch if the energy barrier is exceeded. Switching is an irreversible process whereby electromechanical energy is dissipated and transformed into heat inside the material. This heat generation corresponds to the variation of the remanent strain and polarization. If an adiabatic process is assumed, the temperature rate $\dot{\theta}$ due to domain switching can be calculated using the following equation:

$$\gamma \dot{\Xi} = \rho c_v \dot{\theta}, \tag{5}$$

with $\dot{\Xi}$ denoting the dissipation rate per volume, ρ and c_v are the density and specific heat,respectively. The factor γ describes the amount of energy converted into heat. From the Clausius-Duhem inequality the dissipation rate $\dot{\Xi}$ has the following form:

$$\dot{\Xi} = \left[\sigma_{ij}\dot{\varepsilon}_{ij}^R + E_i \dot{P}_i^R\right] \tag{6}$$

4 Finite element formulation

A finite element formulation based on the principle of virtual work is used. The global system of equations for stationary cases is expressed as follows :

$$\begin{bmatrix} K_{uu} & K_{u\varphi} & -K_{u\theta} \\ K_{\varphi u} & -K_{\varphi\varphi} & K_{\varphi\theta} \\ 0 & 0 & K_{\theta\theta} \end{bmatrix} \begin{bmatrix} u \\ \varphi \\ \theta \end{bmatrix} = \begin{bmatrix} f_u \\ f_\varphi \\ f_\theta \end{bmatrix} \tag{7}$$

It can be seen that the temperature field can be evaluated separately using $K_{\theta\theta}\theta = f_\theta$. In a second step, the temperature effect under combined mechanical and electric loading can be determined by solving the following equations:

$$\begin{bmatrix} K_{uu} & K_{u\varphi} \\ K_{\varphi u} & -K_{\varphi\varphi} \end{bmatrix} \begin{bmatrix} u \\ \varphi \end{bmatrix} = \begin{bmatrix} f_u + K_{u\theta}\theta \\ f_\varphi - K_{\varphi\theta}\theta \end{bmatrix} \tag{8}$$

⇒ TABLE OF CONTENTS

5 Numerical results

To evaluate the temperature influence on the ferroelectric materials behavior a representative volume element for a polycrystal with 125 randomly oriented grains is used, see figure(1-left). A cyclic bipolar external electric loading is applied to the RVE. Taking the material properties as constants during the whole loading time would not capture the real influence of the temperature, because the change of temperature leads to a change of the material properties as well. So in this work, the material properties are taken to be linearly dependent on the temperature, where each material property is expressed as follows:

$$\hat{A}(\theta) = A_1\theta + A_2 \tag{9}$$

Here, A_1 and A_2 are two material parameters based on the materials properties of TSR600 at two different temperatures taken from [5].
Figure(1-right) shows the temperature change with respect to the number of cycles. Passing through one hysteresis loop under cyclic loading, heat generation occurs only during domain switching, which lead to a step-wise temperature increase.

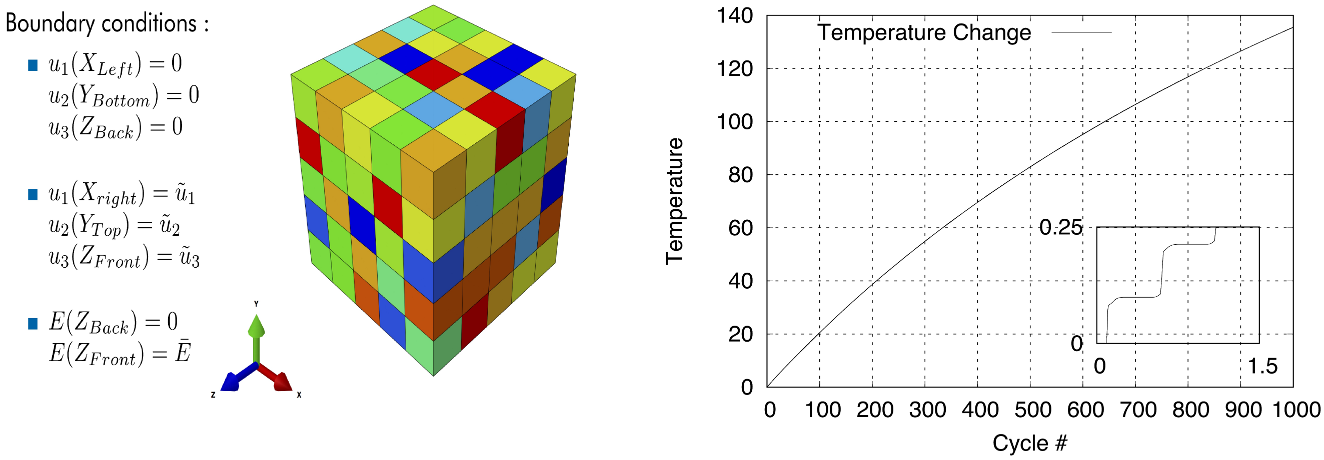

Figure 1: (Left) Representative volume element (RVE) with BC. (Right) Temperature change during cycling

In figure (2) the strain and polarization hysteresis are shown at different number of cycles. One can clearly observe that the change of temperature has an influence on the behavior of ferroelectric materials. From the strain hysteresis, one can see that the maximum strains are decreasing with the increase of temperature each cycle. On the other hand the minimum and remanent strains increase with the increase of temperature. In the case of polarization, a decrease in remanent and maximum polarization is observed with the increase of temperature. Finally, from both figures, one can notice the decrease of the coercive field strength. The behavior is in agreement with the experimental results, except for the case of the remanent strains, where in the experiments, their value decreases with the growing temperature. This disagreement could be due to the inaccuracy of the material properties of TRS600 at the different temperatures [5], or because of the difference of the evaluation of strains between the experiments and simulations.

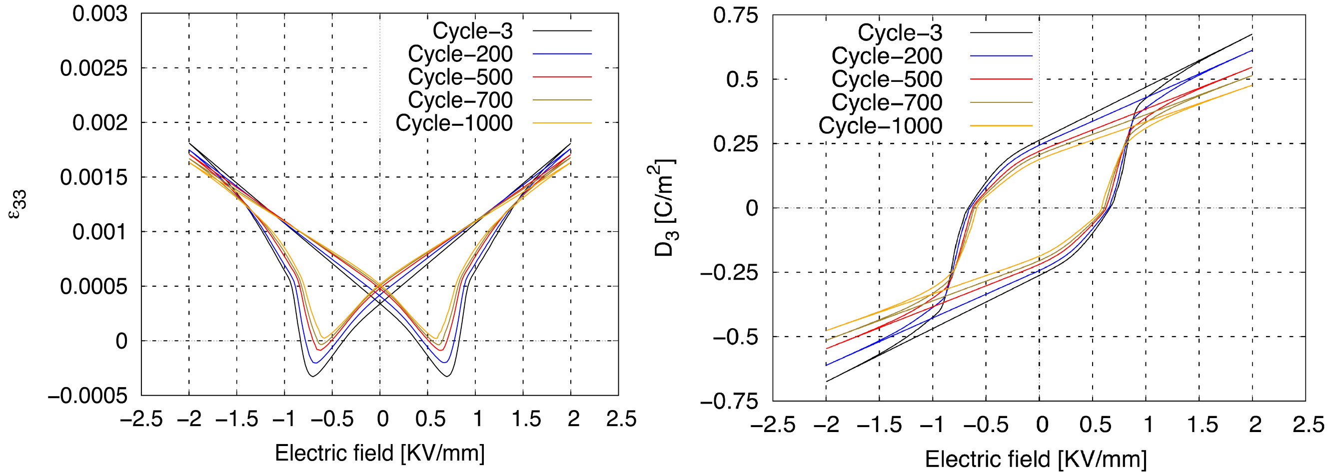

Figure 2: Hysteresis loops. (Left) Strain Hysteresis. (Right) Polarization Hysteresis

In future work, the presented model shall be applied to situations with high field concentrations (cracks, electrodes), since the thermal impact will be most crucial in those cases.

REFERENCES

[1] T. Sakai, and H. Kawamoto. Durability Properties of Piezoelectric Stack Actuator, *J.Appl.Phys*, 37: 5338–5341, 1998.

[2] Q. Li, A. Ricoeur, M. Enderlein, and M. Kuna. Evaluation of electromechanical coupling effect by microstructural modeling of domain switching in ferroelectrics, *Mechanics Research Communications*, 37: 332–336, 2010.

[3] J.E. Huber, N.A. Fleck, C.M. Landis, and R.M. McMeeking. A constitutive model for ferroelectric polycrystals, *J Mech Phys Solids* , 47: 1663–1697, 1999.

[4] A. Pathak, and R.M. McMeeking. Three-dimensional finite element simulations of ferroelectric polycrystals under electrical and mechanical loading, *J Mech Phys Solids*, 56: 663–683, 2008.

[5] L.D. Mauck, and C.S. Lynch. Thermo-electro-mechanical Behavior of Ferroelectric Materials Part I: A Computational Micromechanical Model versus Experimental Results, *JOURNAL OF INTELLIGENT MATERIAL SYSTEMS AND STRUCTURES*, 14, 2003.

ON THE CHOICE OF REPRESENTATIVE VOLUMES FOR RANDOM HETEROGENEOUS MATERIALS

Julian Fischer[1,*]

[1] Institute of Science and Technology Austria,
Am Campus 1, 3400 Klosterneuburg, Austria

Abstract. *The effective large-scale material properties of a material with random microstructure are typically computed by the method of representative volumes: A sample of the material is chosen – the representative volume – and the effective material properties are determined by the cell formula. In principle, for an accurate prediction of the effective material properties it is necessary to capture the statistical properties of the random material well within the representative volume. While this is possible by choosing a large enough representative volume, a larger representative volume comes at the price of a larger computational cost. For this reason, in mechanics, material science, and mathematics methods have been developed to capture fundamental statistical properties of a random material in a better way in a representative volume of a fixed size. Le Bris, Legoll, and Minvielle proposed an approach of selecting a material sample that captures certain statistical properties best. In the setting of linear materials, we provide a rigorous mathematical analysis of their approach: We show that their selection approach for representative volumes essentially never performs worse than a random selection of the material sample and may perform much better if the selection criterion is chosen suitably.*

The effective large-scale properties of materials with random heterogeneities on a small scale are typically determined by the *method of representative volumes*: It basically proceeds by choosing a sample of the random material – the *representative volume* – and computing its properties by the cell formula. To obtain an accurate approximation for the effective material properties, the sample should reflect the statistical properties of the material well. As a consequence, it is desirable to choose a large sample of the random material. However, an increased size of the sample comes with an increased computation cost; for this reason, there have been approaches in material science and mechanics – under the names "special quasirandom structures" [6] and "statistically similar representative volume elements" [5] – towards capturing the statistical properties of the material in a better way in a sample of a fixed size.

Inspired by these attempts, Le Bris, Legoll, and Minvielle [4] have proposed a selection approach for representative volumes: Their idea is to consider a large number of material samples and select the ones that captures certain important statistical properties of the random material best, i. e. the ones that are "most representative" of the material. For example, for a composite of two constituent materials, in the simplest setting of their method they propose to select the material samples in which the volume fractions of the constituent materials match best with the volume fractions of the constituents in the overall material (see Figure 1 for an illustration of this approach). More generally, they consider one or more statistical quantities $\mathcal{F}$ of the material samples and select the representative volume according to the criterion (with $0 < \delta \ll 1$)

$$\big|\mathcal{F} - \mathbb{E}[\mathcal{F}]\big| \leq \delta\sqrt{\operatorname{Var}\mathcal{F}}. \qquad (1)$$

---

[*] Corresponding author: Julian Fischer (✉ julian.fischer@ist.ac.at)

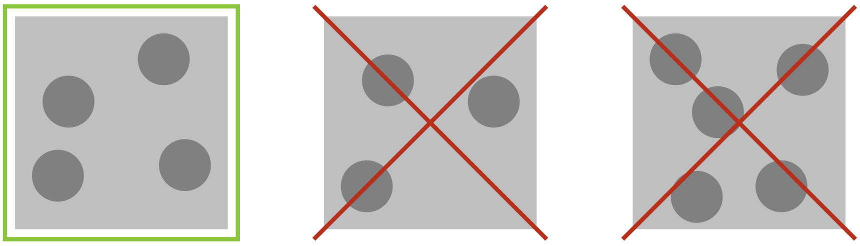

Figure 1: An illustration of the method of Le Bris, Legoll, and Minvielle for a two-material composite. Among the three depicted material samples, the method in its simplest realization would choose the first sample as the representative volume element and discard the other two, as the volume fraction of the inclusions in the first sample is closest to the overall material average. For a better illustration of the method, both the size and the number of material samples have been chosen exaggeratedly small.

Our rigorous mathematical analysis of the method of Le Bris, Legoll, and Minvielle [4] is concerned with the mathematical model case of a linear elliptic equation $-\nabla\cdot(a\nabla u)=f$ with a random coefficient field $a=a(x,\omega)$ with bounded contrast. Here, we assume the probability distribution of a to be spatially homogeneous and feature fast decorrelation on length scales larger than some scale $\varepsilon\ll 1$. Note that this setting describes for example heat conduction or electrostatics in a macroscopically homogeneous material with a random microstructure on the scale ε. The theory of homogenization then ensures that for small ε one may approximate the solution u by the solution u_{hom} of a homogenized effective equation $-\nabla\cdot(a_{\mathrm{hom}}\nabla u_{\mathrm{hom}})=f$ with a constant effective coefficient a_{hom}.

In this context of linear elliptic equations, the method of representative volumes is employed to obtain an approximation a^{RV} for the effective coefficient a_{hom}. Roughly speaking, the approximation a^{RV} is computed by choosing a sample $a|_{[0,L\varepsilon]^d}$ of the random coefficient (for some factor $L\gg 1$), solving the equation for the homogenization corrector $-\nabla\cdot(a(e_i+\nabla\phi_i))=0$ on this sample, and averaging the fluxes

$$a^{\mathrm{RV}}e_i := \frac{1}{|L\varepsilon|^d}\int_{[0,L\varepsilon]^d} a(e_i+\nabla\phi_i)\,dx.$$

This approximation a^{RV} is a random quantity, as it depends on the sample $a|_{[0,L\varepsilon]^d}$ of the random coefficient. In contrast, the macroscopic effective coefficient a_{hom} is deterministic. In fact, as shown by Gloria and Otto [2, 3] the leading-order contribution to the error $a^{\mathrm{RV}}-a_{\mathrm{hom}}$ consists of random fluctuations: The order of the fluctuations of a^{RV} is given by

$$\sqrt{\operatorname{Var} a^{\mathrm{RV}}}\leq CL^{-d/2},$$

while the systematic error is of higher order in the relative size L of the sample

$$\big|\mathbb{E}[a^{\mathrm{RV}}]-a_{\mathrm{hom}}\big|\leq CL^{-d}|\log L|^d.$$

In this setting of linear elliptic equations, the selection approach for representative volumes by Le Bris, Legoll, and Minvielle [4] achieves an increase in computational efficiency by a factor of about 10 in numerical examples with moderate ellipticity contrast if the selection of material samples is based on the spatial average $\mathcal{F}:=\frac{1}{|L\varepsilon|^d}\int_{[0,L\varepsilon]^d} a\,dx$. By designing a more elaborate selection criterion, Le Bris, Legoll, and Minvielle [4] were even able to reduce the

⇒ TABLE OF CONTENTS

computational cost by a factor of about 50. Their numerical examples show that the selection approach achieves its gain in accuracy by reducing the fluctuations of the approximations a^{RV}. The method also maintains the order of magnitude of the systematic error, but it does not decrease it substantially. While the selection approach of Le Bris, Legoll, and Minvielle [4] has been successful in numerical examples, its mathematical analysis has essentially been limited to the one-dimensional setting, in which the homogenization of linear elliptic equations is linear in the inverse coefficients and therefore independent of the geometry of the material.

In the recent work [1], we establish a rigorous mathematical justification of the selection approach for representative volumes by Le Bris, Legoll, and Minvielle. In particular, we quantify the gain in accuracy of the selection approach and prove that the method does never worse than a random selection of samples: Denoting by $a^{\text{sel-RV}}$ the approximation for the effective coefficient obtained by the selection approach for representative volumes with a single selection criterion (1), we derive an estimate of roughly the form

$$\frac{\operatorname{Var} a^{\text{sel-RV}}}{\operatorname{Var} a^{\mathrm{RV}}} \leq 1-(1-\delta^2)|\rho|^2+\frac{C}{(1-|\rho|^2)^{3/2}\delta}L^{-d/2}|\log L|^p$$

where $|\rho|^2$ denotes the fraction of the variance of a^{RV} which is explained by the statistical quantity $\mathcal{F}$. As a consequence, for a suitable choice of the statistical quantity $\mathcal{F}$ the selection approach for representative volumes provides a substantial gain in accuracy.

We also show that the selection method for representative volumes essentially preserves the order of the systematic error in the sense

$$\big|\mathbb{E}[a^{\text{sel-RV}}]-a_{\mathrm{hom}}\big| \leq \frac{C}{(1-|\rho|^2)^{3/2}\delta}L^{-d}|\log L|^p$$

and that the tails (more precisely, the moderate deviations) of the probability distribution of $a^{\text{sel-RV}}$ are reduced just as suggested by the variance reduction. Similar results are proven for the method of Le Bris, Legoll, and Minvielle if the selection of representative volumes is performed based on multiple statistical quantities.

REFERENCES

[1] J. Fischer, *The choice of representative volumes in the approximation of effective properties of random materials*, Preprint (2018).

[2] A. Gloria and F. Otto, *An optimal variance estimate in stochastic homogenization of discrete elliptic equations*, Ann. Probab., 39 (2011), 779–856.

[3] A. Gloria and F. Otto, *An optimal error estimate in stochastic homogenization of discrete elliptic equations*, Ann. Appl. Probab., 22 (2012), 1–28.

[4] C. Le Bris, F. Legoll, and W. Minvielle, *Special quasirandom structures: a selection approach for stochastic homogenization*, Monte Carlo Methods Appl., 22 (2016), 25–54.

[5] J. Schröder, D. Balzani, and D. Brands, *Approximation of random microstructures by periodic statistically similar representative volume elements based on lineal-path functions*, Arch. Appl. Mech., 81 (2011), 975–997.

[6] A. Zunger, S.-H. Wei, L. G. Ferreira, and J. E. Bernard, *Special quasirandom structures*, Phys. Rev. Lett., 65 (1990), 353–356.

⇒ TABLE OF CONTENTS

NUCLEAR MAGNETIC RESONANCE (NMR) STUDY OF LOCAL STRUCTURE IN LEAD-FREE RELAXOR AND FERROELECTRIC MATERIALS

Pedro B. Groszewicz[1*], **Karsten Albe**[2], **Jürgen Rödel**[2], **Gerd Buntkowsky**[1]

[1] Chemistry Department, Technische Universität Darmstadt
Alarich-Weiss-Straße 8, Darmstadt, Germany

[2] Institute of Materials Science, Technische Universität Darmstadt
Alarich-Weiss-Straße 2, Darmstadt, Germany

Abstract. *In this contribution, key aspects of solid-state nuclear magnetic resonance spectroscopy of sodium (^{23}Na NMR) regarding functional ceramics will be introduced. This technique explores interactions between the nucleus and its close surroundings to provide insight into the structure at the atomic scale. Two examples of the application of ^{23}Na NMR to the study of the local structure in perovskite oxides will be discussed.*

In the first example, the characterization of local structure disorder in relaxor ferroelectrics with composition (100-x)($Na_{1/2}$,$Bi_{1/2}$)TiO_3-x$BaTiO_3$ (NBT-BT) will be presented. Its relation to the tilting of oxygen octahedra will be highlighted. Furthermore, its role in the composition-driven ferroelectric-to-relaxor transition observed between rhombohedral and tetragonal phases in this solid-solution will be discussed.[1]

The second example deals with the electrical poling of NBT-xBT bulk ceramic samples and the corresponding changes to the local structure as observed in ^{23}Na MAS NMR spectra of relaxor compositions. These experiments provides evidence of the coexistence of a non-polar matrix of cubic symmetry and polar nanoregions (PNRs) in the ground state of these lead-free relaxor ferroelectrics.[2]

1 Introduction

The research on lead-free electrically functional materials has been stimulated by the need for an environment-friendly substitute to lead-based piezoelectric ceramics.[3-6] Among the bismuth-based alternatives with a perovskite structure, barium-doped bismuth-sodium titanate (NBT-xBT) is considered one of the most promising candidates,[7] mainly due to their large piezoelectric coefficients[8, 9] and their potential use as high-temperature dielectrics.

Nonetheless, key aspects of the structure-property relations in NBT-xBT are still unclear. These intrinsically inhomogeneous perovskites[10] are often found in a relaxor ferroelectric state. In the relaxor state, the structural distortions responsible for electrical polarization exhibit small magnitude and very short coherence length.[11] These characteristics pose a challenge to their characterization with conventional diffraction methods, as their average macroscopic structure is perceived as being cubic.[12, 13] As a consequence, the impact of chemical modifications on the structure and the occurrence of a relaxor ferroelectric state as a function of composition are still unsettled matters. A characterization method sensitive to the local structure may shed new light on these questions.

---

[*] Corresponding author: Pedro B. Groszewicz (groszewicz@chemie.tu-darmstadt.de)

Solid-state Nuclear Magnetic Resonance (NMR) is a powerful tool for investigating changes in the local structure of materials. The frequency and shape of the NMR signal of a given nucleus is determined by short ranged interactions with the environment close to it. Hence, this technique does not rely on a long-range spatial coherence for probing the structure, so that the nanometric character of a phase is no hindrance for its detection. For quadrupolar nuclei, like ^{23}Na (I=3/2), spectral features are mainly determined by the quadrupole coupling, which probes the electrostatic interaction between the nucleus and the electric field gradient (EFG) created by surrounding electric charges (i.e. electrons and nearby atoms).

Owing to its high sensitivity of the electric quadrupolar interaction to subtle changes of local structure and symmetry, we decided to employ ^{23}Na solid-state NMR spectroscopy to study the influence of composition and the effect of electric poling on solid solutions between $Na_{0.5}Bi_{0.5}TiO_3$ and $BaTiO_3$ (NBT-xBT) Depending on the barium content, samples may exhibit either a ferroelectric or a relaxor state.[14] The phase diagram of NBT-xBT shows a rhombohedral (x<5) and a tetragonal (x>11) region, which macroscopically differ with respect to the tilt system that oxygen octahedra adopt. In between these phases there is a transition region often assumed to be a morphotropic phase boundary. Compositions in this transition region are well represented by NBT-6BT, which despite showing enhanced electric properties is essentially cubic to XRD [13] and neutron diffraction [15]. In the next paragraphs the outcome of the present solid-state NMR study of the local structure of NBT-xBT are summarized and illustrated.

2 Local structure disorder, octahedral tilting and the relaxor state in NBT-xBT

In stark contrast to classic ferroelectrics (e.g. $NaNbO_3$), the shape of ^{23}Na 3QMAS NMR signals of NBT-xBT materials indicates their local structure deviates from the average one (Figure 1), in that a continuous distribution of local structural motifs is present. This diversity can be quantified in terms of a distribution of electric field gradients (EFG) through the spectral parameter ΔQIS_{width}

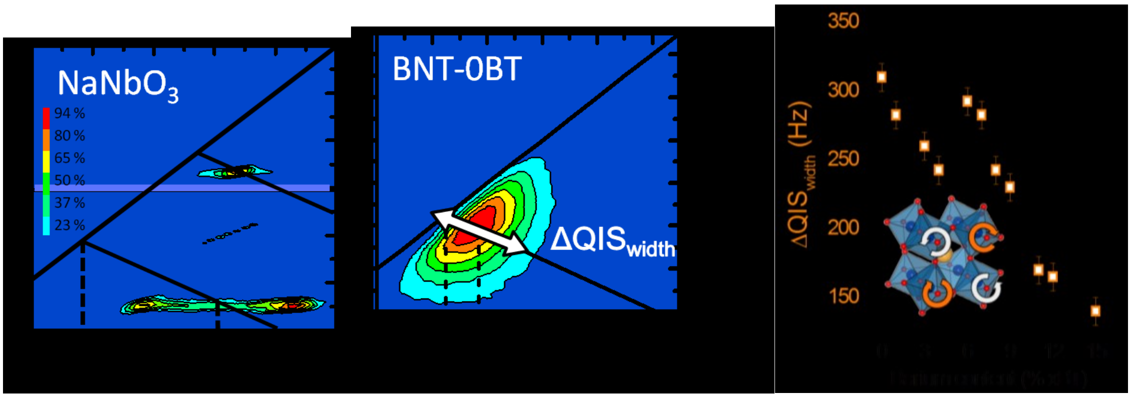

Figure 1: ^{23}Na 3QMAS NMR spectra of a well-ordered perovskite ($NaNbO_3$ - left)[16] and a disordered material ($(Na,Bi)TiO_3$ - middle).[1] The width of EFG distribution (ΔQIS_{width}) is highlighted by the white arrow. Right: Composition dependence of ΔQIS_{width}, a parameter related to the disorder of octahedra tilting.[1]

Upon addition of barium to the structure, both the mean value and the width of the EFG distribution (ΔQIS_{width}) decrease, the latter parameter exhibiting a peculiar composition dependence (Figure 1). Interestingly, this composition dependence correlates strongly with the presence and intensity of frequency dispersion in dielectric spectra of NBT-xBT (ΔT_m in Figure 2). Larger ΔQIS_{width} values are observed for compositions in a relaxor state (e.g. NBT-0BT and NBT-6BT) than those found in a spontaneous ferroelectric state (e.g. NBT-3BT and NBT-12BT). This fact suggests a relation between the degree of local structure disorder and the occurrence of a relaxor state as a function of composition in NBT-xBT.

⇒ TABLE OF CONTENTS

DFT calculations for several structural models revealed the local structure features responsible for the composition dependence of the EFG. The experimental trend of decreasing EFG values upon addition of barium was only reproduced when octahedral tilting was considered, with decreasing equilibrium values of tilt angle and EFG of the ^{23}Na site whenever barium is present. Hence, we could infer that the experimental EFG on ^{23}Na site reflects the behavior of octahedral tilting in these perovskites.

As these materials exhibit a continuous distribution of EFG values, this work demonstrates that the local structure disorder in NBT-xBT can be attributed to a continuous distribution of octahedra tilting. From the correlation between the EFG distribution width (ΔQIS_{width}) and the frequency dispersion in ε(T) curves, it was concluded that octahedral tilting disorder is a local structural trait concurrent with the relaxor state in NBT-xBT.

3 Coexistence of cubic and non-cubic phases in relaxor state of NBT-xBT

By means of ^{23}Na solid-state NMR, it was demonstrated that two local symmetries coexist in NBT-xBT samples in the relaxor state, namely a cubic phase together with a non-cubic one.[2] The amount of cubic phase was estimated for the unpoled, poled and depoled states of each investigated composition (bars in Figure 2), based on the relative area of spectral components attributed to the satellite and central transitions (i.e. the broad and narrow components in the ^{23}Na MAS NMR spectra in Figure 2).

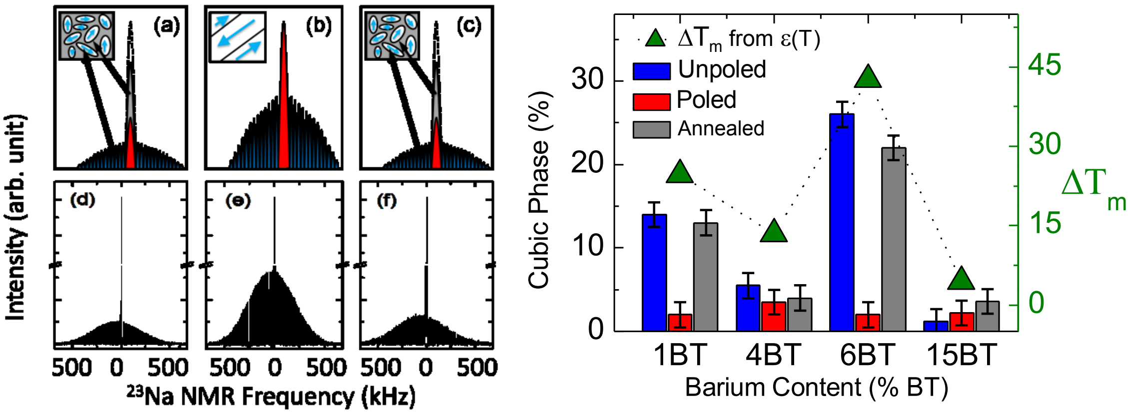

Figure 2: Cubic phase content in NBT-xBT determined with ^{23}Na ssNMR.[2] Correlation to dispersion of the temperature of maximum ε(T) (a sign of the relaxor state).

The presence of a frequency dispersion (ΔT_m) in the ε(T) curves allows one to identify the relaxor state in a given NBT-xBT composition (Figure 2– right axis). The cubic phase is found only for compositions that exhibit relaxor features in their permittivity curves, suggesting that the presence of this phase is intimately connected to the relaxor state.

Relaxor compositions of NBT-xBT bulk ceramics undergo an electric field-induced phase transition into the ferroelectric state after field cooling (electric poling), with the concomitant decrease in the cubic content (red bars in Figure 2). Electric poling enables the growth of PNRs to macroscopic ferroelectric domains, at expense of the cubic matrix, and a ferroelectric state is achieved.

Annealing the poled samples and cooling them without electric field results in the relaxor state again. The reappearance of the cubic phase at comparable amounts to the unpoled samples (grey bars in Figure 2) demonstrates the reversibility of the poled state, and further supports the relation between the cubic phase and the relaxor state. It could also be shown that the electric field induced transition from a relaxor into a ferroelectric state does not only consist of a reorientation of electric

⇒ TABLE OF CONTENTS

dipoles; instead, the cubic phase becomes polarized. These results support a view of the microstructure of relaxors with PNRs embedded in a cubic non-polar matrix.

REFERENCES

[1] P.B. Groszewicz, M. Gröting, H. Breitzke, W. Jo, K. Albe, G. Buntkowsky, J. Rödel, Reconciling Local Structure Disorder and the Relaxor State in (Bi1/2Na1/2)TiO3-BaTiO3, Scientific Reports, 6 (2016) 31739.

[2] P.B. Groszewicz, H. Breitzke, R. Dittmer, E. Sapper, W. Jo, G. Buntkowsky, J. Rödel, Nanoscale phase quantification in lead-free (Bi1/2Na1/2)TiO3-BaTiO3 relaxor ferroelectrics by means of 23Na NMR, Physical Review B, 90 (2014) 220104.

[3] W. Jo, R. Dittmer, M. Acosta, J. Zang, C. Groh, E. Sapper, K. Wang, J. Rödel, Giant electric-field-induced strains in lead-free ceramics for actuator applications – status and perspective, Journal of Electroceramics, 29 (2012) 71-93.

[4] C.-H. Hong, H.-P. Kim, B.-Y. Choi, H.-S. Han, J.S. Son, C.W. Ahn, W. Jo, Lead-free piezoceramics – Where to move on?, Journal of Materiomics, 2 (2016) 1-24.

[5] J. Rödel, W. Jo, K.T.P. Seifert, E.-M. Anton, T. Granzow, D. Damjanovic, Perspective on the Development of Lead-free Piezoceramics, Journal of the American Ceramic Society, 92 (2009) 1153-1177.

[6] J. Rödel, K.G. Webber, R. Dittmer, W. Jo, M. Kimura, D. Damjanovic, Transferring lead-free piezoelectric ceramics into application, Journal of the European Ceramic Society, 35 (2015) 1659-1681.

[7] V.V. Shvartsman, D.C. Lupascu, Lead-Free Relaxor Ferroelectrics, Journal of the American Ceramic Society, 95 (2012) 26.

[8] T. Takenaka, K. Maruyama, K. Sakata, (Bi1/2Na1/2)TiO3-BaTiO3 System for Lead-Free Piezoelectric Ceramics, Jpn. J. Appl. Phys., 30 (1991) 2236.

[9] S.-T. Zhang, A.B. Kounga, E. Aulbach, H. Ehrenberg, J. Rödel, Giant strain in lead-free piezoceramics Bi0.5Na0.5TiO3–BaTiO3–K0.5Na0.5NbO3 system, Applied Physics Letters, 91 (2007) 112906.

[10] W. Jo, S. Schaab, E. Sapper, L.A. Schmitt, H.-J. Kleebe, A.J. Bell, J. Rödel, On the phase identity and its thermal evolution of lead free (Bi1/2Na1/2)TiO3-6 mol% BaTiO3, J. Appl. Phys., 110 (2011) 074106.

[11] G. Burns, F.H. Dacol, Glassy polarization behavior in ferroelectric compounds Pb(Mg13Nb23)O3 and Pb(Zn13Nb23)O3, Solid State Communications, 48 (1983) 853-856.

[12] N. de Mathan, E. Husson, G. Calvarin, A. Morell, Structural study of a poled PbMg13Nb23O3 ceramic at low temperature, Materials Research Bulletin, 26 (1991) 1167-1172.

[13] R. Ranjan, A. Dviwedi, Structure and dielectric properties of (Na0.50Bi0.50)1−xBaxTiO3: 0≤x≤0.10, Solid State Communications, 135 (2005) 394-399.

[14] C. Ma, H. Guo, S.P. Beckman, X. Tan, Creation and Destruction of Morphotropic Phase Boundaries through Electrical Poling: A Case Study of Lead-Free BNT-BaTiO3 Piezoelectrics, Physical Review Letters, 109 (2012) 107602.

[15] R. Garg, B.N. Rao, A. Senyshyn, P.S.R. Krishna, R. Ranjan, Lead-free piezoelectric system (Na0.5Bi0.5TiO3-BaTiO3 Equilibrium structures and irreversible structural transformations driven by electric field and mechanical impact, Physical Review B, 88 (2013) 014103.

[16] J. Koruza, P. Groszewicz, H. Breitzke, G. Buntkowsky, T. Rojac, B. Malič, Grain-size-induced ferroelectricity in NaNbO3, Acta Materialia, 126 (2017) 77-85.

Strain Doping: A New Avenue for Understanding and Controlling Materials

Andreas Herklotz[1,*] **and Thomas Zac Ward**[2]

[1] Institute for Physics, Martin-Luther-University Halle-Wittenberg
Von-Dankelmann-Platz, Halle (Saale), Germany

[2] Material Science and Technology Division, Oak Ridge National Laboratory
One Bethel Valley Road, Oak Ridge, USA

Abstract. *The strong electronic correlations arising from overlapping spin-charge-orbital-lattice order parameters in complex oxides are of fundamental importance to many desirable characteristics such as metal-insulator transitions, ferroicity, colossal magnetoresistance, and high* T_C *superconductivity. Control over the orbital and lattice parameters in these systems is generally achieved through strain engineering imposed by heteroepitaxial film growth on non-lattice-matched substrates. This method involves perturbation in all three unit cell dimensions since the in-plane strain induced into a film's lattice is accommodated by an elastic reaction along the out-of-plane lattice direction driven by the Poisson effect. This talk will give an overview of our recent work in developing low energy, low dose He ion implantation as a means to strain dope thin film materials. Unlike conventional epitaxy-based strain tuning methods, strain doping is an effective means of continuously controlling lattice expansion along the out-of-plane axis while leaving the in-plane axes locked to the substrate. Functionality is then controlled by modifying crystal symmetry and the tuning of orbital polarizations [1].*

I will focus on recent results of several functional materials and demonstrate how this technique delivers never before possible control over crystal phases, octahedral rotation patterns [2], magnetic anisotropy [3] and optical bandgaps [4,5]. I will also discuss the implications of the ability to control a single order parameter in how we interrogate theoretical models of correlated materials.

REFERENCES

[1] S. H. Guo, S. Dong, P. D. Rack, J. D. Budai, C. Beekman, Z. Gai, W. Siemons, C. M. Gonzalez, R. Timilsina, A. T. Wong, A. Herklotz, P. C. Snijders, E. Dagotto and T. Z. Ward, *Physical Review Letters*, 114: 256801, 2015.

[2] A. Herklotz, A. T. Wong, T. Meyer, M. D. Biegalski, H.-N. Lee and T. Z. Ward, *Scientific Reports*, 6: 26491, 2016.

[3] A. Herklotz, Z. Gai, Y. Sharma, A. Huon, S. F. Rus, L. Sun, J. Shen, P. D. Rack and T. Z. Ward, *submitted*.

[4] A. Herklotz, S.F. Rus and T.Z. Ward, *Nano Letters*, 16: 1782-1786, 2016.

[5] A. Herklotz, A. Huon, E.-J. Guo, S. KC, V.R. Cooper, S. F. Rus and T. Z. Ward, *APL Materials*, 5: 066106, 2017.

---

[*] Corresponding author: Andreas Herklotz (herklotza@gmail.com)

ELECTROMECHANICS OF FERROELECTRIC POLYCRYSTALS FROM DIFFRACTION METHODS

Jacob L. Jones[1]

[1] Department of Materials Science and Engineering, North Carolina State University, Raleigh, NC, USA

Abstract. *The behavior of ferroelectric domains in response to field is central to the functionality of numerous multifunctional materials. We have developed and applied rigorous methodologies and analyses for characterizing the behavior of ferroelectric domains and their collective effect on the macroscopic properties. Many of these experiments involve high-energy synchrotron X-ray diffraction, though examples are also provided utilizing neutron diffraction and laboratory X-ray diffractometers. The measurements on numerous material systems reveal the importance and interdependence of strain contributed from domain reorientation, piezoelectric lattice strain, elastic strain, and phase transitions.*

1 Introduction

The response of polycrystalline ferroelectric materials to electrical and mechanical stimuli is crucial to the performance of multifunctional materials. A unique characteristic of polycrystalline materials in both monolithic (often called "bulk") and thin film is the grain structure which is neither present in single crystals nor in epitaxial thin films. Polycrystalline materials can have random or anisometric grains and can be crystallographically textured or randomly oriented in nature. For purposes of this abstract, we consider monolithic, randomly oriented, polycrystalline ferroelectrics.

Two of the most important phenomena for ferroelectric materials are piezoelectricity and ferroelectricity. The piezoelectric response involves a linear change in strain components due to electric field; this type of response is often referred to as an intrinsic effect because it is due to crystal structure changes. The ferroelectric response involves a reorientation of ferroelectric domains, which yields a change in macroscopic polarization state of the sample; this type of response is often referred to as an extrinsic effect because it is not due to crystal structure changes. In polycrystalline ferroelectrics, these mechanisms (and other effects which are mostly weaker) must cooperate in the sense that the polycrystal has to remain cohesive. Fig. 1 shows an illustration of how grains with different orientations may respond to the electric field with different mechanisms:

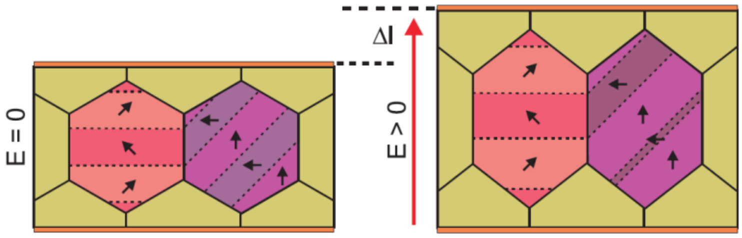

Figure 1: Illustration showing response of two grains with different orientations in a polycrystalline ferroelectric material and their response to field, from Ref. [1]. The grain on the right hand side experiences domain reorientation in response to the field while the grain on the left hand side experiences lattice strain.

---

*Corresponding author: Jacob L. Jones (jacobjones@ncsu.edu)

⇒ TABLE OF CONTENTS

Note that, while the grain on the left hand side in Figure 1 is said to experience piezoelectricity, it also has elastic interactions with the neighboring grains and the lattice strain it experiences may be driven by the field (piezoelectricity), by the mechanical forces it experiences locally (compliance), or both. Though this feature is not discussed rigorously in this document, it is an ongoing discussion point in the correlation of microscopic strain mechanisms to macroscopic strain.

2 Overview of diffraction methods

Diffraction is a tool that is highly suited for the measurement of piezoelectric strain and ferroelectric domain reorientation. A convenient and heavily utilized diffraction geometry combines high-energy X-rays with a 2-dimensional area detector, illustrated in Fig. 2(a). In this geometry, scattering in different sectors of the detector (φ) corresponds to different orientations of crystallographic planes in the various grain orientations of the polycrystalline material. A vertical sector of the detector (φ=0°) is usually utilized to describe the crystal poles most closely parallel to the electric field. Analysis of the positions, intensity, and shape of the $00h$ and $h00$ reflections (h = integer, Fig. 2(b)) is a convenient way to characterize ferroelectric/ferroelastic domain walls and the net effect of their motion. For example, the intensities of these peaks are typically used to quantify the extent of domain alignment (η) as a function of stimulus. For example, for tetragonal perovskite ferroelectric materials, Eq. (1) was derived in Ref. [2] for this purpose,

$$\eta_{00h} = \frac{R_{00h}}{R_{00h}+2R_{h00}} - {}^{1}\!/_{3}\,, \tag{1}$$

where R_{00h} is the ratio of the integrated intensity of the $00h$ reflection to the integrated area of the same reflection in a randomly oriented sample. Other equations exist in our prior work for other crystallographic symmetries.

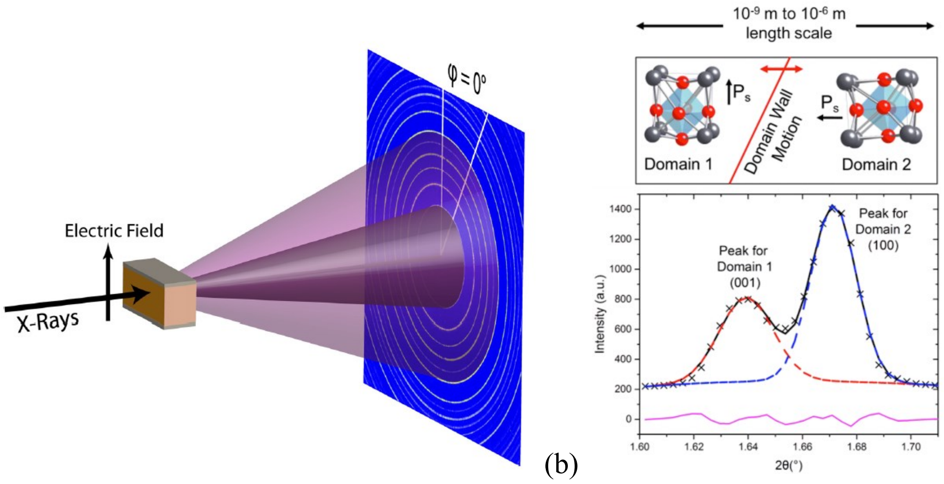

(a) (b)

Figure 2: (a) Schematic of a high-energy X-ray diffraction experiment, showing X-rays penetrating through the sample and Debye-Scherrer rings captured on a detector, from Ref. [3]. (b) Example of 001 and 100 diffraction peaks and their fitting using analytical profile functions, from Ref. [4].

3 Some exemplary results

Using these diffraction and analysis methods, the collective degree of domain alignment in ferroelectrics can be measured as a function of stimuli, *e.g.* electric field and mechanical stress, in order to understand the fundamental physics of ferroelectrics. The response can be characterized as a function of stimulus characteristics (amplitude, frequency, waveform, *etc.*), spatial location on the sample (*e.g.*, scanning over a feature of interest), orientation of grain or crystallographic planes to the stimulus direction, and fatigue or aging condition. An example of the η_{00h} value for a representative lead-free polycrystalline ferroelectric of tetragonal crystal symmetry is shown in Fig. 3; note the parallels between butterfly shape of the domain reorientation and the hysteresis loop that one typically measures macroscopically. Features of the ferroelectric domain behavior including the coercive field for ferroelectric domain reorientation and the maximum and remanent degrees of domain alignment are easily characterized from these experiments.

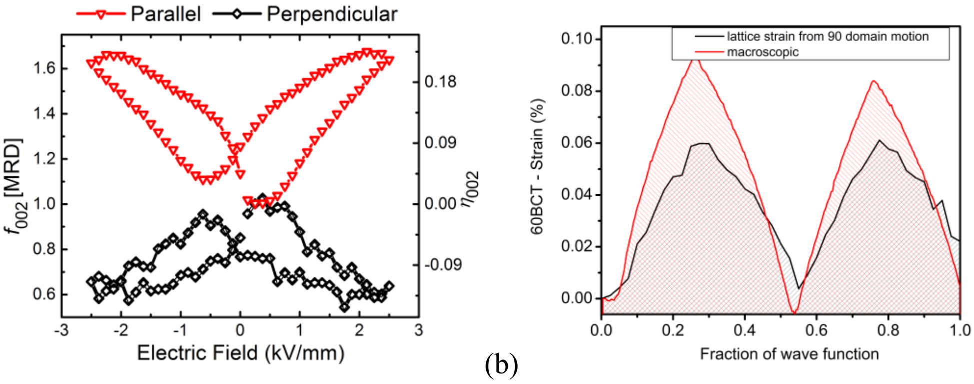

(a) (b)

Figure 3. (a) Degree of domain alignment as a function of applied electric field amplitude and direction for a lead-free composition $0.4(Ba(Zr_{0.2}Ti_{0.8})O_3$-$0.60(Ba_{0.7}Ca_{0.3})TiO_3$, from Ref. [5]. (b) The contribution of this domain alignment (black) to the macroscopic strain (red), from Ref. [3].

4 Further micromechanics-based calculation examples

Because the degree of domain alignment, η, is a quantitative metric and can be measured in all directions of the sample, the values can be used to determine the net contribution of domain reorientation to the macroscopic strain. The equation relating the micromechanics of domain alignment to the macroscale strain (S_{zz} in the z-direction) was derived in Ref. [6] and a simplified version reported in Ref. [1] is shown as Eq. (2). The simplified form is for an initially randomly oriented polycrystalline sample of tetragonal perovskite structure that has a fiber texture after electric field application:

$$S_{zz} = \frac{c-a}{a}\int_{\alpha=0}^{\pi/2}[3\Delta\eta_{00h}(\alpha)\cos^2(\alpha)\sin(\alpha)]\,\mathrm{d}\alpha \,, \tag{2}$$

In our papers on these topics, we also provide the equations for other crystal symmetries as well as equations that can be used in initially textured materials. An example of the application of Eq. (2) is shown in Fig. 3(b): In this sample, changes in domain alignment with field have a major influence on the overall macroscopic strain.

5 Other extensions

Over the past decade, we have extended these approaches substantially to other loading scenarios, sample types, *etc*. Domain alignment and contribution of domain reorientation to strain has been measured under uniaxial compressive stress using both neutron and X-ray diffraction, *e.g.* for $Pb(Zr,Ti)O_3$ compositions in Refs. [7] and [8] and in $BiFeO_3$-$PbTiO_3$ in Ref. [9]. Domain alignment near mechanically loaded crack tips and in the crack wake of compact tension specimens has been studied and compared to theoretical stress distributions in Ref. [10]. Multilayer ceramic actuators have been studied using these techniques [11]. Domain walls can move, albeit smaller distances, under weak, subcoercive electric fields. At weak-field conditions, Rayleigh law is usually applied to macroscopic strain data to characterize the field-amplitude dependence of the response. We have measured domain reorientation under these conditions in high-intensity synchrotron X-ray experiments and been able to describe how domain reorientation contributes nearly entirely the Rayleigh behavior in several systems [1,12]. Phase transitions and interphase boundary motion are easily observed in these types of experiments, as evidenced in Pb(Zr,Ti)O_3 [11] and $BiScO_3$-$PbTiO_3$ [13]. Recently, we developed a smaller *in situ* loading cell that can be used in a laboratory diffractometer and added this capability to a diffractometer furnace. The results show that domain reorientation is thermally activated and fits to an Arrhenius type of behavior [14]. Finally, we have applied advanced statistics for characterizing domain alignment, specifically the application of Bayesian inference with sampling algorithms to determine posterior probability density functions on η_{00h}, providing a much richer uncertainty quantification than available with the equivalent frequentist approach [4].

REFERENCES

[1] A. Pramanick, D. Damjanovic, J. E. Daniels, J. C. Nino, and J. L. Jones, Origins of Electro-Mechanical Coupling in Polycrystalline Ferroelectrics During Subcoercive Electrical Loading, *J. Am. Ceram. Soc*, 94: 293-309, 2011.

[2] J. L. Jones, E. B. Slamovich, and K. J. Bowman, Domain Texture Distributions in Tetragonal Lead Zirconate Titanate by X-ray and Neutron Diffraction, *J. Appl. Phys*, 97:034113, 2005.

[3] G. Tutuncu, B. Li, K. Bowman, and J. L. Jones, Domain wall motion and electromechanical strain in lead-free piezoelectrics: insight from the model system (1-x)Ba($Zr_{0.2}Ti_{0.8}$)O_3-x($Ba_{0.7}Ca_{0.3}$)TiO_3 using in situ high-energy X-ray diffraction during application of electric fields, *J. Appl. Phys*, 115: 144104, 2014.

[4] T. Iamsasri, J. Guerrier, G. Esteves, C. M. Fancher, A. Wilson, R. Smith, E. Paisley, R. Johnson-Wilke, J. Ihlefeld, N. Bassiri-Gharb and J. L. Jones, A Bayesian Approach to Modeling Diffraction Profiles and Application to Ferroelectric Materials, *J. Appl. Crystall.*, 50:211, 2017.

[5] G. Esteves, C. Fancher, J. L. Jones, In situ characterization of polycrystalline ferroelectrics using x-ray and neutron diffraction, *J. Materials Research*, 30: 340, 2015.

[6] J. L. Jones, M. Hoffman, and K. J. Bowman, Saturated domain switching textures and strains in ferroelastic ceramics, *J. Appl. Phys.*, 98:024115, 2005.

[7] J. L. Jones, M. Hoffman, and S. C. Vogel, Ferroelastic Domain Switching in Lead Zirconate Titanate Measured by In Situ Neutron Diffraction, *Mechanics of Materials*, 39:283, 2007.

[8] M. Marsilius, T. Granzow, and J. L. Jones, Quantitative Comparison Between the Degree of Domain Orientation and Nonlinear Properties of a PZT Ceramic Under Electrical and Mechanical Loading, *Journal of Materials Research*, 26:1126, 2011.

[9] T. Leist, K. G. Webber, W. Jo, E. Aulbach, J. Rödel, A. D. Prewitt, J. L. Jones, J. Schmidlin, and C. Hubbard, Stress Induced Structural Changes in La-doped $BiFeO_3$-$PbTiO_3$ High Temperature Piezoceramics, *Acta Materialia*, 58:5962, 2010.

[10] J. L. Jones, S. M. Motahari, M. Varlioglu, U. Lienert, J. V. Bernier, M. Hoffman, and E. Üstündag, Crack Tip Process Zone Domain Switching in a Soft Lead Zirconate Titanate Ceramic, *Acta Materialia*, 55:5538, 2007.

[11] G. Esteves, C. M. Fancher, S. Roehrig, G. Maier, J. L. Jones, and M. Deluca, Electric-Field-Induced Structural Changes in Multi-Layer Piezoelectric Actuators during Electrical and Mechanical Loading, *Acta Materialia,* 132:96, 2017.

[12] G. Tutuncu, J. S. Forrester, J. Chen, and J. L. Jones, Extrinsic contributions to piezoelectric Rayleigh behavior in morphotropic $PbTiO_3$ - $BiScO_3$, *Acta Materialia,* 137:45, 2017.

[13] J. L. Jones, E. Aksel, G. Tutuncu, T.-M. Usher, J. Chen, X. Xing, and A. J. Studer, Domain Wall and Interphase Boundary Motion in a Two-phase Morphotropic Phase Boundary Ferroelectric: Frequency Dispersion and Contribution to Piezoelectric and Dielectric Properties, *Physical Review B*, 86:024104, 2012.

[14] C.C. Chung, C. M. Fancher, C. Isaac, J. Nikkel, E. Hennig, and J. L. Jones, “Temperature dependence of field-responsive mechanisms in lead zirconate titanate,” *J. Am. Ceram. Soc.*, 100:4352, 2017.

⇒ TABLE OF CONTENTS

MICROSCOPIC MODELING AND SIMULATION OF MAGNETORHEOLOGICAL ELASTOMERS

M. Kästner[1,2,*], **K. A. Kalina**[1], **P. Metsch**[1] **and J. Brummund**[1]

[1] Institute of Solid Mechanics, TU Dresden, 01062 Dresden, Germany

[2] Dresden Center for Computational Materials Science (DCMS), TU Dresden, 01062 Dresden, Germany

Abstract. *Herein, a finite strain microscale model for magnetorheological elastomers (MREs) based on a continuum formulation of the magneto-mechanical boundary value problem is presented. The approach enables to consider particles with magnetically soft or hard behavior. In order to predict effective macroscopic quantities from the microscopic fields, a suitable computational homogenization scheme is used. The microstructure of the considered MRE is discretized and the problem is solved numerically in terms of a coupled nonlinear finite element approach. Using the presented framework, principal microscopic deformation mechanisms that lead to contraction or expansion of the samples have been identified. Furthermore, the influence of mechanical preloads, the difference between widely used 2D and more realistic 3D microcopic models, and the behavior of MRE filled with magnetically hard and soft particles are analyzed.*

1 Introduction

Magnetorheological elastomers (MREs) are a class of active composite materials which consist of a polymer matrix filled with micron-sized magnetizable particles. Besides the underlying microstructure, the effective properties of MREs essentially depend on the material behavior of the individual constituents. If the magnetic filler consists of magnetically soft particles with negligible hysteresis such as carbonyl iron, the rearrangement of the microstructure due to the external magnetic field is reversible. A second class of magnetic fillers are magnetically hard particles as NdFeB which exhibit significant magnetic hystereses and a non-vanishing remanence magnetization. If the MRE contains such particles, the microstructural alterations due to the external magnetic field are at least partly irreversible.

In this contribution the macroscopic behavior of MREs is investigated by means of a microscale modeling approach which is based on a general magneto-mechanical continuum formulation as presented in Kalina et al. [3, 4]. This model enables to consider particles with magnetically soft or magnetically hard behavior.

2 Theoretical Framework

As presented in [3], the governing equations for the microscopic stationary magneto-mechanical boundary value problem in the reference configuration are given by the two Maxwell equations and the balance of linear momentum

$$0 = \nabla_{\boldsymbol{X}} \cdot \boldsymbol{B} \quad , \quad \boldsymbol{0} = \nabla_{\boldsymbol{X}} \times \boldsymbol{H} \quad \text{and} \quad \boldsymbol{0} = \nabla_{\boldsymbol{X}} \cdot \boldsymbol{P}^{\text{tot}}, \tag{1}$$

---

[*] Corresponding author: M. Kästner (✉ markus.kaestner@tu-dresden.de)

in which $\boldsymbol{B}$, $\boldsymbol{H}$ and $\boldsymbol{P}^{\text{tot}}$ denote the Lagrangian magnetic induction and field and the total 1st Piola-Kirchhoff stress tensor, respectively. For brevity, the corresponding jump conditions are omitted in the aforementioned equations.

In order to connect the macroscopic and the microscopic magnetic and mechanical quantities, a suitable computational homogenization scheme [2] is used. Therein, the identification of an effective macroscopic quantity $\overline{(\cdot)}$ from the microscopic field distribution within a representative volume element (RVE) is realized by the volume averaging. The resulting nonlinear boundary value problem is solved by means of a coupled finite element (FE) formulation, where the magnetic part of the system is solved by using the magnetic scalar or vector potential.

3 Constitutive Equations

In the following, the constitutive models for particles ($\mathcal{B}_0^{\text{p}}$) and matrix ($\mathcal{B}_0^{\text{m}}$) are formulated seperately, where the amended free energy function $\Omega = \varrho_0 \Psi(\boldsymbol{C}, \boldsymbol{B}, \boldsymbol{Z}^\alpha) + 1/(2\mu_0 J)\boldsymbol{B} \cdot \boldsymbol{C} \cdot \boldsymbol{B}$, with $\boldsymbol{Z}^\alpha$ denoting possible internal variables, is used. According to the procedure of Coleman and Noll, the constitutive relations

$$\boldsymbol{P}^{\text{tot}} = 2\partial_{\boldsymbol{C}}\Omega \cdot \boldsymbol{F}^{\text{T}} \quad , \quad \boldsymbol{H} = \partial_{\boldsymbol{B}}\Omega \quad \text{and} \quad -\partial_{\boldsymbol{Z}^\alpha}\Omega \cdot \dot{\boldsymbol{Z}}^\alpha \geq 0 \tag{2}$$

follow from the evaluation of the Clausius-Duhem inequality. In the aforementioned equation, $\boldsymbol{F}$ denote the deformation gradient.

Polymeric matrix: The matrix material is assumed to be elastic and non-magnetizable. Consequently, the free energy function within $\mathcal{B}_0^{\text{m}}$ only depends on $\boldsymbol{C}$ and is given by the neo-Hookean potential

$$\Psi(\boldsymbol{C}) = \frac{1}{2\rho_0}\left[\mu(\operatorname{tr}\boldsymbol{C} - \ln J - 3) + \frac{\lambda}{2}(J - \ln J - 1)\right] \quad , \tag{3}$$

where λ and μ denote the Lamé parameters.

Magnetically soft particles: Compared to the soft polymer matrix, the magnetizable particles are very stiff, i. e. $\boldsymbol{C} \approx \boldsymbol{I}$ holds within the domain $\mathcal{B}_0^{\text{p}}$. Therefore it is assumed that the particles show negligible magneto-mechanical coupling effects and the free energy function

$$\Psi(\boldsymbol{C}, \boldsymbol{B}) = \Psi^{\text{mech}}(\boldsymbol{C}) + \Psi^{\text{mag}}(\boldsymbol{B}) \quad \text{with} \quad \Psi^{\text{mag}}(\boldsymbol{B}) = \int_0^{|\boldsymbol{B}|} M^{\text{s}} \tanh(\gamma|\tilde{\boldsymbol{B}}|)\, \mathrm{d}|\tilde{\boldsymbol{B}}| \tag{4}$$

can be decomposed into a mechanical part Ψ^{mech} which is chosen equal to Eq. (3) and a magnetic part Ψ^{mag}. The parameters M^{s} and γ denote the saturation magnetization and a scaling parameter, respectively.

Magnetically hard particles: Again, the split introduced in Eq. (4) is used for the free energy function. The magnetic behavior of magnetically hard particles is described by a rate independent hysteresis model [4] which is motivated from the work of Bergqvist [1]. Thus, the free energy function

$$\Psi^{\text{mag}}(\boldsymbol{B}, \boldsymbol{M}^\alpha) = -\sum_{\alpha=1}^{N} \omega^\alpha \boldsymbol{B} \cdot \boldsymbol{M}^\alpha + \sum_{\alpha=1}^{N} \omega^\alpha \int_0^{|\boldsymbol{M}^\alpha|} 1/\gamma \tanh^{-1}(|\tilde{\boldsymbol{M}}^\alpha|/M^{\text{s}})\, \mathrm{d}|\tilde{\boldsymbol{M}}^\alpha| \tag{5}$$

is introduced. In the equation above, ω^α denote the weights for each pinning element with the corresponding part of the magnetization $\boldsymbol{M}^\alpha$, with $\boldsymbol{M} = \sum_\alpha \omega^\alpha \boldsymbol{M}^\alpha$. Applying the principal

⇒ TABLE OF CONTENTS

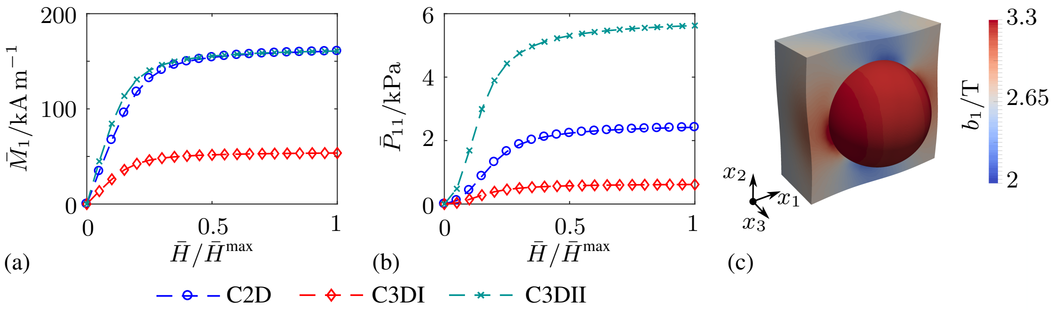

Figure 1: Cubic RVEs: (a) computed effective magnetization $\bar{\boldsymbol{M}}$ and (b) mechanical stress $\bar{\boldsymbol{P}}^{\mathrm{tot}}$ for $\bar{\boldsymbol{F}} = \boldsymbol{I}$, and (c) local induction field within the 3D geometry C3DII for shear loading.

of maximum dissipation, the rate independent behavior of the material is given by the evolution equations for $\boldsymbol{M}^{\alpha}$, the switching conditions ϕ^{α} and the related Kuhn-Tucker conditions:

$$\dot{\boldsymbol{M}}^{\alpha} = \lambda^{\alpha} \frac{\boldsymbol{B}^{\mathrm{i}\alpha}}{|\boldsymbol{B}^{\mathrm{i}\alpha}|} \quad , \; \phi^{\alpha} = |\boldsymbol{B}^{\mathrm{i}\alpha}| - k^{\alpha} \quad \text{and} \quad \lambda^{\alpha}\phi^{\alpha} = 0 \,\cap\, \lambda^{\alpha} \geq 0 \,\cap\, \phi^{\alpha} \leq 0 \quad . \tag{6}$$

Therein, the irreversible field $\boldsymbol{B}^{\mathrm{i}\alpha}$ is defined as $\boldsymbol{B}^{\mathrm{i}\alpha} = -1/\omega^{\alpha}\partial_{\boldsymbol{M}^{\alpha}}\Omega$. λ^{α} and k^{α} denote the Lagrange parameter and the pinning strength, respectively.

4 Results

The presented modeling approach has been applied a various numerical simulations of MREs. In [5], we have shown that the microscopic arrangement of particles has a significant influence on the resulting magneto-mechanical coupling. It was concluded that ideal chain-like microstructures lead to contraction while wavy chains or generally random microstructures yield an extension of the samples in the direction of the magnetic field. Based on these findings, it was demonstrated in [3] that mechanical preloads can alter the microstructure and hence the characteristics of the magneto-mechanical coupling. Below, the results of the two latest studies on 2D/3D RVEs and magnetically hard particles are briefly outlined.

4.1 Comparison of 2D and 3D approaches

A comparison of simplified 2D and full 3D simulations is realized by means of a magnetically soft MRE with underlying cubic microstructure. It is especially suited for a comparison of 2D and 3D simulations because RVEs with the same geometry, i.e. the radii of the inclusions (C2D and C3D-I), as well as the same particle volume fraction (C2D and C3D-II) can be considered.

While the latter two RVEs predict a nearly coinciding effective magnetization, its maximum value is reduced by a factor of three for the C3D-I microstructure, see Fig. 1(a). This effect is directly related to the differences in the particle volume fraction. The variations in the C2D and C3D-II simulations are a result of the cylindrical (2D) and spherical (3D) inclusions and their different demagnetizing factors. If the macroscopic mechanical stresses in Fig. 1(b) are compared, a qualitative agreement can be found for all RVEs. With the macroscopic deformation of the microstructures prevented, i. e. $\bar{\boldsymbol{F}} = \boldsymbol{I}$, $\bar{P}_{11} > 0$ indicates that the RVEs try to contract in the direction of the applied magnetic field. Concerning the quantitative results, considerable differences become apparent.

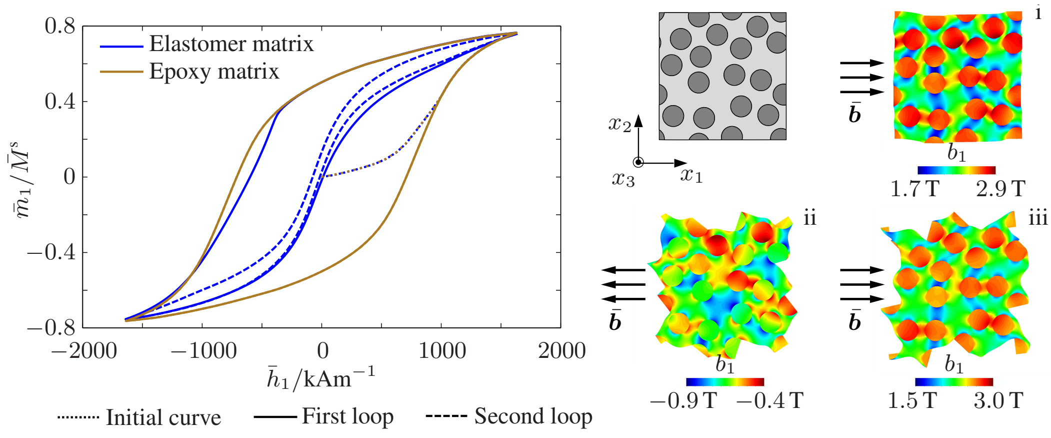

(a) (b)

Figure 2: Magnetically hard MRE: (a) Predicted initial curve as well as first and repeated hysteresis loops of the MRE and a composite with an epoxy resin matrix, and (b) evolution of the MRE microstructure during the first hysteresis loop and local b_1-field.

4.2 Hystereses of magnetically hard MREs

As shown in [4], measured magnetization loops of MREs based on a soft elastomer matrix filled with NdFeB particles differ considerably from the loops of the bulk magnetic component or NdFeB particles fixed in a comparatively stiff matrix as epoxy resin.

In order to investigate such a behavior, numerical homogenization with an RVE containing circular, magnetically hard inclusions is examined. During the simulation, the effective deformation gradient is prescribed to $\bar{\boldsymbol{F}} = \boldsymbol{I}$. The predicted initial magnetization curve as well as the first and second hysteresis loops of the MRE are compared to the hystereses of a composite with NdFeB particles embedded into an epoxy resin matrix, see Fig. 2(a). In accordance with experimental results, the second major hysteresis loop of the MRE is significantly smaller. With the presented modelling approach it could be verified theoretically that the observable macroscopic behavior results from the rotation of the embedded particles, Fig. 2(b).

REFERENCES

[1] A. Bergqvist. Magnetic vector hysteresis model with dry friction-like pinning. *Physica B: Condensed Matter*, 233(4):342 – 347, 1997.

[2] G. Chatzigeorgiou, A. Javili, and P. Steinmann. Unified magnetomechanical homogenization framework with application to magnetorheological elastomers. *Mathematics and Mechanics of Solids*, 19 (2):193–211, 2012.

[3] K. A. Kalina, P. Metsch, and M. Kästner. Microscale modeling and simulation of magnetorheological elastomers at finite strains: A study on the influence of mechanical preloads. *International Journal of Solids and Structures*, 102–103:286 – 296, 2016.

[4] K. A. Kalina, J. Brummund, Metsch P., M. Kästner, D. Yu. Borin, J. M. Linke, and S. Odenbach. Modeling of magnetic hystereses in soft mres filled with ndfeb particles. *Smart Materials and Structures*, 26:105019 – 105031, 2017.

[5] P. Metsch, K. A. Kalina, C. Spieler, and M. Kästner. A numerical study on magnetostrictive phenomena in magnetorheological elastomers. *Computational Materials Science*, 124:364 – 374, 2016.

OPTIMAL ENERGY HARVESTING WITH A PIEZOELECTRIC DEVICE, MODELED BY PREISACH OPERATORS

Barbara Kaltenbacher[1], **and Pavel Krejčí**[2,*],

[1] Institute for Mathematics, Alpen-Adria-Universität, Universitätsstr. 65-67, A-9020 Klagenfurt, Austria

[2] Institute of Mathematics, Czech Academy of Sciences, Žitná 25, CZ-11567 Praha 1, Czech Republic

Abstract. *The problem of optimal energy harvesting for a piezoelectric element driven by mechanical vibrations is stated in terms of an ODE system with hysteresis under the time derivative coupling a mechanical oscillator with an electric circuit with or without inductance. In the piezoelectric constitutive law, both the self-similar piezoelectric butterfly character of the hysteresis curves and feedback effects are taken into account in a thermodynamically consistent way. The physical parameters of the harvester are chosen to be the control variable, and the goal is to maximize the harvested energy for a given mechanical load and a given time interval. If hysteresis is modeled by the Preisach operator, the system is shown to be well-posed with continuous data dependence. For the special case of the play operator, we derive first order necessary optimality conditions and an explicit form of the gradient of the cost functional in terms of solutions to the adjoint system.*

1 Introduction

Most of the work on modeling, simulation, and optimization of energy harvesting so far is restricted to linear models for the energy conversion mechanism and focuses on optimization of the electrical circuit of the harvester. The linear approximation and techniques based on perturbation methods are effective for modeling oscillators with relatively weak nonlinearity or sufficiently small vibrations. However, all smart materials demonstrate a strongly nonlinear constitutive law. Results from piezoelectric energy harvesters and preliminary results from magnetostrictive energy harvesters [1] show that nonlinearities in the material characteristic need to be accounted for in order to maximize, or significantly increase, the energy output of these devices.

The main challenge is to model properly the electromechanical or magnetomechanical "butterfly" shaped curve. A thermodynamic model for magnetostriction was proposed and analyzed in [2]. The underlying idea was motivated by the observation that both the magnetization hysteresis loops and the magnetostrictive butterfly loops manifest a self-similar character parameterized by the applied stress. This has led to the modeling hypothesis that all hysteresis phenomena can be described by one single Preisach operator and its associated energy potential operator acting on an auxiliary self-similar variable. The butterfly-shaped magnetostrictive curve then arises in a natural way from thermodynamic considerations involving the butterfly-shaped Preisach potential operator. A similar model was shown to be applicable in piezoeletricity modeling in [3].

---

[*] Corresponding author: Barbara Kaltenbacher (✉ barbara.kaltenbacher@aau.at)

⇒ TABLE OF CONTENTS

2 Model

The behavior of a simple piezoelectric energy harvester subject to dynamic mechanical loading as in Figure 1 can be modeled (see [5]) by the equations

$$\begin{aligned} \frac{m}{A}\ddot{x} + \bar{\sigma} &= 0 \\ \ddot{D} + \frac{1}{R}\dot{\phi} \left[+ \frac{1}{L}\phi \right] &= 0 \end{aligned} \tag{1}$$

where the last term is skipped if the inductance of the system is not taken into account. In (1), the first equation is the momentum balance and the second equation stands for the Kirchhoff law.

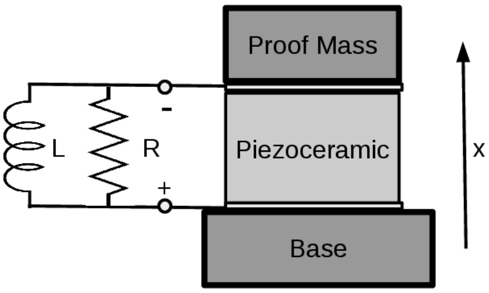

Figure 1: Schematic representation of a piezoelectric harvester

The physical meaning of the symbols in (1) is the following:

x	displacement
$\bar{\sigma} = \sigma_{piezo} + \sigma_{visc} + \sigma_{imp}$	total stress
σ_{piezo}	piezoelectric stress component
σ_{visc}	viscous stress component
σ_{imp}	impressed stress
ϕ	voltage
D	dielectric displacement
m	mass
A	contact area
R	electric resistance
L	inductance

We rewrite system (1) in terms of new unknown quantities

$$\begin{aligned} \varepsilon &= \frac{x}{d} \quad \text{(strain)}, \\ E &= \frac{\phi}{d} \quad \text{(electric field)}, \end{aligned} \tag{2}$$

where d is the thickness of the piezoelectric element. It remains to choose suitable constitutive relations. The authors in [5] use a linear piezoelectric coupling hypothesis.

Experiments described in [4] show that typical piezoelectric materials exhibit strong hysteresis, and a thermodynamically consistent model for piezoelectric hysteresis was proposed in [3]. Here, we suggest to refine the model by taking into account feedback effects. Furthermore,

⇒ TABLE OF CONTENTS

piezoelectric phenomena that take place at "large" deformations and low or vanishing electric fields, like mechanical depolarization, cannot be explained without feedback effects. Our model is based on operator approach in the same form as in [3]. More specifically, we consider a hysteresis operator $\mathcal{P}$ which admits a potential operator $\mathcal{V}$, and replace the linear model from [5] with

$$\begin{aligned} \sigma_{visc} &= \nu\dot{\varepsilon}, \\ \sigma_{piezo} &= c\varepsilon - eE + f'(\varepsilon)\,\mathcal{V}[u] + \tfrac{1}{2}b'(\varepsilon)\mathcal{P}^2[u], \\ D &= e\varepsilon + \kappa E + \mathcal{P}[u], \\ u &= \frac{1}{f(\varepsilon)}(E - b(\varepsilon)\mathcal{P}[u]), \end{aligned} \tag{3}$$

where u is an auxiliary self-similar variable, $f(\varepsilon) > 0$ is a self-similarity function, and $b(\varepsilon) \geq 0$ is a feedback coefficient. The constants appearing in these relations are the viscosity ν, the elasticity modulus c, the piezoelectric coupling coefficient e, and the dielectric constant κ. The primes denote derivatives with respect to ε.

We check that for a suitable choice of the operator $\mathcal{P}$, the model (3) is consistent with classical thermodynamics in the sense that there exists a free energy operator $\mathcal{F}[\varepsilon, E]$ such that for all processes we have

$$\dot{D}E + \dot{\varepsilon}\sigma_{piezo} - \frac{\mathrm{d}}{\mathrm{d}t}\mathcal{F}[\varepsilon, E] \geq 0 \ \text{ a. e.} \tag{4}$$

The left-hand side of (4) is the total energy dissipation rate which has to be non-negative in agreement with the first and the second principles of thermodynamics. We only require the hysteresis energy inequality

$$u\frac{\mathrm{d}}{\mathrm{d}t}\mathcal{P}[u] - \frac{\mathrm{d}}{\mathrm{d}t}\mathcal{V}[u] \geq 0 \ \text{ a. e.} \tag{5}$$

to hold under suitable assumptions. In particular, if $\mathcal{P}$ is the Preisach operator as in [3], then (5) holds for all absolutely continuous functions u. We claim that the right choice for the free energy operator is then

$$\mathcal{F}[\varepsilon, E] = \frac{c}{2}\varepsilon^2 + \frac{\kappa}{2}E^2 + f(\varepsilon)\mathcal{V}[u] + \frac{1}{2}b(\varepsilon)\mathcal{P}^2[u] \tag{6}$$

with u as in (3). An elementary computation now yields

$$\dot{D}E + \dot{\varepsilon}\sigma_{piezo} - \frac{\mathrm{d}}{\mathrm{d}t}\mathcal{F}[\varepsilon, E] = f(\varepsilon)\left(u\frac{\mathrm{d}}{\mathrm{d}t}\mathcal{P}[u] - \frac{\mathrm{d}}{\mathrm{d}t}\mathcal{V}[u]\right) \geq 0 \ \text{ a. e.} \tag{7}$$

by virtue of (5), hence (4) holds.

Combining the constitutive relations (2), (3) with the balance equations (1), we end up with the system

$$\begin{aligned} \rho\ddot{\varepsilon} + \nu\dot{\varepsilon} + c\varepsilon - eE + f'(\varepsilon)\,\mathcal{V}[u] + \tfrac{1}{2}b'(\varepsilon)\mathcal{P}^2[u] &= -\sigma_{imp}, \\ \frac{\mathrm{d}}{\mathrm{d}t}\Big(e\varepsilon + \kappa E + \mathcal{P}[u]\Big) + \alpha E &= 0, \end{aligned} \tag{8}$$

with $\rho = \frac{md}{A}$, $\alpha = \frac{d}{R}$, and u as in (3). System (8) is complemented with initial conditions

$$\varepsilon(0) = \varepsilon_0, \quad \dot{\varepsilon}(0) = \varepsilon_1, \quad E(0) = E_0 \tag{9}$$

with given data $\varepsilon_0, \varepsilon_1, E_0$.

⇒ TABLE OF CONTENTS

Using the locally Lipschitz inversion theorem for hysteresis operators with time dependent coefficients, we rewrite the system in explicit form with locally Lipschitz hysteresis operators only in the right-hand side. This, together with natural global energy estimates, enables us to conclude that the system admits a unique solution for arbitrary initial data which depends continuously on the model parameters.

3 Optimization

The second part of the paper is devoted to a general optimization problem for the energy harvesting process modeled above. The control variable is the vector of physical parameters of the harvester (mass, electric resistivity, inductance). Since the Preisach operator is constructed by averaging a multi-yield continuum of constrained variational inequalities and its memory is described in an infinitely-dimensional state space, no approach is known so far to formulating necessary optimality conditions for Preisach hysteresis models. We therefore consider its simpler single-yield counterpart. The harvester problem is reduced to a system with only one hysteresis operator, namely the play, for both the cases with and without inductance. We approximate the play by a penalty term and show strong convergence if we let the penalty coefficient tend to zero.

The final section is devoted to the problem of maximizing the harvested energy, which corresponds to an integral cost functional with constant control variables representing the physical parameters of the harvester. We derive a formula for the gradient of the cost functional of the penalized problem in terms of solutions of the adjoint problem and prove that it is possible to pass to the limit in both the adjoint system and in the gradient formula. As a corollary, we derive necessary optimality conditions for the original problem.

REFERENCES

[1] D. Davino, A. Giustiniani, and C. Visone, Magnetoelastic energy harvesting: Modeling and experiments, in *Smart Actuation and Sensing Systems - Recent Advances and Future Challenges* (G. Berselli, R. Vertechy and G. Vassura, eds.), InTech, 2012, 487–512.

[2] D. Davino, P. Krejčí, and C. Visone, Fully coupled modeling of magnetomechanical hysteresis through ‘thermodynamic’ compatibility. Smart Materials and Structures **22** (2013), 095009.

[3] B. Kaltenbacher and P. Krejčí, A thermodynamically consistent phenomenological model for ferroelectric and ferroelastic hysteresis. ZAMM – Z. Angew. Math. Mech. **96** (2016), 874–891.

[4] M. Kamlah, Ferroelectric and ferroelastic piezoceramics modeling of electromechanical hysteresis phenomena. Continuum Mechanics and Thermodynamics **13** (2001), 219–268.

[5] J. M. Renno, M. F. Daqaq, and D. J. Inman, On the optimal energy harvesting from a vibration source. Journal of Sound and Vibration **329** (2009) 386–405.

⇒ TABLE OF CONTENTS

THERMOMECHANICS OF FUNCTIONAL CERAMIC BREEDER PEBBLE BEDS FOR FUSION REACTORS

Marigrazia Moscardini[1], Simone Pupeschi[1], Yixiang Gan[2], Ratna Kumar Annabattula[3], Shuo Zhao[4], and Marc Kamlah[1,*]

[1] Institute for Applied Materials, Karlsruhe Institute of Technology, Germany

[2] School of Civil Engineering, The University of Sydney, Australia

[3] Department of Mechanical Engineering, Indian Institute of Technology Madras, India

[4] School of Mechanical Engineering, Hebei University of Science and Technology, China

Abstract. *This presentation gives an overview over the background and the activities of the authors on functional ceramic breeder pebble beds for fusion reactors in the last decade.*

1 Introduction

Fusion reactors offer the option of an unlimited, CO_2-free, and reliable energy source. Fig. 1 shows a design sketch of ITER, the next experimental reactor currently under construction in Cadarache in the south of France. The core of a future fusion reactor is the torus shaped vacuum chamber where a plasma of Deuterium and Tritium is heated up to ~150 million °C to enable the fusion reaction to Helium, whereby high energy neutrons are released as well.

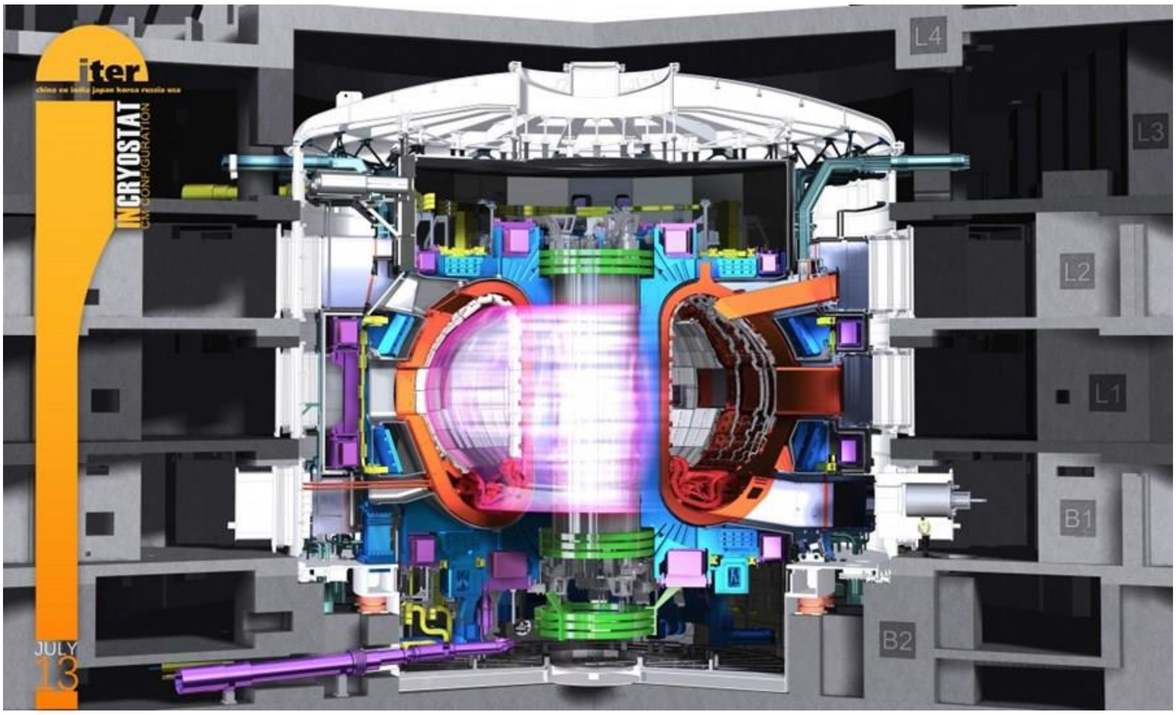

Figure 1: Design sketch of ITER (www.iter.org).

---

[*] Corresponding author: Marc Kamlah (marc.kamlah@kit.edu)

While Deuterium is available to approximately 1% in natural sea water, a fusion reactor has to produce the Tritium fuel itself in a so-called breeding blanket. The solid breeder concept consists of granular Lithium based ceramic breeder material and a granular Beryllium neutron multiplier material in a metallic housing, forming so-called breeder units. The breeding blanket is exposed to severe thermo-mechanical conditions, as well as neutron irradiation due to the vicinity to the burning plasma. An additional issue is the cyclic operation mode of a Tokamak fusion reactor. A review on the status of ceramic breeder pebble bed thermo-mechanics can be found in [1].

2 Modeling the micromechanics of ceramic pebble beds with the Discrete Element Method

The Discrete Element Method (DEM) is the method of choice for micromechanical modeling the collective behavior of granular materials [2]. At KIT, a DEM code was developed in the Institute of Applied Materials (IAM) for, at that time, perfectly spherical particles at highly packed state under quasi-static conditions [3]. This code is able to represent experimental packing structures in a realistic way [4].

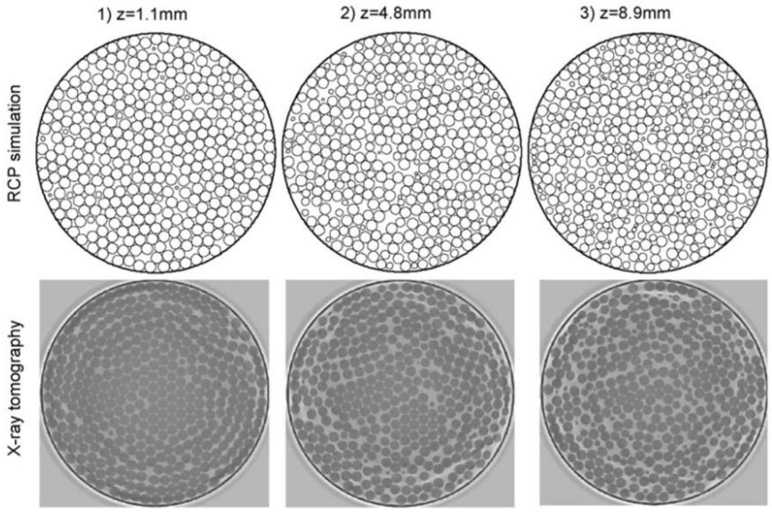

Figure 2: Experimental and simulated packing structures

As seen in Fig. 3, this code represents the typical macroscopic stress-strain-behavior observed in uniaxial compression tests.

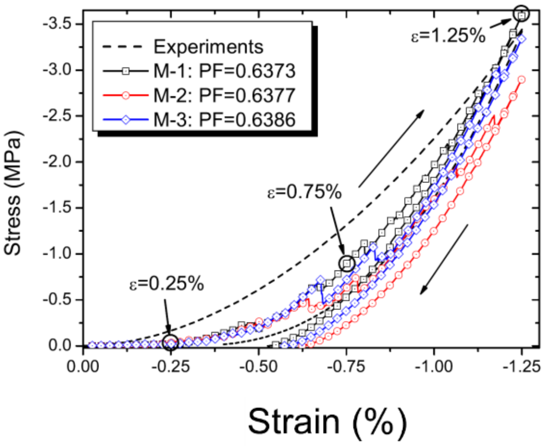

Figure 3: Uniaxial compression test, experiment and simulation

Further aspects considered are size distribution [5] and particle failure [6].

⇒ TABLE OF CONTENTS

3 The effect of particle shape

Depending on the production process, the shape of the ceramic breeder pebbles is close to perfectly spherical, but usually there is a slight deviation. The DEM code was extended in order to simulate the mechanical behavior of ellipsoidal particles [7]. The method chosen to represent non spherical particles was the multi-sphere (MS) approach. It is based on the union of several spheres to obtain the required shape. Fig. 4 shows a typical example.

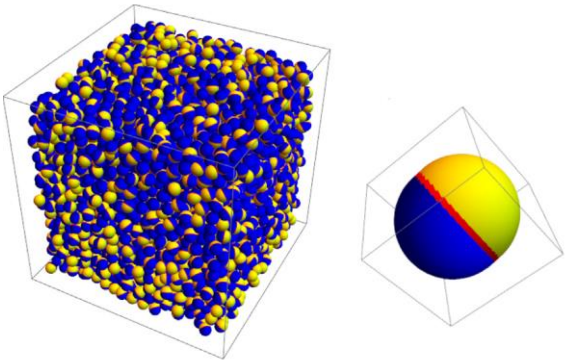

Figure 4: Ellipsoidal particles represented by means of the multisphere method

The MS method leaves the possibility to continue to use the same algorithms developed for spherical particles. In agreement with previous studies carried out on assemblies of spherical pebbles, the initial packing factor is found to noticeably affect the mechanical response of the investigated assemblies. Moreover, a remarkable influence of the shape on the mechanical behavior of the simulated assemblies is observed, as can be seen in Fig. 5.

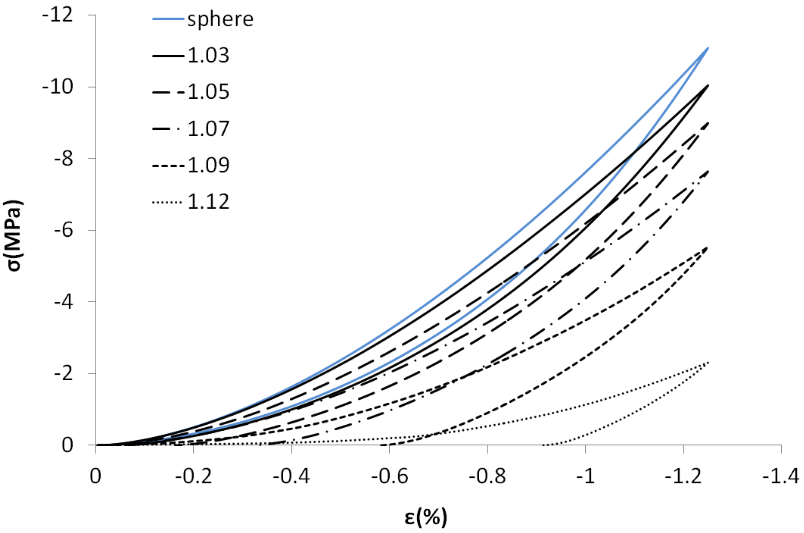

Figure 5: Macroscopic stress-strain-behavior for pebble beds of ellipsoidal particles of different aspect ratio but identical packing factor

4 Effective thermal conductivity

In the breeder blanket both Tritium and heat are generated. Therefore, the effective thermal properties of the packed beds are of major importance. The DEM code was extended to evaluate the effective thermal conductivity of packed granular assemblies [8]. A 3D random network model was implemented to determine the heat exchange in packed systems under an imposed thermal gradient. In the network, particles as the nodes are interconnected by thermal resistors defined by the two types of thermal contact between two particles, namely contact area and separation gap.

⇒ TABLE OF CONTENTS

The code now allows for doing parametric studies to investigate the influence of temperature, compressive stress, type and pressure of the interstitial gas, as well as the grain materials on the effective thermal conductivity of the assembly. The Smoluchowski effect has been implemented in the code allowing simulation of the influence of the gas pressure on the effective thermal conductivity in the Knudsen domain. Furthermore, the coupling with the mechanical part of the code enables the study of the influence of the compressive stress on the effective thermal conductivity. The stresses generated in the pebble bed due to the mechanical constraint were simulated by means of uniaxial compressions and the variation of the effective thermal conductivity was evaluated. Numerical results are compared with existing experimental data in literature and recent experiments carried out in KIT [9] as seen in Fig. 6.

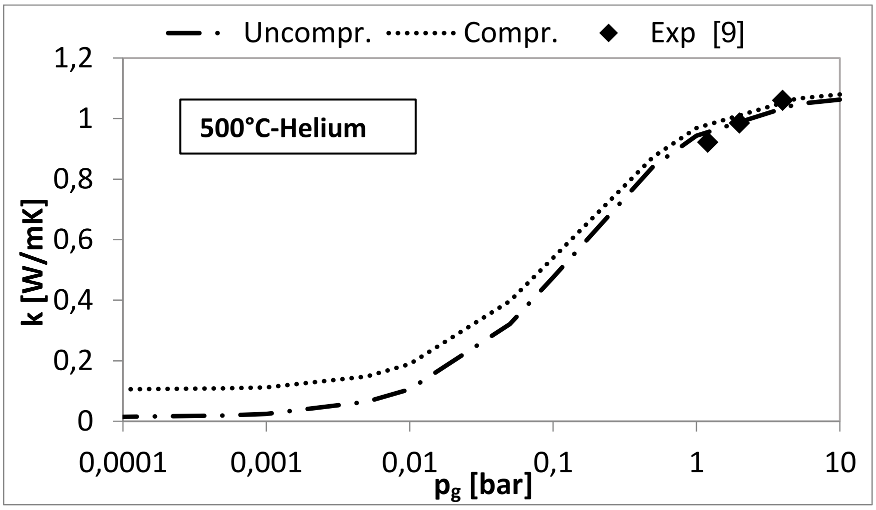

Figure 6: Simulation of the Smoluchowski effect in a pebble bed.

REFERENCES

[1] A. Ying, J. Reimann, L. Boccaccini, M. Enoeda, M. Kamlah, R. Knitter, Y. Gan, J. G. van der Laan, L. Magielsen, P. A. Di Maio, G. Dell'Orco, R. K. Annabattula, J. Van Lew, H. Tanigawa, S. Van Til, S.. Status of Ceramic Breeder Pebble Bed Thermo-mechanics R&D and Impact on Breeder Material Mechanical Strength, *Fusion Engineering and Design* 87(7-8): 1130-1137, 2012.

[2] P. A. Cundall and O. D. L. Strack. A discrete numerical model for granular assemblies. *Geotechnique*, 29(1):47-65, 1979.

[3] Y. Gan, M. Kamlah. Discrete element modelling of pebble beds: With application to uniaxial compression tests of ceramic breeder pebble beds. *J. Mech. Phys. Solids* 58: 129-144, 2010.

[4] Y. Gan, M. Kamlah, J. Reimann. Computer simulation of packing structure in pebble beds, *Fusion Engineering and Design* 85: 1782-1787, 2010.

[5] R. K. Annabattula, Y. Gan, M. Kamlah. Mechanics of binary and polydisperse spherical pebble assembly, *Fusion Engineering and Design* 87: 853-858, 2012.

[6] S. Zhao, Y. Gan, M. Kamlah. Failure initiation and propagation of Li4SiO4 pebbles in fusion blankets, *Fusion Engineering and Design* 88: 8-16, 2013.

[7] M. Moscardini, Y. Gan, R. K. Annabattula, M. Kamlah. A Discrete Element Method to simulate the mechanical behavior of ellipsoidal particles for a fusion breeding blanket, *Fusion Engineering and Design* 121: 22-31, 2017.

[8] M. Moscardini, Y. Gan, S. Pupeschi, M. Kamlah. Discrete element method for effective thermal conductivity of packed pebbles accounting for the Smoluchowski effect, *Fusion Engineering and Design* 127: 192-201, 2018.

[9] S. Pupeschi, R. Knitter, M. Kamlah. Effective thermal conductivity of advanced ceramic breeder pebble beds, *Fusion Engineering and Design* 116: 73-80, 2017.

⇒ TABLE OF CONTENTS

MULTISCALE COMPUTATIONAL STABILITY ANALYSIS OF MAGNETORHEOLOGICAL ELASTOMERS

Marc-André Keip[1,*] **and Elten Polukhov**[1]

[1] Institute of Applied Mechanics (CE), University of Stuttgart
Pfaffenwaldring 7, 70569 Stuttgart, Germany

Abstract. *In this contribution, we treat the computational stability analysis of periodic magnetorheological elastomer (MRE) composites in the context of computational homogenization [7, 8, 9]. Localization-type macroscopic instabilities are detected by the loss of strong ellipticity of macroscopic coupled moduli and bifurcation-type microscopic instabilities are treated by exploiting Bloch-Floquet wave analysis in the context of finite-element discretization [1, 3, 4, 5, 10]. The latter allows to detect the changed critical periodicities at a critical macroscopic loading scenario. We present some representative numerical examples that demonstrate the detection of macroscopic and microscopic instabilities of MRE microstructures.*

1 Introduction

Magnetorheological elastomers (MREs) are smart composite materials with microstructures composed mainly of (i) soft elastomeric matrix and (ii) dispersed magnetizable micro- or nano-sized particles. The particles (e.g. carbonyl iron, coblat-iron alloys, nickel alloys) are embedded into the elastomeric matrix during the crosslinking process, which could yield either anisotropic or isotropic properties depending on whether the mixture is cured under applied magnetic field or not [2, 6]. Under external magnetic field MREs show magnetostrictive response, which makes them interesting for industrial applications as, for example, actuators or variable-stiffness devices [2]. Investigations show that magneto-mechanical coupling of MREs can be further enhanced by tuning geometrical and physical properties of its microstructure [6]. However, such modifications require to study the influence of the new properties on the overall response and to determine (in)stable loading ranges. Considering this, we will discuss an associated modeling approach targeting the stability analysis of MREs.

2 Variational Formulation of Periodic Homogenization

The following primary kinematic fields are considered to describe the response of the microstructure in a finite-strain magneto-mechanical setting

$$\boldsymbol{\varphi} : \begin{cases} \mathcal{B} \times \mathcal{T} \rightarrow \mathcal{R}^3 \\ (\boldsymbol{X}, t) \mapsto \boldsymbol{\varphi}(\boldsymbol{X}, t) \end{cases} \quad \text{and} \quad \boldsymbol{a} : \begin{cases} \mathcal{B} \times \mathcal{T} \rightarrow \mathcal{R}^3 \\ (\boldsymbol{X}, t) \mapsto \boldsymbol{a}(\boldsymbol{X}, t), \end{cases} \tag{1}$$

where $\boldsymbol{\varphi}$ and $\boldsymbol{a}$ denote the deformation map and the magnetic vector potential, respectively. Due to the chosen formulation in terms of magnetic vector potential $\boldsymbol{a}$, the magnetic induction

---

[*] Corresponding author: Marc-André Keip (✉ marc-andre.keip@mechbau.uni-stuttgart.de)

⇒ TABLE OF CONTENTS

$\mathbb{B} = \operatorname{Curl} \boldsymbol{a}$ satisfies $\operatorname{Div}\mathbb{B} = \boldsymbol{0}$ a priori. We further demand that $\det[\boldsymbol{F}] > 0$. The variational formulation of homogenization reads

$$\bar{\psi}(\bar{\boldsymbol{F}}, \bar{\mathbb{B}}; \bar{\boldsymbol{X}}) = \inf_{\tilde{\boldsymbol{\varphi}} \in \mathcal{W}_{\tilde{\boldsymbol{\varphi}}}} \inf_{\tilde{\boldsymbol{a}} \in \mathcal{W}_{\tilde{\boldsymbol{a}}}} \inf_{\theta \in L^2} \sup_{p \in L^2} \frac{1}{|\mathcal{B}|} \left\{ \int_{\mathcal{B}} \left[U(\theta) + p(J - \theta) + \psi^{iso}(J, \boldsymbol{F}) + \psi^{mag}(\boldsymbol{F}, \mathbb{B}) \right] \mathrm{d}V \right\}, \tag{2}$$

where $\boldsymbol{\varphi} = \bar{\boldsymbol{F}} \boldsymbol{X} + \tilde{\boldsymbol{\varphi}}$ and $\boldsymbol{a} = \frac{1}{2} \bar{\mathbb{B}} \times \boldsymbol{X} + \tilde{\boldsymbol{a}}$ are given in terms of the macroscopic tensors $\{\bar{\boldsymbol{F}},\ \bar{\mathbb{B}}\}$ and periodic fluctuations $\{\tilde{\boldsymbol{\varphi}},\ \tilde{\boldsymbol{a}}\}$ on the RVE $\mathcal{B}$. $U(\theta) = \frac{\kappa}{2}(\theta - 1)^2$ describes the volumetric energy in terms of dilatation θ. Thus, the macroscopic energy corresponds to the stationary point of the microscopic energy in admissible spaces

$$\begin{aligned} \tilde{\boldsymbol{\varphi}} \in \mathcal{W}_{\tilde{\boldsymbol{\varphi}}} &:= \left\{ \tilde{\boldsymbol{\varphi}} \in H(\mathrm{Grad}, \mathcal{B}) \,|\, \tilde{\boldsymbol{\varphi}}^+ = \tilde{\boldsymbol{\varphi}}^- \text{on } \partial\mathcal{B} \right\}, \\ \tilde{\boldsymbol{a}} \in \mathcal{W}_{\tilde{\boldsymbol{a}}} &:= \left\{ \tilde{\boldsymbol{a}} \in H(\mathrm{Curl}, \mathcal{B}) \,|\, \tilde{\boldsymbol{a}}^+ = \tilde{\boldsymbol{a}}^- \text{on } \partial\mathcal{B} \right\}. \end{aligned} \tag{3}$$

Considering discontinuous approximations for the dilatation θ and the pressure p across the finite element, these terms can be statically condensed out at element level yielding a positive definite global stiffness matrix until an instability occurs.

After solving the microscopic problem, the macroscopic mechanical stresses and magnetic fields as well as coupled moduli at a macroscopic material point are defined by

$$\bar{\mathsf{P}} = \partial_{\bar{\mathsf{F}}} \bar{\psi}(\bar{\boldsymbol{F}}, \bar{\mathbb{B}}; \bar{\boldsymbol{X}}) \quad \text{and} \quad \bar{\mathbb{C}} = \partial^2_{\bar{\mathsf{F}}\bar{\mathsf{F}}} \bar{\psi}(\bar{\boldsymbol{F}}, \bar{\mathbb{B}}; \bar{\boldsymbol{X}}), \tag{4}$$

where $\bar{\mathsf{F}} := [\bar{\boldsymbol{F}},\ \bar{\mathbb{B}}]^T$ and $\bar{\mathsf{P}} := [\bar{\boldsymbol{P}},\ \bar{\mathbb{E}}]^T$. For more details on the numerical implementation we refer to [7, 8, 9, 10].

3 Macroscopic Stability Analysis

The macroscopic stability analysis is based on the homogeneous elastic perturbations of the form $\bar{\boldsymbol{v}} = \bar{\boldsymbol{p}} f(\bar{\boldsymbol{x}} \cdot \bar{\boldsymbol{n}} - \bar{c}t)$ and $\boldsymbol{\mathcal{L}}_{\bar{\boldsymbol{v}}} \bar{\mathbb{b}} = \bar{\boldsymbol{s}} g(\bar{\boldsymbol{x}} \cdot \bar{\boldsymbol{n}} - \bar{c}t)$ with real wave speed $\bar{c}$ superimposed onto the current configuration [5]

$$\operatorname{div}[\bar{\mathbb{a}} : \nabla \bar{\boldsymbol{v}} + \bar{\mathbb{h}} \cdot \boldsymbol{\mathcal{L}}_{\bar{\boldsymbol{v}}} \bar{\mathbb{b}}] = \boldsymbol{0} \quad \text{and} \quad \operatorname{curl}[\bar{\mathbb{h}}^T : \nabla \bar{\boldsymbol{v}} + \bar{\mathbb{k}} \cdot \boldsymbol{\mathcal{L}}_{\bar{\boldsymbol{v}}} \bar{\mathbb{b}}] = \boldsymbol{0}, \tag{5}$$

where $\bar{\mathbb{a}}_{a\ c}^{\ b\ d} = \bar{J}^{-1} \bar{F}^b_{\ A} \bar{F}^d_{\ B} \{\partial^2_{\bar{\boldsymbol{F}}\bar{\boldsymbol{F}}} \bar{\psi}\}_{a\ c}^{\ A\ B}$, $\bar{\mathbb{h}}_{a\ c}^{\ b} = \bar{F}^b_{\ A} (\bar{F}^{-1})^B_{\ c} \{\partial^2_{\bar{\boldsymbol{F}}\bar{\mathbb{B}}} \bar{\psi}\}_{a\ B}^{\ A}$ and $\bar{\mathbb{k}}_{ab} = \bar{J} (\bar{F}^{-1})^A_{\ a} (\bar{F}^{-1})^B_{\ b} \{\partial^2_{\bar{\mathbb{B}}\bar{\mathbb{B}}} \bar{\psi}\}_{AB}$ are the spatial mechanical, coupled magneto-mechanical and magnetic moduli, respectively. Considering the above given perturbations in (5) yields

$$\bar{\Lambda} = \inf_{|\bar{\boldsymbol{p}}| = |\bar{\boldsymbol{s}}| = |\bar{\boldsymbol{n}}| = 1} \left\{ \bar{\boldsymbol{p}} \cdot \bar{\mathbb{q}}(\bar{\boldsymbol{n}}) \cdot \bar{\boldsymbol{p}} - \frac{[\bar{\boldsymbol{p}} \cdot \bar{\mathbb{r}}(\bar{\boldsymbol{n}}) \cdot \bar{\boldsymbol{s}}][\bar{\boldsymbol{p}} \cdot \bar{\mathbb{r}}(\bar{\boldsymbol{n}}) \cdot \bar{\boldsymbol{s}}]}{\bar{\boldsymbol{s}} \cdot \bar{\mathbb{k}} \cdot \bar{\boldsymbol{s}}} \right\} = \inf_{|\bar{\boldsymbol{p}}| = |\bar{\boldsymbol{s}}| = |\bar{\boldsymbol{n}}| = 1} \{\bar{\rho} \bar{c}^2\} > 0, \tag{6}$$

where $\bar{\mathbb{q}}_{ac} := \bar{\mathbb{a}}_{a\ c}^{\ b\ d} \bar{n}_b \bar{n}_d$ and $\bar{\mathbb{r}}_{ac} := \bar{\mathbb{h}}_{a\ c}^{\ b} \bar{n}_b$. In the latter equation the objective incremental Gauss law $\operatorname{div}[\boldsymbol{\mathcal{L}}_{\bar{\boldsymbol{v}}} \bar{\mathbb{b}}] = 0$ is considered. The critical loading point is considered to correspond to the loss of strong ellipticity when the macroscopic coercivity constant $\bar{\Lambda}$ vanishes.

4 Microscopic Stability Analysis

At a microscopic instability point the critical periodicity of microstructure may change [1]. Therefore, it is important to determine this type of instabilities and the critical periodicities of the microstructure. We employ Bloch-Floquet wave analysis which allows to detect the microscopic instability point and critical periodicities at unit-cell level [1, 4]. In this way, we consider superimposed perturbations which satisfy the following Euler-Lagrange equations

$$\begin{aligned} \mathrm{Div}[\partial^2_{\boldsymbol{F}\boldsymbol{F}}\psi : \mathrm{Grad}\,\mathfrak{v} + \partial^2_{\boldsymbol{F}\mathbb{B}}\psi \cdot \mathrm{Curl}\,\mathfrak{a}] &= \boldsymbol{0} \\ \mathrm{Curl}[\partial^2_{\mathbb{B}\boldsymbol{F}}\psi : \mathrm{Grad}\,\mathfrak{v} + \partial^2_{\mathbb{B}\mathbb{B}}\psi \cdot \mathrm{Curl}\,\mathfrak{a}] &= \boldsymbol{0} \end{aligned} \tag{7}$$

with jump conditions on the boundary $\partial\mathcal{D}$

$$\begin{aligned} [\![\partial^2_{\boldsymbol{F}\boldsymbol{F}}\psi : \mathrm{Grad}\,\mathfrak{v} + \partial^2_{\boldsymbol{F}\mathbb{B}}\psi \cdot \mathrm{Curl}\,\mathfrak{a}]\!] \cdot \boldsymbol{N} &= \boldsymbol{0} \\ [\![\partial^2_{\mathbb{B}\boldsymbol{F}}\psi : \mathrm{Grad}\,\mathfrak{v} + \partial^2_{\mathbb{B}\mathbb{B}}\psi \cdot \mathrm{Curl}\,\mathfrak{a}]\!] \times \boldsymbol{N} &= \boldsymbol{0}, \end{aligned} \tag{8}$$

where $\mathfrak{v}(\boldsymbol{X}) = \tilde{\boldsymbol{\varphi}}(\boldsymbol{X})\exp[\mathrm{i}\boldsymbol{k}\cdot\boldsymbol{X}]$ and $\mathfrak{a}(\boldsymbol{X}) = \tilde{\boldsymbol{a}}(\boldsymbol{X})\exp[\mathrm{i}\boldsymbol{k}\cdot\boldsymbol{X}]$. $\boldsymbol{k}$ is the wave vector. The microscopic instability is associated with the coercivity constant

$$\hat{\Lambda}_{\boldsymbol{n}\mathcal{D}} = \inf_{\boldsymbol{k}} \left\{ \inf_{\tilde{\boldsymbol{\varphi}}\in\mathcal{W}_{\tilde{\boldsymbol{\varphi}}}} \inf_{\tilde{\boldsymbol{a}}\in\mathcal{W}_{\tilde{\boldsymbol{a}}}} \left\{ \int_{\mathcal{D}} \nabla\mathsf{v}^* \cdot \partial^2_{\mathsf{FF}}\psi \cdot \nabla\mathsf{v}\,\mathrm{d}V \Big/ \int_{\mathcal{D}} \nabla\mathsf{v}^* \cdot \nabla\mathsf{v}\,\mathrm{d}V \right\} \right\}, \tag{9}$$

where $\mathcal{D}$ denotes the unit cell, $\mathsf{F} := [\boldsymbol{F},\ \mathbb{B}]^T$ and $\nabla\mathsf{v} := [\mathrm{Grad}\,\mathfrak{v},\ \mathrm{Curl}\,\mathfrak{a}]^T$. In finite-element context the latter equation is considered on the discretized unit cell and the Bloch-Floquet type boundary conditions are applied on this unit cell. When the minimum eigenvalue of the resulting system matrix at a tested Bloch vector vanishes along macroscopic loading, the microscopic instability is considered to be detected. For details on the implementation we refer to [3, 4, 10].

5 Representative Numerical Example

The following energy functions are considered for a numerical example in two dimensions

$$\psi^{iso} = -\frac{\mu\xi}{2}\ln\left[1 - \frac{||\boldsymbol{F}||^2/J - 2}{\xi}\right] \quad \text{and} \quad \psi^{mag} = \frac{1}{2\mu_0}\boldsymbol{C} : (\mathbb{B}\otimes\mathbb{B}), \tag{10}$$

where $\mu_0 = 4\pi\cdot 10^{-1}$ N/kA^2 is the magnetic permeability of free space. In order to account the magnetic saturation phenomenon, the magnetic energy of the inclusions is consided to be sum of (10)$_2$ and the Langevin-type energy

$$\psi^L(\boldsymbol{F},\mathbb{B}) = \frac{J\mu_0 m_s^2}{3\chi}\left\{\ln\left[\frac{3\chi}{\mu_0 m_s J}\sqrt{\boldsymbol{C} : (\mathbb{B}\otimes\mathbb{B})}\right] - \ln\left[\sinh\left(\frac{3\chi}{\mu_0 m_s J}\sqrt{\boldsymbol{C} : (\mathbb{B}\otimes\mathbb{B})}\right)\right]\right\} \tag{11}$$

Material Parameter	Matrix	Inclusion
Poisson's ratio, ν [–]	0.495	0.495
Shear modulus, μ [MPa]	0.04	40
Strain saturation, ξ [–]	100	100
Magnetic susceptibility, χ [–]	0	0.995
Magnetic saturation, m_s [T]	–	2.0

Table 1: The considered material parameters.

The microstructure is loaded by macroscopic mechanical deformation gradient $\bar{\boldsymbol{F}}$ and magnetic induction $\bar{\mathbb{B}}$ which are given in terms of the load parameter $\bar{\gamma}$ and the path angle $\phi = [-90°, 90°]$

$$\bar{\boldsymbol{F}} = \begin{bmatrix} \bar{\lambda} & 0 \\ 0 & \bar{\lambda}^{-1} \end{bmatrix} \quad \text{and} \quad \bar{\mathbb{B}} = \begin{bmatrix} 0 \\ \bar{B}_2 \end{bmatrix},$$

where $\bar{\lambda} = 1 + \bar{\gamma}\sin\phi$, $\bar{B}_2 = c\bar{\gamma}\cos\phi$. In Fig. 1, the influence of the volume fractions of the circular inclusions on the onset of macroscopic and microscopic instabilities is illustrated. The corresponding material parameters are given in Tab. 1.

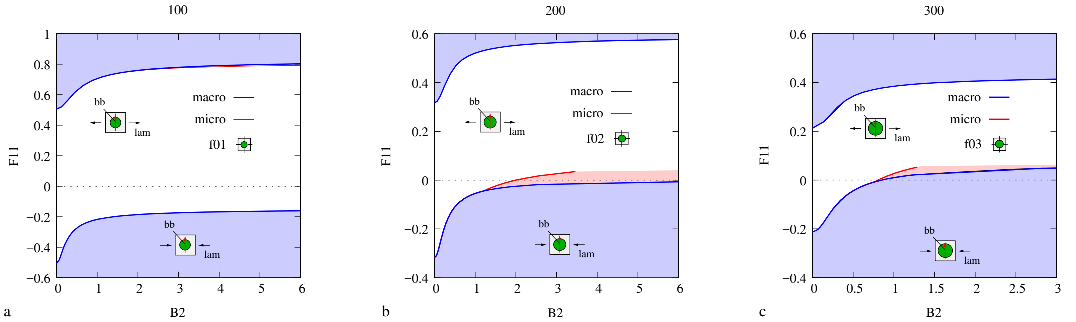

Figure 1: Influence of the volume fraction of circular inclusions on the onset of instability curves. LE denotes the loss of macroscopic ellipticity and MB corresponds to the (bifurcation-type) loss of microscopic stability.

REFERENCES

[1] G. Geymonat, S. Müller and N. Triantafyllidis. Homogenization of nonlinearly elastic materials, microscopic bifurcation and macroscopic loss of rank-one convexity. *Archive for Rational Mechanics and Analysis*, 122: 231–290, 1993.

[2] J.M. Ginder, M.E. Nichols, L.D. Elie and J.L. Tardiff. Magnetorheological elastomers: properties and applications. *Proceedings of SPIE*, 3675: 131–138, 1999.

[3] N. Triantafyllidis, M.D. Nestorović and M.W. Schraad. Failure surfaces for finitely strained two-phase periodic solids under general in-plane loading. *Journal of Applied Mechanics*, 73: 505–515, 2006.

[4] K. Bertoldi, M. Boyce, S. Deschanel, S. Prange and T. Mullin. Mechanics of deformation-triggered pattern transformations and superelastic behavior in periodic elastomeric structures. *Journal of the Mechanics and Physics of Solids*, 56: 2642–2668, 2008.

[5] M. Destrade and R.W. Ogden. On magneto-acoustic waves in finitely deformed elastic solids. *Mathematics and Mechanics of Solids*, 16: 594–604, 2011.

[6] K. Danas, S. Kankanala and N. Triantafyllidis. Experiments and modeling of iron-particle-filled magnetorheological elastomers. *Journal of the Mechanics and Physics of Solids*, 60: 120–138, 2012.

[7] C. Miehe, D. Vallicotti and S. Teichtmeister. Homogenization and multiscale stability analysis in finite magneto-electro-elasticity. Application to soft matter EE, ME and MEE composites. *Computer Methods in Applied Mechanics and Engineering*, 300: 294–346, 2016.

[8] M.-A. Keip and M. Rambausek. A multiscale approach to the computational characterization of magnetorheological elastomers. *International Journal for Numerical Methods in Engineering*, 107: 338–360, 2016.

[9] M.-A. Keip and M. Rambausek. Computational and analytical investigations of shape effects in the experimental characterization of magnetorheological elastomers. *International Journal of Solids and Structures*, 121: 1–20, 2017.

[10] E. Polukhov, D. Vallicotti and M.-A. Keip. Computational stability analysis of periodic electroactive polymer composites across scales. *Computer Methods in Applied Mechanics and Engineering*, 2018, doi.org/10.1016/j.cma.2018.01.020

⇒ TABLE OF CONTENTS

MULTISCALE MODELLING AND SIMULATION OF POLYMER NANOCOMPOSITES USING TRANSFORMATION FIELD ANALYSIS(TFA)

Imad Aldin, Khattab[1] **and Michael, Sinapius**[2]

[1,2]Institute of Adaptronic and Functional Integration (IAF),
Braunschweig University of Technology
Langer Kamp 6,38106 Braunschweig, Germany

Abstract. *High performance fibre-reinforced polymers (FRP) have successfully been established in the aerospace industry. Injection techniques (liquid composite moulding – LCM), such as RTM, VARI, DP-RTM and SLI are alternative manufacturing techniques that have been developed in recent years.*

In order to enhance the properties of these high performance composites and eliminate main disadvantages of the LCM and other alternative techniques; a new method employing nanotechnology is proposed. That the performance of epoxy resins used for carbon fibre reinforced plastics can be significantly improved by the incorporation of nanoparticles.

The objective of this work focuses on the development of mathematical models, i.e. analytically and/or numerically based, for an accelerated multiscale investigation of highly heterogeneous nanocomposite materials. The methods shall be used to predict the effect of the nanocomposite on the stiffness and strength of real aeronautics structures, e.g. a wing-box or a fuselage structure and to save computational resources and time compared to todays established multiscale approaches.

The Transformation Field Analysis proposed by Dvorak and co-workers can be seen as an elegant way of reducing the number of microscopic internal variables by assuming the nanoscopic fields of internal variables to be piecewise uniform.

1 Introduction

Transformation field analysis (TFA) is a method for incremental solution of loading problems in **inelastic heterogeneous media** and composite materials.

Application of the transformation field analysis to elastic-plastic nanocomposites considers a unit cell model consisted of elastic-plastic (LY556 Epoxy) with initial tensile yield stress and elastic nanoparticles (Boehmite 7-10%).

Since the agglomerating fillers with interphase area can be simulated by FEA, [1] and as shown in figure 2, [2], the TFA method described by G. J. Dvorak et al [3,4] is employed to simulate the elastic-plastic response of RVE on a nanoscale level. The results are compared with the FE method.

All the input data are defined and given by [5] in order to make the results comparable. The length edge of RVE is 13.3 [nm], the size of Boehmite particle is 3.1x3x3.1 [nm] (orthorhombic shape) as shown in figure 2.

The overall stress-strain response of the unit cell computed under various mechanical and thermal load components using the TFA method. The response of the unit cell coincides with the solution found by direct evaluation of the overall strains or stresses using elastic-plastic finite element procedure of the ABAQUS program.

The efficiency of the TFA method in comparison with the ABAQUS finite element solution was evaluated in term of the CPU time requested for several load cases.

The TFA tool is utilized in the area of multiscale RVE modelling which is in nature a “micro-macro” approach in finite element method, and to catch the local nano-micro characteristics, an additional nanoscale of transformation field analysis (TFA) method is used to characterize the mechanical properties of nanocomposites with finite element framework.

In this case, the mixture consisting of particles, bulk matrix is homogenized to provide estimates of effective properties of the modified matrix by means of TFA approach, where the overall transformation strains, or stresses, are computed through a multiscale model.

In fact, the implementation of the TFA approach, which centres on treating the nanocomposite medium as elastic with induced local transformations, in the finite element framework does not require generation of an overall instantaneous stiffness matrix, which saves tremendously on the computation time.

Thus, The TFA method of the nanoscale is implemented as a user routine integrated into RVE- micro scale model, as shown in figure 3., where the modified matrix is reinforced by a certain volume fraction of aligned fibers. This yields effective properties of a macroscopic composite element, a fibrous ply.

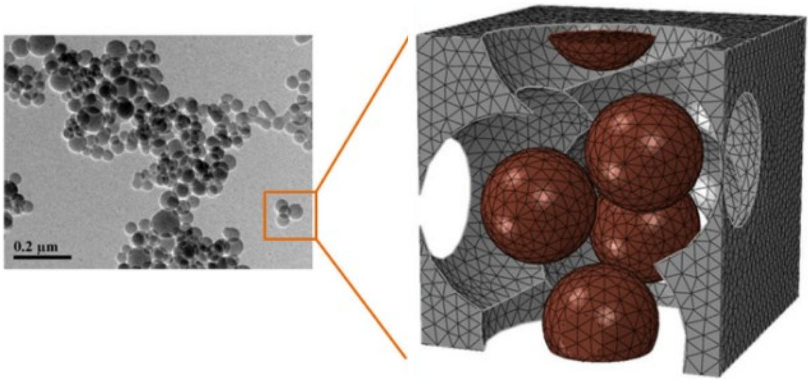

(a) (b)

Figure 1: A multi particulate nanocomposite systems that includes four agglomerated nanoparticles (a) TEM image of silica nanocomposites (b) equivalent finite element model, [2].

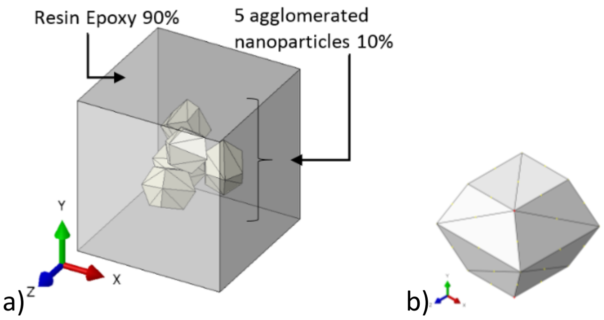

Figure 2: a) A representative volume element (RVE) consists of 90% (weight fraction) resin epoxy and 10% agglomerate boehmite nanoparticles. b) The orthorhombic shape of one boehmite nanoparticle.

⇒ TABLE OF CONTENTS

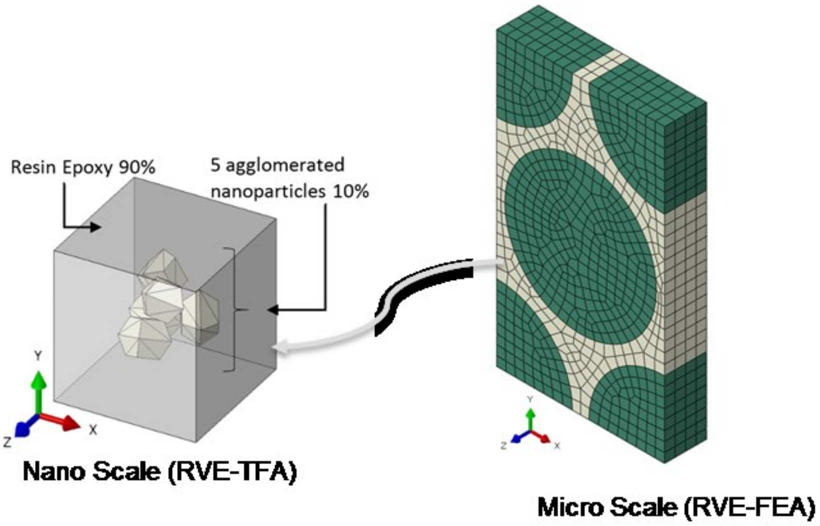

Figure 3: Multi scale approach (TFA/FEA) Nano/Micro scale.

2 References

[1] Cho, M., Yang, S., Chang, S. and Yu, S. (2011). A study on the prediction of the mechanical properties of nanoparticulate composites using the homogenization method with the effective interface concept. Int J. Numer. Meth. Engng 2011; 85:1564–1583.

[2] Shin, H., Yang, S., Choi, J. and Chang, S., & Cho, M. (2015). Effect of interphase on mechanical behavior of nanoparticle-reinforced polymer nancomposites with filler agglomeration: A multiscale approach. Chemical Physics Letters 635, 80-85. Elsevier Science B.V.

[3] Dvorak, G. J., Bahei-El-Din, Y. A., & Wafa, A. M. (1994). Implementation of the transformation field analysis for inelastic composite materials. Computational Mechanics, 14, 201–228.

[4] Dvorak, G. J (2013). Micromechanics of Composite Materials, 1st ed., Springer.

[5] Fankhänel, J., Kempe, A., Rolfes, R. (2016). Simulating Atomic Force Microscopy for the determination of the elastic properties of nano-particle reinforced Epoxy resin. Proceedings ECCOMAS 2016.

⇒ TABLE OF CONTENTS

MAGNETOMECHANICAL FE-ANALYSIS FOR MATERIALS WITH ENERGY-MINIMIZING MICROSTRUCTURE EVOLUTION

Björn Kiefer[1,*], **Thorsten Bartel**[2], **Karsten Buckmann**[2], **and Andreas Menzel**[2,3]

[1] Institute of Mechanics and Fluid Dynamics, TU Bergakademie Freiberg
Lampadiusstr. 4, 09596 Freiberg, Germany

[2] Institute of Mechanics, TU Dortmund University
Leonhard-Euler-Str. 5, 44227 Dortmund, Germany

[3] Division of Solid Mechanics, Lund University
PO Box 118, 22100 Lund, Sweden

Abstract. *In this contribution we present a variational framework which is suitable for the finite element implementation of energy-relaxation based magnetostriction models. Our recent work [3] has shown that energy-relaxation based approaches are able to capture all key response characteristics of multi-ferroic magnetic shape memory alloys (MSMA). In contrast to phenomenological models for MSMA behavior [1, 2]—which are inspired by classical plasticity and also conventional SMA models—these approaches build on concepts of relaxation in the context of non-convex energy landscapes. The difficulty of implementing such constitutive models into Finite-Element codes lies in the fact that the magnetostatic energy stored in the demagnetization field is non-local in nature. In other words, the microstructure evolution at a material point depends on the solution of the boundary value problem in the entire domain. To address this, we propose a micromagnetics-inspired finite element framework, in which the magnetization inside the magnetizable material as well as the demagnetization field are spatially resolved. Our implementation then allows response simulations for arbitrarily shaped samples. Special cases—considering ellipsoidal specimen geometries—are used to verify the magnetization and field-induced strain responses obtained from FE-simulations by comparison to calculations based on the demagnetization tensor concept.*

1 The General Modeling Concept

Our modeling approach builds on the *global variational principle*

$$\{\widetilde{\phi}, \boldsymbol{p}\} = \arg\Big[\sup_{\widetilde{\phi}}\,\inf_{\boldsymbol{p}}\,\widetilde{\Pi}(\widetilde{\phi}, \boldsymbol{p})\Big] \qquad \text{subject to constraints on the values of } \boldsymbol{p}\,, \tag{1}$$

in which the *total potential*—which we later amend to account for dissipation—is defined as

$$\widetilde{\Pi}(\widetilde{\phi}, \boldsymbol{p}) = \int_{\mathcal{B}} \psi(\boldsymbol{p})\,\mathrm{d}v + \frac{\mu_0}{2}\int_{\Omega} \|\widetilde{\boldsymbol{h}}\|^2\,\mathrm{d}v - \int_{\mathcal{B}} \boldsymbol{\varepsilon}(\boldsymbol{p}) : \overline{\boldsymbol{\sigma}}\,\mathrm{d}v - \mu_0\int_{\mathcal{B}} \overline{\boldsymbol{h}}\cdot\boldsymbol{m}(\boldsymbol{p})\,\mathrm{d}v\,. \tag{2}$$

The first term represents the free energy stored in the material, the second the magnetostatic energy stored in all of space. The last two terms relate to the work done by external magnetomechanical loadings on the strains and magnetization. Here $\widetilde{\phi}$ represents the potential for the

---

[*] Corresponding author: Björn Kiefer (✉ Bjoern.Kiefer@imfd.tu-freiberg.de)

demagnetization field, i.e. $\widetilde{\boldsymbol{h}} := -\nabla_{\boldsymbol{x}}\widetilde{\phi}$, and $\overline{\boldsymbol{h}}$ the applied field, so that the total magnetic field strength is given by $\boldsymbol{h} = \widetilde{\boldsymbol{h}} + \overline{\boldsymbol{h}}$. The set of parameters describing the state of the underlying microstructure—variant magnetizations and volume fractions—is denoted $\boldsymbol{p}$, and the magnetization at a material point $\boldsymbol{m}(\boldsymbol{p})$ is assumed to be fully defined by it. In order to reduce the complexity of the problem, we have assumed at this point that the only mechanical contribution comes through the work done by a given, spatially homogeneous stress field on the inelastic strains $\boldsymbol{\varepsilon}(\boldsymbol{p})$ related to martensitic variant switching — elastic energy storage is neglected. In this sense, the relaxation with respect to mechanical degrees of freedom, see [3], is set aside in the current formulation. Our focus lies on the proper numerical treatment of the nonlocal demagnetization field energy and its role in driving the microstructure evolution.

2 Numerical Results

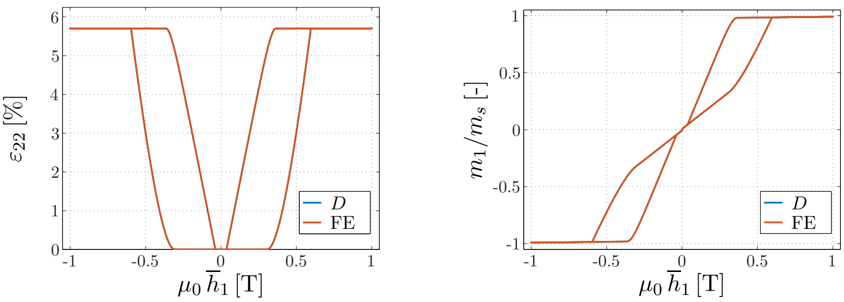

Figure 1: Magnetic-field induced strain (left) and magnetization (right) for a circular sample at constant compressive stress of $\overline{\sigma}_{22} = -1.0\,\mathrm{MPa}$. The response calculations utilizing a demagnetization tensor are compared to body averaged values of finite element simulations.

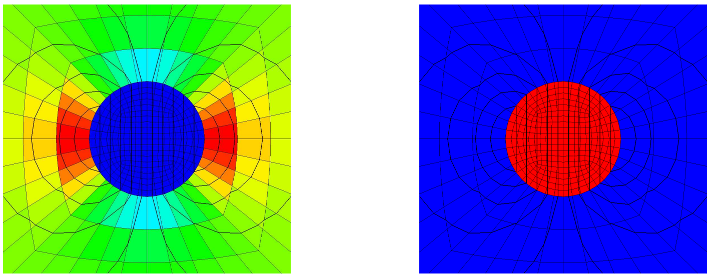

Figure 2: Spatial distribution of the demagnetization field $\widetilde{h}_1$ (left) and the magnetization field m_1 (right) of a circular sample embedded into a free-space box at a constant compressive stress of $\overline{\sigma}_{22} = -1.0\,\mathrm{MPa}$ and cyclic magnetic field loading $\overline{h}_1 > 0$. Additionally, iso-lines of the magnetic potential $\widetilde{\phi}$ are displayed.

REFERENCES

[1] B. Kiefer and D. C. Lagoudas. Modeling the coupled strain and magnetization response of magnetic shape memory alloys under magnetomechanical loading. *Journal of Intelligent Material Systems and Structures*, 20(2):143–170, 2009.

[2] B. Kiefer, T. Bartel, and A. Menzel. Implementation of numerical integration schemes for the simulation of magnetic sma constitutive response. *Smart Materials and Structures*, 21 (9):094007, 2012.

[3] B. Kiefer, K. Buckmann, and T. Bartel. Numerical energy relaxation to model microstructure evolution in functional magnetic materials. *GAMM-Mitteilungen*, 38(1):171–196, 2015.

INVESTIGATION OF MECHANICALLY INDUCED CRACK TIP FIELDS IN FERROELECTRIC MATERIALS

Sergii Kozinov* **and Meinhard Kuna**

Institute of Mechanics and Fluid Dynamics, Department of Solid Mechanics, TU Bergakademie Freiberg
Lampadiusstr. 4, 09599 Freiberg, Germany

Abstract. *In order to investigate the failure mechanism of ferroelectric materials, many mathematical methods were incorporated to obtain solution of simple piezoelectric fracture mechanics problems. But to assess the strength and durability of a practical test specimen, numerical fracture mechanics methods have to be applied to improve the understanding of the effect of domain switching on the fracture process zone. The major difficulty in developing a fracture theory of ferroelectric ceramics lies particularly in the physical understanding of the involved phenomena. The substantial problem is the influence of the electric field on the loading situation at the crack tip, the actual non-linear material state as well as the fracture toughness. In ferroelectric structures the electromechanical material behavior is strongly non-linear due to polarization processes. This means that the mechanical and electrical quantities are inherently coupled at the crack, i.e. besides the mechanical stress intensity factor* K_I *an electric field intensity factor* K_{IV} *occurs.*

In the current research a micromechanical model [1] is used to analyze the material behavior at the crack tip due to the domain switching as an effect of the applied mechanical loading.

1 Introduction

Smart devices made of ferroelectric ceramics have gained a wide popularity due to their extensive application in various fields ranging from those for everyday use (automotive and electronic components, ...) to much more specialized ones such as medical equipment, military instruments, etc. Nevertheless there are some limitations when these materials are applied, because of mechanical failure by fatigue or cracking, partial or total depolarization and others. Some of the reasons are strong electromechanical fields when approaching the notch or crack tip, operating temperature, manufacturing process.

The aim of the paper is to study the influence of the non-linear domain switching zone around a crack in a ferroelectric material by means of the finite element modeling. In the previous work [2] merely the linear piezoelectric near crack-tip solution has been used together with a switching criterion to estimate the size and shape of the switching zone and the resulting change of crack-tip intensity factors. Meanwhile, for ferroelectric materials micromechanically based switching models are available [1], as those implemented in ABAQUS as user material routine in [3], which allow to simulate domain switching in the vicinity of cracks in a much more realistic manner [4].

---

[*] Corresponding author: Sergii Kozinov (✉ sergii.kozinov@imfd.tu-freiberg.de)

⇒ TABLE OF CONTENTS

2 Small scale domain switching model at crack tip

For this purpose, a so-called boundary layer approach is adopted, whereby the analytical solution for the near crack-tip field in a linear piezoelectric material is applied as a boundary conditions on a circular domain including the crack tip in a ferroelectric material, see Fig. 1. This piezoelectric near crack-tip solution has been obtained analytically by means of the Stroh formalism. Hereby, complex functions theory is used to find the eigenvalues $p_\alpha, \alpha \in 1-4$ of the characteristic PDEs for the static electromechanical crack problem, expressed by displacements u_i and electric potential ϕ. The crack faces are assumed to be electrically impermeable. From the solution in polar coordinates (r, θ) around the crack tip, it turned out that the stresses and electric displacements have a $1/\sqrt{r}$ singularity, whereas the mechanical displacement vector and the electric potential behave like $\sqrt{r}$. The magnitude of the near-tip fields is governed by the mechanical stress intensity factor K_I and the dielectric field intensity factor K_IV.

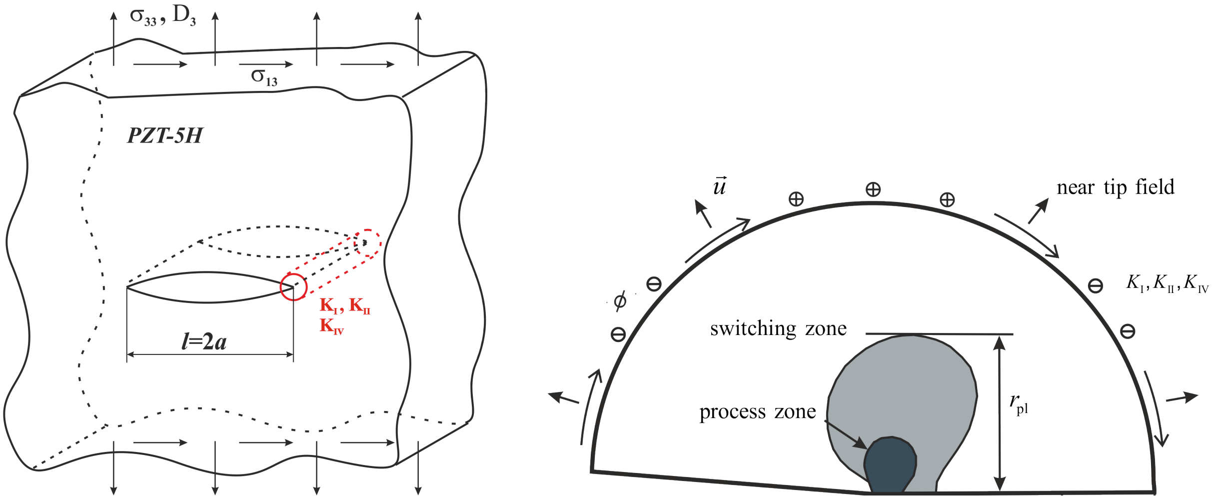

Figure 1: Griffith crack (left) and boundary layer model (right, half-model for illustration purpose) applied to a ferroelectric material

$$u_i(r,\theta) = \sqrt{\frac{2r}{\pi}}\left[K_I d_i^I(\theta) + K_{IV} d_i^{IV}(\theta)\right], \quad \phi(r,\theta) = \sqrt{\frac{2r}{\pi}}\left[K_I\, e^I(\theta) + K_{IV}\, e^{IV}(\theta)\right] \tag{1}$$

The angular functions for the displacements and electric potential are given as follows:

$$d_i^N(\theta) = \sum_{\alpha=1}^{4} \Re\left\{A_i^\alpha\, N_N^\alpha \sqrt{\cos\theta + p_\alpha\, \sin\theta}\right\} \quad \text{for } i \in (1,2,3) \tag{2}$$

$$e^N(\theta) = \sum_{\alpha=1}^{4} \Re\left\{A_4^\alpha\, N_N^\alpha \sqrt{\cos\theta + p_\alpha\, \sin\theta}\right\}, \tag{3}$$

where the matrices A_i^α and N_N^α depend on the elastic, piezoelectric and dielectric material constants. The running index N covers the mechanical and electrical opening modes I and IV. Further details can be found in [2].

3 Finite element analysis of switching processes

The developed FE model, which is considered as a part of the region near the crack tip (Fig. 1), consists of 3D hexahedral elements with biased mesh towards the crack tip (see, e.g.

Fig. 2a). The number of elements along the circumferential and radial directions are considered to be 30 and 21, respectively. The length of the crack $l = 2a = 10$ cm and the radius of the near field model is 1 mm. The model is constructed with the consideration of the plane strain. The material of the specimen is PZT-5H ceramics.

The results of the simulations for a near tip electromechanical fields induced by the applied far-field mechanical loading $\sigma_{33} = 3$ MPa are presented in Fig. 2 (deformations magnified 50 times). For the given crack length and external loading, the SIF $\mathrm{K_I} = 1.189\ \mathrm{MPa} \cdot \mathrm{m}^{1/2}$. The boundary conditions applied along the circumference of the disc are in-plane mechanical displacements defined by the near field solution (1) - (3). The calculations are conducted for the case of poling perpendicular to the crack faces.

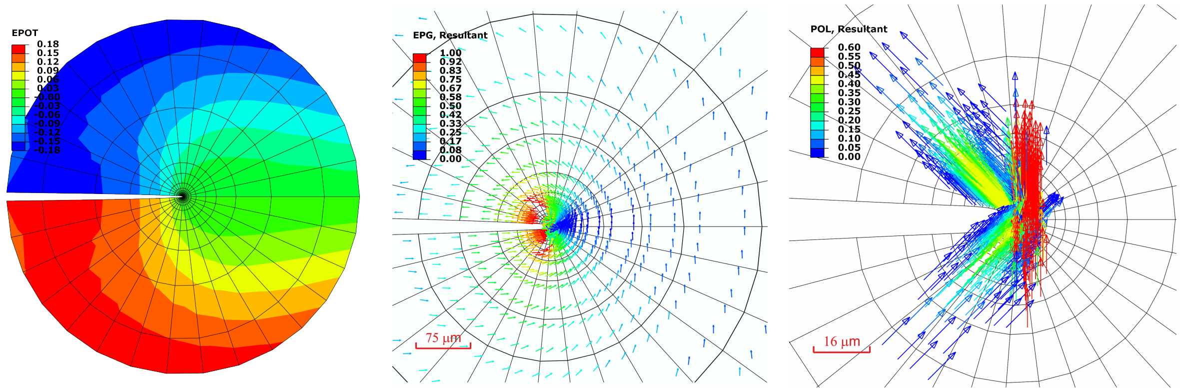

(a) electric potential distribution, kV

(b) vector plot for electric potential gradient, kV/mm

(c) vector plot for the change of ferroelectric polarization, C/m^2

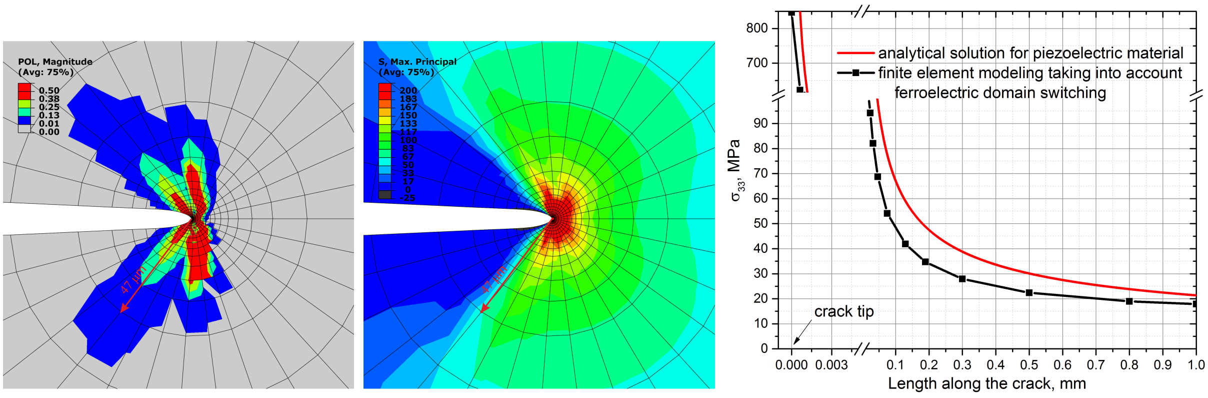

(d) size and shape of the ferroelectric switching zone

(e) maximal principal stresses, MPa

(f) comparison of the singularity of the σ_{33} stresses near the crack tip

Figure 2: Switching zone and electromechanical quantities distribution as a result of the applied $\mathrm{K_I}$ mechanical near tip field

The results for the electric potential, generated due to the piezoelectric coupling under the applied mechanical loading, are presented in Fig. 2a. The constant-length vectors of electric potential gradient, illustrating the electric flow, are presented in Fig. 2b.

The corresponding results for the size and shape of the switching zone are presented in Fig. 2d. It was found that, for the current crack length and $\mathrm{K_I} = 1.189\ \mathrm{MPa} \cdot \mathrm{m}^{1/2}$ dominated near tip field, the maximum size of the switching zone in PZT-5H ceramics is $\approx 47\mu m$. The direction and magnitude of the remanent polarization, illustrated by the constant-length vectors in Fig. 2c, are influenced by the initial ideal poling along the x_3 axis, concentration of the electrical and mechanical fields at the crack tip and the electrically impermeable crack faces, forcing the generated electric field to flow around the crack.

The outcomes for the maximal principal mechanical stresses resulting from the applied mechanical loading and the process of ferroelectric domain switching are shown in Fig. 2e. The arrow illustrates the size of the switching zone region. It is easy to observe that most of the material in the vicinity of the crack tip is experiencing strong tensile stresses, while compressive stresses can be found only close to the crack surface and are due to domain reorientation.

The reduction of the σ_{33} stress singularity near the crack tip due to domain switching is illustrated in Fig. 2f, where results of the analytical solution for the piezoelectric material behavior and the ferroelectric finite modeling are compared.

4 Conclusions

As a result of the current numerical simulations, the electrical and mechanical crack tip fields induced by the pure mechanical K_I near tip solution are investigated. The size and shape of the switching zone in case of the plane strain state are studied. The deviation from the near tip stress singularity due to the domain switching is found. Additional results concern the influence of the near tip fields induced by the electrical K_{IV} and combined K_I and K_{IV} IFs, as well as different directions of the initial material poling.

As a next step, the currently used FE model will be extended by the cohesive zone at the crack tip, where the electromechanical cohesive elements [5] are applied, so the crack growth behavior can be studied under monotonous/cyclic loading. The subsequent results will be analyzed by means of the concept of configurational forces, i.e. calculating the J-integral at the far and near fields, so the fracture criteria can be developed.

Acknowledgements

The research was funded by DFG under grant KU 929/21-1.

REFERENCES

[1] J. Huber, N. Fleck, C. Landis and R. McMeeking. A constitutive model for ferroelectric polycrystals, *J. Mech. Phys. Solids*, 47(8): 1663–1697, 1999.

[2] A. Ricoeur and M. Kuna. A micromechanical model for the fracture process zone in ferroelectrics, *Computational Materials Science*, 27: 235–249, 2003.

[3] Q. Li and M. Kuna. Inhomogeneity and material configurational forces in three dimensional ferroelectric polycrystals, *European Journal of Mechanics, A/Solids*, 31(1): 77–89, 2012.

[4] S. Kozinov and M. Kuna. Micromechanical simulation of ferroelectric domain processes at crack tips, submitted to *Archive of Applied Mechanics*, 2018.

[5] S. Kozinov, M. Kuna and S. Roth. A cohesive zone model for the electromechanical damage of piezoelectric/ferroelectric materials, *Smart Mater. Struct.*, 23: 055024, 2014.

Strain & phase transitions in oxide heterostructures and ultrathin films

Jens Kreisel[1,2]

[1] Department Materials Research and Technology, Luxembourg Institute of Science and Technology
41, rue du Brill, Belvaux, Luxembourg

[2] Physics and Materials Science Research Unit, University of Luxembourg
41, rue du Brill, Belvaux, Luxembourg

Abstract. *Over the past two decades, a significant amount of progress has been achieved in the epitaxial growth of (multi-) functional oxide films. By applying epitaxial strain to thin films, the ferroic transition temperatures can be increased by hundreds of degrees, new phases can be induced, the coupling between different ferroic orders can be modified etc. After a short introduction to the effect of deformations on* ABO_3 *perovskites, we will present in more detail the drastic and intriguing effect of thin film strain in the apparently simple* $LaNiO_3$*. We present evidence that strain can induce multiple phase transitions in* $LaNiO_3$ *films and multilayers. We will specifically show that Raman scattering is a well-adapted probe of strain and phase transitions in thin films, even in very thin layers down to 1.2 nm.*

1 Introduction

In recent years, the engineering of transition-metal perovskite oxides with AMO_3 composition –where A usually stands for an alkali or a rare earth and M for a transition metal– has been a powerful tool to finely tune the interactions between charge, spins, and phonons, leading even to the discovery of emergent properties.

Pivotal to this progress is the use of thin film heteroepitaxies grown on different substrates. The structural mismatch between film and substrates imposes, via the necessary connectivity of the metal coordination polyhedral of the substrates and the films, structural constraints that allow tailoring the film structure [1]. In addition to work on thin and ultrathin-films, a considerable amount of current research goes to thin film oxide *multi*layers - often also called superstructures, superlattices or heterostructures - which are defined as a sequence of thin film layers and which can display specific properties.

Substrate-induced strain is the toggle switch that permits imposing elastic stress, compressive or tensile, on thin films, and it has been much used to modulate properties of a variety of perovskite oxides films and multilayers.

Unfortunately, due to the low film thickness and the often only subtle structural modifications, the structural characterization of (multi-) functional oxide thin films, especially in heterostructures and in the ultra-thin regime, remains challenging. Here, we will show that Raman scattering is a well-adapted probe of strain and phase transitions in embedded layers, thin films and ultrathin films. Three situations will be discussed in particular.

(i) Strain and phase transitions in $BaTiO_3/LaNiO_3/CeO_2$/YSZ multilayer structures on silicon. [1].

(ii) A surprising multitude of strain-induced phase transitions in $LaNiO_3$ thin films under strain [2].

(iii) Strain effects and critical regimes in ultrathin $LaNiO_3$ films down to 1.2 nm of thickness [3].

---

[*] Corresponding author: J. Kreisel (jens.kreisel@list.lu)

2 Figures

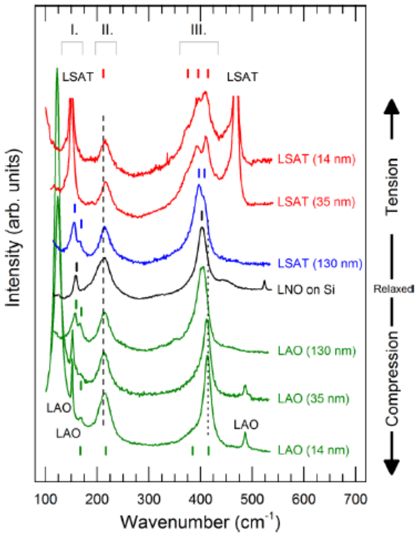

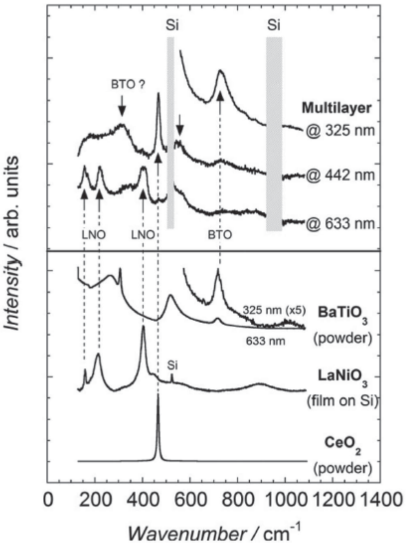

Figure 1:

Raman spectra of $LaNiO_3$ of different indicated thicknesses either on LAO or LSAT substrates. The observed spectral changes indicate structural phase transitions [2].

Figure 2:

Comparison of the Raman spectra of a $BaTiO_3/LaNiO_3/CeO_2$/YSZ//Si(001) multilayer at 325, 442, and 633 nm (top panel,) with reference spectra of the individual layers in the multilayer (bottom panel): $BaTiO_3$ (BTO), $LaNiO_3$ (LNO) and CeO_2 powders and a thick polycrystalline $LaNiO_3$ film deposited on bare Si) [1].

REFERENCES

[1] J. Kreisel, M. C. Weber, N. Dix, F. Sánchez, P. A. Thomas, and J. Fontcuberta, Probing individual layers in functional oxide multilayers by wavelength-dependent Raman scattering, *Adv. Funct. Mat.* 23, 5044, 2012

[2] M.C. Weber, M. Guennou, N. Dix, D. Pesquera, F. Sánchez, G. Herranz, J. Fontcuberta, L. López-Conesa, S. Estradé, F. Peiró, J. Iñiguez, J. Kreisel, Multiple strain-induced phase transitions in $LaNiO_3$ thin films, *Phys. Rev. B* 94, 014118, 2016

[3] J. Fowlie, M. Gibert, G. Tieri, A. Gloter, J. Íñiguez, A. Filippetti, S. Catalano, S. Gariglio, A. Schober, M. Guennou, J. Kreisel, O. Stéphan and J.-M. Triscone, Conductivity and local structure of $LaNiO_3$ thin films, Advanced Materials 29, 1605197, 2017

⇒ TABLE OF CONTENTS

TWO-SCALE HOMOGENIZATION FOR THE PREDICTION OF MAGNETO-ELECTRIC PRODUCT PROPERTIES

Matthias Labusch[1,*], **Jörg Schröder**[1], **and Doru C. Lupascu**[2]

[1] Institute of Mechanics, Department of civil engineering, Faculty of engineering, University Duisburg-Essen
Universitätsstraße 15, 45141 Essen, Germany

[2] Institute for Materials Science and Center for Nanointegration Duisburg-Essen (CENIDE),
University Duisburg-Essen, Universitätsstraße 15, 45141 Essen, Germany

Abstract. *In this contribution we analyze the magneto-electric (ME) coupling of two-phase composites, consisting of a ferroelectric matrix with magnetostrictive inclusions. Therefore, we derived a three dimensional magnetostrictive Preisach model, which approximates the remanent magnetization and remanent strains with a suitable Preisach operator. The characteristic ferroelectric hysteresis curves are described with a switching model based on a ferroelectric/-elastic switching criterion considering a change in the free energy. In order to validate the numerical simulations we compare the results of the ME coefficients with experimental measurements.*

1 Introduction

Multiferroic materials combine two or more ferroic properties and can improve and expand the range of technical applications [2, 1]. Magneto-electric (ME) materials show a change in the electric polarization due to an applied magnetic field or a change in magnetization due to electric fields [12]. Since natural and synthetic single-phase ME materials mostly have a weak coupling at cryogenic temperatures. However, composite materials generate a higher ME coupling at room temperature. Due to the interaction between the ferroelectric and ferromagnetic phase the ME coefficient arises as a strain-induced property. In order to simulate the interaction of

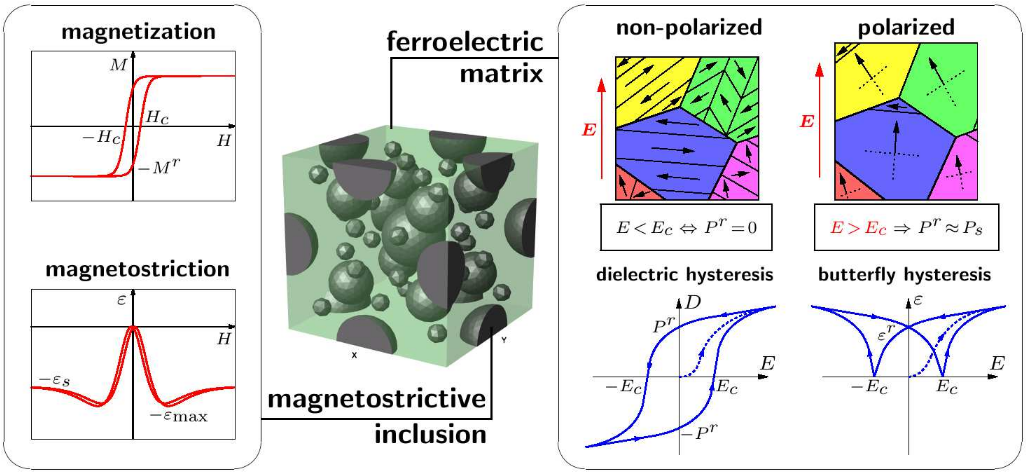

Figure 1: Design of magneto-electric two-phase composites.

---

*Corresponding author: Matthias Labusch (✉ matthias.labusch@uni-due.de)

⇒ TABLE OF CONTENTS

both phases in a composite we use the so-called FE^2-method, see e.g. [9, 5, 10, 11], where the material behavior on the microscopic level is characterized by appropriate material models and the effective macroscopic properties are determined by a two-scale homogenization approach. For the 3D numerical simulations we implemented a ferroelectric/-elastic switching model and a magnetostrictive Preisach model.

2 Homogenization scheme

In order to simplify the readability we summarize the basic quantities in the following table.

sign	description	sign	description	sign	description
$\boldsymbol{u}$	displacement vector	ϕ^e	electric potential	φ^m	magnetic potential
$\boldsymbol{\varepsilon}$	linear strain tensor	$\boldsymbol{E}$	electric field vector	$\boldsymbol{H}$	magnetic field vector
$\boldsymbol{\sigma}$	Cauchy stress tensor	$\boldsymbol{D}$	electric displacement	$\boldsymbol{B}$	magnetic flux density
$\boldsymbol{t}$	traction vector	Q	electric surf. flux density	ζ	magn. surf. flux density
$\boldsymbol{f}$	mech. body forces	q_f	free charge carrier density	$\boldsymbol{f}^{em}$	elec.-magn. body forces

Table 1: Summary of the magneto-electro-mechanical quantities.

For the simulation of magneto-electro-mechanically coupled problems the fundamental macroscopic balance laws and field quantities, in the following denoted with an overline, are given by

$$\begin{aligned} &\mathrm{div}_{\overline{\boldsymbol{x}}}\overline{\boldsymbol{\sigma}} + \overline{\boldsymbol{f}} + \overline{\boldsymbol{f}}^{em} = \boldsymbol{0}\,, \quad \mathrm{div}_{\overline{\boldsymbol{x}}}\overline{\boldsymbol{D}} = \overline{q}_f \quad \text{and} \quad \mathrm{div}_{\overline{\boldsymbol{x}}}\overline{\boldsymbol{B}} = 0 \\ &\overline{\boldsymbol{\varepsilon}} = \mathrm{grad}^{sym}_{\overline{\boldsymbol{x}}}\overline{\boldsymbol{u}}\,, \quad \overline{\boldsymbol{E}} = \mathrm{grad}_{\overline{\boldsymbol{x}}}\overline{\phi}^e \quad \text{and} \quad \overline{H} = \mathrm{grad}_{\overline{\boldsymbol{x}}}\overline{\varphi}^m\,, \end{aligned} \tag{1}$$

where the free charge carriers q_f and the electromagnetic body forces $\overline{\boldsymbol{f}}^{em}$ are neglected. In order to incorporate the influence of the microscopic morphology on the effective properties, we connect the macroscale by underlying representative volume elements (RVEs) and assume a generalized magneto-electro-mechanical Hill-Mandel condition including the individual parts

$$\overline{\boldsymbol{\sigma}} : \dot{\overline{\boldsymbol{\varepsilon}}} = \frac{1}{V}\int_{RVE} \boldsymbol{\sigma} : \dot{\boldsymbol{\varepsilon}}\,\mathrm{d}v\,, \quad \overline{\boldsymbol{D}} \cdot \dot{\overline{\boldsymbol{E}}} = \frac{1}{V}\int_{RVE} \boldsymbol{D} \cdot \dot{\boldsymbol{E}}\,\mathrm{d}v \quad \text{and} \quad \overline{\boldsymbol{B}} \cdot \dot{\overline{\boldsymbol{H}}} = \frac{1}{V}\int_{RVE} \boldsymbol{B} \cdot \dot{\boldsymbol{H}}\,\mathrm{d}v\,, \tag{2}$$

from which we define suitable boundary conditions. After solving the microscopic boundary value problem, the overall material tangent including the mechanical, electric and magnetic properties, is determined.

3 Switching model

The magneto-electric enthalpy function represents the tetragonal symmetry of barium titanate unit cells. A homogenization over multiple unit cells, allocated with an orientation distribution function, yield the microscopic properties. Each of the individual directions can change its orientation due to electric or mechanical fields showing a change in the free energy [3, 11]

$$\Delta\psi = \Delta\psi^{elec} + \Delta\psi^{mech} = \boldsymbol{E} \cdot \Delta\boldsymbol{P}^r + \boldsymbol{\sigma} : \Delta\boldsymbol{\varepsilon}^r\,. \tag{3}$$

The ferroelectric/-elastic criterion for a switching of the individual directions is defined by

$$\frac{\boldsymbol{E} \cdot \Delta\boldsymbol{P}^r_1}{2P_sE_c} \geq 1 \quad \text{and} \quad \frac{\boldsymbol{E} \cdot \Delta\boldsymbol{P}^r_i}{P_sE_c} + \frac{\boldsymbol{\sigma} : \Delta\boldsymbol{\varepsilon}^r_i}{3/2\varepsilon_s\sigma_c} \geq 1 \quad \text{for} \quad i = 2, ..., 5\,, \tag{4}$$

where i denotes the different 90° ferroelectric and ferroelastic polarization switching options.

4 Preisach model

Within the Preisach model [8, 4, 7] the remanent magnetization $\boldsymbol{M}_r$ and remanent strains are approximated by a Preisach operator $\mathcal{P}$, which is determined by a superposition of multiple hysterons, with a small square hysteresis cycle and different *up* and *down* switching thresholds,

$$\boldsymbol{M}_r = \mathcal{P}(\boldsymbol{H})\boldsymbol{a} \quad \text{with} \quad \mathcal{P}(\boldsymbol{H}) = \int_\beta \int_\alpha \omega(\alpha,\beta)\,\gamma(\alpha,\beta)\,\boldsymbol{H}(t)\cdot\boldsymbol{a}\,\mathrm{d}\alpha\,\mathrm{d}\beta\,. \tag{5}$$

Here, the Preisach operator depends on a preferred direction $\boldsymbol{a}$ denoting the magnetization direction, which can rotate into the direction of the local microscopic magnetic field. Furthermore, the magneto-mechanical coupling tensor is factorized with a weighting factor, depending on the current magnetization, in order to depict the characteristic material behavior of cobalt ferrite.

5 Numerical results

In the following simulations we consider a fiber-induced ME composite with magnetostrictive nanopillars in a ferroelectric matrix. To investigate the influence of different polarization states on the ME coefficient, we polarize the electric phase in different simulations with $\overline{E}_3^{max} = 0.5$, $\overline{E}_3^{max} = 1.0$, $\overline{E}_3^{max} = 1.5$ and $\overline{E}_3^{max} = 4.0$ kV/mm. Afterwards, the electric field is removed and the composite is loaded with an alternating magnetic field $\overline{H}_3$. Due to the interaction of both phases we obtain a nonlinear behavior of the strain-induced ME coefficient.

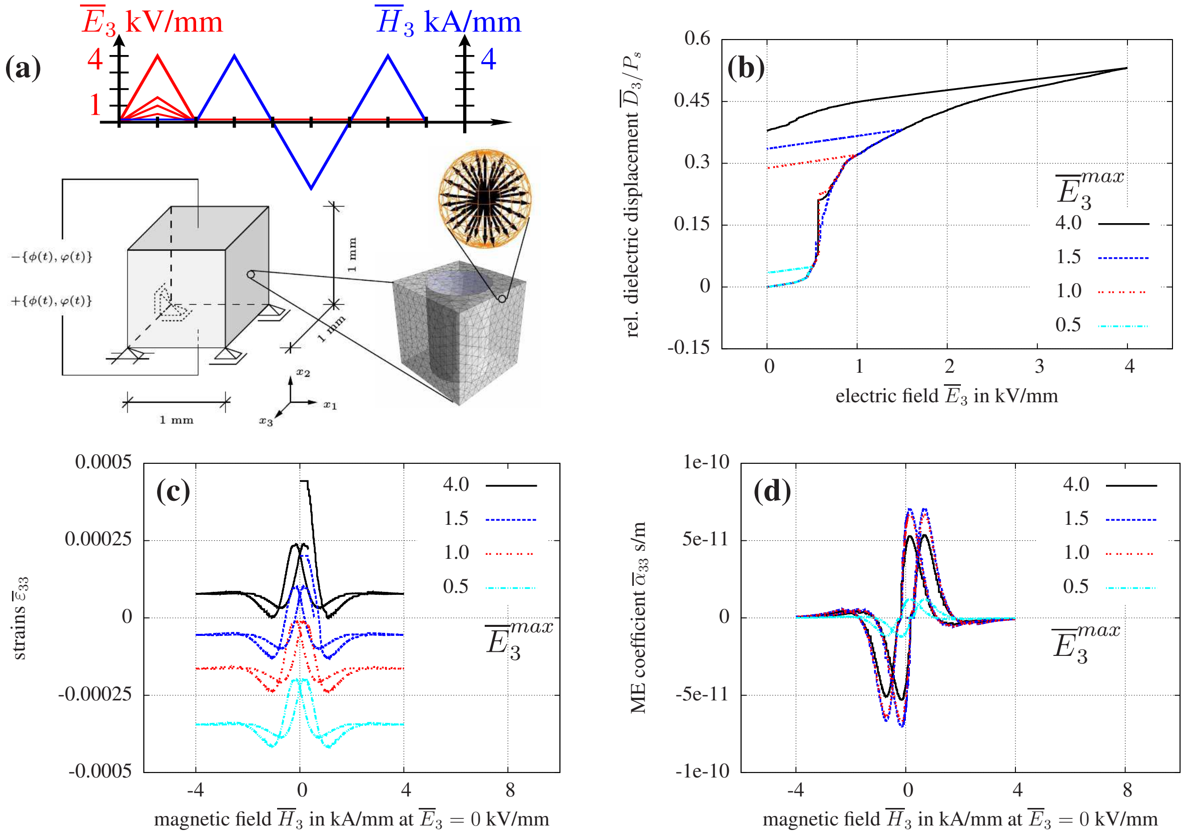

Figure 2: **(a)** Macroscopic boundary value problem with electric and magnetic load curve, **(b)** Relative overall dielectric displacement $\overline{D}_3/P_s$, **(c)** overall magnetostrictive hysteresis loops and **(d)** resulting effective strain-induced magneto-electric coupling coefficient $\overline{\alpha}_{33}$, for four different electric first poling scenarios ($\overline{E}_3^{max} = 0.5$; $\overline{E}_3^{max} = 1.0$; $\overline{E}_3^{max} = 1.5$; $\overline{E}_3^{max} = 4.0$ kV/mm).

⇒ TABLE OF CONTENTS

It can be shown that the prediction of the magnitude as well as the qualitative behavior of the ME coupling is more precise with respect to experimental measurements compared to previous works as [5, 10, 11]. The still deviating prediction can be caused by microscopic defects, which further reduce the ME coupling [6], and by the complex microscopic morphology. The impact of the latter reason will be investigated in future works by considering a realistic microstructure.

Acknowledgments
We gratefully acknowledge the financial support of the German Research Foundation (DFG) in the framework of the research unit FOR 1509 “ Ferroic functional Materials” (SCHR 570/12-2).

REFERENCES

[1] M. Bibes and A. Barthélémy. Multiferroics: Towards a magnetoelectric memory. *Nature Materials*, 7(6):425–426, 2008. ISSN 1476-1122.

[2] W. Eerenstein, N. D. Mathur, and J. F. Scott. Multiferroic and magnetoelectric materials. *Nature*, 442(7104):759–765, 2006.

[3] S.C. Hwang, C.S. Lynch, and R.M. McMeeking. Ferroelectric/ferroelastic interactions and a polarization switching model. *Acta Metallurgica et Materialia*, 43(5):2073–2084, 1995.

[4] M. Kaltenbacher, B. Kaltenbacher, T. Hegewald, and R. Lerch. Finite Element Formulation for Ferroelectric Hysteresis of Piezoelectric Materials. *Journal of Intelligent Material Systems and Structures*, 2010.

[5] M. Labusch, M. Etier, D.C. Lupascu, J. Schröder, and M.-A. Keip. Product properties of a two-phase magneto-electric composite: Synthesis and numerical modeling. *Computational Mechanics*, 54:71–83, 2014.

[6] M. Labusch, J. Schröder, and D.C. Lupascu. Multiscale homogenization of magneto-electric porous two-phase composites. In *Insights and Innovations in Structural Engineering, Mechanics and Computation*, 2017.

[7] I.D. Mayergoyz and G. Friedman. Generalized preisach model of hysteresis. *IEEE Transactions on Magnetics*, 24:212–217, 1988.

[8] F. Preisach. über die magnetische Nachwirkung. *Zeitschrift für Physik*, 94:277–302, 1935.

[9] J. Schröder. A numerical two-scale homogenization scheme: the FE^2–method. In J. Schröder and K. Hackl, editors, *Plasticity and Beyond*, volume 550 of *CISM Courses and Lectures*, pages 1–64. Springer, 2014.

[10] J. Schröder, M. Labusch, M.-A. Keip, B. Kiefer, D. Brands, and D.C. Lupascu. Computation of non-linear magneto-electric product properties of 0-3 composites. *GAMM-Mitteilungen*, 38(1):1–8, 2015.

[11] J. Schröder, M. Labusch, and M.-A. Keip. Algorithmic two-scale transition for magneto-electro-mechanically coupled problems - FE^2-scheme: Localization and Homogenization. *Computer Methods in Applied Mechanics and Engineering*, 302:253–280, 2016.

[12] N.A. Spaldin and M. Fiebig. The Renaissance of Magnetoelectric Multiferroics. *Science*, 309:391–392, 2005.

⇒ TABLE OF CONTENTS

DIELECTRIC EFFECTS IN PEROVSKITE SOLAR CELL ABSORBERS

Doru C. Lupascu[1], Irina Anusca[1], Sergejus Balčiūnas[2], Pascale Gemeiner[3], Šarūnas Svirskas[2], Christian Fettkenhauer[1], Jaroslavas Belovickis[2], Vytautas Samulionis[2], Maksim Ivanov[2], Brahim Dkhil[3], Juras Banys[2], and Vladimir V. Shvartsman[1]

[1] Institute for Materials Science and Center for Nanointegration Duisburg-Essen (CENIDE),
University of Duisburg-Essen, Universitätsstrasse 15, 45141 Essen, Germany

[2] Faculty of Physics, Vilnius University, Sauletekio 9/3, LT-10222 Vilnius, Lithuania

[3] Laboratoire Structures, Propriétés et Modélisation des Solides, CentraleSupélec, CNRS-UMR8580
Université Paris-Saclay, Bâtiment G. Eiffel, 3 rue Joliot Curie, 91190 Gif-Sur-Yvette, France

Abstract. *The markedly exceptional performance of solar cells based on the hybrid perovskite absorbers of ABX_3 type, with A being the methylammonium ion, B lead, and X iodine or mixtures with bromine, has brought up the question why this performance is so outstanding. We here summarize the effects of dielectric contributions to charge carrier screening and the resultant high mobility of these species yielding an unprecedented mobility of charges in highly defect-loaded lattices. Previously discussed ferroelectric effects can be excluded according to our study.*

1 Introduction †

All solar cells contain an absorbing semiconductor. In this semiconductor the incident light is absorbed and a charge pair, the exciton, is formed. This exciton must split up into the two single charge carriers, namely an electron in the conduction band and a hole in the valence band, in order to be able to generate an externally available electric energy. This split-up necessitates thermal excitation to overcome the binding energy (Equation 1 in the case of the Wannier-exciton) and a driving force to actually separate the charge carriers geometrically. In the case of classical *pn*-junction cells (two adjacent doped semiconductors of same basic material and thus same band structure) the driving force for charge separation is the internal electric field at the junction of the two doped semiconductors. This field itself emerges from a finite diffusion process that is the equilibrium state between a diffusion and a drift current of the dopant carriers at the junction itself [2]. Heterojunction cells, on the other hand, contain at least two adjacent semiconductors of appropriately chosen *different* band structures. The charge carrier then enters the relevant semiconductor of lower or higher energy band edge value for the electron / hole, respectively.

$$\boldsymbol{E_n = -\frac{m_r^2 e^4}{8h^2\varepsilon_0^2\varepsilon_r^2}\frac{1}{n^2}} \qquad (1)$$

As can be seen in the explicitly known binding energy of the case of the Wannier exciton (Eq. 1), this energy inversely depends on the square of the relative dielectric permittivity $\boldsymbol{\varepsilon_r^2}$. Thus, a host material of high dielectric constant will facilitate charge separation enormously. In the case of silicon, this value is $\varepsilon_r = 11$ and the moderate field at a typical *pn*-junction can easily separate the charge carriers. In organic solar cell materials, this is much more difficult, because their dielectric constant ranges around 2-3. We here show, that methylammonium lead halides exhibit a very high dielectric constant over a very broad frequency range easily facilitating exciton break-up. Furthermore, the same high dielectric constant electrically screens structural defects in the lattice making them

---

[*] Corresponding author: Doru C. Lupascu (doru.lupascu@uni-due.de)

† This abstract is an abbreviated version of reference [1]. Certain text passages and especially figure captions are equal.

ineffective as charge carrier traps for the passing electronic carriers. Thus, despite the very high ionic defect density, the methylammonium lead halides provide excellent charge carrier mobility.

2 Experimental Results

We grew numerous single crystals from different solutions up to several mm edge lengths. These samples were electroded and then subjected to low voltage electric loading. Dielectric spectroscopy was then applied using different methods. For more details refer to [1].

Figure 1 shows the low temperature phase transition of the three methylammonium lead halides as reflected in their dielectric response. The first order character of the phase transition can be well seen in the temperature hysteresis of the transition (Fig. 1 a). The inverse of dielectric constant is typically linear with temperature, if a Curie-Weiss law applies, which is typical for ferroic phase transitions. Figure 1b shows that the intercepts of the tangents to this reverse dielectric constant arise at negative temperatures which is a typical signature of transitions into antipolar low temperature structures. As we showed elsewhere, no ferroelectric hysteresis can be observed even in the low temperature phase. So the antipolar structure appears to be the reasonable assumption. As we were not able to apply very high electric fields, it is not clear whether the antipolar structure will also be antiferroelectric, because no switching could be induced at moderate fields.

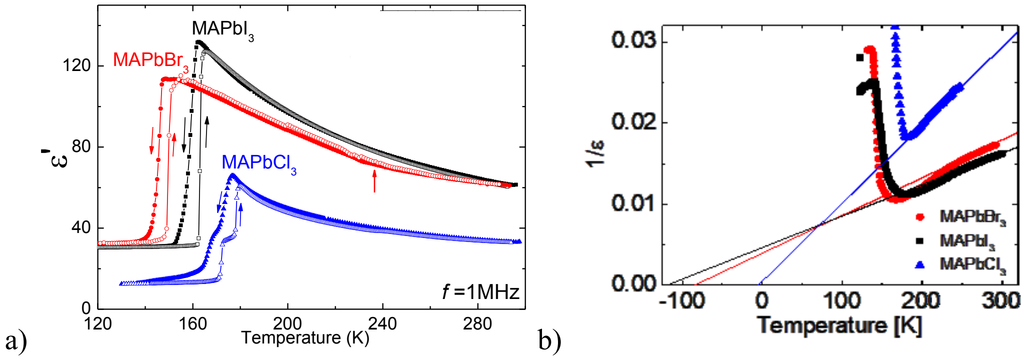

Figure 1†: Dielectric constant around the ordering temperature into the antipolar orthorhombic low temperature phase. © Wiley.

Figure 2 shows the dielectric response derived from impedance spectroscopy using Equation 2.

$$\varepsilon^* = \varepsilon_\infty + \frac{\Delta\varepsilon}{1+(i2\pi f\tau_c)^{1-\alpha}} \qquad (2)$$

It is clearly visible that the low temperature phase transition is frequency dependent (Fig. 2a). The corresponding frequency dispersion is shown in Fig. 2b. Even at 5 * 10^{10} Hz the dielectric constant is still around $\boldsymbol{\varepsilon_r = 30}$. Thus any mechanism in the cell evolving on a timescale of 50 ps still encounters high dielectric response and only in the infrared a transition to refractive index values around 3 corresponding to ~~d~~ $\boldsymbol{\varepsilon_r = 10}$ arises.

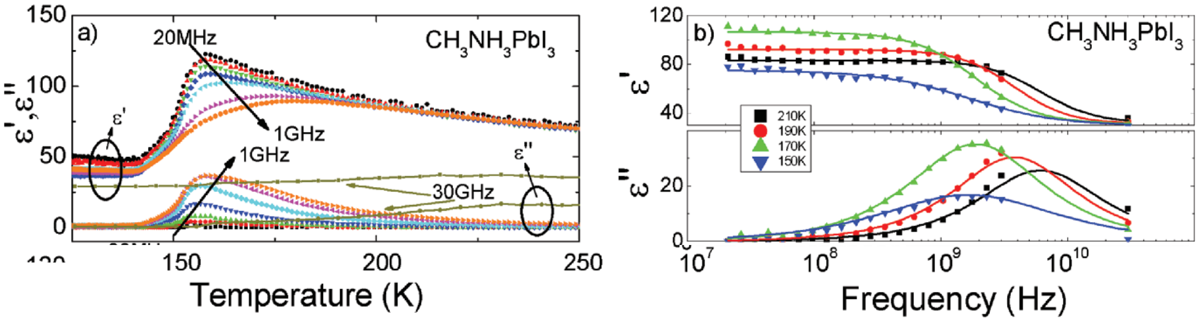

Figure 2†: Dielectric dispersion of $CH_3NH_3PbI_3$. © Wiley.

⇒ TABLE OF CONTENTS

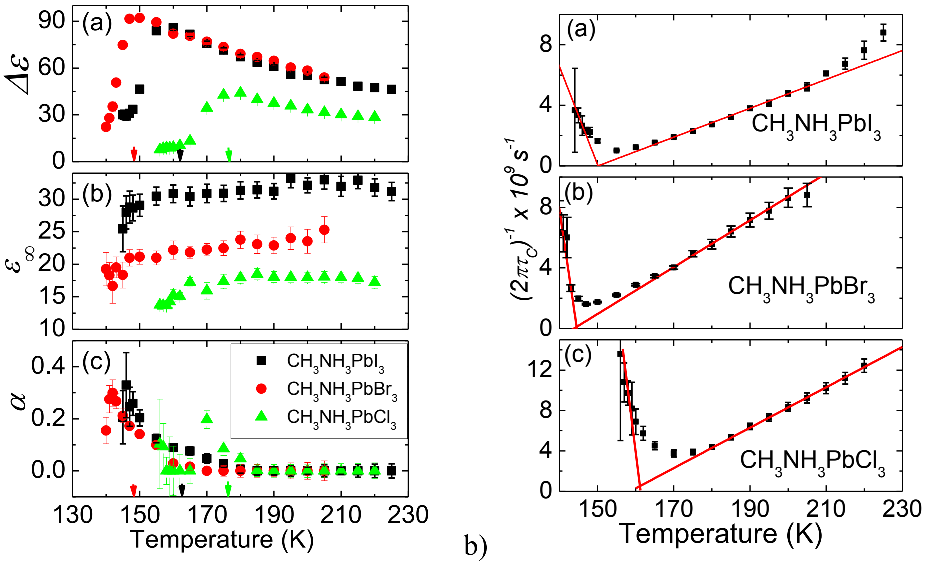

a) b)

Figure 3†: Left: Temperature dependences of the best Cole-Cole fit parameters: (a) relaxation strength, (b) high-frequency permittivity, and (c) exponent α. Right: Temperature dependences of the Cole-Cole relaxation time for (a) CH$_3$NH$_3$PbI$_3$ and (b) CH$_3$NH$_3$PbBr$_3$ single crystals and (c) CH$_3$NH$_3$PbCl$_3$ poly-crystal. Solid lines show the best fit to the equation $\tau_C \sim \frac{1}{T - T_0}$. © Wiley.

Figure 3 displays the jump in dielectric constant (relaxation strength) at the low temperature phase transition and the inverse relaxation time constants.

3 Discussion

From our data we conclude that screening of static defects like ionic vacancies is very effective in the methylammonium lead halides. Dielectric constants around $\varepsilon_r = 60$ are encountered. Thus, charge carrier screening, which is simply provided by Coulombs law (Equation 3), is very strong.

$$\mathbf{F} = \frac{\mathbf{1}}{\mathbf{4\pi\varepsilon_0\varepsilon_{stat}}}\frac{\mathbf{Q_{defect}\cdot q}}{\mathbf{r^2}} \qquad (3)$$

Typical screening length is then on the order of one to two unit cells extension from the defect.

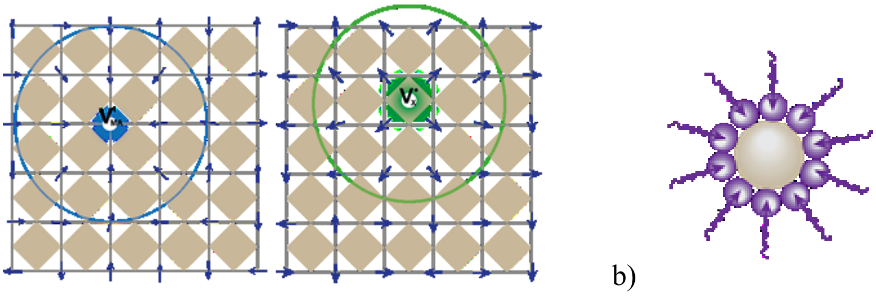

a) b)

Figure 4†: (a) Orientation of MA-dipoles around a vacancy (analogous to electronic defects [13]). Beyond the sketched kT-radius all MA+-dipoles are disordered among their 12 permitted orientations. Their projections onto this plane (MA-X-plane) lie along the unit cell edges. The underlying octahedra (in the Pb-X-plane) are shown to illustrate the dipole positions. (b) Screening of charged particles by polar molecules in a dispersion of analogous screening structure. © Wiley.

For mobile carriers, similar screening arises. From the frequency dependence of the dielectric constant we conclude that two contributions arise in the dielectric screening, the classical well known Fröhlich-polaron and a second contribution the micellon. This type is a new quasi-particle. It arises as a reorientation state of the methylammonium dipoles in the structure as illustrated in Figure 5. Both contributions have different frequency characteristics and thus permit to screen the mobile large polaron from different dynamics of the surrounding. We could thus show that the large polaron suggested by Zhu and coworkers exists [3]. As we could not observe any ferroelectric hysteresis and none of the observed phase transitions suggest ferroelectric but rather antipolar ordering, we *exclude* the ferroelectric state, which was suggested by Frost and co-workers as the major help for charge mobility in these materials [4].

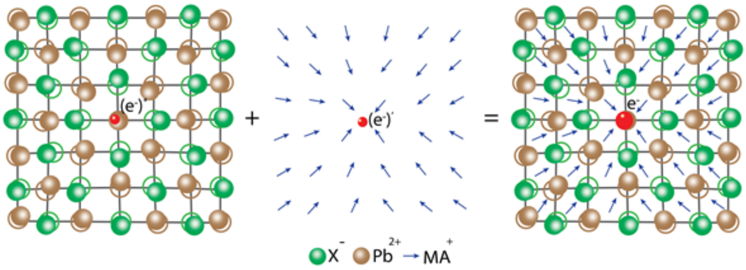

Figure 5†: Artistic illustration of the Fröhlich (lattice) polaron (left), micellon (center), and the resulting hyper-polaron (right). Effectively, one electron is fully screened by both mechanism (right), so partial electronic charge is matching either polarization mechanism summing up to one screened charge entity: (e-)* + (e-)' = e-. © Wiley.

4 Conclusion

We found that the methylammonium lead halides exhibit exceptionally high dielectric constants up to very high frequencies and in a broad temperature range across several phase transitions. The dielectric structure at low temperature (beneath 170K) is antipolar while at higher temperature fluctuating regimes dominate. No signature of ferroelectricity was found.

REFERENCES

[1] I. Anusca, S. Balciunas, P. Gemeiner, M. Sanalialp, G. Lackner, C. Fettkenhauer, J. Belovickis, V. Samulionis, M. Ivanov, B. Dkhil, J. Banys, V.V. Shvartsman, and D.C. Lupascu. Dielectric Response: Answer to Many Questions in the Methylammonium Lead Halide Solar Cell Absorbers, *Advanced Energy Materials*, 7: 1700600, 2017.

[2] Jenny Nelson, *The Physics of Solar Cells*, Imperial College Press, London, 2003.

[3] X.-Y. Zhu, and V. Podzorov, Charge carriers in hybrid organic−inorganic lead halide perovskites might be protected as large polarons, *The Journal of Physical Chemistry Letters,* 6: 4758−4761, 2015.

[4] J.M. Frost, K.T. Butler, and A. Walsh, Molecular ferroelectric contributions to anomalous hysteresis in hybrid perovskite solar cells, *APL Materials,* 2: 081506, 2014.

⇒ TABLE OF CONTENTS

DOMAIN EFFECTS IN NANOSCALE MULTIFERROIC HETEROSTRUCTURES

Peng Lv and Christopher S. Lynch[1,2]

[1] University of California Los Angeles

Mechanical and Aerospace Engineering, Engineering 4

Los Angeles, CA 90095

[2] University of California Riverside (July 1, 2018)

Abstract.

The NSF nanoscale engineering research center Translational Applications of Nanoscale Multiferroic Systems (NSF-TANMS) is focused on the development of nanoscale multiferroic heterostructures. Finite elements based computational tools have been developed capable of modeling piezoelectrically generated strain coupled to magnetostrictive behavior at the sub-micron scale. Although FEM based design tools for magnetoelectric heterostructures are now available, a number of research challenges remain; for example, obtaining a homogeneous strain field at the nanoscale. Relaxor single crystals of PMN-xPT have been used as a strain generating substrate to explore the ability to control magnetostriction at the nanoscale. The [011] cut produces a biaxial surface strain state but the magnetic behavior of the heterostructures has been inconsistent. Mapping the strain across the surface of the crystals at the micron scale has indicated that the surface strain is inhomogeneous. This has been hypothesized to be the result of domain structure in the ferroelectric crystals. A phase field model developed for relaxor rhombohedral ferroelectric single crystals is being used to gain insight into the strain inhomogeneity, yet the phase field results have not produced the inhomogeneous strain field. The explanation for the observed strain inhomogeneity may be nanopolar regions in relaxors, or possibly spatial compositional inhomogeneity in the crystals that have not yet been incorporated in the phase field models.

Introduction

Magnetoelectricity has a long history that has led up to our current work on strain mediated magnetoelectric heterostructures. Feibig, in a CISM lecture [1], provided a historical review of the development of multiferroics that is briefly summarized here. The first discussion of possible coupling between polarization and magnetization in the context of coupled constitutive laws was by P. Curie in 1894 [2]. In 1926, P. Debye introduced the term magnetoelectric to describe this effect[3]. In 1957, Landau and Lifshitz showed that the magnetoelectric effect can only occur in time-asymmetric materials and predicted the effect in chromium [4]. This was first observed by Astrov (electric field induced magnetization change) [5] and by Folen, Rado, and Stalder (magnetic field induced polarization change in 1960-61 [6]. The intrinsic magnetoelectric effect is small, on the order of a few to a few hundred pT/Vm^{-1}. In 1972 van Suchtelen described composites with product properties where the product of the electro-mechanical and the magneto-mechanical coupling in each constituent gives rise to magneto-electric coupling [7]. Around the year 2000, research on composite strain

---

[*] Corresponding author: First Co. Author (name@e-mail.adress)

mediated multiferroics gained momentum when Ryu made a layered composite of Terfenol-D and PZT [8]. A large number of publications on magnetoelectric composites followed. In 2004, Zheng et. al. introduced self assembled nanocomposites with nanopillars of $BaTiO_3$ and $CoFe_2O_4$ [9]. Soon after this, research attention began to focus on multiferroic heterostructures [10, 11] and the NSF-TANMS NERC was formed. This ERC emphasizes multiferroics at the nanoscale where size, shape, and strain have significant effects on the magnetic behavior.

Design and Fabrication of Heterostructures

One of the first challenges of the NERC was to strain individual magnetostrictive islands on a substrate material. This is generally very difficult because the deposition of a piezoelectric layer on a substrate such as a Si wafer results in the piezoelectric being clamped in-plane. Releasing the piezoelectric to drive the magnetostrictor requires a complex physical structure requiring multiple layer deposition and etching. A simpler to fabricate approach was developed, using edge effects near electrode edges [12]. Figure 1 shows how patterned electrodes can be used to produce a highly localized strain field using a PZT plate. This produces the ability to induce soft and hard directions in magnetic Ni.

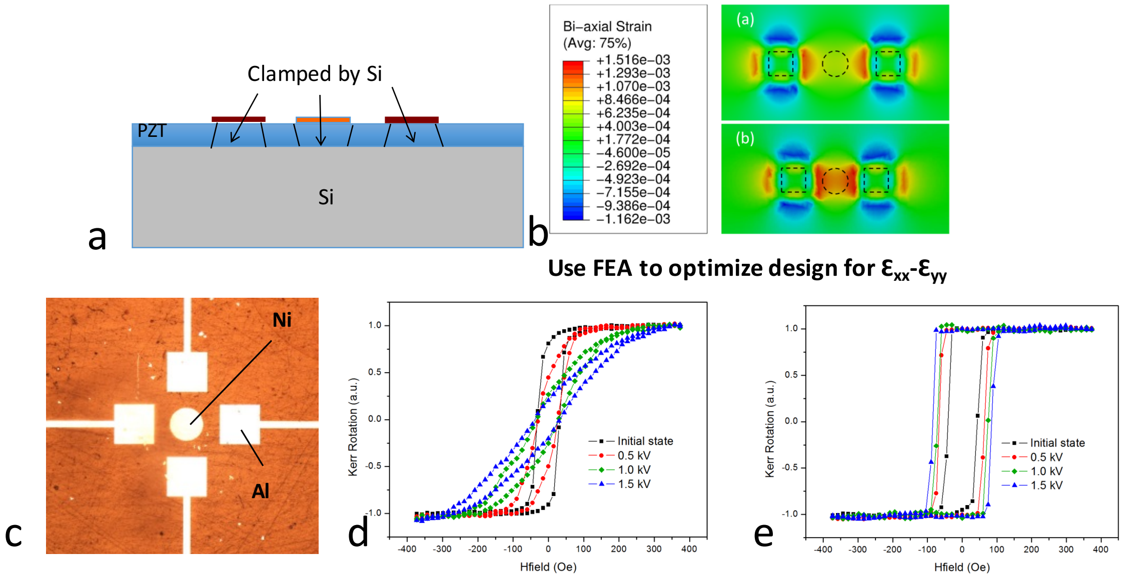

Use FEA to optimize design for ε_{xx}-ε_{yy}

Design and fabricate structure

Figure 1. a) Clamping effect of PZT on Si. b) FEA used to find electrode spacing capable of producing strain in the thin film. c. Electrodes and Ni on PZT plate (mm scale). d. e. Strain induced hard and soft directions.

After demonstration at the millimeter scale, structures were produced on sol gel deposited PZT. Figure 2 demonstrates that this approach works at the micron scale where MFM was used to observe the effect of the strain on the “onion” state [13]. Note the motion of the magnetic pole in the figure at the lower left.

⇒ TABLE OF CONTENTS

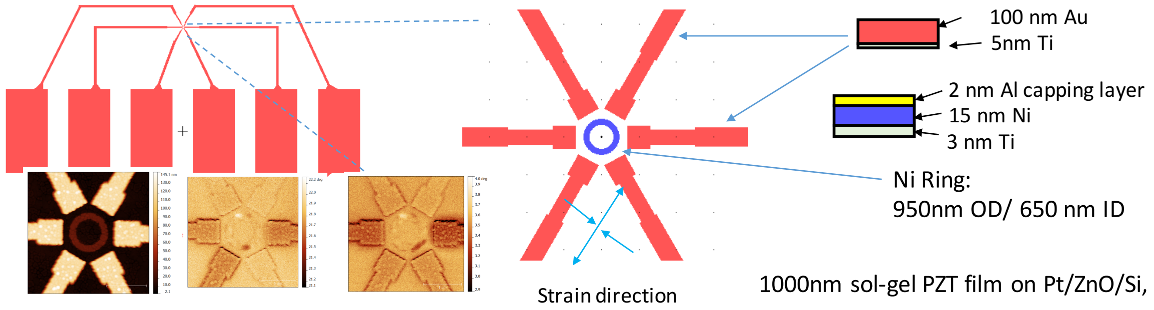

Figure 2. a) Patterned electrodes on sol gel PZT on a Si substrate

Single crystals of [011] cut relaxor rhombohedral ferroelectric PMN-xPT (28<x<32) have been used to test the response of magnetoelectric heterostructues, but the results have been inconsistent. This is apparent when arrays of magnetoelectric heterostructures are fabricated, magnetically initialized, and subjected to strain. Not all of the elements give the same response. After extensive investigation of possible issues with the magnetostrictive heterostructures, it was found that the single crystals were producing an inhomogeneous surface strain at the micron and smaller scale [14]. This inhomogeneity in the strain field produced by the PMN-xPT crystals is currently being explored using a phase field model recently developed for the rhombohedral crystals.

The phase-field method applied to ferroelectric materials is based on polarization as an order parameter and the time-dependent Ginzburg-Landau (TDGL) equation governing evolution of the order parameter. Chen et al applied a semi-implicit Fourier-spectral method [15] to phase-field modeling of ferroelectric domain formation in three-dimensional space [16] and domain structures in ferroelectric thin films [17]. Zhang and Bhattacharya used a finite difference framework [18] whereas Schrade et al [19] implemented a phase field model in a finite element framework as did Su and Landis [20].

Most phase field modeling has addressed materials with a tetragonal structure such as $BaTiO_3$, $PbTiO_3$ and certain compositions of PZT with high Ti content because an energy function was not available for rhombohedral phase relaxor-PbTiO3 single crystals. Lv and Lynch developed a 10th order Landau-Devonshire energy function for rhombohedral PIN-PMN-PT single crystals [21]. Results of implementation of this energy function in a phase field model are presented here.

In the phase field model, the total free energy density of the system is written as the sum of the Landau-Devonshire energy, gradient energy, elastic energy and electrical energy, Eq. (1).

$$f = f_{\text{L-D}} + f_{\text{grad}} + f_{\text{elas}} + f_{\text{elec}} \quad (1)$$

The 10th order polynomial used for the Landau-Devonshire energy is given by Eq. (2).

$$\begin{aligned} f_{\text{L-D}} &= \alpha_1\left(p_y^2+p_z^2\right)+\frac{1}{2}\alpha_{11}\left(2p_y^4+p_z^4\right)+\frac{1}{4}\alpha_{12}\left(4p_y^2p_z^2+p_z^4\right)+\frac{1}{4}\alpha_{111}\left(4p_y^6+p_z^6\right) \\ &+\frac{1}{4}\alpha_{112}\left(4p_y^4p_z^2+p_z^6+2p_y^2p_z^4\right)+\frac{1}{4}\alpha_{123}p_y^2p_z^4+\frac{1}{8}\alpha_{1111}\left(8p_y^8+p_z^8\right) \\ &+\frac{1}{8}\alpha_{1112}\left(2p_y^2p_z^6+p_z^8+8p_y^6p_z^2\right)+\frac{1}{16}\alpha_{1122}\left(8p_y^4p_z^4+p_z^8\right) \\ &+\frac{1}{4}\alpha_{1123}\left(p_y^4p_z^4+p_y^2p_z^6\right)+\frac{1}{16}\alpha_{11112}\left(2p_y^2p_z^8+p_z^{10}+16p_y^8p_z^2\right) \\ &+\frac{1}{16}\alpha_{11223}\left(4p_y^4p_z^6+p_y^2p_z^8\right)+\frac{1}{8}\alpha_{11123}\left(2p_y^6p_z^4+p_y^2p_z^8\right) \end{aligned} \tag{2}$$

The coefficients are from reference [21] and temperature was set to 25°C for α1.

The gradient energy is given by Eq. (3).

$$f_{\text{grad}}=\frac{1}{2}G\left(p_{y,y}^2+p_{z,z}^2+p_{y,z}^2+p_{z,y}^2\right) \tag{3}$$

The gradient energy affects the domain wall thickness, which is proportional to the square root of G [20].

The elastic energy is given by Eq. (4).

$$f_{\text{elas}}=\frac{1}{2}C_{ijkl}\varepsilon_{ij}^{\text{el}}\varepsilon_{kl}^{\text{el}} \tag{4}$$

The superscript "el" is used to represent the elastic components of the strain tensor. Here the elastic stiffness tensor C_{ijkl} has the same symmetry as the high temperature cubic phase. The three independent components are C_{11} = 12x10^{10}N/m2, C_{12} = 10x10^{10}N/m2 and C_{44} = 6x10^{10}N/m^2. These values are estimated based on the measurements [22]. Standard tensor and matrix notations are used for the elastic constants.

The nonzero elastic strain components were calculated using the displacement components u_y and u_z and the eigenstrain produced by the polarization as indicated by Eq. (5).

$$\begin{aligned} &\varepsilon_{yy}^{\text{el}}=u_{y,y}-\varepsilon_{yy}^0 && \varepsilon_{yy}^0=\left(Q_{13}p_z^2+Q_{33}p_y^2\right) \\ &\varepsilon_{zz}^{\text{el}}=u_{z,z}-\varepsilon_{zz}^0 && \varepsilon_{zz}^0=\frac{1}{2}\left(Q_{13}+Q_{33}+Q_{44}\right)p_z^2+Q_{13}p_y^2 \\ &\varepsilon_{yz}^{\text{el}}=\frac{1}{2}\left(u_{y,z}+u_{z,y}\right)-\varepsilon_{yz}^0 && \varepsilon_{yz}^0=Q_{44}p_yp_z \end{aligned} \tag{5}$$

where the eigenstrain is given by Eq. (6)

$$\begin{aligned} &\varepsilon_{11}^0=Q_{33}P_1^2+Q_{13}P_2^2+Q_{13}P_3^2 && \varepsilon_{23}^0=Q_{44}P_2P_3 \\ &\varepsilon_{22}^0=Q_{13}P_1^2+Q_{33}P_2^2+Q_{13}P_3^2 && \varepsilon_{13}^0=Q_{44}P_1P_3 \\ &\varepsilon_{33}^0=Q_{13}P_1^2+Q_{13}P_2^2+Q_{33}P_3^2 && \varepsilon_{12}^0=Q_{44}P_1P_2 \end{aligned} \tag{6}$$

The electrostrictive coefficients Q_{33} = 0.066m^4/C^2, Q_{13} = -0.032m^4/C^2 and Q_{44} = 0.023m^4/C^2 are taken from reference [21].

The electrical energy has two contributions, one from the material, and the other from the free space occupied by the material, Eq. (7).

$$f_{\text{elec}} = -E_y p_y - E_z p_z - \frac{1}{2}\kappa_0\left(E_y^2 + E_z^2\right) \tag{7}$$

where E_y and E_z are the electric field components along y and z axes, and κ_0 is the permittivity of free space.

The temporal evolution of the polarization is described by the TDGL equations. In the 2D system, they are expressed as Eq. (8)

$$\begin{aligned}\beta \dot{p}_y &= \left(\frac{\partial f}{\partial p_{y,y}}\right)_{,y} + \left(\frac{\partial f}{\partial p_{y,z}}\right)_{,z} - \frac{\partial f}{\partial p_y}\\ \beta \dot{p}_z &= \left(\frac{\partial f}{\partial p_{z,y}}\right)_{,y} + \left(\frac{\partial f}{\partial p_{z,z}}\right)_{,z} - \frac{\partial f}{\partial p_z}\end{aligned} \tag{8}$$

Mechanical equilibrium and Gauss' law are given by Eq. (9)

$$\begin{aligned}\sigma_{ij,j} &= 0\\ D_{i,i} &= 0\end{aligned} \tag{9}$$

The TDGL equation, mechanical equilibrium and electric Gauss law are solved simultaneously in the fully coupled phase-field model.

RESULTS

The energy function defines the energy density as a function of the three components of the magnitude and direction of the polarization vector. Preliminary simulations indicated that the polarization remained almost entirely within a set of {110} planes. This led to the significantly less computationally intensive approach of restricting the polarization to a single {110} plane as shown in Figure 3.a and performing two dimensional simulations using quasi-periodic boundary conditions. The polarization was defined in terms of py and pz as indicated in Figure 3.b.

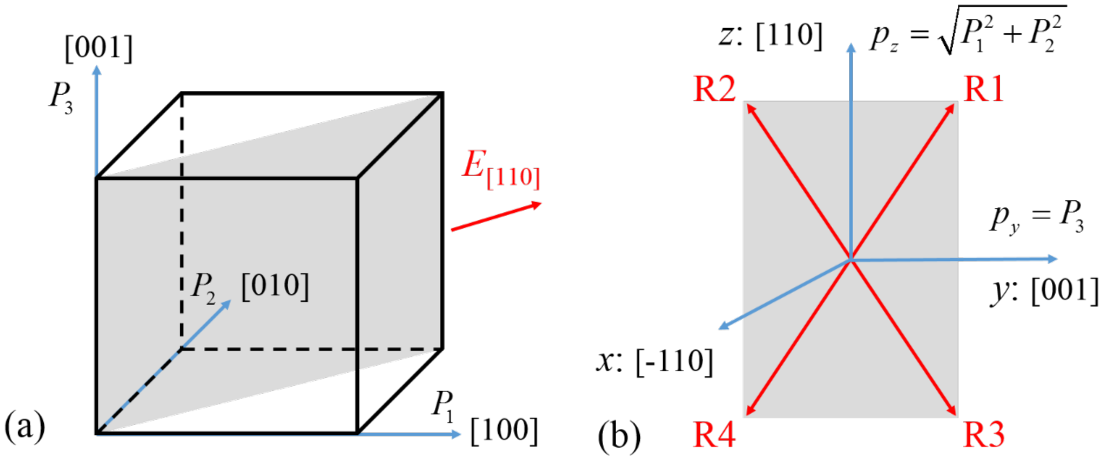

⇒ TABLE OF CONTENTS

Figure 3. a) The polarization is defined in a cubic coordinate system and b) the components are redefined in terms of a coordinate system in a {011} plane.

The polarization of each element in the simulation is initially near zero with an imposed random noise term as indicated in Figure 4.a. This is allowed to evolve, resulting in a domain structure as seen in Figure 4.b-h. The element size is set to 10% of the intrinsic length scale which is governed by the gradient energy term and the Landau Devonshire energy.

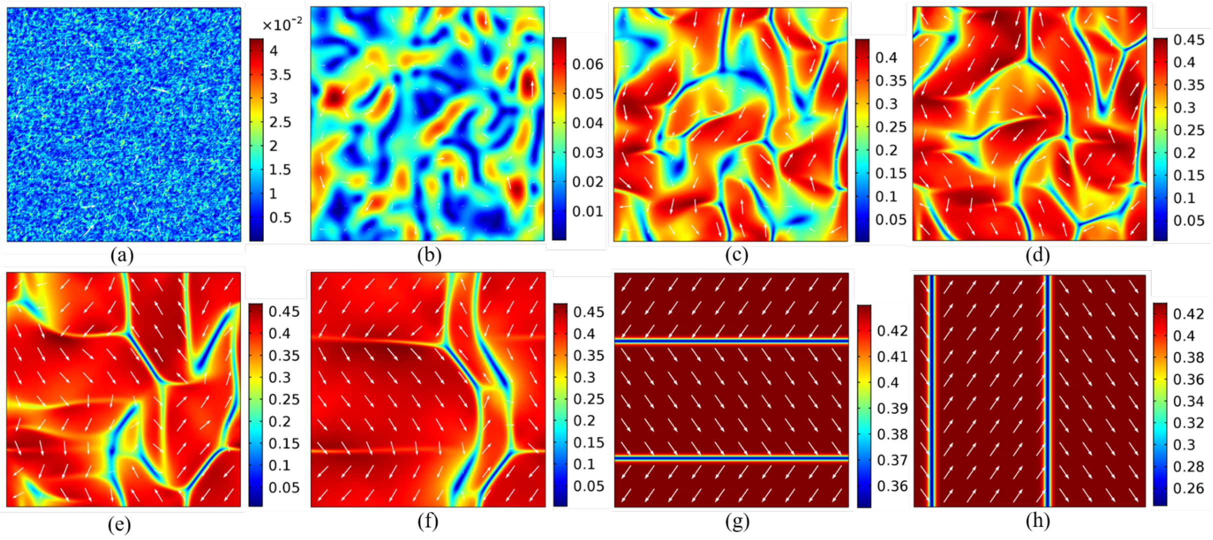

(a) (b) (c) (d)

(e) (f) (g) (h)

Figure 4. a-h Evolution of domain structure from an initially near zero polarization with a superimposed random term.

After the material was poled, the polarization reorientation process was investigated by cycling the electric field. This produced hysteresis loops as show in Figure 5. Although these have the right shape, the TDGL equation represents a viscous type behavior. This results in a coercive field that is dependent on the rate at which the electric field is applied. There is an upper bound where homogeneous switching occurs, but a domain wall will move even at very low applied field levels without the pinning effects of defects or intersection with other domains.

⇒ TABLE OF CONTENTS

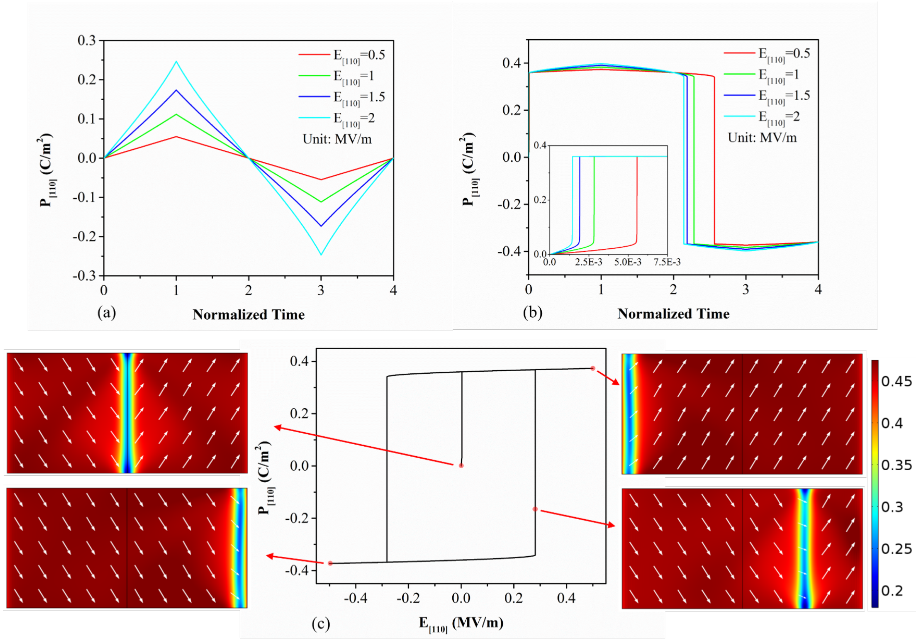

Figure 5. Given an initial domain structure and the polarization fixed at the left and right sides to maintain a domain wall in the simulation, a) the electric field was cycled with different amplitudes b) the polarization changed with time as the domain wall moved left – right, and c) a P-E loop is shown with the domain wall location indicated at several locations around the P-E loop.

DISCUSSION

When magnetoelectric heterostructures are fabricated on {011} cut and poled PMN-32PT, they do not all behave in the same way. Some behave as predicted by Landau Lifshitz Gilbert (LLG) based phase field simulations, but there is a lot of inconsistency. These magnetostrictive heterostructures are on the top surfaces of the domain structures shown in Figure 5. Whether the polarization is up or down, the in-plane component of the spontaneous strain has little variation, and when fully poled th strain on that surface is uniform. This has led us to postulate that it is not likely that domain walls of the type shown in Figure 5 intersecting the surface are causing the inhomogeneous strain. Rather, it is more likely that there is a laminar structure of R1 and R2 type domains layered out-of-plane when the material is fully poled. This suggests that it might be possible to achieve a plate with only R1 type domains by either cutting the crystal at an angle to give preference to R1 domain formation, or by first poling the plate in-plane and then out-of-plane to populate the R1 domains. This is ongoing work.

REFERENCES

[1] Ferroic Functional Materials, Springer2018.

[2] P. Curie, Sur la symétrie dans les phénomènes physiques, symétrie d'un champ électrique et d'un champ magnétique, J. Phys. Theor. Appl. 3(1) (1894).

[3] P. Debye, Bemerkung zu einigen neuen Versuchen über einen magneto-elektrischen Richteffekt, Zeitschrift für Physik 36(4) (1926) 300-301.

[4] Landau and Lifshitz, Electrodynamics of Continuous Media, Pergamon, Oxford, 1960.

[5] D.N. Astrov, J. Exptl. Teor. Fiz. 38(984) (1960).

[6] J. Folen and E. W. Stalder, Phys Rev Lett 6 (1961).

⇒ TABLE OF CONTENTS

[7] J. van Suchtelen, Product Properties: A New Application of Composite Materials, Phillips Research Reports 27(1) (1972).

[8] J. Ryu, A. V. Carazo, K. Uchino, H.-E. Kim, Magnetoelectric Properties in Piezoelectric and Magnetostrictive Laminate Composites, Japanese Journal of Applied Physics 40(8R) (2001) 4948.

[9] W.J. Zheng H, Lofland SE, Ma Z, Mohaddes-Ardabili L, Zhao T, Salamanca-Riba L, Shinde SR, Ogale SB, Bai F, Viehland D, Jia Y, Schlom DG, Wuttig M, Roytburd A, Ramesh R., Multiferroic BaTiO3-CoFe2O4 Nanostructures, Science 303(5658) (2004).

[10] A.D. Rata, A. Herklotz, K. Nenkov, L. Schultz, K. Dörr, Strain-Induced Insulator State and Giant Gauge Factor of ${\mathrm{La}}_{0.7}{\mathrm{Sr}}_{0.3}{\mathrm{CoO}}_{3}$ Films, Physical Review Letters 100(7) (2008) 076401.

[11] C. Thiele, K. Dörr, O. Bilani, J. Rödel, L. Schultz, Influence of strain on the magnetization and magnetoelectric effect in, Physical Review B 75(5) (2007) 054408.

[12] J. Cui, J.L. Hockel, P.K. Nordeen, D.M. Pisani, C.-y. Liang, G.P. Carman, C.S. Lynch, A method to control magnetism in individual strain-mediated magnetoelectric islands, Applied Physics Letters 103(23) (2013) 232905.

[13] J. Cui, C.-Y. Liang, E.A. Paisley, A. Sepulveda, J.F. Ihlefeld, G.P. Carman, C.S. Lynch, Generation of localized strain in a thin film piezoelectric to control individual magnetoelectric heterostructures, Applied Physics Letters 107(9) (2015) 092903.

[14] R. Lo Conte, Z. Xiao, C. Chen, C.V. Stan, J. Gorchon, A. El-Ghazaly, M.E. Nowakowski, H. Sohn, A. Pattabi, A. Scholl, N. Tamura, A. Sepulveda, G.P. Carman, R.N. Candler, J. Bokor, Influence of Nonuniform Micron-Scale Strain Distributions on the Electrical Reorientation of Magnetic Microstructures in a Composite Multiferroic Heterostructure, Nano Letters 18(3) (2018) 1952-1961.

[15] L.Q. Chen, J. Shen, Applications of semi-implicit Fourier-spectral method to phase field equations, Computer Physics Communications 108(2) (1998) 147-158.

[16] H.-L. Hu, L.-Q. Chen, Three-Dimensional Computer Simulation of Ferroelectric Domain Formation, Journal of the American Ceramic Society 81(3) (1998) 492-500.

[17] Y.L. Li, S.Y. Hu, Z.K. Liu, L.Q. Chen, Effect of substrate constraint on the stability and evolution of ferroelectric domain structures in thin films, Acta Materialia 50(2) (2002) 395-411.

[18] W. Zhang, K. Bhattacharya, A computational model of ferroelectric domains. Part I: model formulation and domain switching, Acta Materialia 53(1) (2005) 185-198.

[19] D. Schrade, R. Mueller, B.X. Xu, D. Gross, Domain evolution in ferroelectric materials: A continuum phase field model and finite element implementation, Computer Methods in Applied Mechanics and Engineering 196(41) (2007) 4365-4374.

[20] Y. Su, C.M. Landis, Continuum thermodynamics of ferroelectric domain evolution: Theory, finite element implementation, and application to domain wall pinning, Journal of the Mechanics and Physics of Solids 55(2) (2007) 280-305.

[21] P. Lv, L. Wang, C.S. Lynch, A phenomenological thermodynamic energy function for PIN-PMN-PT relaxor ferroelectric single crystals, Acta Materialia 137 (2017) 93-102.

[22] E. Sun, W. Cao, W. Jiang, P. Han, Complete set of material properties of single domain 0.24Pb(In1/2Nb1/2)O3-0.49Pb(Mg1/3Nb2/3)O3-0.27PbTiO3 single crystal and the orientation effects, Applied Physics Letters 99(3) (2011) 032901.

STRESS-INDUCED PHASE TRANSITIONS IN LEAD-FREE FERROELECTRIC MATERIALS

Alexander Martin* and Kyle G. Webber

[1]Department of Materials Science, Friedrich-Alexander-Universität Erlangen-Nürnberg, 91058 Erlangen, Germany

Abstract. *In this presentation, the importance of mechanical stress on lead-free ferroelectric materials will be discussed. Each material displays different stress-induced phase transitions and, therefore, different ferroelastic behavior. At first, the ferroelectric-to-paraelectric transition will be explained on the example of barium titanate ($BaTiO_3$, BT). Here, closed stress-strain hysteresis loops are observed, which can have significant implications for the mechanical properties. The stress—induced relaxor to ferroelectric transition, which is found in polycrystalline $0.93(Na_{1/2}Bi_{1/2})TiO_3$-$0.07BaTiO_3$, will be discussed in the second part. Recent experimental investigations have shown a time- and rate-dependence in the mechanical response of this material during mechanical loading will be discussed. A stress-induced interferroelectric phase transition can be found in NKN-based materials around their orthorhombic-to-tetragonal phase transition temperature.*

1 Introduction

Due to electromechanical coupling, piezoelectric materials are used in various transducer applications, such as sensors and actuators. The primarily used materials are based on the lead zirconate titanate ($Pb(Zr_{1-x}Ti_x)O_3$, PZT) system [1]. However, governmental restrictions on the use of hazardous substances in electronic devices has lead to intensive research efforts to identify lead-free piezoelectric alternatives [1]. Candidates with the most potential are based on $BaTiO_3$ (BT) [2], $K_{0.5}Na_{0.5}NbO_3$ (KNN) [3], and $Na_{1/2}Bi_{1/2}TiO_3$ (NBT) [4].

The observation of the mechanical behavior is of importance, as domains can be switched by an applied electric field as well as by a mechanical stress through ferroelastic switching of domains. The latter can cause depolarization depending on the direction of the stress in regards to the polarization vector [5]. The critical coercive stress required to induce ferroelastic switching is crucial for the implementation of a material into various devices. In addition to depolarization, ferroelastic switching can also have a positive impact on the fracture toughness of these ceramics. Stresses at the crack tip can cause domain switching, thereby shielding the crack propagation and resulting in ferroelastic toughening [6,7]. In addition to influencing the domain structure, stress-induced phase transitions can also be observed in a variety of different materials. In regards to their ferroelastic behavior, closed hysteresis loops are measured in the vicinity of specific phase transitions temperatures. This behavior has significant implications for the mechanical properties, as ferroelastic toughening process occurs less around these phase transition temperatures. The increased coercive stress coupled with the low remanent strain, suggests reduced domain switching during crack formation and limited internal stresses from switched domains.

Thus, this presentation will provide a short overview of two different compositions and the effect of stress on their mechanical behavior.

2 Ferroelectric ↔ Paraelectric Transition in $BaTiO_3$

---

*Corresponding author: Alexander Martin (alexander.am.martin@fau.de)

Barium titanate isone of the most thoroughly investigated ferroelectric materials. Many experiments on single as well as polycrystalline BT have been conducted and published. One major drawback of BT, which limits implementation in many applications, is its relatively low Curie temperature (T_C = 130 °C) [8]. Nevertheless, researchers found new compositions with BT, such as $Na_{1/2}Bi_{1/2}TiO_3$-$xBaTiO_3$ (NBT-*x*BT) and $Ba(Zr_{0.2}Ti_{0.8})O3$-$x(Ba_{0.7}Ca_{0.3})TiO_3$ (BZT-*x*BCT), which display large electromechanical responses and are considered promising lead-free alternatives [2,4,9]. Besides the structural phase transition from a tetragonal (*P*4*mm*) to a cubic (*Pm*3*m*) crystal symmetry at 130 °C, BT also has a rhombohedral (*R*3*m*) to orthorhombic (*Amm*2) and orthorhombic to tetragonal transition at –90 °C and 0 °C, respectively. These values can be estimated via dielectric permittivity measurements as a function of temperature. By compressing the sample during such measurements, Schader *et al.* showed a shift of the ferroelectric to paraelectric transition to higher temperatures (Figure 1) [8]. These results suggested that the tetragonal phase is more stable under compression, which has further implications for the ferroelastic behavior. By compressing the material at temperatures higher than its T_C a closed hysteresis curve can be detected, as well as an increase and decrease of the coercive stress and remanent strain, respectively.

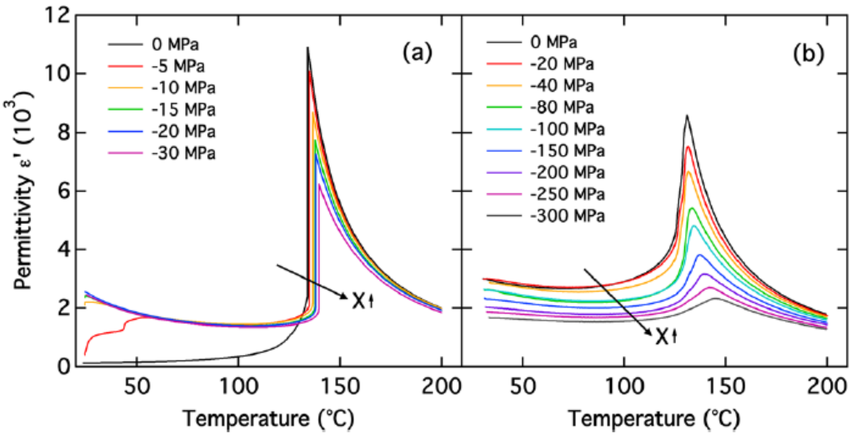

Figure 1: Permittivity of single crystal (a) and polycrystalline (b) BT as a function of temperature and compressive stress. The small signal dielectric measurements were performed at 1 kHz [8].

3 Relaxor → Ferroelectric Transition in $0.93(Na_{1/2}Bi_{1/2})TiO_3$-$0.07BaTiO_3$

Among the various NBT-based compositions, solid solutions of $(1\text{-}x)Na_{1/2}Bi_{1/2}TiO_3$-$xBaTiO_3$ (NBT-BT) have been the most widely investigated. This is due to the excellent large field strain response observed near the morphotropic phase boundary (MPB) that separates the ferroelectric rhombohedral (*R*3*c*) and ferroelectric tetragonal (*P*4*mm*) phases at a BT content of approximately 6 − 7 mol % at room temperature [10,11]. In addition, compositions around the MPB show an enhanced large field electromechanical coupling, which is understood to be due to an electric field-induced transformation from a relaxor state to long-range ferroelectric order [10,11]. Importantly, this relaxor-to-ferroelectric transition can also be induced with an external mechanical field [12].

Recent experimental investigations showed a significant rate-dependence of the mechanical response of polycrystalline $0.93(Na_{1/2}Bi_{1/2})TiO_3$-*0.07*$BaTiO_3$ during mechanical. The tests were performed over five orders of magnitude and revealed a substantial change in the critical RE-FE stress as well as remanent strain.

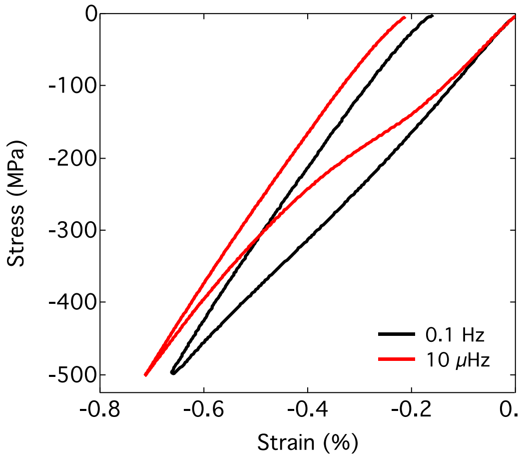

Figure 2. Representative rate-dependent stress-strain behavior of NBT-7BT.

4 Ferroelectric ↔ Ferroelectric Transition in ($Li_{0.06}Na_{0.47}K_{0.47}$)$NbO_3$

($Na_{0.5}K_{0.5}$)NbO_3 (NKN)-based lead-free piezoelectrics have drawn considerable scientific and industrial attention due to their attractive electromechanical properties, such as high acoustic vibration velocities, relatively high electromechanical coupling, high Curie temperature (T_C = 420°C), and low density[3]. Even though NKN-based materials have been studied since the 1950s, only under certain conditions have alkaline niobate-based materials shown comparable piezoelectric properties to those of PZT. One possibility to improve this deficiency is by doping NKN lead-free ceramics with Li, which shows significant improvement of the piezoelectric properties by shifting the orthorhombic (*Amm*2) to tetragonal (*P*4*mm*) phase transition temperature $T_{O\text{-}T}$ to room temperature [13].

In recent investigation, we revealed a nonlinear constitutive behavior around the $T_{O\text{-}T}$, which was consistent with a stress-induced phase transformation and ferroelastic domain switching. Figure 3 shows the changes of these measurements for $Li_{0.06}Na_{0.52}K_{0.42}NbO_3$ with several additives (LNKN6-a) at various temperatures. At 150 °C, this material showed a closed hysteresis loop, which is characteristic for a phase transformation. These results suggested a stress-induced tetragonal-to-orthorhombic phase transition.

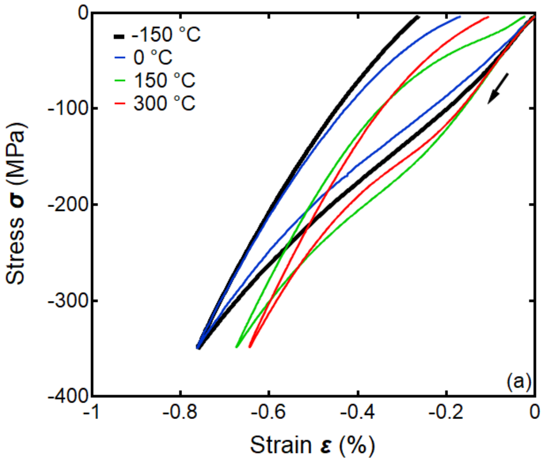

Figure 3. Representative stress-strain behavior at several temperatures of LNKN6-a.

⇒ TABLE OF CONTENTS

5 References

[1] J. Rödel, K.G. Webber, R. Dittmer, W. Jo, M. Kimura, and D. Damjanovic. Transferring lead-free piezoelectric ceramics into application, *J. Eur. Ceram. Soc.,* 35: 1659–1681, 2015.

[2] W. Liu, and X. Ren. Large piezoelectric effect in Pb-free ceramics, *Phys. Rev. Lett.,* 103: 1–4, 2009.

[3] S. Priya and S. Nahm, *Lead-free piezoelectrics*, Springer, New York, 2012.

[4] S.T. Zhang, A.B. Kounga, E. Aulbach, H. Ehrenberg, and J. Rödel. Giant strain in lead-free piezoceramics $Bi_{0.5}Na_{0.5}TiO_3$-$BaTiO_3$- $K_{0.5}Na_{0.5}Nb\ O_3$ system, *Appl. Phys. Lett.* 91: 10–13, 2007.

[5] S.C.I. Hwang, C.S. Lynch, and R.M. McMeeking. Ferroelectric/ferroelastic interactions and a polarization switching model, *Acta Metall. Mater.* 43: 2073–2084, 1995.

[6] J.L. Jones, and M. Hoffman. R-curve and stress–strain behavior of ferroelastic ceramics. *J. Am. Ceram. Soc.* 89: 3721–3727, 2006.

[7] C.M. Landis. On the fracture toughness of ferroelastic materials. *J. Mech. Phys. Solids.* 51: 1347–1369, 2003.

[8] F.H. Schader, E. Aulbach, K.G. Webber, and G.A. Rossetti. Influence of uniaxial stress on the ferroelectric-to-paraelectric phase change in barium titanate. *J. Appl. Phys.* 113: 1-9, 2013.

[9] M. McQuarrie, and F.W. Behnke. Structural and dielectric studies in the system $(Ba,Ca)(Ti,Zr)O_3$. *J. Am. Ceram. Soc.* 37: 539–543, 1954.

[10] G. Picht, J. Töpfer, and E. Hennig. Structural properties of $(Bi_{0.5}Na_{0.5})1\text{-}xBaxTiO_3$ lead-free piezoelectric ceramics. *J. Eur. Ceram. Soc.* 30: 3445–3453, 2010.

[11] C. Ma, H. Guo, S.P. Beckman, and X. Tan. Creation and destruction of morphotropic phase boundaries through electrical poling: A case study of lead-free $(Bi_{1/2}Na_{1/2})TiO_3$-$BaTiO_3$ piezoelectrics. *Phys. Rev. Lett.* 109: 1–5, 2012.

[12] F.H. Schader, Z. Wang, M. Hinterstein, J.E. Daniels, and K.G. Webber. Stress-modulated relaxor-to-ferroelectric transition in lead-free $(Na_{1/2}Bi_{1/2})TiO_3$-$BaTiO_3$ ferroelectrics. *Phys. Rev. B.* 93: 1–11, 2016.

[13] Y. Guo, K. Kakimoto, and H. Ohsato. Phase transitional behavior and piezoelectric properties of $(Na_{0.5}K_{0.5})NbO_3$-$LiNbO_3$ ceramics. *Appl. Phys. Lett.* 85: 4121–4123, 2004.

⇒ TABLE OF CONTENTS

Magnetoelectric Composites for Magnetic Field Measurements

Dirk Meyners[1,*], **Eckhard Quandt**[1]

[1] Institute for Materials Science, Inorganic Functional Materials, Faculty of Engineering, Kiel University
Kaiserstrasse 2, 24143 Kiel, Germany

Abstract. *Two different approaches to highly sensitive magnetic field sensors are discussed, i.e. magnetoelectric cantilevers and surface acoustic wave sensors. Both concepts are based on combining magnetostrictive and piezoelectric phases in bulk micromachined composites to generate a measurable electric voltage response to an external magnetic field. In the magnetoelectric cantilevers magnetostrictive strain produces mechanical stress in the piezoelectric layer. In presence of an alternating magnetic field, the cantilevers oscillate with the same frequency. At mechanical resonance highest sensitivities and a low limit of detection of the order of few pT/Hz*$^{1/2}$ *can be reached. The surface acoustic wave sensors comprise a piezoelectric substrate, two transducer electrodes and a magnetostrictive coating in between. Submitted to an external magnetic field, the wave propagation properties change due to the ΔE-effect. Using the resulting phase change as signal, a sensor with wide bandwidth can be realized. In both concepts, the control of magnetic domain activity plays a vital role in the reduction of sensor noise. Exchange coupled magnetostrictive multilayers are discussed as a new class of materials with large magnetic susceptibility and controlled magnetization reversal making them to promising candidates for the application in such sensor structures.*

1 Introduction

In the last decade research interest in magnetoelectric (ME) materials increased continuously [1]. Especially, composites consisting of magnetostrictive and piezoelectric constituents were investigated intensively [2, 3]. They offer the opportunity to optimize the magnetic and piezoelectric properties almost independently. As a result, the magnetoelastic coupling can be orders of magnitude larger than in single phase multiferroics. Several application scenarios have been proposed such as tunable microwave devices, memories and magnetic field sensors [2]. For the latter, the challenge is to provide a reasonably priced sensor, which can be operated at room temperature, offers a detection limit (LoD, limit of detection) below 1 pT/Hz$^{1/2}$ and a sufficiently wide bandwidth in a frequency range from DC to several kilohertz.

A promising candidate fulfilling the above mentioned requirements is seen in ME composites, in which the coupling is strain-mediated. As a measure of coupling strength in such composites, the ME voltage coefficient α_{ME} can be introduced:

$$\alpha_{ME} = \frac{\partial E}{\partial H} = \frac{1}{\epsilon_{ij}} \frac{\partial P}{\partial \sigma} \frac{\partial \sigma}{\partial \lambda} \frac{\partial \lambda}{\partial H} , \qquad (1)$$

with the following notations:

E:	electrical field	P:	electrical polarization
H:	magnetic field	σ:	mechanical stress
ε_{ij}:	permittivity	λ:	magnetostrictive strain.

---

[*] Corresponding author: dm@tf.uni-kiel.de

⇒ TABLE OF CONTENTS

Here, $\partial P/\partial\sigma$ and $\partial\lambda/\partial H$ denote the piezoelectric and the pseudo piezomagnetic coefficients of the two functional phases, whereas $\partial\sigma/\partial\lambda$ describes the mechanical coupling among those two. From a magnetic material's point of view, a large ME coefficient requires large saturation magnetostriction and susceptibility. In the following paragraph, sensors are considered based on FeCoBSi layers deposited by magnetron sputtering. These layers combine moderate saturation magnetostriction with soft magnetic properties.

Surface acoustic waves (SAW) have been broadly discussed in literature and several SAW devices have been implemented such as humidity, pressure and position sensors [4]. Interestingly, the use of SAW devices for the purpose of magnetic field sensing has attracted minor attention so far [5-7]. On the other hand, SAW sensors coated with a thin magnetostrictive layer have great potential to detect magnetic fields with high sensitivity and wide bandwidth. More details on this are provided in the third paragraph of this abstract.

2 Magnetostrictive multilayers for magnetoelectric cantilevers

Figure 1 summarizes the magnetoelectric characteristics of a bulk micromachined Si cantilever sensor with lateral dimensions of 25 mm in length (23 mm are freestanding), 2.2 mm in width and about 300 µm in thickness. The functional coating Ta 15/FeCoSiB 2970/Ta 15/Pt 150/AlN 1600/Cr 5/Au 100 [thickness in nm] was patterned by standard optical lithography. The FeCoSiB and the AlN layers work as magnetostrictive and piezoelectric phases, respectively. The other metals serve as seed and electrode layers. The magnetic anisotropy of the FeCoSiB was set in a temperature treatment with a magnetic field perpendicular to the long cantilever axis. Fig. 1a) shows the magnetoelectric voltage as a function of an externally applied AC magnetic field. The effect enhancement for a particular frequency about 876 Hz is clearly visible. At this frequency, mechanical resonance occurs and the ME voltage increases to 1 V/Oe. The voltage output and accordingly the ME coefficient also strongly depend on an optionally applied bias field as can be seen in Fig. 1b). The measurements in Fig. 1 a) and b) reveal the sensor's optimum working point with maximum ME response, i.e. optimum frequency and bias field. The need for a magnetic bias can be removed by introducing a tilted unidirectional anisotropy into the magnetostrictive phase [8].

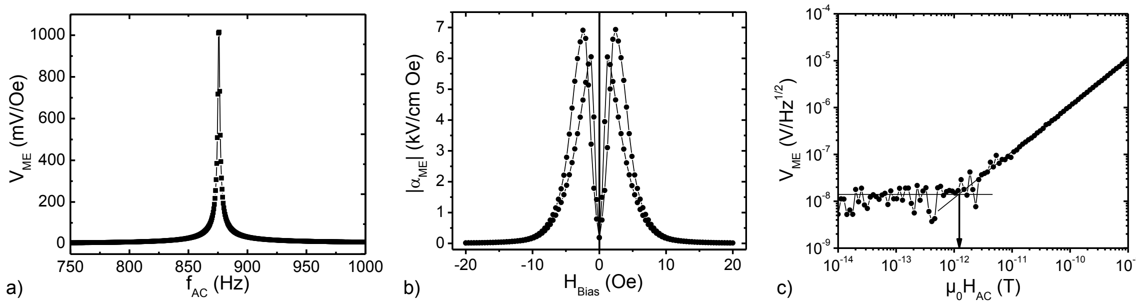

Figure 1: a) ME voltage recorded for an AC magnetic field H_{AC} = 1 mOe and a bias H_{Bias} = 2.4 Oe. b) Absolute value of the magnetoelectric coefficient for H_{AC} = 1 mOe at mechanical resonance. c) ME voltage versus H_{AC} at the optimum working point (H_{BIAS} = 2.4 Oe and f_{AC} = 876 Hz). Solid lines indicate linear fits of V_{ME} and the noise level. Their intersection determines the limit of detection (arrow). Adapted from [3].

At the optimum working point the sensors detection limit was determined by an ME voltage measurement inside an acoustically and magnetically shielded chamber (Fig. 1c)). For the resonant AC field, the LoD amounts to about 1 pT/Hz$^{1/2}$. Hence, simple ME cantilever sensors are capable of detecting small AC magnetic fields. However, the best LoD is only observed for a narrow frequency band close to the mechanical resonance frequency.

To overcome this limitation, magnetic frequency conversion (MFC) is a feasible solution [9]. Instead of a DC bias field, a strong modulating field is applied. Because of the non-linearity of the magnetostriction curve, the sensor acts as a frequency mixing device (Fig. 2a). In order to gain the ME response to a small AC field out of resonance, the frequency of the modulation field is chosen in such a way that the sum frequency equals the resonance frequency again.

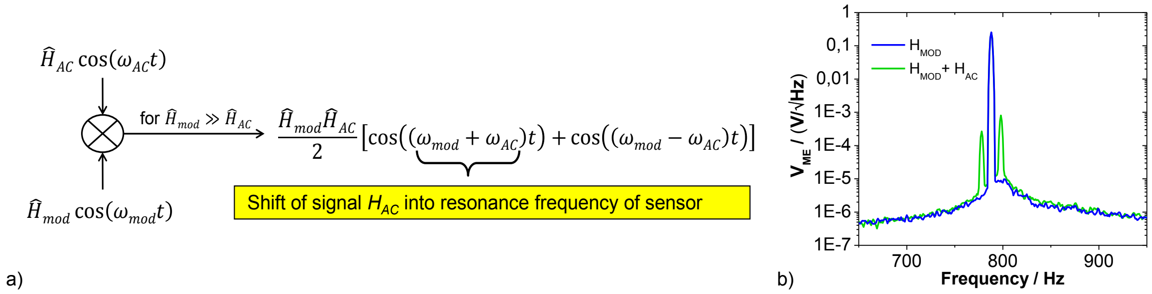

Figure 2: a) Concept of frequency mixing in presence of a modulating field H_{mod} and the desired signal H_{AC}. At the sensors terminals a spectrum can be detected containing sum and difference frequencies. This frequencies appear as upper and lower sidebands adjacent to the H_{mod} peak (3c).

By MFC the sensitivity of an ME cantilever sensor can be increased by more than three orders of magnitude. The detection limit for out of resonance signals can be improved as well, provided that additional sensor noise in presence of H_{mod} is avoided. Here, exchange coupled magnetostrictive multilayers show better performance than simple magnetostrictors based on single FeCoSiB layers. Details of the concept, fabrication issues, magnetic und and ME measurements are discussed during the presentation.

3 Surface acoustic wave sensors for magnetic fields

Compared to other approaches using surface acoustic waves (SAW) for detecting magnetic fields [4-6], this SAW magnetic sensor system benefits from a new technique to substantially increase the magnetoelastic coupling as described in [7]. This device uses so-called Love waves, i.e. shear horizontal acoustic surface waves that are guided in an amorphous SiO_x guiding layer, with an amorphous magnetostrictive FeCoSiB thin film as the sensing element on top. The velocity of the Love waves changes according to the magnetic field-induced change of the shear modulus, the so-called ΔE-effect that effects all elastic constants. The SAW sensor is operated in a delay line configuration at approximately 150 MHz and thus translates the magnetic field-induced velocity change into a corresponding phase shift.

The presented Love wave SAW magnetic field sensor uses a 500 µm ST-cut quartz substrate. The two IDT electrode are made of 300 nm thick Au in a double-finger structure of 25 pairs with a periodicity of 28 µm and a finger width of 3.5 µm. They form a delay line with a length of 3.8 mm. To excite only shear waves the propagation direction of the wave is orthogonal to the X-axis of the ST-cut quartz wafer. Using a PECVD process a 4.5 µm thick amorphous SiO_x film is deposited which covers the IDTs and the delay line and acts as a guiding layer resulting in a wave energy concentration at the surface of the device and thus in the magnetostrictive layer on top. This 200 nm thick amorphous FeCoSiB magnetostrictive layer is magnetron sputtered on the guiding layer in a magnetic bias field applied along the Y-axis and finally structured by a lift-off process. This configuration results in a maximum phase shift of 340°. From the slope of the measured phase a maximum sensitivity of approximately 500°/mT is obtained.

In order to obtain a low phase noise of the SAW sensor and thus a high signal-to-noise ratio, the readout circuit uses an inherent phase noise suppression. To achieve this, a low phase noise signal of a numerically controlled oscillator (NCO) at 50 kHz is transposed to the operating frequency range of the SAW magnetic field sensor and received using a floating local oscillator, which eliminates the phase noise of the local oscillator. The phase detection is achieved in the digital domain after analog-to-digital conversion. Further details are described in [7]. The measurements shows a phase noise level of 115 dBc/Hz$^{1/2}$ for a frequency of 10 Hz. At 10 Hz and 100 Hz a limit of detection (LoD) of 250 pT/ Hz$^{1/2}$ and 80 pT/ Hz$^{1/2}$ are achieved, respectively. The bandwidth is restricted to 50 kHz due to the frequency of the used NCO.

In biomagnetic applications the dynamic magnetic field range is of extreme importance. Any measurements without magnetic shielding would be based on differential measurements that allow to extract the biomagnetic signals from the million-times higher background. Thus, a dynamic range of at least 6 orders of magnitude is required for these measurements. The Love wave SAW sensor shows a linear response approximately from 100 pT to 100 µT. Hence, this SAW sensor shows the required dynamic range and is suitable for unshielded measurements as it would not be saturated by earth's magnetic field.

REFERENCES

[1] Y. J. Wang, J. Q. Gao, M. H. Li, Y. Shen, D. Hasanyan, J. F. Li, D. Viehland. A review on equivalent magnetic noise of magnetoelectric laminate sensors, *Philosophical transactions. Series A, Mathematical, physical, and engineering sciences*, **372,** 20120455 (2009)

[2] C.-W. Nan, M. I. Bichurin, S. Dong, D. Viehland, and G. Srinivasan. Multiferroic magnetoelectric composites: Historical perspective, status, and future directions, *J. Appl. Phys.*, **103**, 031101 (2008).

[3] V. Röbisch, S. Salzer, N. O. Urs, J. Reermann, E. Yarar, A. Piorra, C. Kirchhof, E. Lage, M. Höft, G. Schmidt, R. Knöchel, J. McCord, E. Quandt, D. Meyners. Pushing the detection limit of thin film magnetoelectric heterostructures. *Journal of Materials Research*, **32**(6), 1009-1019 (2017).

[4] A. Pohl. A review of wireless SAW sensors. *IEEE transactions on ultrasonics, ferroelectrics, and frequency control*, **47**(2), 317-332 (2000).

[5] S. M. Hanna. Magnetic field sensors based on SAW propagation in magnetic films. *IEEE Transactions on Ultrasonics Ferroelectrics and Frequency Control*, **34**, 191-194 (1987).

[6] M. Elhosni, O. Elmazria, S. Petit-Watelot, L. Bouvot, S. Zhgoon, A. Talbi, M. Hehn, A. Michel, A. Keltouma, S. Hage-Ali, D. Lacour, F. Sarry, O. Boumatar. Magnetic field SAW sensors based on magnetostrictive-piezoelectric layered structures: FEM modeling and experimental validation. *Sensors and Actuators A: Physical*, **240**, 41-49 (2016).

[7] A. Kittmann, P. Durdaut, S. Zabel, J. Reermann, J. Schmalz, B. Spetzler, D. Meyners, N. Sun, J. McCord, M. Gerken, G. Schmidt, M. Höft, R. Knöchel, F. Faupel, E. Quandt. Wide Band Low Noise Love Wave Magnetic Field Sensor System. *Scientific reports*, **8**(1), 278 (2018).

[8] E. Lage, C. Kirchhof, V. Hrkac, L. Kienle, R. Jahns, R. Knöchel, E. Quandt, and D. Meyners. Exchange biasing of magnetoelectric composites, *Nat. Mater.* **11**, 523-529 (2012).

[9] R. Jahns, H. Greve, E. Woltermann, E. Quandt, R. Knöchel. Sensitivity enhancement of magnetoelectric sensors through frequency-conversion. *Sensors and Actuators A: Physical*, **183**, 16-21 (2012).

PHASE FIELD MODELLING OF FERROELECTRIC-FERROMAGNETIC INTERFACES

Wolfgang Dornisch*, **and Ralf Müller**

Institute of Applied Mechanics, Department of Mechanical and Process Engineering, TU Kaiserslautern
Gottlieb-Daimler-Str., 67663 Kaiserslautern, Germany

Abstract. *Magneto-electric coupling along interfaces between ferroelectric and ferromagnetic materials allows the magnetization in ferromagnetic layers to be controlled by electrical fields. The coupling effect is mainly due to the deformation coupling between the layers. Thus, further coupling effects at the interfaces are neglected in this contribution. Phase field formulations are used to model the polarization and magnetization in the ferroelectric and ferromagnetic layers, respectively. A coupling between the phase field and the strains is introduced in each layer in combination with a mechanical coupling at the interface. The numerical formulation for the ferroelectric layer is taken from literature. A special focus is set on the discretization of the length-constrained order parameter in the ferromagnetic layer. We show a new approach to enforce this constraint and provide a numerical simulation which illustrates the magneto-electric coupling effect.*

1 Introduction

Materials in which both the ferroelectric and the ferromagnetic effect occur are called multiferroic. The coupling between both effects is called magneto-electric effect, but this direct coupling is in general very weak [12], which limits the use of this effect in real applications [13]. The idea of multiferroic heterostructures is to combine materials with pronounced ferroelectric properties with materials with pronounced ferromagnetic properties. The coupling between both effects is achieved in an indirect way by a mechanical coupling along the interface between the different functional materials [6]. This is conceptually simpler [9] and paves the way for industrial applications. Experiments conducted in [4, 6] show that magnetic domain wall motions in multiferroic heterostructures can be controlled by electric fields, whereby the elastic coupling along the interface is the driving mechanism [8].

The numerical modeling of multiferroic heterostructures is of huge importance for the development of magneto-electric devices [5]. Micromagnetic and FE^2 models have been presented in [3] and [11], respectively. Within the present work, a continuum mechanics model is used, where the polarization and the magnetization in the ferroelectric and the ferromagnetic layer, respectively, are modeled with the help of phase fields. The resulting equations are discretized by the finite element method, whereby the layers are coupled by shared degrees of freedom. This approach has been presented in [2]. The ferroelectric layer is modeled according to [10] with displacements, spontaneous polarization and electric potential being the independent field variables. The ferromagnetic layer is modeled using spherical coordinates, which has been proposed in [14] in order to enforce the length constraint of the magnetization vector. In contrast to [14], a different interpolation scheme for the magnetization vectors is used.

---

*Corresponding author: Wolfgang Dornisch (🖂 dornisch@rhrk.uni-kl.de)

⇒ TABLE OF CONTENTS

2 Basic equations for the electric and the magnetic layer

The body $\mathcal{B}$ with boundary $\partial\mathcal{B}$ is divided into ferroelectric regions $\mathcal{B}^{\mathrm{FE}}$ and ferromagnetic regions $\mathcal{B}^{\mathrm{FM}}$. Small mechanical displacements $\boldsymbol{u}$ are assumed. The equilibrium and the kinematic relation are given by

$$\operatorname{div}\boldsymbol{\sigma} = \boldsymbol{0} \quad \text{in } \mathcal{B} \qquad \text{and} \qquad \boldsymbol{\varepsilon} = \frac{1}{2}\left(\nabla\boldsymbol{u} + (\nabla\boldsymbol{u})^{\mathrm{T}}\right) \quad \text{in } \mathcal{B}\,, \tag{1}$$

respectively. Hereby, body forces and inertia terms are neglected and $\boldsymbol{\sigma}$ and $\boldsymbol{\varepsilon}$ denote the mechanical stresses and strains, respectively. The boundary conditions are given by

$$\boldsymbol{u} = \bar{\boldsymbol{u}} \quad \text{on } \partial\mathcal{B}_{\mathrm{u}} \qquad \text{and} \qquad \boldsymbol{\sigma}\boldsymbol{n} = \bar{\boldsymbol{t}} \quad \text{on } \partial\mathcal{B}_{\mathrm{t}}\,, \tag{2}$$

where $\boldsymbol{n}$ is the surface normal vector pointing outwards from $\mathcal{B}$ and $\boldsymbol{t}$ denotes the surface tractions. The evolution equation of the polarization $\boldsymbol{P}$ in the ferroelectric layer is given by a generalized form of the Ginzburg–Landau equation

$$\beta\dot{\boldsymbol{P}} = \operatorname{div}\frac{\partial H_{\mathrm{FE}}}{\partial\nabla\boldsymbol{P}} - \frac{\partial H_{\mathrm{FE}}}{\partial\boldsymbol{P}}\,, \tag{3}$$

where β denotes the mobility constant and H_{FE} the free energy potential; see [10]. The evolution equation of the magnetization $\boldsymbol{M}$ in the ferromagnetic layer is given by the Landau–Lifshitz–Gilbert equation

$$\dot{\boldsymbol{M}} = -\frac{\gamma_0}{\mu_0}\boldsymbol{M} \times \left(\operatorname{div}\frac{\partial H_{\mathrm{FM}}}{\partial\nabla\boldsymbol{M}} - \frac{\partial H_{\mathrm{FM}}}{\partial\boldsymbol{M}} - \frac{\alpha\mu_0}{\|\boldsymbol{M}\|}\dot{\boldsymbol{M}}\right)\,, \tag{4}$$

which enforces the constraint $\|\boldsymbol{M}\| = \text{const.}$ on the continuum level, see [7, 14]. The free energy potential of the ferromagnetic layer is referred to as H_{FM}. For more details on the constants in Eq. (4) and the details of the employed phase field models we refer the interested reader to [2].

3 Discretization using the finite element method

The coupled differential equations given in Sec. 2 are solved using the finite element method. Thus, Eqs. (1)-(4) are brought into the weak form and unknown quantities and their associated test functions are discretized. This yields

$$\begin{aligned} \boldsymbol{u}^h &= \sum_I N_I \boldsymbol{u}^I\,, & \boldsymbol{\eta}_{\mathrm{u}}^h &= \sum_I N_I \boldsymbol{\eta}_{\mathrm{u}}^I \\ \varphi^h &= \sum_I N_I \varphi^I\,, & \eta_{\varphi}^h &= \sum_I N_I \eta_{\varphi}^I \\ \boldsymbol{P}^h &= \sum_I N_I \boldsymbol{P}^I\,, & \boldsymbol{\eta}_{\mathrm{P}}^h &= \sum_I N_I \boldsymbol{\eta}_{\mathrm{P}}^I\,, \end{aligned} \tag{5}$$

in the ferroelectric layer with N_I being trilinear Lagrange basis functions for 3D brick elements and φ denoting the electrical field. In the ferromagnetic layer, the order parameter $\boldsymbol{M}$ is replaced by an auxiliary order parameter $\boldsymbol{\theta} = (\theta_1, \theta_2)$, which are the spherical coordinates describing the unit magnetization vector $\boldsymbol{m} = \frac{\boldsymbol{M}}{|\boldsymbol{M}|}$. Thus, the magnetic field ϕ and the auxiliary order parameter as well as the associated test functions are interpolated by

$$\begin{aligned} \phi^h &= \sum_I N_I \phi^I\,, & \eta_{\phi}^h &= \sum_I N_I \eta_{\phi}^I \\ \theta_1^h &= \sum_I N_I \theta_1^I\,, & \eta_{\theta_1}^h &= \sum_I N_I \eta_{\theta_1}^I \\ \theta_2^h &= \operatorname{atan2}(\bar{q}, \bar{p})\,, & \eta_{\theta_2}^h &= \sum_I N_I \eta_{\theta_2}^I \\ \bar{q} &= \sum_I N_I \sin\theta_2^I\,, & \bar{p} &= \sum_I N_I \cos\theta_2^I\,. \end{aligned} \tag{6}$$

The interpolation for θ_2 using the $\mathrm{atan2}$ function is equivalent to using a circular mean interpolation, which ensures a consistent interpolation of the angles θ_2, see [1, 2].

4 Numerical example

The simulation of the pattern transfer between ferroelectric and ferromagnetic layers is tested with the help of the sandwich structure depicted in Fig. 1. The upper, ferroelectric layer consist of Barium-Titanate and the lower, ferromagnetic layer of Galfenol. The gap between the layers is used only for the visualization, it is not present in the computations. The ferroelectric layer is poled in a uniform direction at the beginning, while the magnetization is chosen to be randomly distributed. The simulation of the relaxation process reveals that the polarization in the ferroelectric layer does not change at all, while the magnetization in the ferromagnetic layer aligns with the direction of the polarization in the ferroelectric layer. The results for the ferromagnetic layer are shown in Fig. 2. This example shows that pattern from the ferroelectric layer can be transferred to the ferromagnetic layer. These results are in accordance with the experiments conducted in [3]. For more details see [2].

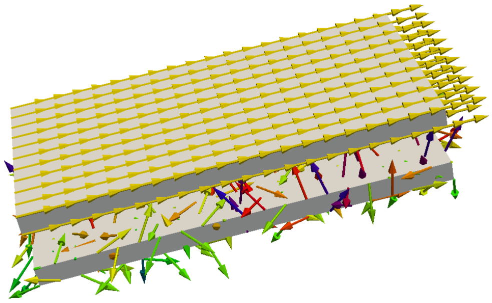

Figure 1: System sketch for the multiferroic sandwich heterostructure.

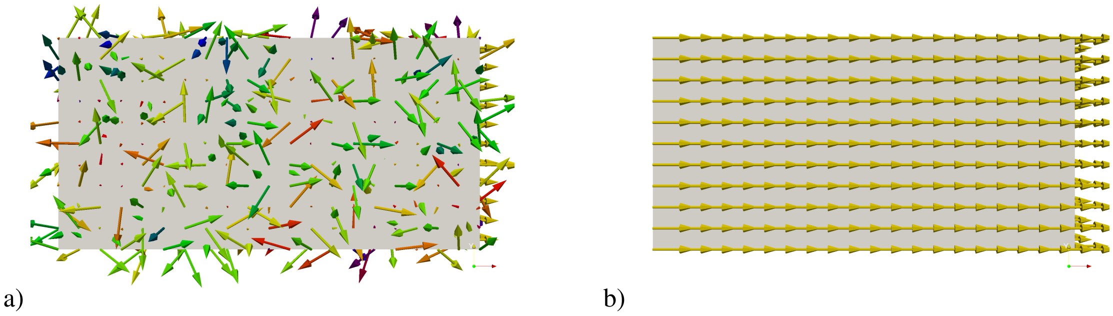

a)

b)

Figure 2: Initial (a) and final (b) states of the magnetization vectors in the ferromagnetic layer.

5 Conclusion

A framework for the coupled simulation of ferroelectric and ferromagnetic layers has been presented. The polarization/magnetization is described by phase fields. A new and robust interpolation for the constrained magnetization vector has been presented. The numerical example shows that the domain pattern transfer from the ferroelectric layer to the ferromagnetic layer can be simulated.

Acknowledgements

W. Dornisch was partially supported by the German Research Foundation (DFG) within the Research Group FOR 1509, grant number MU 1370/8-2. This support is gratefully acknowledged.

⇒ TABLE OF CONTENTS

REFERENCES

[1] W. Dornisch, D. Schrade, J. Wolf, and R. Müller. Numerical methods for the modeling of the magnetization vector in multiferroic heterostructures. *Proc. Appl. Math. Mech.*, 17(1): 503–504, 2017.

[2] W. Dornisch, D. Schrade, B.-X. Xu, M.-A. Keip, and R. Müller. Coupled phase field simulations of ferroelectric and ferromagnetic layers in multiferroic heterostructures. *submitted to Arch. Appl. Mech.*, 2018.

[3] K. J. A. Franke, T. H. E. Lahtinen, and S. van Dijken. Field tuning of ferromagnetic domain walls on elastically coupled ferroelectric domain boundaries. *Phys. Rev. B*, 85(9): 09442, 2012.

[4] K. J. A. Franke, B. van de Wiele, Y. Shirahata, S. J. Hämäläinen, T. Taniyama, and S. van Dijken. Reversible Electric-Field-Driven Magnetic Domain-Wall Motion. *Phys. Rev. X*, 5 (1), 2015.

[5] J.-M. Hu, L.-Q. Chen, and C.-W. Nan. Multiferroic Heterostructures Integrating Ferroelectric and Magnetic Materials. *Adv. Mater.*, 28(1):15–39, 2016.

[6] T. H. E. Lahtinen, J. O. Tuomi, and S. van Dijken. Pattern transfer and electric-field-induced magnetic domain formation in multiferroic heterostructures. *Adv. Mater.*, 23(28): 3187–3191, 2011.

[7] C. M. Landis. A continuum thermodynamics formulation for micro-magneto-mechanics with applications to ferromagnetic shape memory alloys. *J. Mech. Phys. Sol.*, 56(10): 3059–3076, 2008.

[8] D. C. Lupascu, H. Wende, M. Etier, A. Nazrabi, I. Anusca, H. Trivedi, V. V. Shvartsman, J. Landers, S. Salamon, and C. Schmitz-Antoniak. Measuring the magnetoelectric effect across scales. *GAMM-Mitteilungen*, 38(1):25–74, 2015.

[9] F. Matsukura, Y. Tokura, and H. Ohno. Control of magnetism by electric fields. *Nat. Nanotechnol.*, 10(3):209–220, 2015.

[10] D. Schrade, R. Müller, D. Gross, M.-A. Keip, H. Thai, and J. Schröder. An invariant formulation for phase field models in ferroelectrics. *Int. J. Solids. Struct.*, 51(11-12): 2144–2156, 2014.

[11] J. Schröder, M. Labusch, and M.-A. Keip. Algorithmic two-scale transition for magneto-electro-mechanically coupled problems: Fe2-scheme: localization and homogenization. *Comput. Methods Appl. Mech. Engrg.*, 302:253–280, 2016.

[12] Y. Tokura. Multiferroics—toward strong coupling between magnetization and polarization in a solid. *J. Magn. Magn. Mater.*, 310(2):1145–1150, 2007.

[13] P. Torelli. Magnetic phase transitions in multiferroics (Conference Presentation). In Henri-Jean Drouhin, Jean-Eric Wegrowe, and Manijeh Razeghi, editors, *SPIE Nanoscience + Engineering*, SPIE Proceedings, page 99312L. SPIE, 2016. doi: 10.1117/12.2230654.

[14] M. Yi and B.-X. Xu. A constraint-free phase field model for ferromagnetic domain evolution. *Proc. R. Soc. A*, 470(2171):20140517, 2014.

⇒ TABLE OF CONTENTS

STRAIN-MEDIATED MAGNETO-ELECTRIC COUPLING IN SOFT COMPOSITES

Matthias Rambausek* and **Marc-André Keip**

Institute of Applied Mechanics, Chair of Material Theory, University of Stuttgart
Pfaffenwaldring 7, 70569 Stuttgart, Germany

Abstract. *In an analytical study Liu and Sharma (2013; Phys. Rev. E 88, 040601) described strong magneto-electro-elastic coupling in soft-matter based composites. Their analytical study suggests that such a realization of magneto-electric coupling could be an alternative to existing approaches based on ceramic materials. Motivated by these findings we provide numerical multiscale studies to assess the performance of prototypical soft magneto-electric composites.*

1 Introduction

The research on magneto-electrically coupling materials was re-initiated more than a decade ago by the works [14, 2], among others. Since then, significant improvements have been achieved on the experimental side [4, 3]. These findings lead to continuum-mechanical multiscale approaches for the description of magneto-electric effects [9, 8, 1, 13]. The latter contributions considered ferroic composites of *hard* constituents in order to achieve magneto-electric product properties. However, as highlighted by [10], there is a possibility of magneto-electric coupling in *soft*-matter based composites, which strongly relies on effects at *finite deformations*.

Motivated by the latter work, we pursue the realization of magneto-electric devices based on soft-composites. For this purpose we perform two-scale simulations (FE^2 [7, 13]) of magnetorheological elastomers (MREs) in two dimensions under homogeneous applied fields. Such a setting is inspired by our recent works on soft magneto-elastic bodies [5, 6].

2 Theory

In the quasi-static setting in absence of free currents, the governing (Maxwell) equations for the electric and magnetic fields are given as

$$\mathrm{div}\boldsymbol{d} = q, \qquad \mathrm{div}\boldsymbol{b} = 0, \qquad \mathrm{curl}\,\boldsymbol{e} = \boldsymbol{0} \qquad \text{and} \qquad \mathrm{curl}\,\boldsymbol{h} = \boldsymbol{0}, \tag{1}$$

where $\boldsymbol{d}$ denotes the electric displacement, q the free electric charge density, $\boldsymbol{b}$ the magnetic induction, $\boldsymbol{e}$ the electric field and $\boldsymbol{h}$ the magnetic field. On the mechanical side, we have the balance of linear momentum and the compatibility condition

$$\mathrm{Div}\,\boldsymbol{P} = -\boldsymbol{f}_0^b \qquad \text{and} \qquad \mathrm{Curl}\,\boldsymbol{F} = \boldsymbol{0}, \tag{2}$$

respectively. In the latter equation $\boldsymbol{P}$ is the *total* first-Piola-Kirchhoff-type stress and $\boldsymbol{f}_0^b$ the mechanical body force per referential volume. The kinematic quantity dual to $\boldsymbol{P}$ is the deformation gradient $\boldsymbol{F}$ of which the Curl has to vanish.

---

*Corresponding author: Matthias Rambausek (✉ matthias.rambausek@mechbau.uni-stuttgart.de)

⇒ TABLE OF CONTENTS

At this point we would like to note that the *lowercase* differential operators $\{\mathrm{div}, \mathrm{grad}, \mathrm{curl}\}$ refer to derivatives with respect to Eulerian coordinates $\boldsymbol{x}$. Conversely, their uppercase counterparts $\{\mathrm{Div}, \mathrm{Grad}, \mathrm{Curl}\}$ denote derivatives with respect to Lagrangian coordinates $\boldsymbol{X}$. The deformation map $\boldsymbol{\varphi}$ relates the current (Eulerian) to the initial (Lagrangian) configuration. Accordingly, $\boldsymbol{F}$ is defined in terms of $\boldsymbol{\varphi}$ as $\boldsymbol{F} = \mathrm{Grad}\,\boldsymbol{\varphi}$.

In this contribution, we consider free-energy densities $\Psi(\boldsymbol{F}, \boldsymbol{D}, \boldsymbol{B})$ with $\boldsymbol{D} = J\boldsymbol{F}^{-1} \cdot \boldsymbol{d}$ and $\boldsymbol{B} = J\boldsymbol{F}^{-1} \cdot \boldsymbol{b}$. In order to account for incompressibility, we introduce the energy density $\Psi^*(\boldsymbol{F}, \boldsymbol{D}, \boldsymbol{B}) = \Psi(\boldsymbol{F}^*, \boldsymbol{D}, \boldsymbol{B})$ [12] with $\boldsymbol{F}^* = \frac{1}{J^{1/d}}\boldsymbol{F}$. The duals to $\boldsymbol{F}$, $\boldsymbol{D}$ and $\boldsymbol{B}$ are given as

$$\{\boldsymbol{P}, \boldsymbol{E}, \boldsymbol{H}\} = \{\frac{\partial \Psi}{\partial \boldsymbol{F}}, \frac{\partial \Psi}{\partial \boldsymbol{D}}, \frac{\partial \Psi}{\partial \boldsymbol{B}}\} \qquad \text{and} \qquad \{\boldsymbol{P}^*, \boldsymbol{E}, \boldsymbol{H}\} = \{\frac{\partial \Psi^*}{\partial \boldsymbol{F}}, \frac{\partial \Psi^*}{\partial \boldsymbol{D}}, \frac{\partial \Psi^*}{\partial \boldsymbol{B}}\}. \tag{3a}$$

Variational principle at the macroscopic scale. At the macroscale we employ $\overline{\boldsymbol{\varphi}}$, $\overline{\boldsymbol{D}}$ and $\overline{\boldsymbol{B}}$ as primary fields, with $\overline{\{\bullet\}}$ emphasizing their macroscopic nature. The resulting functional is

$$\begin{aligned}\overline{\mathcal{L}}\left(\overline{\boldsymbol{\varphi}}, \overline{\boldsymbol{D}}, \overline{\boldsymbol{B}}, \overline{p}, \overline{\phi}^{\mathrm{e}}, \overline{\phi}^{\mathrm{m}}\right) = &\int_{\overline{\mathcal{B}}} \overline{\Psi}^*\left(\overline{\boldsymbol{F}}, \overline{\boldsymbol{D}}, \overline{\boldsymbol{B}}; \overline{\boldsymbol{X}}\right) + \overline{p}(\overline{J} - 1)\,\mathrm{d}\overline{V} + \int_{\overline{\Omega}\setminus\overline{\mathcal{B}}} \overline{\Psi}\left(\overline{\boldsymbol{F}}, \overline{\boldsymbol{D}}, \overline{\boldsymbol{B}}; \overline{\boldsymbol{X}}\right)\,\mathrm{d}\overline{V} \\ &+ \int_{\overline{\Omega}} -\overline{\phi}^{\mathrm{e}}(\overline{\mathrm{Div}}\,\overline{\boldsymbol{D}} - \overline{q}_0(\overline{\boldsymbol{X}})) - \overline{\phi}^{\mathrm{m}}(\overline{\mathrm{Div}}\,\overline{\boldsymbol{B}})\,\mathrm{d}\overline{V} + \overline{\Pi}^{ext},\end{aligned} \tag{4}$$

where $\overline{\mathcal{B}}$ is the domain of the body in the initial configuration. $\overline{\Omega}$ denotes the whole computational domain consisting of $\overline{\mathcal{B}}$ and the surrounding free space $\overline{\mathcal{B}}'$. The functional $\overline{\Pi}^{ext}$ in above equation represents external loading. Finally, we arrive at the variational saddle-point principle

$$\left\{\hat{\overline{\boldsymbol{\varphi}}}, \hat{\overline{\boldsymbol{D}}}, \hat{\overline{\boldsymbol{B}}}, \hat{\overline{p}}, \hat{\overline{\phi}}^{\mathrm{e}}, \hat{\overline{\phi}}^{\mathrm{m}}\right\} = \arg\left\{\inf_{\substack{\overline{\boldsymbol{\varphi}} \\ \in \\ \mathcal{W}_{\overline{\boldsymbol{\varphi}}}}} \inf_{\substack{\overline{\boldsymbol{D}} \\ \in \\ \mathcal{W}_{\overline{\boldsymbol{D}}}}} \inf_{\substack{\overline{\boldsymbol{B}} \\ \in \\ \mathcal{W}_{\overline{\boldsymbol{B}}}}} \sup_{\substack{\overline{p} \\ \in \\ \mathcal{W}_{\overline{p}}}} \sup_{\substack{\overline{\phi}^{\mathrm{e}} \\ \in \\ \mathcal{W}_{\overline{\phi}^{\mathrm{e}}}}} \sup_{\substack{\overline{\phi}^{\mathrm{m}} \\ \in \\ \mathcal{W}_{\overline{\phi}^{\mathrm{m}}}}} \overline{\mathcal{L}}\left(\overline{\boldsymbol{\varphi}}, \overline{\boldsymbol{D}}, \overline{\boldsymbol{B}}, \overline{p}, \overline{\phi}^{\mathrm{e}}, \overline{\phi}^{\mathrm{m}}\right)\right\}. \tag{5}$$

Variational principle at the microscopic scale and homogenization. At the microscale, we resort to a charge-free formulation of magneto-electro-elasticity [11] in terms of electric and magnetic vector potentials $\boldsymbol{A}^e$ and $\boldsymbol{A}^m$, respectively. Accordingly, we define the macroscopic energy density of the representative volume element ($\mathcal{RVE}$) $\mathcal{B}[\overline{\boldsymbol{X}}]$,

$$\overline{\Psi}^*\left(\overline{\boldsymbol{F}}, \overline{\boldsymbol{D}}, \overline{\boldsymbol{B}}\right) = \inf_{\substack{\boldsymbol{\varphi} \\ \in \\ \mathcal{W}_{\boldsymbol{\varphi}}(\overline{\boldsymbol{F}})}} \inf_{\substack{\boldsymbol{A}^e \\ \in \\ \mathcal{W}_{\boldsymbol{A}^e}(\overline{\boldsymbol{D}})}} \inf_{\substack{\boldsymbol{A}^m \\ \in \\ \mathcal{W}_{\boldsymbol{A}^m}(\overline{\boldsymbol{B}})}} \sup_{\substack{p \\ \in \\ \mathcal{W}_p}} \frac{1}{|\mathcal{B}[\overline{\boldsymbol{X}}]|}\int_{\mathcal{B}[\overline{\boldsymbol{X}}]} \Psi^*(\boldsymbol{F}^*, \boldsymbol{D}, \boldsymbol{B}) + p(J-1)\,\mathrm{d}V. \tag{6}$$

3 Examples

We consider a two-dimensional MRE specimen exposed to a homogeneous external magnetic and electric field as depicted in Figure 1. The free-energy function we employ for incompressible media is

$$\psi = \frac{\mu}{2}(\mathrm{tr}\,\boldsymbol{C}^* - 3) + \frac{1}{2\epsilon_0}\|\boldsymbol{d}\|^2 - \frac{1}{2\epsilon_0}\frac{\chi^{\mathrm{e}}}{J + \chi^{\mathrm{e}}}\|\boldsymbol{d}\|^2 + \frac{1}{2\mu_0}\|\boldsymbol{b}\|^2 - \frac{m^{\mathrm{s}}}{\gamma}\ln\left[\cosh\left(\gamma\,\|\boldsymbol{b}\|\right)\right] \tag{7}$$

with $\boldsymbol{C}^* = (\boldsymbol{F}^*)^T \cdot \boldsymbol{F}^*$ and $\gamma = J\chi^m/(m^{\mathrm{s}}\,(J + \chi^m))$. The material parameters for the elastomer matrix are set to $\{\mu, \chi^e, m^{\mathrm{s}}, \chi^m\} = \{0.06667, 7, 0, 0\}$ and to $\{\mu, \chi^e, m^{\mathrm{s}}/\sqrt{\mu_0}, \chi^m\} = \{66.67, 700, 1, 10\}$ for the inclusions. The free space on the macroscopic scale is modeled

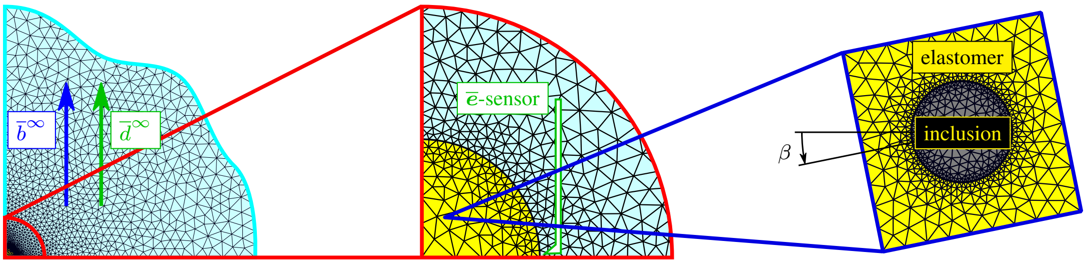

MRE in free space (macro) MRE body zoomed (macro) $\mathcal{RVE}$ (micro)

Figure 1: The circular MRE specimen is embedded into a sufficiently sized free space with homogeneous external fields $\overline{\boldsymbol{d}}^\infty$ and $\overline{\boldsymbol{b}}^\infty$ (left). In the zoomed view of the specimen we indicate the location of an electric field sensor. The microstructure is depicted at the very right.

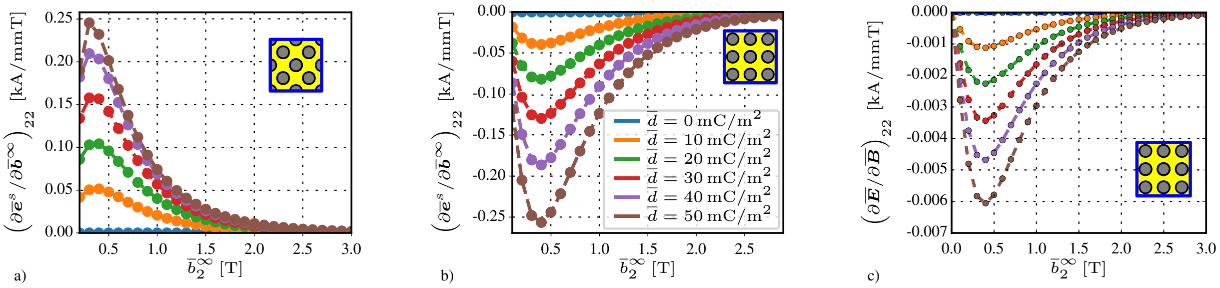

Figure 2: In a) we show the sensitivity of the detectable electric field at the specimen scale for a microstructure with angle $\beta = \pi/4$. In b) we show the same graph for the case of $\beta = 0$. Obviously, the corresponding effective magneto-electric modulus depicted in c) is orders of magnitudes smaller.

with $\{\mu, \chi^e, m^s, \chi^m\} = \{0.001, 0, 0, 0\}$, whereby the mechanical term in (7) is replaced by a compressible neo-Hookean energy density with $\lambda = 0$. The constants ϵ_0 and μ_0 are set to 8.854×10^{-6} and 0.4π.

In Figure 2 we depict the sensitivity of the electric field $\overline{\boldsymbol{e}}^s$ detected by a sensor with respect to the external magnetic field $\overline{\boldsymbol{b}}^\infty$ on the macroscale. There we see the influence of the applied electric free charge density in the electrodes. We also investigate the effect of the microstructure orientation. Next to the ME coupling device property we show the corresponding material modulus, which obviously does not play a significant role.

4 Conclusion

In this contribution we studied the performance of MREs as magnetic-field sensors by multiscale simulations. We conclude that the macrostructural magneto-electric effects dominate their counterparts at the microscale. However, the microstructural effects strongly influence the magneto- and electro-mechanical macro-response and thus the ME device coupling.

Acknowledgements

The financial support of the German Research Foundation (DFG) in the framework of the Cluster of Excellence in “Simulation Technology” (EXC 310/2) at the University of Stuttgart and as well as of the *Ministerium für Wissenschaft, Forschung und Kunst des Landes Baden-Württemberg* is gratefully acknowledged.

REFERENCES

[1] A. Avakian and A. Ricoeur. Constitutive modeling of nonlinear reversible and irreversible ferromagnetic behaviors and application to multiferroic composites. *J Intel Mat Syst Str*, 27(18):2536–2554, 2016.

[2] W. Eerenstein, N. D. Mathur, and J. F. Scott. Multiferroic and magnetoelectric materials. *Nature*, 442(7104):759–765, 2006.

[3] M. Etier, V. V. Shvartsman, Y. Gao, J. Landers, H. Wende, and D. C. Lupascu. Magnetoelectric Effect in (0–3) $CoFe_2O_4$-$BaTiO_3$(20/80) Composite Ceramics Prepared by the Organosol Route. *Ferroelectrics*, 448(1):77–85, 2013.

[4] H. Greve, E. Woltermann, H.-J. Quenzer, B. Wagner, and E. Quandt. Giant magnetoelectric coefficients in (Fe90Co10)78Si12B10-AlN thin film composites. *Appl Phys Lett*, 96 (18):182501, 2010.

[5] M.-A. Keip and M. Rambausek. A multiscale approach to the computational characterization of magnetorheological elastomers. *Int J Numer Meth Eng*, 107(4):338–360, 2016.

[6] M.-A. Keip and M. Rambausek. Computational and analytical investigations of shape effects in the experimental characterization of magnetorheological elastomers. *Int J Solids Struct*, 121:1–20, 2017.

[7] M.-A. Keip, P. Steinmann, and J. Schröder. Two-scale computational homogenization of electro-elasticity at finite strains. *Comput Method Appl M*, 278:62–79, 2014.

[8] M. Labusch, M. Etier, D. C. Lupascu, J. Schröder, and M.-A. Keip. Product properties of a two-phase magneto-electric composite: Synthesis and numerical modeling. *Comput Mech*, 54:71–83, 2014.

[9] J. Lee, J. G. Boyd, and D. C. Lagoudas. Effective properties of three-phase electro-magneto-elastic composites. *Int J of Eng Sci*, 43(10):790–825, 2005.

[10] L. Liu and P. Sharma. Giant and universal magnetoelectric coupling in soft materials and concomitant ramifications for materials science and biology. *Phys Rev E*, 88(4):040601, 2013.

[11] C. Miehe, D. Vallicotti, and S. Teichtmeister. Homogenization and multiscale stability analysis in finite magneto-electro-elasticity. Application to soft matter EE, ME and MEE composites. *Comput Method Appl M*, 300:294–346, 2016.

[12] J.-P. Pelteret, D. Davydov, A. McBride, D. K. Vu, and P. Steinmann. Computational electro- and magneto-elasticity for quasi-incompressible media immersed in free space. *Int J Numer Meth Eng*, 108(11):1307–1342, 2016.

[13] J. Schröder, M. Labusch, and M.-A. Keip. Algorithmic two-scale transition for magneto-electro-mechanically coupled problems: FE^2-scheme: Localization and homogenization. *Comput Method Appl M*, 302:253–280, 2016.

[14] N. A. Spaldin and M. Fiebig. The Renaissance of Magnetoelectric Multiferroics. *Science*, 309(5733):391–392, 2005.

MODELING INTERFACE CRACKS IN MULTIFERROIC COMPOSITES WITH AN EXTENDED COHESIVE ZONE MODEL

Alexander Schlosser[1] **and Andreas Ricoeur**[2]

[1,2] Institute of Mechanics, Chair of Engineering Mechanics/ Continuum Mechanics, University of Kassel
Moenchebergstr. 7, 34125 Kassel, Germany
e-mail: alexander.schlosser@uni-klassel.de

Abstract. *In this paper an extended cohesive zone model for delamination under magneto-electromechanical loading is presented. The developed tool enables the simulation of interface cracks in multiferroic composites.*

1 Introduction

The efficiency in converting magnetic into electric energy and vice versa makes magneto-electric (ME) composites promising candidates for many technical applications. The ferroelectric matrix as well as the magnetostrictive inclusions of particle composites and the layers of laminates are mostly ceramics or other brittle materials, thus being prone to cracking. Independent from the kind of composite the transmission of stresses via the interfaces between the constituents plays the key role in the functionality of ME composites. Therefore, the investigation of delamination processes is of great interest for the prediction of durability and coupling factors. In order to investigate delamination processes in ME composites, cohesive elements are being developed and applied in combination with nonlinear ME finite elements described in [1] and [2]. Those cohesive elements must be able to describe delamination fracture processes under magnetoelectromechanical loadings as seen in Figure 1. Under such loadings, phenomena like Maxwell stresses also have to be taken into account.

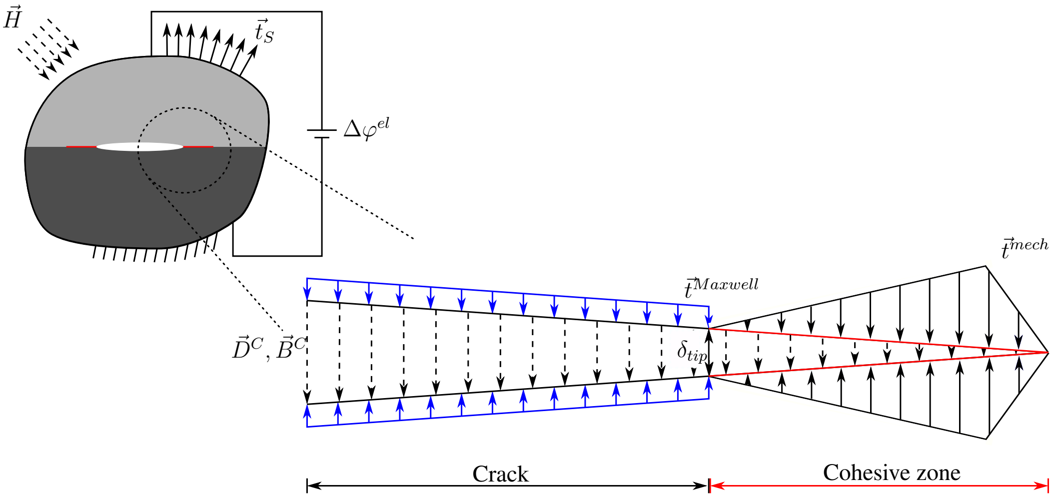

Figure 1: Interface crack under magnetoelectromechanical loading

⇒ TABLE OF CONTENTS

2 Theoretical framework

2.1 Magnetoelectroelastic behavior during delamination

For the finite element the variation of a cohesive potential

$$\delta\Pi^{coh} = \int\limits_{\Gamma_{coh}} \left(t_i \delta\Delta u_i + \omega^{el}\delta\Delta\varphi^{el} + \omega^{mag}\delta\Delta\varphi^{mag}\right) \mathrm{d}\Gamma \tag{1}$$

is used, with Δu_i, $\Delta\varphi^{el}$ and $\Delta\varphi^{mag}$ being the displacement and potential jumps at the interface. The stress t_i, the electric surface charge $\omega^{el} = -\kappa E_i n_i$ and the magnetic surface normal $\omega^{mag} = -\mu H_i n_i$ need to be described by the model, where μ and κ are the magnetic and electric permeability, respectively.

The mechanical stress t_i in the cohesive zone consists of three parts: An elastic part t_i^{mech}, the Maxwell stresses t_i^{Max} and a piezomagnetic/piezoelectric part t_i^{piezo}:

$$t_i = t_i^{mech} + t_i^{Max} + t_i^{piezo} \tag{2}$$

The elastic part is described by a bilinear traction separation law as first suggested by [3]

$$t_i^{mech} = c_{ij}(1-f)\Delta u_j. \tag{3}$$

c_{ij} are the elastic constants of the cohesive zone and f is a damage variable which in general depends on both the normal separation and the tangential displacement jump to take into account mechanical mixed mode conditions. The Maxwell stresses, acting at crack faces, have amongst others been deduced in [6]. Being extended by a magnetic contribution and under the assumtption that both fields are perpendicular to the crack the Maxwell stresses can be written as

$$t_i^{Max} = \frac{1}{2}\left(E^C\right)^2\left(\kappa(f) - \frac{\kappa(f)^2}{\kappa_{Bulk}}\right)n_i + \frac{1}{2}\left(H^C\right)^2\left(\mu(f) - \frac{\mu(f)^2}{\mu_{Bulk}}\right)n_i. \tag{4}$$

Here, E^C and H^C are the electric and the magnetic field in the cohesive zone with the corresponding permeabilities $\kappa(f)$ and $\mu(f)$. The permeabilities are damage dependent to take a into account the delamination process as in [5]. The permeabilities decrease from an undamaged value to the permeabilities of air or vacuum respectively. The third contribution to the tractions in the cohesive zone are the piezoelectric and piezomagnetic effects in the interface:

$$t_i^{piezo} = -e_{ij}(f)E_j^C - q_{ij}(f)H_j^C. \tag{5}$$

Electric displacement and magnetic flux are modeled via the capacitor analogy [4] and a piezoelectric as well as a piezomagnetic contribution:

$$E_i^C = \frac{\Delta\varphi^{el}}{\Delta u_n + \Delta_0}n_i + \tilde{e}(f)_{ij}\Delta u_j, \qquad H_i^C = \frac{\Delta\varphi^{mag}}{\Delta u_n + \Delta_0}n_i + \tilde{q}_{ij}(f)\Delta u_j. \tag{6}$$

The parameter Δ_0 avoids numerical instabilities when the normal separation is close to zero.

⇒ TABLE OF CONTENTS

3 Results

3.1 Test specimen

A composite of one layer $\mathrm{BaTiO_3}$ (upper half) and one layer $\mathrm{CoFe_2O_4}$ (lower half) is investigated. Both materials exhibit linear behavior and are perfectly poled in x_2-direction meaning that no switching processes occur. Cohesive zone elements with the above described behavior are implemented between the two layers. The piezoelectric and -magnetic properties of the cohesive zone are both neglected. The permeabilities, including κ_{Bulk} nad μ_{Bulk} are defined as averages between the upper and lower layer. Two test cases have been simulated. In both cases first an electric field and an opening displacement u_{COD} are applied creating a Mode I/II/IV/V-loading. The Mode-II contribution arises from the asymmetry of the specimen in combination with the piezoelectric effect. In the first set of simulations the opening displacement was increased until the crack has grown through the whole specimen. In the second case, a constant displacement is applied in a way that the crack only partly propagates through the specimen.

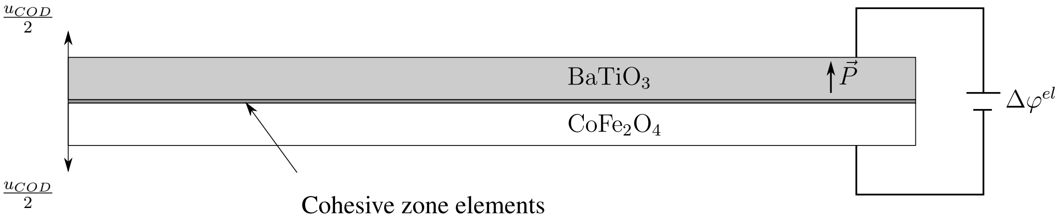

Figure 2: Two-layer-composite made of $\mathrm{BaTiO_3}$ and $\mathrm{CoFe_2O_4}$

3.2 Fracture behavior under mode I/II/IV/V loading

Figure 3 shows load-displacement-curves for different electric loadings ranging from -1000 to 1000 V/mm. For positive signs, the electric field is parallel to the poling direction and for negative ones it is antiparallel. One can clearly see a significant nonlinear influence of the electric field on the fracture behavior and at the same time an independece of the sign of the electric

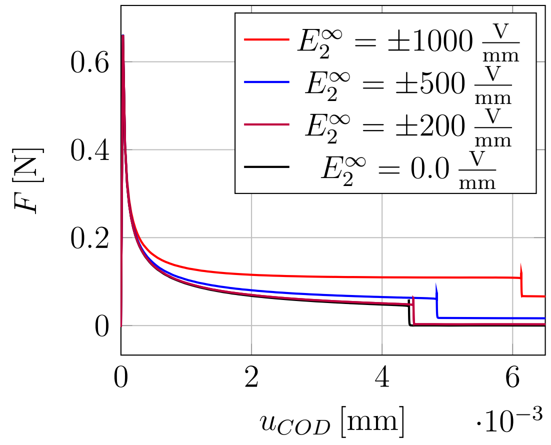

Figure 3: Load-displacement curves of the DCB-specimen with linearly increased opening displacements and different electric fields.

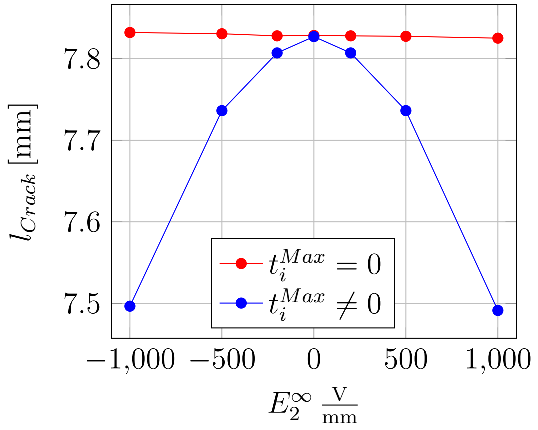

Figure 4: Crack lengths for a constant opening displacement $u_{COD} = 1.0 \cdot 10^{-3}$ mm and different electric fields simulated with and without Maxwell stresses.

⇒ TABLE OF CONTENTS

field. This leads to the conclusion that, lacking piezoelectric properties of the cohesive or fracture process zone, the only relevant influence of the electric load on the fracture behavior comes from the Maxwell stresses which are proportional to the square of the electric field in the crack. The same conclusion can be drawn from the results shown in figure 4. Here, the crack lengths for a constant opening displacement $u_{COD} = 1.0 \cdot 10^{-3}$ mm and various electric fields simulated with and without Maxwell stresses are shown. The crack lengths show a quadratic dependence on the electric field due to the Maxwell stresses. The results without Maxwell stresses show a small ($\ll 1\%$) dependence on the electric field which might be caused by the Mode-II contribution of the loading.

4 Conclusion

A cohesive zone element for delamination under magnetoelectromechanical loading has been developed and implemented in the commercial FEM software ABAQUS. The influence of Maxwell stresses on the fracture behavior under mode I/II/IV/V loading has been shown at a bimaterial DCB-specimen.

REFERENCES

[1] Avakian, A., Gellmann, R., and Ricoeur, A. (2015). Nonlinear modeling and finite element simulation of magnetoelectric coupling and residual stress in multiferroic composites. Acta Mechanica, 226(8), 2789-2806.

[2] Avakian, A., and Ricoeur, A. (2016). Constitutive modeling of nonlinear reversible and irreversible ferromagnetic behaviors and application to multiferroic composites. Journal of Intelligent Material Systems and Structures, 27(18), 2536-2554.

[3] Hillerborg A, Modéer M, Petersson PE. Analysis of crack formation and crack growth in concrete by means of fracture mechanics and finite elements. Cement Concrete Res 1976;6:773-82.

[4] Hao, T., Shen, Z.: A new electric boundary condition of electric fracture mechanics and its applications. Eng. Fract. Mech. 47, 793802 (1994)

[5] Kozinov, S., Kuna, M., & Roth, S. (2014). A cohesive zone model for the electromechanical damage of piezoelectric/ferroelectric materials. Smart Materials and Structures, 23(5), 055024.

[6] Ricoeur, A., & Kuna, M. (2009). Electrostatic tractions at crack faces and their influence on the fracture mechanics of piezoelectrics. International journal of fracture, 157(1-2), 3.

⇒ TABLE OF CONTENTS

A LAMINATE-BASED MATERIAL MODEL APPLIED TO FERROELECTRICS

R. Schulte[1,*], **A. Menzel**[1,2], **and B. Svendsen**[3,4]

[1] Institute of Mechanics, Mechanical Engineering, TU Dortmund University
Leonhard-Euler-Str. 5, 44227 Dormtund, Germany

[2] Division of Solid Mechanics, Construction Sciences, Lund University
P. O. Box 118, 22100 Lund, Sweden

[3] Chair of Material Mechanics, Construction Sciences, RWTH Aachen University
Schinkelstrasse 2, 52062 Aachen, Germany

[4] Microstructure Physics and Alloy Design, Max-Planck-Institute for Iron Research GmbH
Max-Planck-Strasse 1, 40237 Duesseldorf, Germany

Abstract. *In this contribution, a micromechanically motivated material model for ferroelectric materials is developed via a laminate-based modelling approach to simulate the single- and polycrystalline tetragonal ferroelectric material behaviour In this model, the volume average of the occurring variant fractions are directly taken into account at the material point level. Fischer-Burmeister nonlinear complementarity functions (NCP) are employed and investigated considering the efficiency to solve the complementarity conditions of the applied internal variables. Additionally, finite element based simulation results are compared to experimental hysteresis data for barium titanate piezoceramics.*

1 Introduction

In order to predict the material behaviour of ferroelectrics, mathematically sound models are required which can be divided into three different groups. On the one hand, phenomenological models can be formulated while on the other hand, micromechanically motivated material models, as the presented laminate-based model, can be applied. In contrast to the first type which accounts for macroscopic effects, the latter is based on the unit cell switching. If the microstructure needs to be resolved in space and time, phase field or level sets methods can be employed. Laminate-based models are based on the mixture theory and can predict the evolving microstructures. Domain engineering, the construction of energy minimizing multi-rank laminates and polarization as well as strain compatibility conditions were introduced by [6, 8]. In the following a laminate-based model is presented to analyse the rate- and external stress-dependent domain evolution. Thus, a Gibbs energy is developed with an underlying rate-dependent evolution of the multi-rank laminate fractions. The inequality constraints for the laminate fractions are efficiently solved via Fischer-Burmeister (FB) NCP functions. In the following, numerical investigations as well as parameter studies with experimental data, and simulations are conducted.

---

[*] Corresponding author: R. Schulte (✉ robin.schulte@tu-dortmund.de)

⇒ TABLE OF CONTENTS

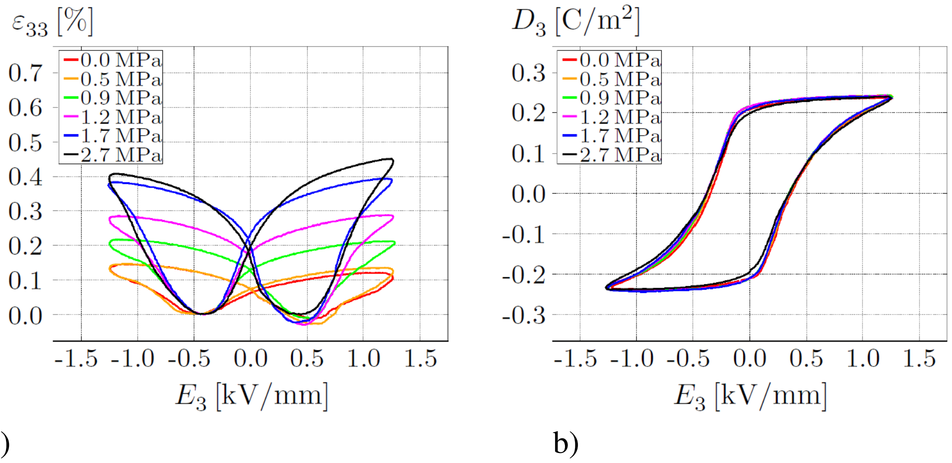

Figure 1: Experimental butterfly curves a) and dielectric hysteresis loops b) for [001]-oriented single crystal tetragonal $\mathrm{BaTiO_3}$, cp. [1, 2, 7].

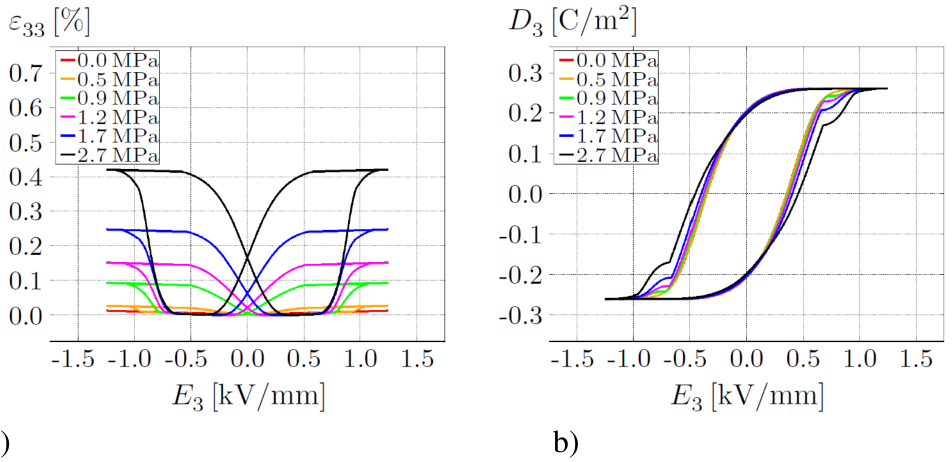

Figure 2: Simulated butterfly curves a) and dielectric hysteresis loops b) obtained under homogeneous deformation for an electromechanical loading path. Varying magnitudes of compressive loading remain constant and cyclic electrical field applied at 0.2 Hz, cp. [1, 2].

2 Laminate-based material model for ferroelectric materials

Considering ferroelectric materials, e.g. $\mathrm{BaTiO_3}$, the crystal lattice consists of a tetragonal crystal structure below the Curie temperature with a spontaneous polarization direction. In total, six different variants can occur depending on this polarization direction. At the material point level, the contribution of each variant can be captured by applying the concept of volume fractions with the theory of mixtures. Thus, the volume fractions λ_j are related to the six possible variants, cp. [1, 2, 3]. To take the laminate microstructure of the material into account, the volume fractions can be transferred into laminate fractions via the following equations

$$\mu^j = \begin{cases} 0 & \text{for} \quad \sum_{\alpha=1}^{j-1} \lambda_\alpha = 1\,, \\ \dfrac{\lambda_j}{1-\sum_{\alpha=1}^{j-1}\lambda_\alpha} & \text{otherwise}\,, \end{cases} \tag{1}$$

⇒ TABLE OF CONTENTS

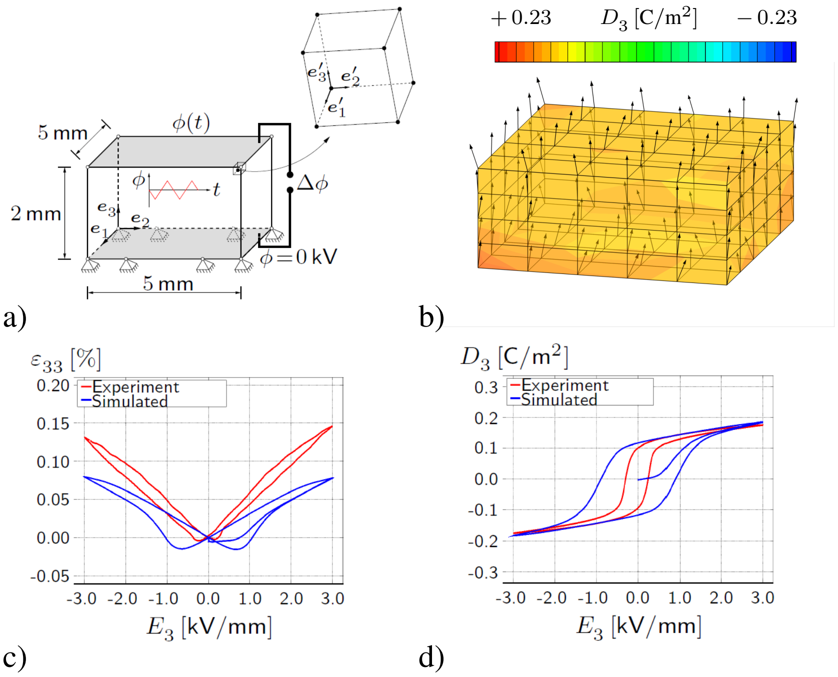

Figure 3: The boundary conditions and cyclic electrical load curve are shown in a) and a snapshot of the FEM simulation in b) while the comparison of experimental and simulated butterfly curves and dielectric hysteresis loops can be seen in c) and d), respectively, cp. [1, 2].

with $j = 1, \ldots, n_v - 1$. Next, the following Gibbs energy function H can be introduced, containing a fully electro-mechanically coupled piezoelectric and a remanent contribution

$$H(\boldsymbol{\varepsilon}^{\mathrm{e}}, \boldsymbol{e}, \boldsymbol{\mu}) = H^{\mathrm{piezo}}(\boldsymbol{\varepsilon}^{\mathrm{e}}, \boldsymbol{e}, \boldsymbol{\mu}) + H^{\mathrm{rem}}(\boldsymbol{\mu}) \,, \tag{2}$$

$$H^{\mathrm{piezo}} = \frac{1}{2}\,\boldsymbol{\varepsilon}^{\mathrm{e}} : \mathsf{E}^{\mathrm{M}} : \boldsymbol{\varepsilon}^{\mathrm{e}} - \boldsymbol{e} \cdot \mathbf{e}^{\mathrm{M}} : \boldsymbol{\varepsilon}^{\mathrm{e}} - \frac{1}{2}\,\boldsymbol{e} \cdot \boldsymbol{\epsilon}^{\mathrm{M}} \cdot \boldsymbol{e} - \boldsymbol{p}^{\mathrm{M}} \cdot \boldsymbol{e} \,, \tag{3}$$

$$H^{\mathrm{rem}} = \frac{1}{c}\left[\frac{1}{2}\,p^{\mathrm{sat}}\,\ln\big(1 - [\,p^{N}(\boldsymbol{\mu})\,]^{2}\big) + \|\boldsymbol{p}^{\mathrm{M}}\|\,\mathrm{arctanh}\big(p^{N}(\boldsymbol{\mu})\big)\right] , \tag{4}$$

where $[\bullet]^{\mathrm{M}}$ denotes the volume averaging at the material point level. Finally, the following rate dependent evolution equations can be introduced,

$$\dot{\mu}^{j} = \frac{1}{\eta}\,\big\langle |f^{j}| - q^{\mathrm{c},j}(\boldsymbol{\mu})\big\rangle^{m}\,\frac{f^{j}}{|f^{j}|} \qquad \text{for} \qquad j = 1, \ldots, n_v - 1 \,, \tag{5}$$

wherein $\langle[\bullet]\rangle = \max\{0, [\bullet]\}$, which can be shown to satisfy the dissipation inequality $\sum_{j=1}^{n_v-1} f^{j}\,\dot{\mu}^{j} \geq 0$. Figures 1-3 are presenting comparisons between experimental and simulated results corresponding to the presented laminate-based material model.

3 Investigations on Fischer-Burmeister NCP functions

For the previously introduced laminate fractions as internal variables, additional constraints $r_I^j := \mu^j \geq 0$ and $r_{II}^j := 1 - \mu^j \geq 0$ need to be fulfilled. By introducing Lagrange multipliers Γ_j^i, the following complementarity conditions can be achieved

$$r_i^j \geq 0, \qquad \Gamma_i^j \geq 0, \qquad r_i^j\,\Gamma_i^j = 0, \qquad i = I, II \,. \tag{6}$$

This system of equality and inequality constraints can be efficiently solved by reformulating the equality constraint into the FB NCP function. In this work, several selected approaches for the following smoothed version of the FB NCP function, such as

⇒ TABLE OF CONTENTS

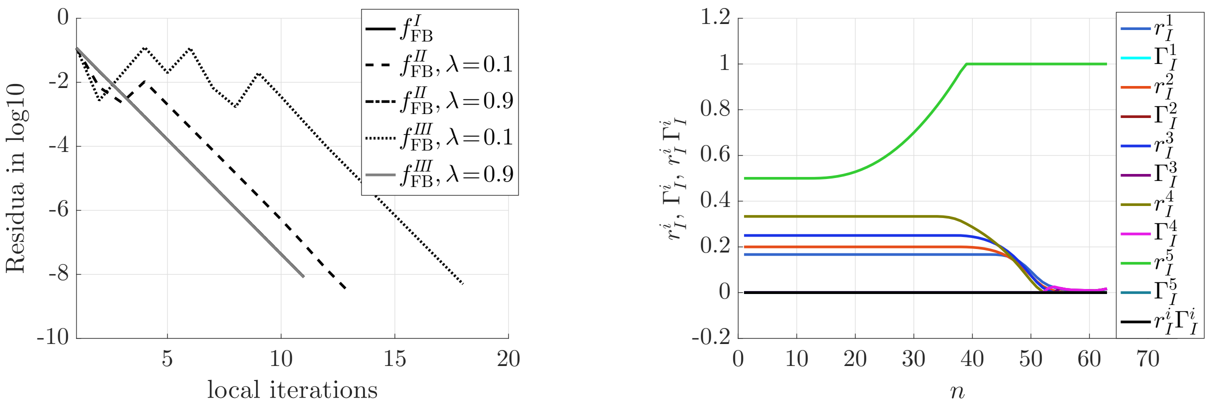

a) b)

Figure 4: a) Local convergence for different FB functions at $t = 1.1$ s for $\delta = 10^{-6}$ with $\Delta t = 0.02$s and b) evolution of the first set of constraints for laminate fractions.

$$f^{I}_{\mathrm{FB}} := \sqrt{[r^j_i]^2 + [\Gamma^j_i]^2 + 2\,\delta^2} - [r^j_i + \Gamma^j_i]\,, \tag{7}$$

cp. [4, 5], are investigated in terms of convergence. In Figure 4, the local convergence is exemplarily shown for three different FB approaches at a certain time step. Figure 4b) shows the evolution of the first set of constraints of the laminate fractions, which are fulfilled for all time steps.

REFERENCES

[1] D.K. Dusthakar, A. Menzel, and B. Svendsen. Laminate-based modelling of single and polycrystalline ferroelectric materials application to tetragonal barium titanate, *Mechanics of Materials*, 117: 235–254, 2018.

[2] D.K. Dusthakar. Computational modelling of single and polycrystalline ferroelectric materials, *PhD thesis*, TU Dortmund, 2017.

[3] D.K. Dusthakar, A. Menzel, and B. Svendsen. Comparison of phenomenological and laminate-based models for rate-dependent switching in ferroelectric continua, *GAMM Mitteilungen*, 38: 147–170, 2015.

[4] C. Kanzow. Some noninterior continuation methods for linear complementarity problems, *SIAM Journal on Matrix Analysis and Applications*, 17(4): 851–868, 1996.

[5] B. Kiefer, T. Bartel, and A. Menzel. Implementation of numerical integration schemes for the simulation of magnetic SMA constitutive response, *Smart Materials and Structures*, 21: 094007, 2012.

[6] J.Y. Li, and D. Liu. On ferroelectric crystals with engineered domain configurations, *Journal of the Mechanics and Physics of Solids*, 52(8): 1719–1742, 2004.

[7] J. Shieh, J.-H. Yeh, Y.-C. Shu, and J.-H. Yen. Operation of multiple 90° switching systems in barium titanate single crystals under electromechanical loading, *Applied Physics Letters*, 91(6): 062901, 2003.

[8] J.H. Yen, Y.C. Shu, J. Shieh, and J.H. Yeh. A study of electromechanical switching in ferroelectric single crystals, *Journal of the Mechanics and Physics of Solids*, 56(6): 2117–2135, 2008.

⇒ TABLE OF CONTENTS

PHASE-FIELD MODELING OF FRACTURING IN ANISOTROPIC PIEZOELECTRIC MATERIALS

A. Sridhar[1] **and M.-A. Keip**

[1] Institute of Applied Mechanics (CE), University of Stuttgart
Pfaffenwaldring 7, 70569, Stuttgart, Germany

Abstract. *Structural reliability analysis of piezoelectric ceramics needs the modeling of failure under coupled electro-mechanical actions. Based on experimental results available in the literature, we suggest a non-associative dissipative framework where the fracture phase field is driven by the mechanical part of the coupled electro-mechanical driving force. Proposed degradation functions account for different electrical crack boundary conditions. The modeling capability of the framework is demonstrated by means of representative numerical examples.*

1 Introduction

In the past decades a lot of research has been done in the field of coupled electromechanical fracturing. Comprehensive overviews of theoretical approaches are provided the works [1, 2, 3, 5, 6]. Recent works [7, 8] have focused on electro-mechanical boundary conditions on the crack faces. In this work we focus on extending the isotropic fracture criteria to account for transverse isotropy in the coupled electro-mechanical setting while accounting for electrical crack conditions by appropriate choice of degradation functions.

2 Phase-field approximation of anisotropic crack topology

Let $\mathcal{B} \subset \mathcal{R}^{\omega}$ represent the configuration of a material body with dimension $\omega \in [1, 2, 3]$ in space and let $\partial\mathcal{B} \subset \mathcal{R}^{\omega-1}$ represent it's surface. Then we consider the crack phase field

$$\alpha : \begin{cases} \mathcal{B} \times \mathcal{T} \rightarrow [0, 1] \\ (\mathbf{x}, t) \mapsto \alpha(\mathbf{x}, t) \end{cases} , \tag{1}$$

characterizing for $\alpha = 0$ the unbroken and for $\alpha = 1$ the fully broken state of the material at $\mathbf{x} \in \mathcal{B}$. Following the recent work of [9], we propose the first-order anisotropic crack density function as,

$$\gamma_l(\alpha, \nabla\alpha; \mathbf{A}) = \frac{1}{2l}\alpha^2 + \frac{l}{2}\nabla\alpha \cdot \mathbf{A} \cdot \nabla\alpha \,, \tag{2}$$

where $\mathbf{A}$ is a generic second-order structural tensor that characterizes the anisotropic microstructure of the material. Note that the choice $\mathbf{A} = \mathit{1} := \delta_{ij}\mathbf{e}_i \otimes \mathbf{e}_j$ recovers isotropy. For a transversely isotropic microstructure the tensor $\mathbf{A}$ can be defined as

$$\mathbf{A} := \mathit{1} + \beta\mathbf{M} \quad \text{with} \quad \mathbf{M} := \mathbf{a} \otimes \mathbf{a} \,, \tag{3}$$

where $\mathbf{a}$ is a given structural director with $||\mathbf{a}|| = 1$ and β is a measure of anisotropy.

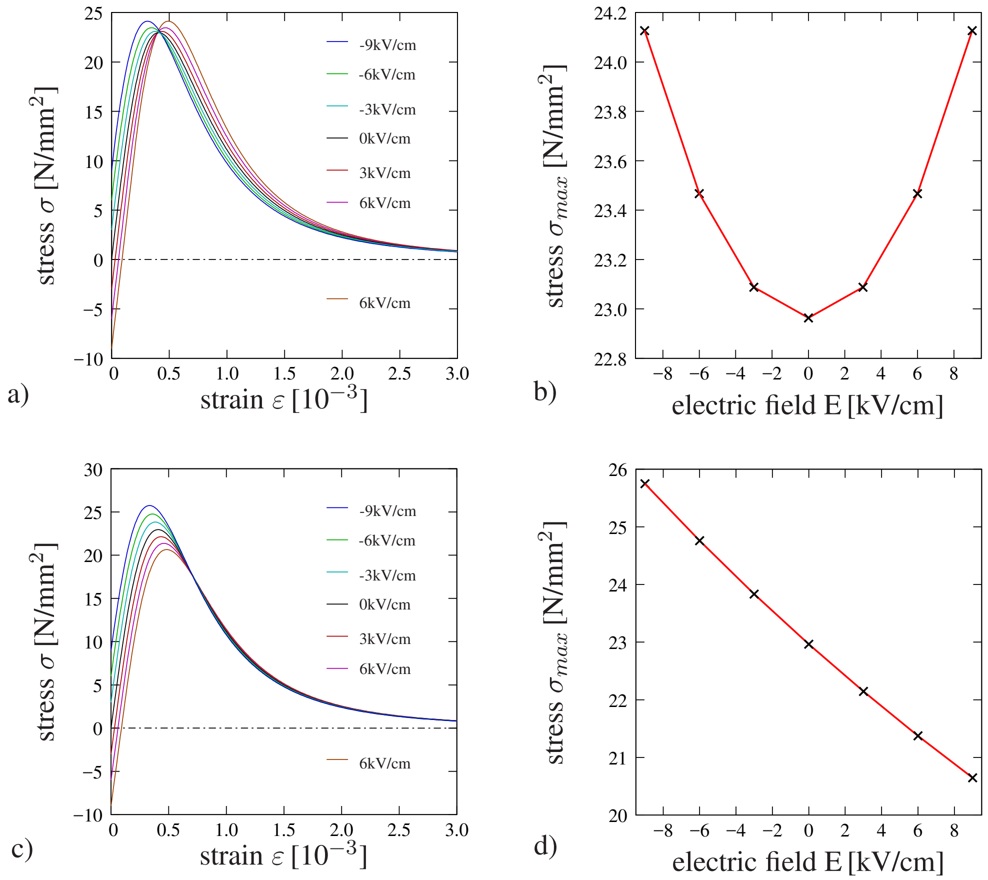

Figure 1: Response of one-dimensional electro-mechanical damage model with complete electro-mechanical energy and pure mechanically driven damage accumulation. a) and c) show the stress-strain response for both the models for different applied electric fields E. b) and d) show the dependence of the maximum stress before fracture versus the applied electric field.

3 Variational principle for evolution of fracture phase field in piezoelectrics

Here we focus on a theory of fracture in linear piezoelectrics by considering a total pseudo-energy functional

$$W(\mathbf{u},\phi,\alpha) := E(\mathbf{u},\phi,\alpha) + \Gamma_l(\alpha) := \int_{\mathcal{B}} w(\nabla_s\mathbf{u}, -\nabla\phi, \alpha, \nabla\alpha)\, dV\,, \tag{4}$$

where $\mathbf{u} \in \mathcal{R}^{\omega}$ is the displacement and $\phi \in \mathcal{R}$ is the electric potential of the material point $\mathbf{x} \in \mathcal{B}$. $E(\mathbf{u},\phi,\alpha)$ is the stored total energy functional of the bulk and $\Gamma_l(\alpha)$ is the regularized anisotropic crack surface functional. The constitutive total pseudo-energy-density function $w(\boldsymbol{\varepsilon},\mathbf{E},\alpha,\nabla\alpha)$ can be split such that

$$w(\boldsymbol{\varepsilon},\mathbf{E},\alpha,\nabla\alpha) = \Psi(\boldsymbol{\varepsilon},\mathbf{E},\alpha) + g_c\gamma_l(\alpha,\nabla\alpha;\mathbf{A})\,. \tag{5}$$

Where Ψ is a specific representation of the bulk electo-mechanical total energy of the piezoelectric material, γ_l is the anisotropic crack surface density function introduced in Eq.(2) and g_c is a material parameter. With the standard definition of the linearized strain tensor $\boldsymbol{\varepsilon} = \nabla_s\mathbf{u}$ and electric field $\mathbf{E} = -\nabla\phi$.The energy $\Psi(\boldsymbol{\varepsilon},\mathbf{E},\alpha;\mathbf{a})$ is given as

$$\Psi(\boldsymbol{\varepsilon},\mathbf{E},\alpha;\mathbf{a}) := g_m(\alpha)\psi_m(\boldsymbol{\varepsilon}) + g_{em}(\alpha)\psi_{em}(\boldsymbol{\varepsilon},\mathbf{E};\mathbf{a}) + g_e(\alpha,\xi)\psi_e(\mathbf{E}) + \Psi_{vac}(\mathbf{E})\,. \tag{6}$$

---

[*] Corresponding author: A. Sridhar (✉ sridhar@mechbau.uni-stuttgart.de)

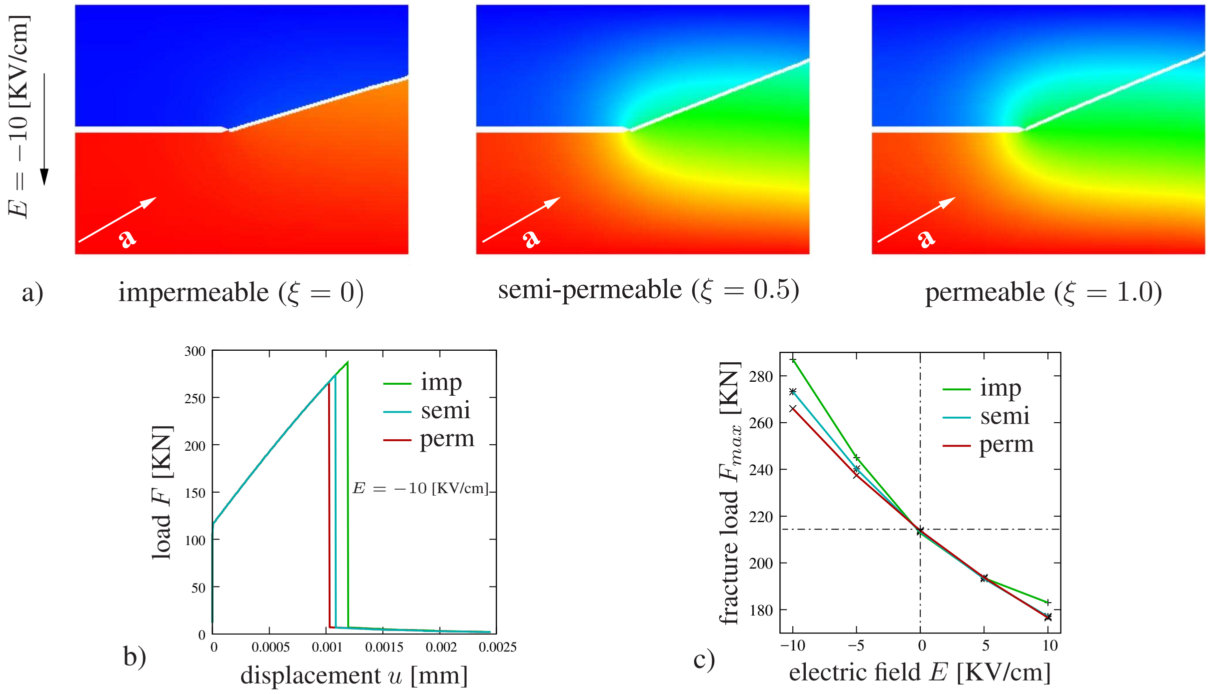

a) impermeable ($\xi = 0$) semi-permeable ($\xi = 0.5$) permeable ($\xi = 1.0$)

b) c)

Figure 2: Anisotropic crack propagation for different electrical properties of the crack. a) Contours of the electric-potential distribution are plotted for different crack conditions characterized by $\xi = 0$ impermeable, $\xi = 0.5$ semi-permeable and $\xi = 1$ permeable. b) Load-displacement plot for applied electric field of $E = -10$ KV/cm shows influence of crack conditions and c) fracture load plotted for different applied electric fields.

Where g_m, g_{em} and g_e are the mechanical, coupled and electric degradation functions respectively and are chosen as,

$$g_m := g_{em} := (1-\alpha)^2 \quad \text{and} \quad g_e := 1 + 2(\xi - 1)\alpha + (1-\xi)\alpha^2 \quad \text{with} \quad \xi := \epsilon_c/\epsilon_s \,. \tag{7}$$

Where $\xi := \epsilon_c/\epsilon_s$ is the ratio of the crack permitivitty to the permitivitty of the bulk solid. Varied crack boundary conditions can be obtained by appropriate choice of ξ, see Fig. 2. Furthermore, consider a dissipation potential functional

$$D(\dot{\alpha}) = \int_{\mathcal{B}} \Phi(\dot{\alpha})\, dV \,, \tag{8}$$

that depends on a convex and non-smooth dissipation potential density function Φ. The phase field formulation is specified to a setting accounting for irreversibility of the fracture phase field. This is achieved by choosing the non-smooth dissipation potential function

$$\Phi(\dot{\alpha}) = I(\dot{\alpha}) + \frac{\eta}{2}\dot{\alpha}^2 \,, \tag{9}$$

in terms of the non-smooth indicator function of the set $\mathcal{R}_+$ of positive real numbers. The two functionals W and D define the rate-potential functional

$$\Pi(\dot{\mathbf{u}}, \dot{\phi}, \dot{\alpha}) = \frac{\mathrm{d}}{\mathrm{d}t} W + D \,, \tag{10}$$

that governs the variational principle for the evolution problem for coupled electro-mechanical fracturing,

$$\{\dot{\mathbf{u}}, \dot{\phi}, \dot{\alpha}\} = \mathrm{Arg}\{ \inf_{\dot{\mathbf{u}} \in \mathcal{W}_{\dot{\mathbf{u}}}} \sup_{\dot{\phi} \in \mathcal{W}_{\dot{\phi}}} \inf_{\dot{\alpha} \in \mathcal{W}_{\dot{\alpha}}} \Pi(\dot{\mathbf{u}}, \dot{\phi}, \dot{\alpha}) \} \,. \tag{11}$$

⇒ TABLE OF CONTENTS

The Euler-Lagrange equations of the formulation are obtained as the balance of liner momentum, Gauss's law of electrostatics and a generalized Ginzburg-Landau type evolution equation for the phase field

$$\operatorname{div}[\partial_{\nabla_s \mathbf{u}} w] = \boldsymbol{0}, \quad \operatorname{div}[\partial_{-\nabla\phi} w] = 0 \quad \text{and} \quad \dot{\alpha} = \Big\langle -\frac{1}{\eta}\delta_\alpha w \Big\rangle_+ . \tag{12}$$

We choose in this work the mechanical driving force as the fracture driving force, following the works of [5] and [4]. Such a framework characterizes the dissipative framework as a *non-associative setting* and captures the fracture phenomenon seen in experiments, see Fig. 3.

4 Numerical Example

A piezoelectric ceramic poled at 30° is subjected to a mode 1 tensile test under combined electro-mechanical loading. The crack propagation follows the poling direction as can be seen from the contour plots. The load-versus-displacement plots and the fracture load for various applied electric fields are plotted. The results are in agreement with experimental observations [4].

REFERENCES

[1] Y.E. Pak. Linear electro-elastic fracture mechancis of piezoelectric materials. *International Journal of Fracture*, 54: 79–100, 1992.

[2] H. Gao, T. Zhang and P. Tong. Local and global energy release rates for an electrically yielded crack in a piezoelectric ceramic. *Journal of the Mechanics and Physics of Solids*, 45: 491–510, 1997.

[3] Z. Suo, C. Kuo, D. Barnett and J. Willis. Fracture mechancis for piezoelectric ceramics. *Journal of the Mechancis and Physics of Solids*, 40: 739–765, 1992.

[4] S. Park and C.-T. Sun, Fracture Criteria for Piezoelectric Ceramics, *Journal of the American Ceramic Society*, 78: 1475–1480, 1995.

[5] C. Miehe, F. Welschinger, M. Hofacker, A phase field model of electromechanical fracture, *Journal of the Mechanics and Physics of Solids*, 58: 1716–1740, 2010.

[6] B.-X. Xu, D. Schrade, D. Gross and R. Müller, Fracture simulation of ferroelectrics based on the phase field continuum and a damage variable, *International Journal of Fracture*, 166: 163–172, 2010.

[7] C.M. Landis. Energetically consistent boundary conditions for electromechanical fracture. *International Journal of Solids and Structures*, 41: 6291–6315, 2004.

[8] A. Abdollahi and I. Arias. Phase-field modeling of the coupled microstructure and fracture evolution in ferroelectric single crystals. *Acta Materialia*, 59: 4733–4746, 2011.

[9] S. Teichtmeister, D. Kienle, F. Aldakheel and M.-A. Keip. Phase field modeling of fracture in anisotropic brittle solids. *International Journal of Non-Linear Mechanics*, 97: 1–21. 2017.

Characterizing Magnetoelectricity at Local Scale

Harsh Trivedi[1,*], Vladimir V. Shvartsman[1], Robert C. Pullar[2], Pavel Zelenovisky[3], Vladimir Ya. Shur[3], Doru C. Lupascu[1]

[1]Institute for Materials Science and Center for Nanointegration Duisburg-Essen (CeNIDE), University of Duisburg-Essen, 45141, Essen, Germany

[2]CICECO, University of Aveiro, 3810-193, Aveiro, Portugal

[3]Center for Shared Use "Modern Nanotechnology", Institute of Natural Sciences, Ural FederalUniversity,620000, Yekaterinburg, Russia

Abstract. *A growing interest in studying local manifestations of macroscopic functionalities has led to a wide spread development in Scanning Probe Microscopy (SPM). In this study we demonstrate the potential of various cantilever based microscopic techniques like Piezoresponse Force Microscopy (PFM), Magnetic Force Microscopy (MFM), and Kelvin Probe Force Microscopy (KPFM), in conjunction with near-field optical microscopy, for studying the local manifestations of the strain mediated magnetoelectric effect in various classical composite systems like $AFe_2O_4 – BaTiO_3$ (A = Co, Ni) and $AFe_{12}O_{19} – BaTiO_3$ (A = Ba, Sr). The outcomes not only present an opportunity to gauge the magnitude of the effect locally, but also reveals interesting magneto-electro-mechanical interplay contribution that could be rationalized through theoretical modeling.*

1 Introduction

One possible way to induce the magnetoelectric (ME) effect in composites of piezoelectric and magnetostrictive phases is strain. The magnetically/electrically induced strain in the magnetostrictive/piezoelectric phase leads to a mechanical stress on the adjacent phase, which ultimately results in voltage/magnetic flux generation [1–4]. Due to a wide range of choices available for suitably-performing magnetostrictive and piezoelectric phases, the composite approach to form a magnetoelectric material has been well exploited. However, the performance of such composites, which is gauged by the magnetoelectric coefficient α, is often found to be weak and highly variable even within a given material system [5–7]. Of the various possible phase connectivity schemes for magnetoelectric composites, the multilayered configuration (2-2) is the simplest, and also most frequently studied due to the high magnetoelectric coefficient values and the option of mechanical resonators [8]. More convenient processing routes, such as powder technology, yield more complex connectivity schemes (e.g., 0-0, 3-3) resulting in weaker and highly variable magnetoelectric coefficients. The effective coupling is highly localized in such complex connectivity schemes, and is often difficult to measure due to the high electrical leakage. Hence, to fully characterize the magnetoelectric effect, it becomes essential to devise methods to observe the coupling at the local scale.

In recent years, there have been significant advances in microscopic techniques for imaging ferroelectric (Piezoresponse Force Microscopy; PFM), as well as ferromagnetic (Magnetic Force Microscopy; MFM), domains [9–11]. Taking advantage of these techniques, several interesting studies of local magnetoelectricity have followed [12–13]. Zavaliche et al. were the first to demonstrate the direct imaging of electrically switched magnetic orientation of self-organized

---

[*] Corresponding author: H. Trivedi (harsh.trivedi@uni-due.de)

$CoFe_2O_4$ columns in a $BiFeO_3$ thin-film matrix [14]. The results have so far mostly been only qualitative in nature. An accurate quantitative estimation of order parameter changes at the nanoscale is still a challenge. Some reports claim a rough estimation of the local ME coefficient using a change of MFM contrast [15]. However, such estimations are not very accurate. Above all, a key question which is unanswered yet concerns the fact that, since the constituents are ferroic, it could be either a locally induced polarization/magnetization change, and/or a stress induced motion of domain walls. Both mechanisms can contribute to the overall ME effect in composites.

2 Overview of The Microscopic Methods

Technically MFM is realized by operating an AFM in non-contact mode with a magnetic tip. The interaction between tip and the magnetic surface structures leads to a variation in the dynamic properties of the cantilever, which is sensed in the form of the output signal. MFM senses field gradients and not the field itself hence the output has to be interpreted carefully. For example, depending on the orientation of the magnetization vector: in plane or out of plane, the maximum MFM signal will correspond to a domain itself or to a domain wall. Furthermore, the quantification of the MFM signal in terms of magnetization is a non-trivial task.

PFM is a modification of contact AFM especially developed for investigating nanoscale properties of ferroelectrics. It is based on the detection of local electromechanical deformations of a ferroelectric sample, $\Delta z(\omega) = d_{33} \cdot V_{ac}$, caused by an external ac electric voltage, V_{ac}, applied between the conducting AFM tip and a counter electrode. Field induced vibration of the sample surface is transmitted into a periodical deflection of the cantilever that is detected using a lock-in amplifier. Monitoring the first harmonics of this cantilever deflection allows visualizing electromechanical response of the ferroelectric domains.

3 Key Results

By means of PFM, it was possible to explore various effects of the applied magnetic field onto the ferroelectric domains. The key outcomes of this study were: i) piezoelectric coefficient is locally

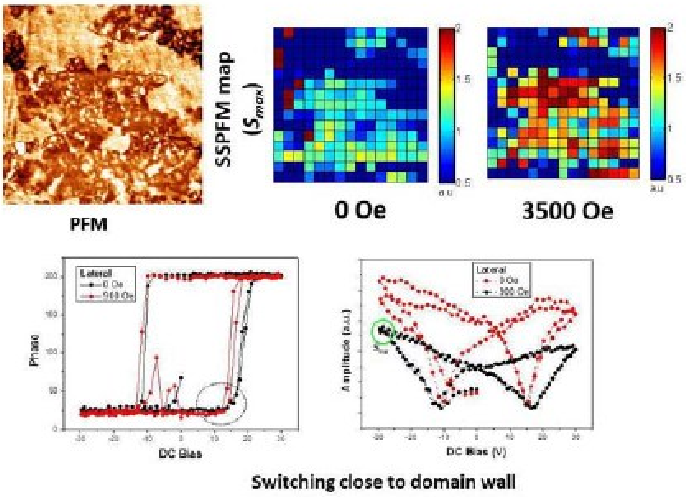

Figure 1: SSPFM experiment over a spatial grid on $BaTiO_3 – BaFe_{12}O_{19}$ sample. The maps on the to-right represents the magnetic field modulation of the reverse switching field (demonstrated by circle in the hysteresis loop in bottom left graph). The graph in bottom left displays the modulation of local piezoelectric coupling upon application of magnetic field [16].

modulated under the effect of the magnetically induced stress, and that ii) the stress also modulates trapped charges at the interface, which was visible in the modulated local switching dynamics. These results are summarized in the switching spectroscopy PFM (SSPFM) experiments over a spatial grid (Figure 1). The effect of the applied magnetic field on the local piezoelectric coupling can be mathematically expressed as [16]:

$$\Delta d_{kij} = Q_{ijml}(\alpha_{ln}\Delta H_n \varepsilon_{mk} + \alpha_{mn}\Delta H_n \varepsilon_{lk}) \qquad (3)$$

In the variable-field PFM experiment one effectively measures Δd_{eff} (x, y) = f (x, y, H0, E0, ΔH), and hence an exact observation of equation (3) is not trivial. Despite this limitation, PFM can reveal the intensity of the ME effect at a local scale, which could be useful information to relate the ME coupling to the material properties as well as microstructure.

Secondly, MFM was used to measure the residual magnetic domains state after application of electric field via the SPM tip. It can be seen from Figure 2 that a significant stochastic change of magnetic domain state has taken place after the application of electric field. Certain generalization about the MFM contrast mechanism were used in conjunction with image processing algorithms to extract the values of domain-wall width change, based on which the induced change in magnetoelastic anisotropy was estimated. Later on, a comparison of the induced changes and the applied field was carried out based on energy scales to further evaluate the coupling strength at the the local scale.

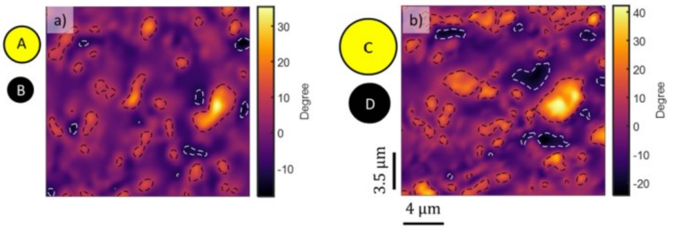

Figure 2: MFM (phase) images for the unpoled (a) and poled (b) states overlaid with the contours obtained at a heuristically chosen signal altitude (black dashed lines; bright contrast) and ½ of the minimum signal (white dashed lines; dark contrast). The small yellow and black circles on the left of each image are the circles with area equivalent to the total bright and dark regions respectively, marked by the contour corresponding to the image above [17].

4 Conclusion

Magnetoelectric coupling in composite multiferroics is visible at the local scale by PFM and MFM. It was expected that the respective domains will interact due to strain coupling. The additional effect of modification of the grain boundary by free charges was observed additionally. It is assigned to the occurrence of a heterojunction of two (wide bandgap) semiconductors, namely the ferroelectric and the magnetic oxides.

REFERENCES

[1] M. Fiebig. Revival of the magnetoelectric effect, *Journal of Physics D: Applied Physics, 38*:123, 2005.

[2] M. I. Bichurin, I. A. Kornev, V. M. Petrov, I. V. Lisnevskaya. Investigation of magnetoelectric interaction in composite, *Ferroelectrics,* 204:289, 1997.

[3] G. Srinivasan, E. T. Rasmussen, J. Gallegos, R. Srinivasan, Y. I. Bokhan, V. M. Laletin. Magnetoelectric bilayer and multilayer structures of magnetostrictive and piezoelectric oxides, *Physical Review B, 64*:214408, 2001.

[4] C. W. Nan. Magnetoelectric effect in composites of piezoelectric and piezomagnetic phases *Physical Review B, 50*:6082, 1994.

[5] M. Etier, C. Schmitz-Antoniak, S. Salamon, H. Trivedi, Y. Gao, A. Nazrabi, J. Landers, D. Gautam, M. Winterer, D. Schmitz, H. Wende, V. V. Shvartsman, D. C. Lupascu, Magnetoelectric coupling on multiferroic cobalt ferrite–barium titanate ceramic composites with different connectivity schemes, *Acta Materialia, 90*, 10.1016/j.actamat.2015.02.032, 2015.

[6] V. Corral-Flores, D. Bueno-Baques, D. Carrillo-Flores, J. A. Matutes-Aquino, , Enhanced magnetoelectric effect in core-shell particulate composites *J. Appl. Phys., 99:*08J503/1-3, 2006.

[7] C. Schmitz-Antoniak, D. Schmitz, P. Borisov, de Groot, F. M., S. Stienen, A. Warland, B. Krumme, R. Feyerherm, E. Dudzik, W. Kleemann, H. Wende, Electric in-plane polarization in multiferroic $CoFe_2O_4$/$BaTiO_3$ nanocomposite tuned by magnetic fields, *Nat. Commun.*, *4*:3051/1-8, 2013.

[8] H. Greve, E. Woltermann, H-J. Quenzer, B. Wagner, E. Quandt, Low damping resonant magnetoelectric sensors, Appl. Phys. Lett., 98(18):182501, 2010.

[9] A. L. Kholkin, S. V. Kalinin, A. Roelofs, A. Gruverman, in *Scanning Probe Microscopy* (Ed.: S. V. Kalinin, A. Gruverman) Springer. New York, p. 173, 2007.

[11] A. Ehresmann, I. Krug, A. Kronenberger, A. Ehlers, D. Engel, In-plane magnetic pattern separation in NiFe/NiO and Co/NiO exchange biased bilayers investigated by magnetic force microscopy, *J. Magn. Magn. Mater.*, *280*:369-376*,* 2004.

[12] H. Trivedi, V.V. Shvartsman, D.C. Lupascu, M.S.A. Medeiros, R.C. Pullar, A.L. Kholkin, P. Zelenovskiy, A. Sosnovskikh, V.Y. Shur, Local manifestations of a static magnetoelectric effect in nanostructured $BaTiO_3$-$BaFe_{12}O_9$ composite multiferroics, Nanoscale, 7:4489-4496, 2015.

[13] H. Miao, X. Zhou, S. Dong, H. Luo, F. Li, Magnetic-field-induced ferroelectric polarization reversal in magnetoelectric composites revealed by piezoresponse force microscopy, Nanoscale, 6:85158520, 2014.

[14] F. Zavaliche, H. Zheng, L. Mohaddes-Ardabili, S. Y. Yang, Q. Zhan, P. Shafer, E. Reilly, R. Chopdekar, Y. Jia, P. Wright, D. G. Schlom, Y. Suzuki, and R. Ramesh, Electric Field-Induced Magnetization Switching in Epitaxial Columnar Nanostructures, *Nano Lett*, *5*:1793, 2005.

[15] D.-F. Pan, M.-X. Zhou, Z.-X. Lu, H. Zhang, J.-m. Liu, G.-H. Wang, J.-g. Wan, Local Magnetoelectric Effect in La-Doped $BiFeO_3$ Multiferroic Thin Films Revealed by Magnetic-Field-Assisted Scanning Probe Microscopy, *Nanoscale Res. Lett., 11*:318/1-7, 2016.

[16] D.C. Lupascu, H. Wende, M. Etier, A. Nazrabi, I. Anusca, H. Trivedi, V.V. Shvartsman, J. Landers, S. Salamon, C. Schmitz-Antoniak, Measuring the magnetoelectric effect across scales, GAMM-Mitteilungen, 38:25-74, 2015.

[17] H. Trivedi, V.V. Shvartsman, D. C. Lupascu, M. S. A. Medeiros, R. C. Pullar, Stress induced magnetic-domain evolution in magnetoelectric composites, Nanotechnology, 29: /10.1088/1361-6528, 2018.

⇒ TABLE OF CONTENTS

PHASE TRANSITIONS IN LEAD ZIRCONATE TITANATE INDUCED BY ELECTRIC FIELDS: A MODELING APPROACH

Philip Uckermann[1,*], **Stephan Lange**[1], **and Andreas Ricoeur**[1]

[1] Institute of Mechanics, Chair of Engineering Mechanics and Continuum Mechanics, University of Kassel
Mönchebergstr. 7, 34125 Kassel, Germany

Abstract. *This research is about implementing multi-phase materials with phase transitions within the context of the condensed method. To represent lead zirconate titanate for different chemical compositions appropriately, it is necessary to consider the constituents of the compound separately and to allow for different phases in each constituent with the possibility to change their phase volume fractions. To distinguish phase transitions and domain switching, an adapted evolution law was developed. To describe the inelastic strain of phase transitions the deformation gradient for two triclinic unit cells was derived.*

1 Introduction

Ferroelectric materials are used for a variety of technical applications, for example fuel injections and thermal sensors. Despite containing lead, lead zirconate titanate (PZT) remains one of the most common actuator materials because of its favorable electromechanical properties, particularly at the morphotropic phase boundary (MPB). PZT consists of the two constituents lead titanate and lead zirconate which can both exhibit tetragonal and rhombohedral unit cells, see Fig. 1. One of the most accepted theories for the favorable properties at the MPB is the existence of fourteen instead of six (tetragonal) or eight (rhombohedral) domain variants due to a coexistence of both crystal phases. It is also undoubted today that phase transitions have a non-negligible contribution as well.

The condensed method (CM) was developed to calculate e.g. hysteresis loops or residual stresses for polycrystalline materials without spatial discretization of the grain structure, resulting in low computational effort and large numerical stability [1]. It is suitable for efficient implementation of various constitutive behaviors, accounting for interactions of grains or different constituents of a material compound. Hitherto, it has been applied to tetragonal ferroelectrics, ferromagnetics and multiferroic compounds [2] as well as to life time predictions in ferroelectrics [3].

2 Motivation

Lead zirconate titanate consists of lead zirconate sintered together with lead titanate. Pure lead zirconate at room temperature is made up of rhombohedral unit cells while lead titanate prefers tetragonal ones. That changes in the sintered material, see Fig. 1. Most compositions of PZT are either completely tetragonal or rhombohedral, depending on the preferred phase of the material with the higher content. The exception to this rule is the MPB where both phases coexist. Take for example $\mathrm{Pb(Ti_{0.2}Zr_{0.8})O_3}$ and $\mathrm{Pb(Ti_{0.3}Zr_{0.7})O_3}$ both of which are

---

[*] Corresponding author: Philip Uckermann (Γ philip.uckermann@uni-kassel.de)

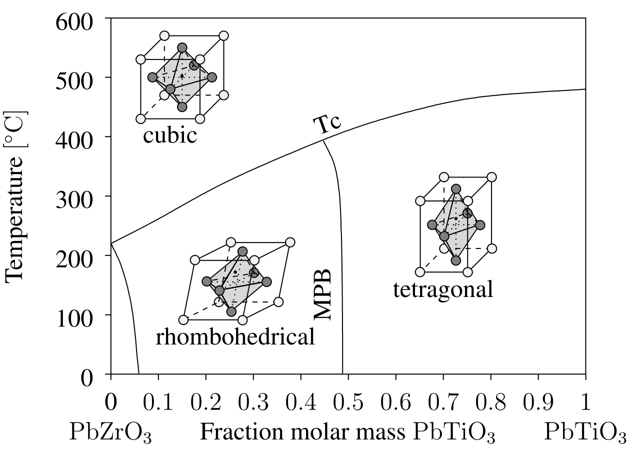

Figure 1: Phase diagram of PZT

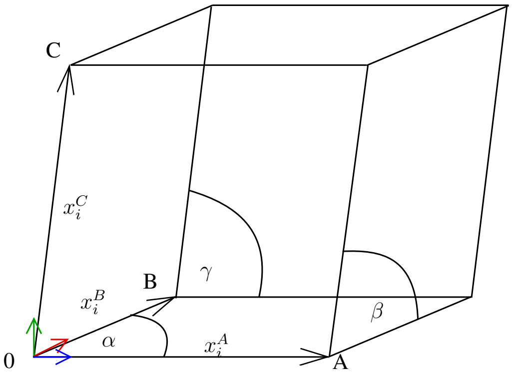

Figure 2: Triclinic unit cell with edge lengths $|x_i^A|$, $|x_i^B|$, $|x_i^C|$, angles α, β, γ and positions of lead ions A, B, C

rhombohedral. Most models use one set of material properties for each phase of PZT, taken from experiments, and average over phase volume fractions to discern macroscopic properties. The material in the first example, however, consists of eighty percent rhombohedral lead zirconate and twenty percent rhombohedral lead titanate. The same holds for the second example with different percentages. Assuming the constituents do not have the same properties, different results are expected when averaging over both phase and constituent volume fractions. This research shows the advantages of distinguishing the constituents instead of just the phases.

3 Kinematics

To describe spontaneous strains caused by phase transitions the unit cell before the transition will be used as reference configuration and the one after the transition as current configuration. Assuming no translation and homogeneous strains inside the volume undergoing the transition the deformation gradient F_{ij} relates coordinates of the reference and the current configuration, i.e. X_i and x_i:

$$x_i = F_{ij} X_j . \tag{1}$$

Both tetragonal and rhombohedral unit cells are special cases of triclinic configurations. Using one lead ion as the origin of the corrdinates the position of the others can be described with a set of edge lengths and angles, see Fig. 2. From the displacements $x_i - X_i$ of three ions A,B,C a system of nine equations is obtained to determine the nine tensor coordinates of $F_{ij}^{(\zeta\rightarrow\xi)}$:

$$x_i^A = F_{ij}^{(\zeta\rightarrow\xi)} X_j^A , \quad x_i^B = F_{ij}^{(\zeta\rightarrow\xi)} X_j^B , \quad x_i^C = F_{ij}^{(\zeta\rightarrow\xi)} X_j^C , \tag{2}$$

where ζ describes the domain in reference configuration and ξ in current configuration after transition. The strain tensor is then derived from the deformation gradient.

4 Some aspects of the constitutive model

The associated variables stress σ_{ij} and electric displacement D_i are connected with the independent variables strain ε_{ij} and electric field E_i by the constitutive equations

$$\sigma_{ij} = C_{ijkl} \left(\varepsilon_{kl} - \varepsilon_{kl}^{\text{irr,ds}} - \varepsilon_{kl}^{\text{irr,pt}} \right) - e_{kij} E_k , \tag{3}$$

$$D_i = e_{ikl} \left(\varepsilon_{kl} - \varepsilon_{kl}^{\text{irr,ds}} - \varepsilon_{kl}^{\text{irr,pt}} \right) + \kappa_{ij} E_j + P_i^{\text{irr,ds}} + P_i^{\text{irr,pt}} . \tag{4}$$

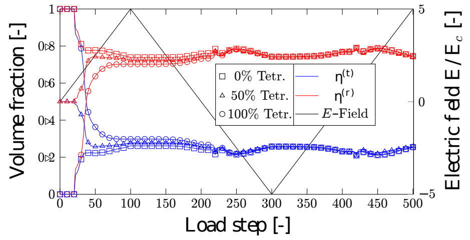

Figure 3: Phase volume fractions for three different initial compositions with properties of PZT at the MPB

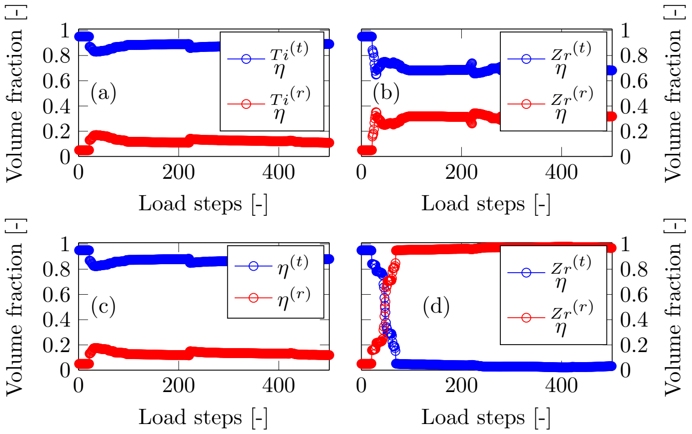

Figure 4: Phase volume fractions: (a), (b) and (c) from one calculation with $\mathrm{Pb(Ti_{0.95}Zr_{0.05})O_3}$, (a) the 95% $\mathrm{PbTiO_3}$, (b) the 5% $\mathrm{PbZrO_3}$, (c) the complete PZT; (d) calculation for pure $\mathrm{PbZrO_3}$

The irreversible terms in Eqs. (3) and (4) are results of domain switching (ds) or phase transitions (pt). These constitutive laws are used at grain level and in a modified form on the macroscopic scale [1]. Using the VOIGT–approximation they represent a solvable system of equations. Since material properties are known only on the domain scale, homogenization is needed. Volume averages are used to determine properties on the next higher level. For example the properties of the six tetragonal variants are weighted with the volume fraction of each domain ν_t^i to get properties on the phase level. The properties at phase level are weighted with the phase volume fraction η to get constituent's properties. Those are weighted with molar mass fraction for grain properties. The CM finally introduces polycrystalline behavior on the macroscopic scale. The energy barriers for phase transitions are modeled in the style of domain switching using only electrical contributions:

$$w^{(\mathrm{crit})}_{(\zeta\to\xi)} = E_c \frac{P_i^{(\zeta\to\xi)}}{|P_i^{(\zeta\to\xi)}|} P_i^{(\zeta\to\xi)}. \tag{5}$$

If the dissipative energy $w^{(\mathrm{diss})}_{(\zeta\to\xi)}$, depending on stresses and electric fields at grain level in connection with spontaneous strains and polarizations respectively, is larger than this barrier a small part of the volume fraction $\mathrm{d}\nu^{(\zeta)} = -\mathrm{d}\nu^{(\xi)} = -\mathrm{d}\nu_0$ changes. This can be described by an evolution law, containing the HEAVISIDE–function and a related function $\mathcal{A}(x)$ differing only by yielding zero for $x = 0$:

$$\mathrm{d}\nu^{(\zeta)} = -\mathrm{d}\nu^{(\xi)} = \begin{cases} -\mathrm{d}\nu_0 \mathcal{H}\left(\dfrac{w^{\mathrm{diss}}_{(\zeta\to\xi),\mathrm{ds}}}{w^{\mathrm{crit}}_{(\zeta\to\xi),\mathrm{ds}}} - 1\right) \mathcal{A}\left(\dfrac{w^{\mathrm{diss}}_{(\zeta\to\xi),ds}}{w^{\mathrm{diss,max}}_{(\mathrm{pt})}} - 1\right) \\ -\mathrm{d}\eta_0 \mathcal{H}\left(\dfrac{w^{\mathrm{diss}}_{(\zeta\to\xi),\mathrm{pt}}}{w^{\mathrm{crit}}_{(\zeta\to\xi),\mathrm{pt}}} - 1\right) \mathcal{A}\left(\dfrac{w^{\mathrm{diss}}_{(\zeta\to\xi),pt}}{w^{\mathrm{diss,max}}_{(\mathrm{ds})}} - 1\right) \end{cases} . \tag{6}$$

5 Some results

Fig. 3 shows phase volume fractions for a material with properties at the MPB exposed to one electric load cycle. The energetically optimal ratio seems to be around seventy to eighty percent of the rhombohedral phase, no matter the material is initially pure rhombohedral or tetragonal. One reason is that in a statistically oriented grain there is a better chance for the eight rhombohedral variants to have their polarization vector aligned along the external field

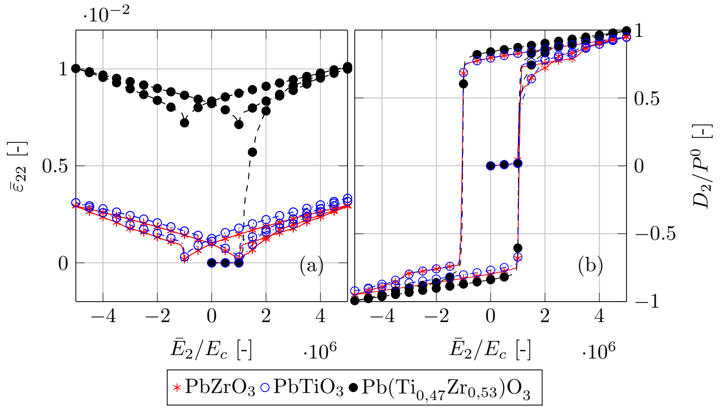

Figure 5: (a) strain and (b) normalized electric displacement vs. normalized electric load

than for the six tetragonal ones. Secondly, the spontaneous strain is larger for the tetragonal phase, thus impeding its alignment. The behavior in Fig. 3 is not realistic, yielding a distinct phase composition independent of the initial state. The chemical composition in terms of the constituents $\mathrm{PbZrO_3}$ and $\mathrm{PbTiO_3}$ with their different material properties has to be introduced in connection with different energy barriers accounting for the direction of the transition.

In Fig. 4, especially comparing plots (b) and (d), the effect of multiple constituents can be seen. PZT with enough ($> 60\%$) lead titanate is almost tetragonal (see Fig. 4 (c)) including the normally rhombohedral lead zirconate, see Fig. 4 (d). In the composition $\mathrm{Pb(Ti_{0.95}Zr_{0.05})O_3}$ lead zirconate changes its behavior, now preferring the tetragonal phase, see Fig. 4 (b).

In Fig. 5 hysteresis loops for pure lead titanate, pure lead zirconate and PZT at the MPB are shown. In (b) the material at the MPB has a slightly larger electric displacement, explained by the better alignment of polarization vectors along the external field. Both remanent and maximum strains in (a) are significantly larger at the MPB, as known from experiments.

6 Conclusion

A constitutive model for ferroelectrics with variable chemical composition and two crystal phases per constituent has been developed and implemented within the framework of the condensed method. Phase transition is taken into account.

REFERENCES

[1] Lange, S. and Ricoeur, A., A condensed microelectromechanical approach for modeling tetragonal ferroelectrics, International Journal of Solids and Structures 54, 2015, pp. 100 – 110.

[2] Ricoeur, A., Avakian, A. and Lange, S., Microstructured multiferroic materials: modelling approach towards efficiency and durability. In: Altenbach et al. (eds.), Advances in Mechanics of Materials and Structural Analysis, Advanced Structural Materials, 80, Springer 2018, pp. 297 – 328.

[3] Lange, S. and Ricoeur, A., High cycle fatigue damage and life time prediction for tetragonal ferroelectrics under electromechanical loading, International Journal of Solids and Structures 80, 2016, pp. 181 – 192.

NONLINEAR THERMO-ELECTROMECHANICAL MODELING OF FERROELECTRIC MATERIALS: VARIATIONAL PRINCIPLES AND TEMPERATURE CHANGES IN CYCLICALLY LOADED SAMPLES

Marius Wingen[1,*] and **Andreas Ricoeur**[1]

[1] Institute of Mechanics, Chair of Engineering Mechanics / Continuum Mechanics, University of Kassel
Mönchebergstr. 7, 34109 Kassel, Germany

Abstract. *The presented results are based on a micromechanically and physically motivated nonlinear constitutive model. The model considers the mutual nonlinear coupling of thermal and electromechanical fields. The numerical calculations show the effects of temperature on the electromechanical field quantities and vice versa. They also reveal switching processes in ferroelectrics and associated heating, taking into account their dependence on temperature. Results of temperature changes at a crack tip due to domain switching at subcritical electric loading and of the heating of a bulk specimen are compared to experimental findings, just as polarization hystereses at different temperatures.*

1 Introduction

With the increasing use of ferroelectric materials for industrial applications, one recognizes, besides the great advantages, more and more problems with the materials. One of these is component durability and resistance. Long neglected temperature changes, especially in cyclically loaded samples, cause damage and property changes of such components. This paper will briefly compare some numerical calculations with experimental results for the temperature changes in ferroelectric materials under alternating electric fields. Without elaborating on the components, the algebraic system of equations

$$\begin{bmatrix} 0 & 0 & 0 \\ 0 & 0 & 0 \\ [D_{\Theta u}] & [D_{\Theta\phi}] & [D_{\Theta\Theta}] \end{bmatrix} \begin{bmatrix} \{\dot{u}\} \\ \{\dot{\phi}\} \\ \{\dot{\Theta}\} \end{bmatrix} + \begin{bmatrix} [K_{uu}] & [K_{u\phi}] & [K_{u\Theta}] \\ [K_{\phi u}] & [K_{\phi\phi}] & [K_{\phi\Theta}] \\ 0 & 0 & [K_{\Theta\Theta}] \end{bmatrix} \begin{bmatrix} \{u\} \\ \{\phi\} \\ \{\Theta\} \end{bmatrix} = \begin{bmatrix} \{f_u\} + \{f_u^e\} \\ \{f_\phi\} + \{f_\phi^e\} \\ \{f_\Theta\} + \{f_\Theta^e\} \end{bmatrix} \quad (1)$$

is the basis for solving nonlinear thermo-electromechanical boundary value problems by implementation into the commercial FE-software abaqus as a user defined element. On the right hand side of Eq. (1), $\{f_u\}$, $\{f_\phi\}$ and $\{f_\Theta\}$ represent nodal loads due to ferroelectric switching, where u, ϕ and Θ stand for displacement, electric potential and temperature change, respectively. For stationary problems, just

$$\{f_\Theta\} = \int\limits_V [N_\Theta]^T \left([\sigma] \frac{\Delta\{\epsilon^{irr}\}}{\Delta t} + \{E\} \frac{\Delta\{P^{irr}\}}{\Delta t} \right) dV \quad (2)$$

effectuates the impact of electromechanical fields on the temperature. Besides the shape functions [N$_\Theta$], stresses $\{\sigma\}$, electric field $\{E\}$, switching strain $\{\epsilon^{irr}\}$ and polarization $\{P^{irr}\}$, Δt appears in Eq. (2) as a time parameter to introduce the switching power. Further derivations of the theoretical framework have been abandoned in favor of numerical examples at this point.

---

[*] Corresponding author: Marius Wingen (✉ marius.wingen@uni-kassel.de)

⇒ TABLE OF CONTENTS

2 Numerical examples

2.1 Plate of polycrystalline PZT under alternating electric field

In this section, the experimental result of Chen et al. [1] for the heating of a polycrystalline PZT-5 plate under sinusoidal bipolar electric loading of 1 Hz and an amplitude of 1.2E$_c$ is compared with simulations. Before the temperature change, presented in Fig. 1(a), was measured, the specimen (12mm x 6mm x 6mm) was poled along the 12mm edge with $\bar{E}$ = 2E$_c$. The experiment shows that any amplitude above E$_c$ results in similar heating within the sample, while lower electric fields scarcely lead to temperature changes. For the simulation, a two-dimensional boundary value problem of a plate with the dimensions 12mm x 6mm is considered. The model consists of 800 finite elements with 4 integration points each, thus, within the framework of our constitutive model, representing a system of 3200 statistically oriented grains. As in the experiment, the sample was first poled numerically along the 12mm edge, before being cyclically loaded with 1.2E$_c$ for recording the temperature change. On the bottom, the system is mechanically fixed. The term with time derivatives in Eq. (1), representing the linear transient elasto- and electrocaloric effects, is neglected ([D$_{\Theta u}$] = 0, [D$_{\Theta \phi}$] = 0, [D$_{\Theta\Theta}$] = 0) in all calculations, so the switching process is assumed to be dominant for temperature changes of the material. For the calculations, the material data for PZT-5 were used. As caloric Dirichlet boundary condition, the temperature change at all edges is chosen Θ_S = 0K. Accordingly, a temperature Θ_∞ far from the specimen has to be determined, whereupon Θ_S - Θ_∞ is the experimentally measured heating which, according to Fig. 1(a), is Θ_S - Θ_∞ = 0.14K per half cycle. The heat transfer coefficient

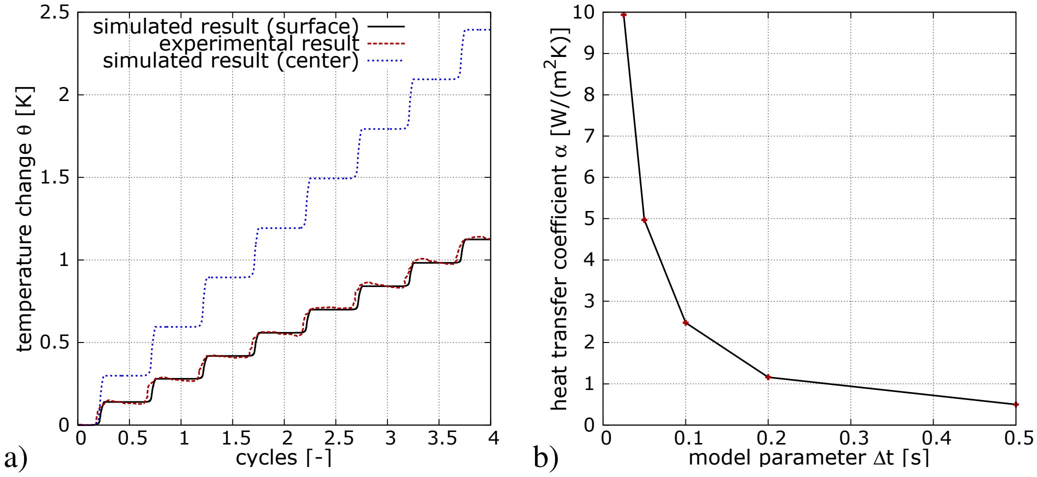

Figure 1: a) Comparison of the temperature vs. electric load cycles between experimental [1] and numerical results; b) heat transfer coefficient α vs. model parameter Δt.

$$\alpha = \frac{q_s(\Delta t)}{\Theta_S - \Theta_\infty} \tag{3}$$

is thus calculated from the heat flux density q$_s$ averaged across the longer edges of the specimen. According to Eqs. (1) and (2), Δt has a decisive impact on q$_s$. Fig. 1(b) shows the calculated heat transfer coefficient α vs. various model parameters Δt. The plot follows a 1/Δt^2-function. Typical heat transfer coefficients of free convection at a vertical wall are around $5\frac{\mathrm{W}}{\mathrm{m^2K}}$, providing Δt $\approx$ 0.05s. The solid black line in Fig. 1(a) represents Θ_S - Θ_∞ from the simulation with α = $5\frac{\mathrm{W}}{\mathrm{m^2K}}$ and Δt = 0.05s. The core temperature of the specimen has been calculated with the same parameters, providing the blue dotted line in Fig. 1(a).

⇒ TABLE OF CONTENTS

2.2 Temperature dependence of ferroelectric properties

Lacking the values for PZT-5, the temperature dependence of the spontaneous polarization P_0 and the coercivity E_c is taken from PZT-5A and of the spontaneous strain ϵ_D from PZT 20/80 [3]. Therefore, somewhat qualitative comparisons between simulated and experimental results are shown here. The parameter $\Delta t = 0.05s$ and the boundary value problem for the calculations remain the same as in Sec. 2.1.

Fig. 2(a) shows a comparison of the calculated dielectric hysteresis in the centre of the specimen with experimental results of the sponaneous polarization for PZT-5A [3]. The simulations reveal the temperature-induced change in the coercive field E_c, as the hysteresis narrows at higher temperatures, just as the experimental data show. The height of the simulated hysteresis at 25°C is distinctly smaller than the one at 250°C. The difference is explained by the sponaneous polarization, which is larger for 250°C than for 25°C. The simulations, however, still do not take into account the frequency dependence of the material parameters.

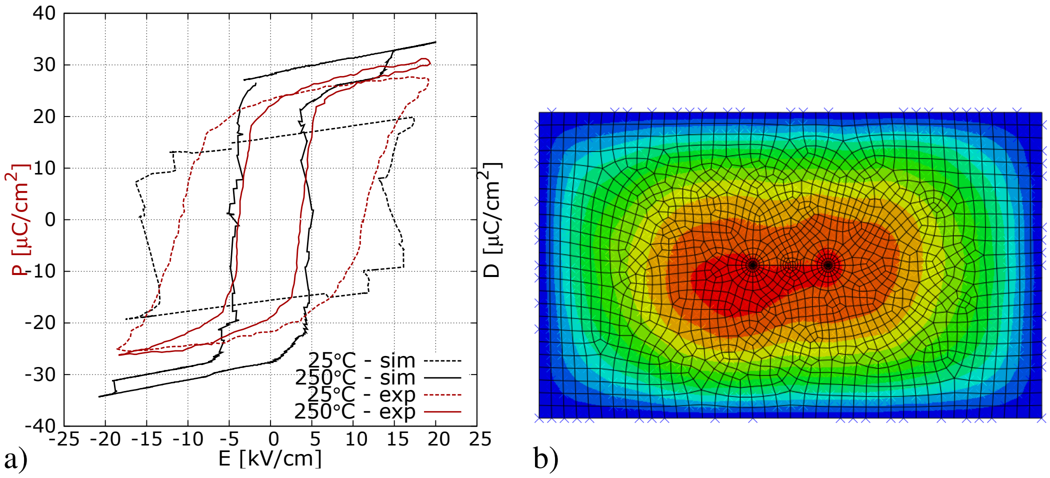

a) b)

Figure 2: a) Comparison of experimental [3] and numerical hystereses for two ambient temperatures; b) temperature distribution of a sample with two crack tips after 4 load cycles.

2.3 Temperature evolution at crack tips

Experiments have shown that an alternating electric field with high frequency or large amplitude, applied to a ferroelectric solid, lead to a significant increase of the temperature at crack tips [2]. Fig. 3(b) shows the experimentally determined temperature evolution at a crack tip at high electric frequency up to 20000 load cycles for a stationary crack. For the simulation, a two-dimensional boundary value problem of a 20 x 12mm plate with a 3mm centre crack running parallel to the longer edges is considered. The plate consists of 1808 finite elements with 4 integration points each, thus representing a system of 7232 grains. The caloric boundary condition is Θ_S = 0K at all edges. Fig. 2(b) shows the temperature distribution for an alternating electric field along the shorter axes with the subcritical amplitude of $0.75E_c$. Obviously, the heating is induced by the domain switching in the vicinity of the crack. In Fig. 3(a), the temperature evolution due to switching events at the crack tip is shown for four load cycles. The temperature change is in a range of 4mK per cycle. Ignoring the temperature-dependence of material parameters, the temperature profile from Fig. 3(a) can be extrapolated to 20000 load cycles, which has been done in Fig. 3(b) and compared to experimental results [2]. It can be seen that the magnitudes of the temperature changes of calculation and experiment are similar

⇒ TABLE OF CONTENTS

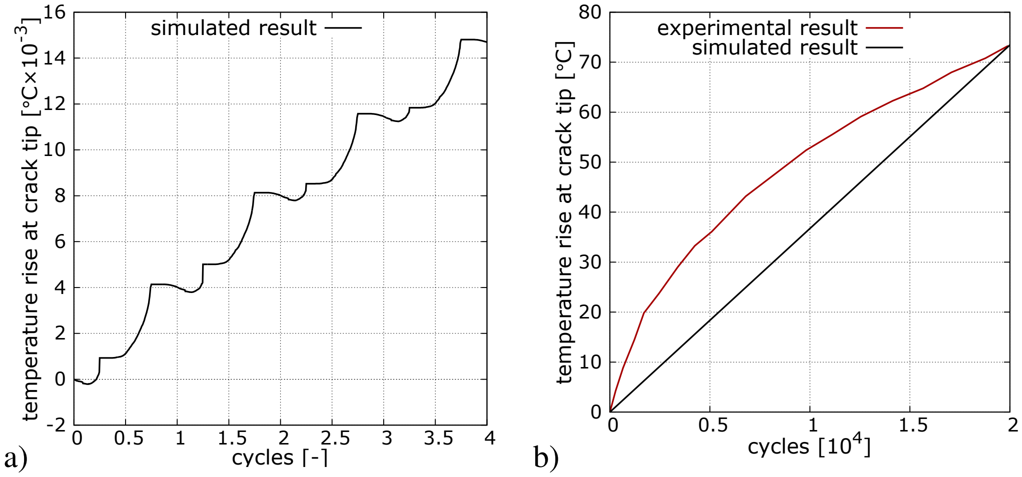

Figure 3: a) Simulated temperature evolution at crack tip under subcritical electric loading; b) comparison of extrapolated calculated temperature evolution and experimental result [2].

and even identical after 20000 cycles. The concave curvature of the experiment is partly due to the reduced E_c and ϵ^{irr} and thus heat source intensity with increasing temperature and partly due to the increasing heat flux across the surfaces.

REFERENCES

[1] H.-S. Chen, Y.-M. Pei, B. Liu, and D.-N. Fang. Rate dependent heat generation in single cycle of domain switching of lead zirconate titanate via in-situ spontaneous temperature measurement. *Applied Physics Letters*, 102, 242912; doi: 10.1063/1.4811702, 2013.

[2] H.-S. Chen, H.-L. Wang, Y.-M. Pei, Y.-J. Wei, B. Liu and D.-N. Fang. Crack instability of ferroelectric solids under alternative electric loading. *Journal of the Mechanics and Physics of Solids*, 81, 75-90, 2015.

[3] M.W. Hooker. Properties of PZT-Based Piezoelectric Ceramics Between -150 and 250°C. *Lockhead Martin Engineering and Sciences Co.*, NASA/CR-1998-208708, Hampton, Virginia, 1998.

[4] Y.C. Song, A.K. Soh, and Y. Ni. Phase field simulation of crack tip domain switching in ferroelectrics. *Journal of Physics D: Applied Physics*, doi: 10.1088/002-3727/40/4/040, 2007

PHASE-FIELD MODELING OF FLEXOELECTRICITY IN FERROELECTRICS

Bai-Xiang Xu* **and Shuai Wang**

Institute of Materials Science, Department of Materials and Geosciences, TU Darmstadt
Otto-Berndt-Strasse 3, Darmstadt, Germany

Abstract. *A phase-field model is presented in this work to study the flexoelectric effect in ferroelectric materials. Starting with the thermodynamic analysis, the flexo induced electric field is demonstrated. On the basis of the extended Landau free energy, the phase-field model is formulated by using the spontaneous polarization as the order parameter. Thereby the piezoelectricity, electrostriction, and flexoelectricity are taken in account explicitly. Benchmark example on a ferroelectric thin film under concentrated force is studied. It shows that the strain gradient induced by the concentrated force leads to a flexo electric field and thus can switch the polarization by 180 degree, in contrast to the well-known mechanical-stress-induced 90 degree switching.*

1 Landau free energy: flexoelectricity induced bias field

The flexoelectric effect is an electromechanical effect which indicates the linear coupling between the polarization and the strain gradient. The inverse effect implies the coupling between the strain and the polarization gradient. Different from ferroelectricity or piezoelectricity, flexoelectricity is a universal property exist in the materials which does not depend on any symmetry of the crystal structure. [1] Flexoelectricity has been utilized in microstructural functional materials designing, domain engineering and ferroelectric memory writing. Moreover, flexoelectric effect has been used to explain peculiar phenomena at nanoscale, e.g. mammalian hearing mechanism through hair cells. For a simply thermodynamic study, one can use the extended Landau free energy (shown for 1D case) in the following form:

$$\tilde{\mathcal{F}} = \mathcal{F}(P) - \frac{1}{2} f P \nabla \varepsilon = \alpha_1(T)P^2 + \alpha_{11}P^4 + \alpha_{111}P^6 + \alpha_{1111}P^8 - \frac{1}{2} f P \nabla \varepsilon, \tag{1}$$

where T, P, f and ε are temperature, polarization, flexocoupling coefficient and strain, respectively. Similar to the analysis for conventional ferroelectrics, minimization of free energy $\tilde{\mathcal{F}}$ gives rise to spontaneous polarization. On the other hand, from minimization of electrical entropy $\tilde{\mathcal{F}} - EP$, one obtains further the $P - E$ loop. Figure 1a-b shows the Landau energy and P-E loop in dependency on the strain gradient. Thereby, the coefficients for Barium Titanate are used: $\alpha_1(T) = 4.124(T - 388) \times 10^5\ C^{-2} \cdot m^2 \cdot N, \alpha_{11} = -209.7 \times 10^6\ C^{-4} \cdot m^6 \cdot N, \alpha_{111} = 129.4 \times 10^7\ C^{-6} \cdot m^{10} \cdot N, \alpha_{1111} = 3.863 \times 10^{10}\ C^{-8} \cdot m^{14} \cdot N$. The flexocoupling coefficient f is assumed to be 10V. In the paraelectric phase, for the case without strain gradient, the spontaneous polarization $P_s = 0$. As the strain gradient increases, P_s is increased from zero to finite number. P-E loops are also shifted. Similarly, in the ferroelectric phase, the spontaneous

---

*Corresponding author: Bai-Xiang Xu (✉ xu@mfm.tu-darmstadt.de)

⇒ TABLE OF CONTENTS

polarization can also altered by the strain gradient (Fig. 1a). As the strain gradient increases, the spontaneous polarization P_s also increase, and the P-E loop is thus shifted. In other words, flexoelectric effect induces a bias field of $f\nabla\varepsilon$.

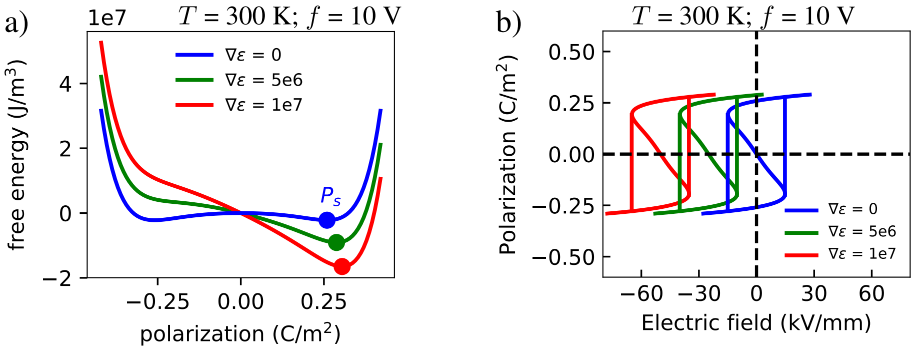

Figure 1: Influence of flexoelectricity on spontaneous polarization (a) and hysteresis loop.

2 Phase-field model

In the following the previous phase-field model [3, 4, 5] is extended to include the flexoelectricity. The mentioned previous models take the spontaneous polarization as an order parameter, with the piezoelectric effect and electrostriction taking explicitly into account. By making use of the extended Landau free energy discussed in the last section, a mechanically fully coupled model is presented in the following. Denote the space occupied by the solid body and its boundary by $\mathcal{B}$ and $\partial\mathcal{B}$, respectively. The governing equations consist of two parts: mechanics and electrostatics. The related

$$\sigma_{ij,j} + f_i = 0, \quad \varepsilon_{ij} = (u_{i,j} + u_{j,i})/2 \quad \texttt{in}\ \mathcal{B} \tag{2}$$

$$D_{i,i} = q, \quad E_i = -\phi_{,i} \quad \texttt{in}\ \mathcal{B} \tag{3}$$

where $\sigma_{ij}, \varepsilon_{ij}, u_i, f_i$ is the stress, strain, displacement and body force, respectively, while D_i, E_i, φ, q the electric displacement, electric field, electric potential and body charge.

According to the second law of thermodynamics, under the isothermal condition, the change rate in the Helmholtz free energy $\mathcal{H} = \mathcal{H}(\varepsilon_{ij}, D_i, P_i, P_{i,j})$ in the control volume should not be greater than the external power expended on the control volume, i.e.,

$$\{\int_{\mathcal{B}} \mathcal{H}\mathrm{dv}\}^{\cdot} \leq \mathcal{W}^{ext}, \quad \mathcal{W}^{ext} = \int_{\mathcal{B}} (f_i\dot{u}_i + q\dot{\phi} + \gamma_i\dot{P}_i)\mathrm{dv} + \int_{\partial\mathcal{B}} (\bar{t}_i\dot{u}_i + \bar{\omega}\dot{\phi} + \bar{\mu}_i\dot{P}_i)\mathrm{ds} \tag{4}$$

Here $\gamma_i, \bar{\mu}_i$ are the microforce and traction [6]. By Legendre transformation $\mathcal{H}_2 = \mathcal{H} - E_iD_i$,

$$\int_{\mathcal{B}} \Big\{(\sigma_{ij} - \frac{\partial\mathcal{H}_2}{\partial\varepsilon_{ij}})\dot{\varepsilon}_{ij} - (D_i + \frac{\partial\mathcal{H}_2}{\partial E_i})\dot{E}_i + (\xi_{ji} - \frac{\partial\mathcal{H}_2}{\partial P_{i,j}})\dot{P}_{i,j} - (\frac{\partial\mathcal{H}_2}{\partial P_i} - \gamma_i - \xi_{ji,j})\dot{P}_i\Big\}\mathrm{dv} \geq 0 \tag{5}$$

The last inequality holds for any admissible fields, one has

$$\sigma_{ij} = \frac{\partial\mathcal{H}_2}{\partial\varepsilon_{ij}} \qquad D_i = -\frac{\partial\mathcal{H}_2}{\partial E_i} \qquad \xi_{ji} = \frac{\partial\mathcal{H}_2}{\partial P_{i,j}} \tag{6}$$

Assuming $\dot{P}_i$ is negatively proportional to the terms in the bracket in front of it in the inequality and considering the third equation in the last equations, one arrives at

$$\dot{P}_i = -\frac{1}{\beta}\left(\frac{\partial\mathcal{H}_2}{\partial P_i} - (\frac{\partial\mathcal{H}_2}{\partial P_{i,j}})_{,j} - \gamma_i\right). \tag{7}$$

⇒ TABLE OF CONTENTS

where β is a positive constant. In this way, we obtain the Ginzburg-Landau type evolution equation for the polarization. In the current phase-field model, the electrical enthalpy consists of six parts, $\mathcal{H}_2 = \mathcal{H}^{el} + \mathcal{H}^{st} + \mathcal{H}^{pi} + \mathcal{H}^{sp} + \mathcal{H}^{gr} + \mathcal{H}^{fl}$ Here $\mathcal{H}^{el}$ is the classical elastic energy, $\mathcal{H}^{st}$ electric energy, $\mathcal{H}^{pi}$ piezoelectric coupling energy, $\mathcal{H}^{sp}$ the domain separation energy $\mathcal{H}^{gr}$ the interface energy and $\mathcal{H}^{fl}$ the flexoelctric energy. Details are given in the following:

$$\begin{aligned}
\mathcal{H}^{el} &= \frac{1}{2}C_{ijkl}(\varepsilon_{ij} - \varepsilon^0_{ij})(\varepsilon_{kl} - \varepsilon^0_{kl}), \quad \mathcal{H}^{st} = -\frac{1}{2}\kappa_{ij}E_iE_j - E_iP_i, \quad \mathcal{H}^{pi} = b_{ijk}(\varepsilon^0_{ij} - \varepsilon_{ij})E_k, \\
\mathcal{H}^{sp} &= \beta_1(G/\lambda)\mathcal{F}(P_i), \quad \mathcal{H}^{gr} = \beta_2(G\lambda)P_{i,j}P_{i,j}, \qquad \mathcal{H}^{fl}{=}-\frac{1}{2}f_{ijkl}\left(P_k\frac{\partial\varepsilon_{ij}}{\partial x_l} - \varepsilon_{ij}\frac{\partial P_k}{\partial x_l}\right)
\end{aligned}$$

where $C_{ijkl}, \kappa_{ij}, b_{ijk}, f_{ijkl}$ is the stiffness tensor, the dielectric tensor, the piezoelectric tensor, and flexoelectric tensor, respectively. In particular, β_1, β_2 can be explicitly expressed by the domain wall energy G and the domain wall thickness parameter λ. More details can be found in the previous work [4, 5] Inserting the electrical enthalpy into the constitutive and evolution equations, one derives at

$$\sigma_{ij} = \frac{\partial\mathcal{H}_2}{\partial\varepsilon_{ij}} = C_{ijkl}(\varepsilon_{kl} - \varepsilon^0_{kl}) - b_{ijk}E_k + \frac{1}{2}f_{ijkl}\frac{\partial P_k}{\partial x_l} \tag{8}$$

$$D_i = -\frac{\partial\mathcal{H}_2}{\partial E_i} = \kappa_{ij}E_j + b_{ijk}(\varepsilon_{kl} - \varepsilon^0_{kl}) + P_i \tag{9}$$

$$\dot{P}_k = -\frac{1}{\beta}\left(\frac{\partial\mathcal{H}^{sp}}{\partial P_k} - 2\beta_2P_{k,jj} - E_k - f_{ijkl}\varepsilon_{ij,l}\right) \tag{10}$$

The third equation implies that the flexo effect gives rise to a flexo electric field $f_{ijkl}\varepsilon_{ij,l}$, in accordance with the thermodynamic analysis. The first equation shows that the inverse flexoelectricity, i.e. polarization gradient induced stress, is also included in the phase-field model.

3 Numerical results

As a benchmark test, a ferroelectric thin film under a concentrated force is considered, which resembles to certain extend the mechanical situation induced by Piezoresponse force microscopy tip, as shown in Fig.2. It is known from elasticity, that a concentrated force leads to a decreasing vertical displacement in negative z direction, and thus a negative strain gradient $\varepsilon_{zz,z}$. Through flexoelectric effect, this strain gradient gives rise to the flexo-induced electric field $E_{fl} = f\varepsilon_{zz,z}$. Given a positive flexo-coefficient, the flexo-induced electric field E_{fl} should point downwards. Theoretically, this field may induce polarization switching of an initially upward poled sample, if the flexo effect is strong enough. Using the presented phase-field model, finite element simulation confirms the possibility. As it is shown in Fig. 3c, the polarization in the region below the concentrated force was switched from the upward to downward by 180 degree. Thereby the force F applied is 5 μN and the related flexo coefficient is taken as $f = 10V$. For comparison, two other cases were also considered: a) $f = 10V$, $F = 0.2\mu N$ and b) $f = 0V$, $F = 5\mu N$. In the case a) no switching is observed, due to the limited loading, while in the case b) only mechanically induced 90 degree switching was observed, due to the absence of flexo effect.

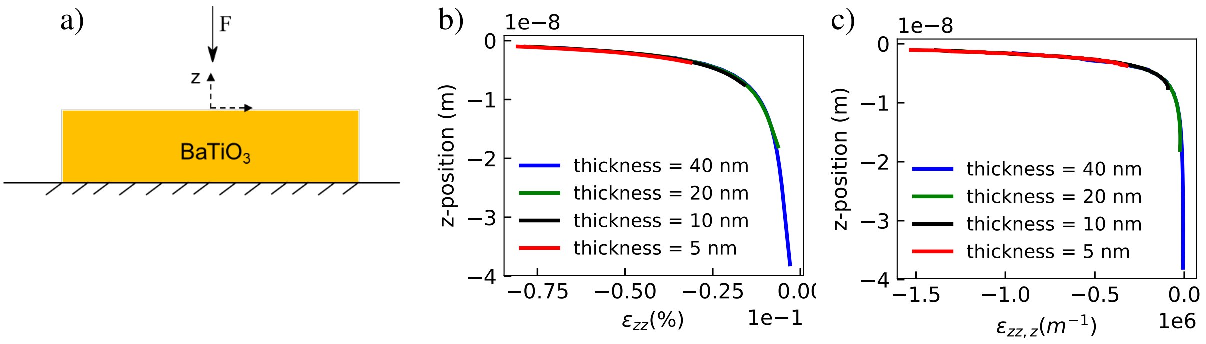

Figure 2: Distribution of the vertical strain (b) and its gradient (c) along the cross section directly under the concentrated force, illustrated in (a).

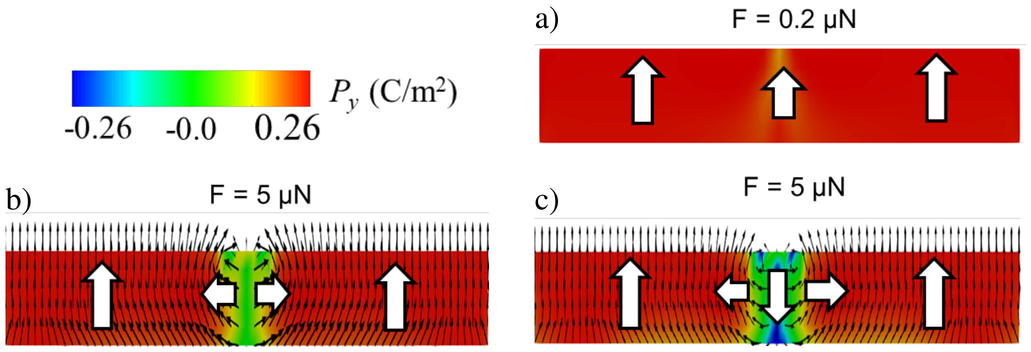

Figure 3: Domain configuration in a thin film under a concentrated force. a) Small concentrated force cannot induce switching. b) Piezoelectricity induced 90° switching if flexo effect is absent $f = 0$, while c) Flexoelectricity induced 180° switching for the case $f = 10, F = 5\mu N$.

REFERENCES

[1] P.V. Yudin and A.K. Tagantsev. Fundamentals of flexoelectricity in solids, *Nanotechnology*, 24(43): 432001, 2013.

[2] Y.L. Li, L.E. Cross and L.Q. Chen. A phenomenological thermodynamic potential for BaTiO$_3$ single crystals. *Journal of Applied Physics* 98(6): 064101, 2005.

[3] B.X. Xu, D. Schrade, R. Mueller, and D. Gross. Micromechanical analysis of ferroelectric structures by a phase field method. *Computational Materials Science* 45(3): 832-836, 2009

[4] B.X. Xu, D. Schrade, R. Müller, and D. Gross. Phase field simulation of domain structures in cracked ferroelectrics. *International journal of fracture* 165(2): 163-173, 2010

[5] B.X. Xu, D. Schrade, R. Müller, D. Gross, T. Granzow, and J. Rödel. Phase field simulation and experimental investigation of the electromechanical behavior of ferroelectrics. *ZAMM - Journal of Applied Mathematics and Mechanics* 18: 623-632, 2010.

[6] S. Wang, M. Yi, and B.X. Xu. A phase-field model of relaxor ferroelectrics based on random field theory. *International Journal of Solids and Structures* 83: 142-153, 2016.

VOLTAGE-DRIVEN MAGNETIZATION SWITCHING IN MAGNETOELECTRIC HETEROSTRUCTURE

Min Yi and Bai-Xiang Xu

Division Mechanics of Functional Materials, Institute of Materials Science, Technical University of Darmstadt
Otto-Berndt-Strasse 3, 64287 Darmstadt, Germany

Abstract. *Voltage control of magnetization switching without electric currents provides the possibility for revolutionizing the spintronics towards ultra-low power and high density. In this talk, for the voltage induced magnetization switching in magnetoelectric heterostructures, we present two kinds of interfacial mechanisms: interface strain transfer and interface charge modulation. By using the interface strain coupling, the electric-field control of magnetic states in the model heterostructure, which is constituted of the soft nanomagnet Co and the piezoelectric substrate PMN-PT, is demonstrated via the mechanically coupled phase-field simulations. Alternatively, by using the interface charge modulation, we show the voltage-driven 180° magnetization switching in epitaxial Pt/FePt/MgO nano-heterostructure at room temperature by combining first-principles calculations and temperature-dependent magnetization dynamics simulations. The study provides useful information for the design of low-power, reliable, and fast voltage-controlled spintronics.*

1 Introduction

Recently, the voltage control of magnetism without electric current has been extensively studied in order to achieve minimum power consumption and device miniaturization in next-generation spintronics. Such a control is usually implemented through the magnetoelectric (ME) coupling in heterostructures which possess coupled magnetic and electric properties. Generally, in ME heterostructures voltage controls the magnetism through the interfacial mechanisms such as elastic coupling via strain transfer, charge modulation, interface bonding, and exchange coupling. By using these various mechanisms, a voltage induced magnetization switching can be realized. For example, in order to achieve a high signal-to-noise ratio in magnetic tunnel junction (MTJ), a significantly large electric resistance change of MTJ is required, which can only be achieved by a 180° switching in the free layer of MTJ. In this talk, we present the voltage-driven magnetization switching in magnetoelectric heterostructures by using two kinds of interfacial mechanisms, i.e. interface strain transfer and interface charge modulation.

2 Interface strain mediated magnetization switching

For the ferromagnetic/ferroelectric heterostructures, elastic coupling mechanism is most extensively investigated, i.e. a strain generated in a ferroelectric layer by a voltage is transferred to the ferromagnetic layer through the interface and thus can be used to tailor magnetization through the magnetoelastic coupling. The model heterostructure is shown in Fig. 1a, including a nanomagnetic layer Co and a piezoelectric substrate PMN-PT. The nanomagnet is assumed

---

*Corresponding author: Min Yi, Bai-Xiang Xu (✉ yi@mfm.tu-darmstadt.de, xu@mfm.tu-darmstadt.de)

⇒ TABLE OF CONTENTS

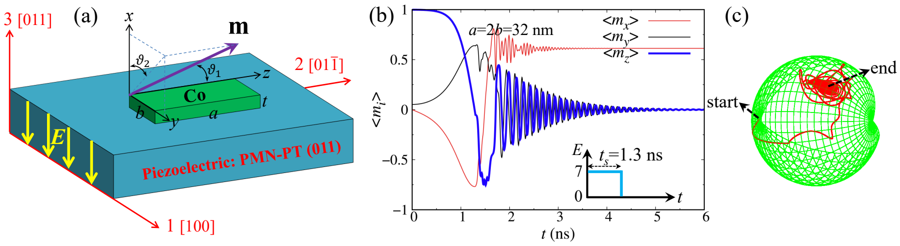

Figure 1: (a) Model heterostructure containing magnetic Co and piezoelectric PMN-PT(011). (b) Electric-field pulse induced dynamics of average magnetization components $\langle m_i \rangle$, $a = 2b = 32$ nm. (c) 3D magnetization trajectory. Ref. [4].

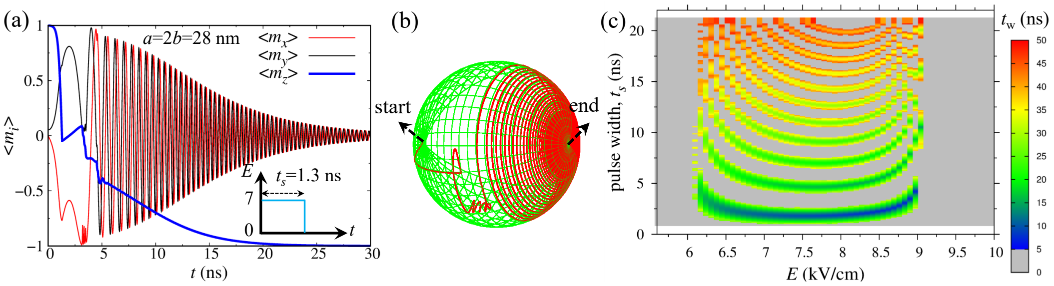

Figure 2: (a) Electric-field pulse induced dynamics of average magnetization components $\langle m_i \rangle$, $a = 2b = 28$ nm. (b) 3D magnetization trajectory. (c) 180° switching time t_w as a function of electric field magnitude E and pulse width t_s. Gray region denotes no switching. Ref. [4].

to be much smaller than the substrate so that the strain transferred from the PMN-PT to the Co nanomagnet is nearly uniform. In order to simulate the voltage induced magnetization switching in the Co/PMN-PT heterostructure, we use the mechanically coupled phase-field model. For the details of the model, readers are suggested to refer to our previous work in Refs. [1, 2, 3].

As show in Fig. 1a, two angles ϑ_1 and ϑ_2 are adopted to represent the magnetic state. In the phase-field model, the generalized evolution equation for the order parameters ϑ_1 and ϑ_2 takes the form [1]

$$\frac{1}{M_s}\left(\frac{\partial \mathcal{H}}{\partial \vartheta_{\mu,j}}\right)_{,j} - \frac{1}{M_s}\frac{\partial \mathcal{H}}{\partial \vartheta_\mu} + \zeta_\mu^{\text{ex}} = \frac{1}{\gamma_0} L_{\mu\gamma}\frac{\partial \vartheta_\gamma}{\partial t} \quad \text{with} \quad L_{\mu\gamma} = \begin{bmatrix} \alpha & -\sin\vartheta_1 \\ \sin\vartheta_1 & \alpha\sin^2\vartheta_1 \end{bmatrix}. \tag{1}$$

In addition, the mechanical equilibrium equation and the Maxwell equation which governs the magnetic part, i.e. $(\partial\mathcal{H}/\partial\varepsilon_{ij})_{,j} = \mathbf{0}$ and $(-\partial\mathcal{H}/\partial H_j)_{,j} = 0$, are incorporated.

By using the six degrees of freedom $[u_1, u_2, u_3, \phi, \vartheta_1, \vartheta_2]^{\mathrm{T}}$, a three-dimensional nonlinear finite element implementation is performed to solve the above governing equations. The nanomagnet size is $a = 2b$ and $t = 2$ nm. The materials parameters and simulation details are presented in Ref. [4]. The strain generated by applying an electric field to the PMN-PT is estimated as $\varepsilon_{yy} = Ed_{31}$ and ε_{zz}=Ed_{32} in the nanomagnet Co, as shown in Fig. 1a. Fig. 1b shows the dynamics of average magnetization components $\langle m_i \rangle$. The magnetization dynamics is induced by an electric field with a pulse width of 1.3 ns. It can be found that in the case of $a = 2b = 32$ nm, $\langle m_z \rangle$ does not change from the initial 1 to the final -1, i.e. no 180° switching is achieved. In contrast, $\langle m_x \rangle$ changes from the initial 0 to the final ~ 0.62, indicating a partial switching and a vortex-like magnetic state. The 3D magnetization trajectory in Fig. 1c also indicates the partial switching. If the nanomagnet size is decreased to $a = 2b = 28$ nm, an electric field pulse induced 180° switching is possible, as shown in Fig. 2a and b. We further manipulate both the electric field magnitude and pulse width to give a systematic insight onto the 180° switching condition and the switching time, as shown in Fig. 2c. It can be seen that the minimum electric field for a 180° switching is around 6.1 kV/cm and the maximum is around 9 kV/cm. In order to achieve a 180° switching, both the electric field magnitude and pulse width should be carefully designed. In the case of E ~8.9 kV/cm and $t_s = 3.7$ ns, a fast switching with t_w ~7.4 ns can be achieved. More details on the realization of 180° switching and the formation of vortex-like state can be found in Ref. [4].

3 Interface charge mediated magnetization switching

Interface charge modulation has been deemed as an ideal way for realizing magnetic switching in thin film heterostructures. The voltage induced interface charge change can modulate the interface magnetic properties, and provide the possibility of switching magnetization by voltage. In this talk, we take epitaxial Pt/FePt/MgO heterostructures (Fig. 3a) as a model system with a lateral size of several tens of nanometers. An elliptical shape of FePt (Fig. 3b) is chosen. By controlling the electric field, epitaxial strain and magnetization dynamics, the in-plane and perpendicular 180° magnetization switching (Fig. 3c) is achievable in the case of in-plane and perpendicular equilibrium magnetic state, respectively. Specifically, combining first-principles calculation and temperature-dependent magnetization dynamics, we demonstrate the in-plane and perpendicular 180° magnetization switching at room temperature. More details on the first-principles calculations and finite-temperature magnetization dynamics simulations can be found in Ref. [5].

Fig. 3d indicates that in the case of an electric field of 0.9 V/nm, the charge density around Pt and Fe atoms which are close to the interface is evidently decreased. The effect of electric field extends to the first two layers of FePt next to the interface. The charge change will affect the d-orbital hybridization and thus the magnetocrystalline anisotropy energy (MAE). Details on the first-principles results of the voltage-controlled MAE are provided in Ref. [5].

By using the first-principles results as input, we perform magnetization dynamics simulations based on the model in Fig. 3b to study the 180° switching. Fig. 4 compares the switching behaviors at 0 K with those at 300 K. It can be found from Fig. 4a that at 0 K, the 180° switching is deterministic, with a minimum switching time around 2 ns. When the temperature is involved, statistical methodology should be applied. As shown in Fig. 4b and c at 300 K, a switching probability (the percentage of successful 180° switching) is obtained. Fig. 4b shows that at room temperature the probability of the 180° switching reaches 70%. If we apply a

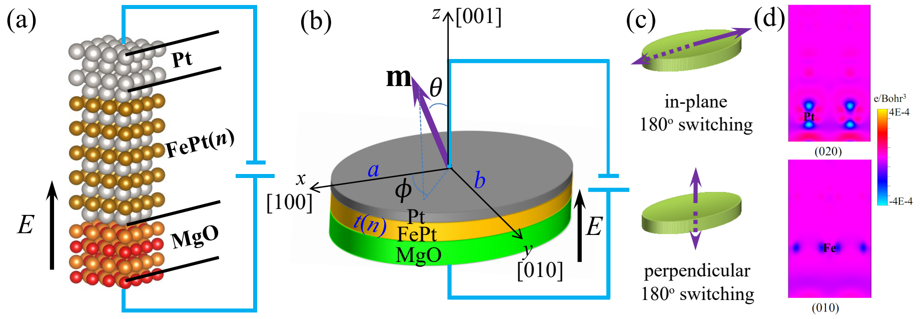

Figure 3: (a) Material model system for a first-principles calculations and (b) magnetization dynamics simulation. (c) Illustrations of in-plane and perpendicular 180° switching. (d) First-principles results on the electric field ($E = 0.9$ V/nm) induced charge density change near Pt and Fe atoms close to the MgO/FePt interface. Ref. [5].

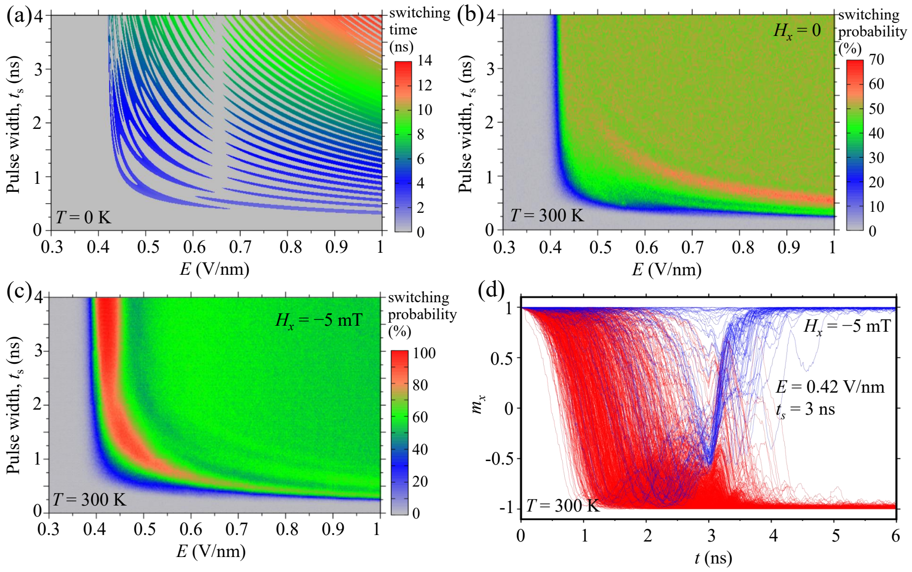

Figure 4: In-plane 180° switching. (a) Switching time at 0 K. Switching probability at 300 K: (b) no bias field and (c) bias field $H_x = -5$ mT. (d) 1,000 trajectories with a switching probability of $\sim 93.2\%$ at 300 K. Ref. [5].

small bias magnetic field $H_x = -5$ mT which is the strength of a typical refrigerator magnet, a switching probability above 90% can be achieved (Fig. 4c). In Fig. 4d, we present 1,000 switching trajectories for in-plane switching. The switching time is found to be around 4 ns. The switching probability is $\sim 93.2\%$. Undeniably, decreasing the error probability as much as possible is desirable. However, the achieved switching probability around 90% here is still reasonable or may be adequate for memory applications where different on-chip error detection and correction schemes exist.

Acknowledgments

The financial support from the German Science Foundation (XU 121/7-1, XU 121/4-2) is appreciated. The authors also greatly acknowledge the access to the Lichtenberg High Performance Computer of TU Darmstadt.

REFERENCES

[1] M. Yi and B-.X. Xu. A constraint-free phase field model for ferromagnetic domain evolution, *Proceedings of the Royal Society A*, 470(2171): 20140517, 2014.

[2] M. Yi, B.-X. Xu, and Z. Shen. 180° magnetization switching in nanocylinders by a mechanical strain. *Extreme Mechanics Letters*, 3: 66–71, 2015.

[3] M. Yi, B.-X. Xu, and D. Gross. Mechanically induced deterministic 180° switching in nanomagnets. *Mechanics of Materials*, 87: 40–49, 2015.

[4] M. Yi, B.-X. Xu, R. Müller and D. Gross. Strain-mediated magnetoelectric effect for the electric-field control of magnetic states in nanomagnets. *Acta Mechanica*, https://doi.org/10.1007/s00707-017-2029-7, 2017.

[5] M. Yi, H. Zhang, and B.-X. Xu. Voltage-driven charge-mediated fast 180 degree magnetization switching in nanoheterostructure at room temperature. *npj Computational Materials*, 3: 38, 2017.

Modeling and Simulation of 3D Printing of Functionalized Materials with Machine-Learning System Design

Tarek Zohdi

Webpage: http://www.me.berkeley.edu/faculty/zohdi/
Chancellor's Professor, Dept. of Mech. Eng., UC Berkeley

Will C. Hall Family Endowed Chair in Engineering

Chair, UC Berkeley Comp. and Data Sci. and Eng. Programhttp://citris-uc.org/decse-organization/

6117 Etcheverry Hall, UC, Berkeley, CA 94720-1740
Email: zohdi@berkeley.edu Phone: (510) 642-9172

Within the last decade, several industrialized countries have stressed the importance of advanced manufacturing to their economies. Many of these plans have highlighted the development of additive manufacturing techniques, such as 3D printing, which are still in their infancy. The objective is to develop superior products, produced at lower overall operational costs. For these goals to be realized, a deep understanding of the essential ingredients comprising the materials involved in additive manufacturing is needed. The combination of rigorous material modeling theories, coupled with the dramatic increase of computational power can potentially play a significant role in the analysis, control, and design of many emerging additive manufacturing processes. Specialized materials and the precise design of their properties are key factors in the processes. Specifically, particle-functionalized materials play a central role in this field, in three main ways: (1) to endow filament-based materials by adding particles to a heated binder (2) to ``functionalize'' inks by adding particles to freely flowing solvents and (3) to directly deposit particles, as dry powders, onto surfaces and then to heat them with a laser, e-beam or other external source, in order to fuse them into place. The goal of these processes is primarily to build surface structures, coatings, etc., which are extremely difficult to construct using classical manufacturing methods. The objective of this presentation is to introduce the audience to basic techniques which can allow them to rapidly develop and analyze particulate-based materials needed in new additive manufacturing processes. This presentation is broken into two main parts: continuum and discrete element approaches. The materials associated with methods (1) and (2) are types of continua (particles embedded in a continuous binder) and are treated using continuum approaches. The materials in method (3), which are of a discrete particulate character, are analyzed using discrete element methods. Integration of these processes within free-form robotic systems consisting of attaching a heated extruder to a robot arm which then releases material mixtures in free-space. These approaches are becoming popular because they utilize widely-available, highly-programmable, robots. However, often the release of a complex mixture in free-space is somewhat uncontrollable, thus electromagnetic field control has been proposed as one possible remedy to enhance the precision of such processes. Specifically, electromagnetic control of the material is achieved by electrifying and/or magnetizing the released material in the presence of a prescribed ambient electromagnetic field, in order to guide it to the desired position. Numerical simulations are undertaken to illustrate the overall system, which is comprised of an assembly of submodels. The submodular system structure allows for easy replacement of submodels within the overall framework. A Machine Learning Algorithm (MLA) is developed to identify and optimize the proper system parameters, which deliver a desired printed pattern. Specifically, an MLA is developed to ascertain the appropriate combination of robotic

---

[*] Corresponding author: First Co. Author (name@e-mail.adress)

motion and electromagnetic fields needed to create structures which would be difficult or impossible to achieve by purely mechanical means alone.

REFERENCES

[1] Zohdi, T. I. (2013). Rapid simulation of laser processing of discrete particulate materials. Archives of Computational Methods in Engineering. 20: 309-325.

[2] Zohdi, T. I. (2014). A direct particle-based computational framework for electrically-enhanced thermo-mechanical sintering of powdered materials. Mathematics and Mechanics of Solids.vol. 19, no. 1, 93-113.

[3] Zohdi, T. I. (2014) Additive particle deposition and selective laser processing-a computational manufacturing framework. Computational Mechanics. Vol 54, 171-191.

[4] Zohdi, T. I. (2015). Modeling and simulation of cooling-induced residual stresses in heated particulate mixture depositions. Computational Mechanics. Volume 56, 613-630.

[5] Zohdi, T. I. (2015). Modeling and efficient simulation of the deposition of particulate flows onto compliant substrates. The International Journal of Engineering Science. Volume 99, 74-91. doi:10.1016/j.ijengsci.2015.10.012

[6] Zohdi, T. I. (2015). Modeling and simulation of laser processing of particulate-functionalized materials. Archives of Computational Methods in Engineering. 10.1007/s11831-015-9160-1, 1-25.

[7] Zohdi, T. I. (2016). A discrete element and ray framework for rapid simulation of acoustical dispersion of microscale particulate agglomerations. Computational Mechanics.Volume 57, Issue 3, pp 465-482

[8] Ganeriwala, R. and Zohdi, T. I. (2016). A coupled discrete element finite difference model of selective laser sintering. Granular Matter.18:21, DOI 10.1007/s10035-016-0626-0

[9] Zohdi, T. I. (2017). Computational modeling of electrically-driven deposition of ionized polydisperse particulate powder mixtures in advanced manufacturing processes. Journal of Computational Physics 340 309–329

[10] Zohdi, T. I. (2017). Construction of a rapid simulation design tool for thermal responses to laser-induced feature patterns. Computational Mechanics https://doi.org/10.1007/s00466-017-1503-3

[11] Zohdi, T. I. (2017). Laser-induced heating of dynamic depositions in additive manufacturing. Computer Methods in Applied Mechanics and Engineering. https://doi.org/10.1016/j.cma.2017.11.003

[12] Zohdi, T. I. (2017). Dynamic thermomechanical modeling and simulation of the design of rapid free-form 3D printing processes with evolutionary machine learning. Computer Methods in Applied Mechanics and Engineering. https://doi.org/10.1016/j.cma.2017.11.030

[13] Zohdi, T. I. and Wriggers, P. (Book, 2005, 2008) Introduction to computational micromechanics. Second Reprinting (Peer Reviewed). Springer-Verlag: http://www.bookmetrix.com/detail/book/806553f6-2a54-4071-a34d-f2d58bb5713f#downloads

[14] Zohdi, T. I. (Book, 5/2017). Modeling and simulation of functionalized materials for additive manufacturing and 3D printing: continuous and discrete media (Peer Reviewed). Springer-Verlag. http://www.springer.com/us/book/9783319700779

In dieser Schriftenreihe bisher erschienene Berichte:

Nr. 1 (2004) *Ein Modell zur Beschreibung finiter anisotroper elasto-plastischer Deformationen unter Berücksichtigung diskreter Rissausbreitung*, J. Löblein, Dissertation, 2004.

Nr. 2 (2006) *Polyconvex Anisotropic Energies and Modeling of Damage applied to Arterial Walls*, D. Balzani, Dissertation, 2006.

Nr. 3 (2006) *Kontinuumsmechanische Modellierung ferroelektrischer Materialien im Rahmen der Invariatentheorie*, H. Romanowski, Dissertation, 2006.

Nr. 4 (2007) *Mehrskalen-Modellierung polykristalliner Ferroelektrika basierend auf diskreten Orientierungsverteilungsfunktionen*, I. Kurzhöfer, Dissertation, 2007.

Nr. 5 (2007) *Proceedings of the First Seminar on the Mechanics of Multifunctional Materials*, J. Schröder, D.C. Lupascu, D. Balzani (Ed.), Tagungsband, 2007.

Nr. 6 (2008) *Zur Modellierung und Simulation diskreter Rissausbreitungsvorgänge*, O. Hilgert, Dissertation, 2008.

Nr. 7 (2009) *Least-Squares Mixed Finite Elements for Solid Mechanics*, A. Schwarz, Dissertation, 2009.

Nr. 8 (2010) *Design of Polyconvex Energy Functions for All Anisotropy Classes*, V. Ebbing, Dissertation, 2010.

Nr. 9 (2012) *Modeling of Electro-Mechanically Coupled Materials on Multiple Scales*, M.-A. Keip, Dissertation, 2012.

Nr. 10 (2012) *Geometrical Modeling and Numerical Simulation of Heterogeneous Materials*, D. Brands, Dissertation, 2012.

Nr. 11 (2012) *Modeling and simulation of arterial walls with focus on damage and residual stresses*, S. Brinkhues, Dissertation, 2012.

Nr. 12 (2014) *Proceedings of the Second Seminar on the Mechanics of Multifunctional Materials*, J. Schröder, D.C. Lupascu, M.-A. Keip, D. Brands (Ed.), Tagungsband, 2014.

Nr. 13 (2016) *Mixed least squares finite element methods based on inverse stress-strain relations in hyperelasticity*, B. Müller, Dissertation, 2016.

Nr. 14 (2016) *Electromechanical Modeling and Simulation of Thin Cardiac Tissue Constructs*, R. Frotscher, Dissertation, 2016.

Nr. 15 (2017) *Least-squares mixed finite elements for geometrically nonlinear solid mechanics*, K. Steeger, Dissertation, 2017.

Nr. 16 (2017)	*Scale-Bridging of Elasto-Plastic Microstructures using Statistically Similar Representative Volume Elements*, L. Scheunemann, Dissertation, 2017.
Nr. 17 (2018)	*Modeling of Self-healing Polymers and Polymeric Composite Systems*, S. Specht, Dissertation, 2017.
Nr. 18 (2014)	*Proceedings of the Third Seminar on the Mechanics of Multifunctional Materials*, J. Schröder, D.C. Lupascu, H. Wende, D. Brands (Ed.), Tagungsband, 2018.